



Transverse Seismic Design of Bridges with Longitudinal Keyway Joints



Prepared by:
Christopher W. Price, Ph.D. Candidate
Mervyn J. Kowalsky, Professor, Ph.D.
James M. Nau, Professor, Ph.D.
Rudolf Seracino, Professor, Ph.D.

24 May 2019

Prepared for:
Alaska Department of Transportation & Public Facilities
Statewide Research Office
3132 Channel Drive
Juneau, AK 99801-7898

Alaska Department of Transportation & Public Facilities

Research & Technology Transfer

REPORT DOCUMENTATION PAGE

Form approved OMB No.

Public reporting for this collection of information is estimated to average 1 hour per response, including the time for reviewing instructions, searching existing data sources, gathering and maintaining the data needed, and completing and reviewing the collection of information. Send comments regarding this burden estimate or any other aspect of this collection of information, including suggestion for reducing this burden to Washington Headquarters Services, Directorate for Information Operations and Reports, 1215 Jefferson Davis Highway, Suite 1204, Arlington, VA 22202-4302, and to the Office of Management and Budget, Paperwork Reduction Project (0704-1833), Washington, DC 20503

1. AGENCY USE ONLY (LEAVE BLANK) 4000(161)		2. REPORT DATE May 24, 2019	3. REPORT TYPE AND DATES COVERED FINAL REPORT, May 2016 through May 2019	
4. TITLE AND SUBTITLE Transverse Seismic Design of Bridges with Longitudinal Joints			5. FUNDING NUMBERS State Project Numbers HFHWY00038 Federal project numbers 4000(161)	
6. AUTHOR(S) Christopher W. Price, Ph.D. Candidate Mervyn J. Kowalsky, Professor, Ph.D. James M. Nau, Professor, Ph.D. Rudolf Seracino, Professor, Ph.D.				
7. PERFORMING ORGANIZATION NAME(S) AND ADDRESS(ES) Department of Civil, Construction, and Environmental Engineering North Carolina State University Raleigh, NC 27606			8. PERFORMING ORGANIZATION REPORT NUMBER 4000(161)	
9. SPONSORING/MONITORING AGENCY NAME(S) AND ADDRESS(ES) Alaska Department of Transportation and Public Facilities Research, Development & Technology Transfer 3132 Channel Drive Juneau, Alaska 99811-2500			10. SPONSORING/MONITORING AGENCY REPORT NUMBER Federal project numbers 4000(161)	
11. SUPPLEMENTARY NOTES				
12a. DISTRIBUTION / AVAILABILITY STATEMENT No restrictions			12b. DISTRIBUTION CODE	
13. ABSTRACT (Maximum 200 words) This research evaluated the seismic behavior of bridges with longitudinal joints. The experimental portion of the work consisted of ten full scale sub-assembly tests modelled after a typical as-built keyway joint. The joint was tested under pure shear to determine the joint shear-slip response and associated limit states (grout cracking, embedded rebar yielding/rupture, and girder cover concrete cracking). The analytical portion consisted of developing inelastic shear springs between girders using the response from the experiments and implementing springs into superstructure models to determine global response. In addition, moment curvature analysis was done to develop equations for nominal yield curvature of bridge superstructures. An alternative keyway connection was proposed to improve performance at the service limit state.				
14. KEYWORDS: Earthquake Engineering, Longitudinal Shear key, Transverses Loading, Bridges, Polyester Polymer Concrete, High Strength Grout., Shear-Slip, Yield Curvature			15. NUMBER OF PAGES 277	
			16. PRICE CODE N/A	
17. SECURITY CLASSIFICATION OF REPORT Unclassified	18. SECURITY CLASSIFICATION OF THIS PAGE Unclassified	19. SECURITY CLASSIFICATION OF ABSTRACT Unclassified	20. LIMITATION OF ABSTRACT None	

Notice

This document is disseminated under the sponsorship of the U.S. Department of Transportation in the interest of information exchange. The U.S. Government assumes no liability for the use of the information contained in this document.

The U.S. Government does not endorse products or manufacturers. Trademarks or manufacturers' names appear in this report only because they are considered essential to the objective of the document.

Quality Assurance Statement

The Federal Highway Administration (FHWA) provides high-quality information to serve Government, industry, and the public in a manner that promotes public understanding. Standards and policies are used to ensure and maximize the quality, objectivity, utility, and integrity of its information. FHWA periodically reviews quality issues and adjusts its programs and processes to ensure continuous quality improvement.

Author's Disclaimer

Opinions and conclusions expressed or implied in the report are those of the author. They are not necessarily those of the Alaska DOT&PF or funding agencies.

SI* (MODERN METRIC) CONVERSION FACTORS

APPROXIMATE CONVERSIONS TO SI UNITS

Symbol	When You Know	Multiply By	To Find	Symbol
LENGTH				
in	inches	25.4	millimeters	mm
ft	feet	0.305	meters	m
yd	yards	0.914	meters	m
mi	miles	1.61	kilometers	km
AREA				
in ²	square inches	645.2	square millimeters	mm ²
ft ²	square feet	0.093	square meters	m ²
yd ²	square yard	0.836	square meters	m ²
ac	acres	0.405	hectares	ha
mi ²	square miles	2.59	square kilometers	km ²
VOLUME				
fl oz	fluid ounces	29.57	milliliters	mL
gal	gallons	3.785	liters	L
ft ³	cubic feet	0.028	cubic meters	m ³
yd ³	cubic yards	0.765	cubic meters	m ³
NOTE: volumes greater than 1000 L shall be shown in m ³				
MASS				
oz	ounces	28.35	grams	g
lb	pounds	0.454	kilograms	kg
T	short tons (2000 lb)	0.907	megagrams (or "metric ton")	Mg (or "t")
TEMPERATURE (exact degrees)				
°F	Fahrenheit	5 (F-32)/9 or (F-32)/1.8	Celsius	°C
ILLUMINATION				
fc	foot-candles	10.76	lux	lx
fl	foot-Lamberts	3.426	candela/m ²	cd/m ²
FORCE and PRESSURE or STRESS				
lbf	poundforce	4.45	newtons	N
lbf/in ²	poundforce per square inch	6.89	kilopascals	kPa

APPROXIMATE CONVERSIONS FROM SI UNITS

Symbol	When You Know	Multiply By	To Find	Symbol
LENGTH				
mm	millimeters	0.039	inches	in
m	meters	3.28	feet	ft
m	meters	1.09	yards	yd
km	kilometers	0.621	miles	mi
AREA				
mm ²	square millimeters	0.0016	square inches	in ²
m ²	square meters	10.764	square feet	ft ²
m ²	square meters	1.195	square yards	yd ²
ha	hectares	2.47	acres	ac
km ²	square kilometers	0.386	square miles	mi ²
VOLUME				
mL	milliliters	0.034	fluid ounces	fl oz
L	liters	0.264	gallons	gal
m ³	cubic meters	35.314	cubic feet	ft ³
	cubic meters	1.307	cubic yards	yd ³
MASS				
g	grams	0.035	ounces	oz
kg	kilograms	2.202	pounds	lb
Mg (or "t")	megagrams (or "metric ton")	1.103	short tons (2000 lb)	T
TEMPERATURE (exact degrees)				
°C	Celsius	1.8C+32	Fahrenheit	°F
ILLUMINATION				
lx	lux	0.0929	foot-candles	fc
cd/m ²	candela/m ²	0.2919	foot-Lamberts	fl
FORCE and PRESSURE or STRESS				
N	newtons	0.225	poundforce	lbf
kPa	kilopascals	0.145	poundforce per square inch	lbf/in ²

TABLE OF CONTENTS

LIST OF TABLES	v
LIST OF FIGURES	vi
Executive Summary	xxi
Chapter 1 Introduction.....	1
1.1 Background.....	1
1.2 Motivation.....	4
1.3 Scope and Layout.....	5
Chapter 2 Literary review.....	6
2.1 Bulb-Tee Girder Bridges with Longitudinal Keyway Joints	6
2.2 Shear connectors in Prestressed Diaphragms	17
2.3 Modeling of Joints between Precast Members	23
Chapter 3 Study Plan.....	25
3.1 Research Gap	25
3.2 Objectives	26
Chapter 4 Experimental Program.....	27
4.1 Test Conceptualization.....	28
4.2 Experimental Test Setup.....	30
4.3 Instrumentation	33
4.4 Specimen Detailing.....	35
4.5 Specimen Construction	37
4.6 As Built Joint Detailing	40
4.6.1 Steel Connector.....	40
4.6.2 Longitudinal Shear Key	41
4.7 Material Properties.....	42
4.7.1 Concrete	42
4.7.2 Steel.....	44
4.7.3 Grout	46
4.7.3.1 High Strength Grout Material Study.....	48
4.7.3.2 Polyester Polymer Concrete Material Study.....	52
4.8 Loading Protocol.....	57
4.8.1 Maximum Shear Flow Parametric Study	60

Chapter 5 Experimental Phase I	64
5.1 Test 1a.....	64
5.1.1 Test 1a Summary	66
5.1.2 Test 1a Conclusion.....	72
5.2 Test 1b.....	74
5.2.1 Test 1b Summary	75
5.2.2 Test 1b Conclusion	85
5.3 Test 2.....	87
5.3.1 Test 2 Summary	88
5.3.2 Test 2 Conclusion	99
5.4 Test 3.....	100
5.4.1 Test 3 Summary	103
5.4.2 Test 3 Conclusion	113
5.5 Test 4.....	114
5.5.1 Test 4 Summary	117
5.5.2 Test 4 Conclusion	127
5.6 Test 5.....	128
5.6.1 Test 5 Summary	130
5.6.2 Test 5 Conclusion	142
5.7 Test 6.....	144
5.7.1 Test 6 Summary	146
5.7.2 Conclusion	155
5.8 Phase I Experimental Observations	158
5.9 Alternate Connections.....	167
5.9.1 Design Strength.....	171
Chapter 6 Experimental Phase II.....	175
6.1 Test 7.....	175
6.1.1 Test 7 Summary	178
6.1.2 Test 7 Conclusion	187
6.2 Test 8.....	188
6.2.1 Test 8 Summary	191
6.2.2 Test 8 Conclusion	204
6.3 Test 9.....	208

6.3.1	Test 9 Summary	211
6.3.2	Test 9 Conclusion	224
6.4	Test 10.....	225
6.4.1	Test 10 Summary	228
6.4.2	Test 10 Conclusion	243
6.5	Phase II Experimental Observations	246
6.6	Limit States	252
Chapter 7 Global Computational Bridge Model.....		253
7.1	Sub-Assembly Computational Model.....	253
7.2	Pinching 4 Material Model	256
7.3	Global Bridge Modeling Approach	257
7.4	Validation.....	258
7.5	Bridge 537 Super Structure.....	264
Chapter 8 Evaluating Yield Limit States for Bridge Superstructures		267
8.1.1	Slab Bridges	267
Chapter 9 Summary, Recommendations And Future Work.....		272
9.1	Experimental Program	272
9.2	Global Computational Model	275
9.3	Evaluating Yield Limit States for Bridge Super Structures.....	276
REFERENCES		278
Appendix	284	

LIST OF TABLES

Table 4.1:	Experimental Program	28
Table 4.2:	Average Concrete Compressive Strength	44
Table 4.3:	Phase I Material Properties of A706 #4 Rebar	45
Table 4.4:	Phase II Material Properties of A706 #4 Rebar	45
Table 4.5:	Phase I Material Properties of A36 ¼ in. Steel Plate Coupons.....	45
Table 4.6:	Phase II Material Properties of A36 ¼ in. Steel Plate Coupons	45
Table 4.7:	Phase II Material Properties of A36 1 in. Steel Plate Coupons	46
Table 4.8:	Average Grout Compressive Strength	48
Table 4.9:	Material Properties of Dayton Superior Sure-Grip High Performance Grout	50
Table 4.10:	Material Properties of Dayton Superior 1107 Advantage Grout	50
Table 4.11:	Material Properties of Sakrete Non-Shrink Construction Grout.....	51
Table 4.12:	Material Properties of BASF Master Flow 928 Grout.....	51
Table 4.13:	Material Properties of PPC 1121	54
Table 4.14:	Maximum Shear Flow Parametric Study Results	63
Table 5.1:	Phase I Damage State Progression Force and Displacement.....	165
Table 6.1:	Phase II Damage State Progression Force and Displacement	251
Table 6.2:	Longitudinal Shear Key Limit State Displacements.....	252
Table 8.1:	Slab Bridge Yield Curvature Coefficient Study Matrix	268

LIST OF FIGURES

Figure 1.1:	Typical Longitudinal Keyway Joint (a) Global View (b) Local View.	2
Figure 1.2:	Saftey Sound Estuary Bridge (a) Damaged Pier (b) Damaged Longitudinal Keyway Joint.	3
Figure 1.3:	Bridge Response (a) Global Superstructure Response (b) Pier Response.	4
Figure 2.1:	Maximum Horizontal Shear Force (Z. Ma, Chaudhury, Millam, & Hulsey, 2007)	7
Figure 2.2:	Comparison of Deflections (a) Loading G3; (b) Loading G2; (c) Loading G1 (Li & Ma, 2010)	8
Figure 2.3:	Keyway and Connector Details (Stanton & Mattock, 1987)	10
Figure 2.4:	Test Setup (H.-Y. Kim et al., 2013)	11
Figure 2.5:	Confinement Systems (Y. H. Kim & Trejo, 2014)	12
Figure 2.6:	Proposed New Joint Details (Li, Ma, Griffey, et al., 2010)	13
Figure 2.7:	Test Set Up (Zhu, Ma, Cao, & French 2012)	15
Figure 2.8:	Proposed New Joint Details (Sennah & Afefy, 2015)	17
Figure 2.9:	Shear Connectors (Venuti, 1970)	18
Figure 2.10:	Hairpin Connector (Jose A. Pincheira et al., 1998)	19
Figure 2.11:	Vector Connector (Fattah Shaikh & Feile, 2004)	20
Figure 2.12:	(a) Stud Welded Plate, (b) Bent Wing Connector, (c) Structural Tee Connector,(d) Mesh and Angle Connector, (e) Bent Plate Connector (José A. Pincheira et al., 2005)	21
Figure 2.13:	Shear Connectors (Cao & Naito, 2009; Naito et al., 2009)	22
Figure 4.1:	Induced Shear Flow through Longitudinal Joints	29
Figure 4.2:	Conceptualization of the Specimen	29
Figure 4.3:	Test Setup Conceptual View	31
Figure 4.4:	Test 3 Setup in CFL at NC State	32

Figure 4.5:	Instrumentation of Test Specimen	33
Figure 4.6:	Electrical Resistant Strain Gage Rosettes Applied to Connector Plate	34
Figure 4.7:	Specimen Detailing Plan (a) Front View (b) Side View.....	35
Figure 4.8:	Side Block Detailing Plan (a) Front View (b) Side View.....	36
Figure 4.9:	Reaction Block Detailing Plan (a) Front View (b) Side View.....	37
Figure 4.10:	Specimen Construction (a) Specimen (b) Side Block (c) Reaction Block	39
Figure 4.11:	Shear Connector (a) Top View (b) Side View	40
Figure 4.12:	Shear Connector Inserts (a) Top View (b) Side View.....	41
Figure 4.13:	Shear Connector Inserts (a) Specimen (b) Side Block.....	41
Figure 4.14:	Longitudinal Shear Key	42
Figure 4.15:	Longitudinal Shear Key Block Out.....	42
Figure 4.16:	ASTM C39 Cylinder Test.....	43
Figure 4.17:	ASTM 370 Tension Test.....	46
Figure 4.18:	Moist Curing of Grouted Specimen	47
Figure 4.19:	PPC 1121 Compressive Strength Comparison of Cube and Cylinders	55
Figure 4.20:	PPC 1121 Cube Compressive Strength f'_c Variation due to Temperature.....	55
Figure 4.21:	PPC 1121 1x1x11¼ Prism Shrinkage Strain	56
Figure 4.22:	Cyclic Force Loading Protocol	59
Figure 4.23:	Cyclic Displacement Loading Protocol	59
Figure 4.24:	Bridge 537 (a) Elevation View (b) Elevation View of Pier 2 (c) Typical Cross Section (d) Typical Cross Section of Girder.....	62
Figure 5.1:	Test 1a Force-Displacement Response	65
Figure 5.2:	Test 1a Rigid Body Rotation.....	65

Figure 5.3:	Test 1a Connector Plate Pocket at $\frac{1}{4}$ Plate Yield (a) Left Side (b) Right Side	66
Figure 5.4:	Test 1a Connector Plate Pocket at $\frac{1}{2}$ Plate Yield (a) Left Side (b) Right Side	67
Figure 5.5:	Test 1a Connector Plate Pocket on the way to $\frac{3}{4}$ Plate Yield (a) Left Side (b) Right Side	68
Figure 5.6:	Test 1a Connector Plate Pocket at Emergency Stop (a) Left Side (b) Right Side	68
Figure 5.7:	Test 1a Connector Plate Pocket Prior Strength Loss (a) Left Side (b) Right Side	69
Figure 5.8:	Test 1a Connector Plate Pocket After Strength Loss (a) Left Side (b) Right Side	70
Figure 5.9:	Test 1a Connector Plate Pocket at End of Test (a) Left Side (b) Right Side	70
Figure 5.10:	Test 1a Damage to the Shear Connector Pocket (a) Concrete Pocket (b) Embedded Rebar	71
Figure 5.11:	Plastic Moment of Embedded Rebar	72
Figure 5.12:	Test 1a Welds of Embedded Plates	72
Figure 5.13:	Test 1a. Damage to the Shear Connector Pocket (a) Concrete Pocket (b) Embedded Rebar	73
Figure 5.14:	Test 1b Force-Displacement Response	74
Figure 5.15:	Test 1b Rigid Body Rotation of Specimen vs Displacement	75
Figure 5.16:	Test 1b Grouted Shear Key at $\frac{1}{4}$ f't (a) r Side (b) Right Side	76
Figure 5.17:	Test 1b Grouted Shear Key at $\frac{1}{2}$ f't (a) Left Side (b) Right Side	76
Figure 5.18:	Test 1b Grouted Shear Key at $\frac{3}{4}$ f't (a) Left Side (b) Right Side	77
Figure 5.19:	Test 1b Grouted Shear Key at f't (a) Left Side (b) Right Side	77
Figure 5.20:	Test 1b Grouted Shear at Key Max Capacity (a) Left Side (b) Right Side	78
Figure 5.21:	Test 1b Grouted Shear Key at 0.25 in. RAM Δ (a) Left Side (b) Right Side	79

Figure 5.22:	Test 1b Grouted Shear Key at 0.50 in. RAM Δ (a) Left Side (b) Right Side	80
Figure 5.23:	Test 1b Grouted Shear Key at 0.75 in. RAM Δ (a) Left Side (b) Right Side	80
Figure 5.24:	Test 1b Grouted Shear Key at 1.00 in. RAM Δ (a) Left Side (b) Right Side	81
Figure 5.25:	Test 1b Grouted Shear Key at 1.50 in. RAM Δ (1) (a) Left Side (b) Right Side	82
Figure 5.26:	Test 1b Grouted Shear Key at 0.00 in. RAM Δ (1) (a) Left Side (b) Right Side	82
Figure 5.27:	Test 1b Grouted Shear Key at 1.50 in. RAM Δ (2) (a) Left Side (b) Right Side	83
Figure 5.28:	Test 1b Grouted Shear Key at 0.00 in. RAM Δ (2) (a) Left Side (b) Right Side	83
Figure 5.29:	Post Test 1b. Damage (a) Test Specimen and Side Blocks (b) Shear Key Grout	85
Figure 5.30:	Test 1b. Grouted Shear Key at 0.75 in. of displacement (a) Left Side (b) Right Side.....	86
Figure 5.31:	Test 2 Force-Displacement Response	87
Figure 5.32:	Test 2 Rigid Body Rotation of Specimen vs Displacement.....	88
Figure 5.33:	Test 2 Right Side of Grouted Shear Key at $\frac{1}{2}$ f't.....	89
Figure 5.34:	Test 2 Grouted Shear Key at $\frac{3}{4}$ f't (a) Left Side (b) Right Side	89
Figure 5.35:	Test 2 Grouted Shear Key at f't (a) Left Side (b) Right Side	90
Figure 5.36:	Test 2 Grouted Shear at Key Max Capacity (a) Left Side (b) Right Side	91
Figure 5.37:	Test 2 Grouted Shear Key at 0.44 in. RAM Δ (a) Left Side (b) Right Side	92
Figure 5.38:	Test 2 Grouted Shear Key at 0.48 in. RAM Δ (a) Left Side (b) Right Side	93
Figure 5.39:	Test 2 Right Side Grouted Shear Key at 0.58 in. RAM Δ	93
Figure 5.40:	Test 2 Grouted Shear Key at 0.74 in. RAM Δ (a) Left Side (b) Right Side	94
Figure 5.41:	Test 2 Grouted Shear Key at 1.04 in. RAM Δ (a) Left Side (b) Right Side	95

Figure 5.42:	Test 2 Grouted Shear Key at -0.06 in. RAM Δ (a) Left Side (b) Right Side	96
Figure 5.43:	Test 2 Left Side Grouted Shear Key at 0.96 in. RAM Δ	97
Figure 5.44:	Test 2 Grouted Shear Key at -0.07 in. RAM Δ (a) Left Side (b) Right Side	97
Figure 5.45:	Test 2 Post Damage (a) Undetached Test Specimen (b) Detached Test Specimen.....	98
Figure 5.46:	Test 2 Post Damage (a) Left Joint (b) Right Joint	99
Figure 5.47:	Test 2 Plate Welds (a) Left Shear Tab (b) Left Embedded Plate (c) Right Shear Tab (d) Right Embedded Plate.....	99
Figure 5.48:	Test 3 Force History.....	100
Figure 5.49:	Test 3 Displacement History.....	101
Figure 5.50:	Test 3 Force-Displacement Response	101
Figure 5.51:	Test 3 Force-Displacement Response Prior to Significant Strength Loss	102
Figure 5.52:	Test 3 Rigid Body Rotation	102
Figure 5.53:	Test 3 Grouted Shear Key $q_{\text{average}} = 0.0\text{k/in}$ (a) Left Side (b) Right Side	103
Figure 5.54:	Test 3 Grouted Shear Key $q_{\text{average}} = 1.0\text{k/in}$ (a) Left Side (b) Right Side – Third Cycle	104
Figure 5.55:	Test 3 Left Side of Grouted Shear Key $q_{\text{average}} = 1.8\text{k/in}$ – Third Cycle.....	104
Figure 5.56:	Test 3 HSS Load Spreader (a) Pre-Altered Test Setup (b) Post-Altered Test Setup	105
Figure 5.57:	Test 3 Grouted Shear Key Pocket $q_{\text{average}} = 2.6\text{k/in}$ (a) Left Side (b) Right Side– Third Cycle	106
Figure 5.58:	Test 3 Grouted Shear Key Pocket $q_{\text{average}} = 3.2\text{k/in}$ (a) Left Side (b) Right Side– Third Cycle	107
Figure 5.59:	Test 3 Grouted Shear Key $\Delta = -4.093$ in. (a) Left Side (b) Right Side.....	108
Figure 5.60:	Test 3 Removed Material (a) Left Side (b) Right Side.....	109
Figure 5.61:	Test 3 Grouted Shear Key $\Delta = -4.093$ in. with Material Removed (a) Left Side (b) Right Side.....	109

Figure 5.62:	Test 3 Damage to Shear Connector Inserts at $\Delta = -4.093$ in. (a) Left Side (b) Right Side.....	110
Figure 5.63:	Test 3 Damage to Right Side Shear Connector Inserts at $\Delta = 4.423$ in.	111
Figure 5.64:	Test 3 Test Specimen 3 at $\Delta = 0.082$ in.	111
Figure 5.65:	Test 3 Removed Shear Connector Plate (a) Top View Left Connector (b) Bottom View Left Connector (c) Top View Right Connector (d) Bottom View Right Connector	112
Figure 5.66:	Test 4 Displacement History.....	114
Figure 5.67:	Test 4 Load History	115
Figure 5.68:	Test 4 Force-Displacement Response.....	115
Figure 5.69:	Test 4 Rigid Body Rotation	116
Figure 5.70:	Test 4 Grouted Shear Key with Applied Load = 0 kips (a) Left Side (b) Right Side.....	117
Figure 5.71:	Test 4 Right Side of Grouted Shear Key with Applied Load = -153 kips	118
Figure 5.72:	Test 4 Grouted Shear Key with Applied Load = -306 kips (a) Left Side (b) Right Side.....	118
Figure 5.73:	Test 4 Grouted Shear Key Δ_{c1} (a) Left Side (b) Overall View –First Cycle	119
Figure 5.74:	Test 4 Left Side of Grouted Shear Key Cracking Δ_{c1} –First Cycle	119
Figure 5.75:	Test 4 Grouted Shear Key $-\Delta_{c1}$ –First Cycle.....	121
Figure 5.76:	Test 4 Grouted Shear Key $-\Delta_{c1}$ –Third Cycle	121
Figure 5.77:	Test 4 Grouted Shear Key Δ_{c3} –Second Cycle.....	123
Figure 5.78:	Test 4 Grouted Shear Key $-\Delta_{c6}$ –First Cycle.....	123
Figure 5.79:	Test 4 Grouted Shear Key $-\Delta_{c12}$ –First Cycle	124
Figure 5.80:	Test 4 Damage to Shear Connector Inserts at Δ_{c12} (a) Left Connector (b) Right Connector –Second Cycle.....	124
Figure 5.81:	Test 4 Grouted Shear Key $-\Delta_{c12}$ –Third Cycle.....	125

Figure 5.82:	Test 4 Damage to Right Side Shear Connector Insert at Δ_{c12} –Third Cycle.....	125
Figure 5.83:	Test 4 Damage to Left Side Shear Connector Insert at Δ_{c16} –Second Cycle	125
Figure 5.84:	Test 4 Removed Shear Connector Plate (a) Top View Left Connector (b) Bottom View Left Connector (c) Top View Right Connector (d) Bottom View Right Connector	126
Figure 5.85:	Test 5 Displacement History.....	128
Figure 5.86:	Test 5 Load History	129
Figure 5.87:	Test 5 Force-Displacement Response.....	129
Figure 5.88:	Test 5 Rigid Body Rotation	130
Figure 5.89:	Test 5 Grouted Shear Key with Applied Load = 0 kips (a) Left Side (b) Right Side.....	131
Figure 5.90:	Test 5 Grouted Shear Key with Applied Load = 106 kips (a) Left Side (b) Right Side.....	131
Figure 5.91:	Test 5 Grouted Shear Key with Applied Load = -213 kips	132
Figure 5.92:	Test 5 Grouted Shear Key with Applied Load = -266 kips	133
Figure 5.93:	Test 5 Grouted Shear Key with Applied Load = 280 kips.....	134
Figure 5.94:	Test 5 Grouted Shear Key – Significant Strength loss	135
Figure 5.95:	Test 5 Grouted Shear Key – Significant Strength Loss (a) Left Side (b) Right Side.....	135
Figure 5.96:	Test 5 Grouted Shear Key - Δ_{c1} –Third Cycle	137
Figure 5.97:	Test 5 Grouted Shear Key - Δ_{c4} –Third Cycle	137
Figure 5.98:	Test 5 Damage to Right Side Shear Connector Insert at Δ_{c6} –First Cycle	138
Figure 5.99:	Test 5 Damage to Right Side Shear Connector Insert at - Δ_{c6} – Frist Cycle.....	138
Figure 5.100:	Test 5 Damage to Left Side Shear Connector Insert at - Δ_{c6} – Frist Cycle.....	139
Figure 5.101:	Test 5 Damage to Shear Connector Insert at Δ_8 –First Cycle.....	140

Figure 5.102: Test 5 Removed Shear Connector Plate (a) Top View Left Connector (b) Bottom View Left Connector (c) Top View Right Connector (d) Bottom View Right Connector	141
Figure 5.103: Test 5 Removed Grouted Shear Key (a) Left Side (b) Right Side.....	142
Figure 5.104: Test 6 Displacement History.....	144
Figure 5.105: Test 6 Load History	145
Figure 5.106: Test 6 Test 6 Force-Displacement Response	145
Figure 5.107: Test 6 Rigid Body Rotation	146
Figure 5.108: Test 6 Right Side Grouted Shear Key with Applied Load = 0 kips.....	147
Figure 5.109: Test 6 Right Side Grouted Shear Key with Applied Load = 260 kips.....	148
Figure 5.110: Test 6 Grouted Shear Key with Applied Load = -300 kips	148
Figure 5.111: Test 6 Grouted Shear Key with Applied Load = 320 kips.....	149
Figure 5.112: Test 6 Grouted Shear Key $-\Delta_{c1}$ –Third Cycle (a) Left Side (b) Right Side	150
Figure 5.113: Grouted Shear Key $-\Delta_{c2}$ –First Cycle (a) Left Side (b) Right Side	151
Figure 5.114: Left Side of Grouted Shear Key $-\Delta_{c2}$ –Third Cycle	151
Figure 5.115: Grouted Shear Key $-\Delta_{c3}$ –Third Cycle	152
Figure 5.116: Damage to Left Side Shear Connector Insert at $-\Delta_{c6}$ – Second Cycle	153
Figure 5.117: Right Side Longitudinal Joint Gap at $-\Delta_{c6}$ – Second Cycle	153
Figure 5.118: Test 6 Removed Shear Connector Plate (a) Top View Left Connector (b) Bottom View Left Connector (c) Top View Right Connector (d) Bottom View Right Connector	154
Figure 5.119: Force-Displacement Response Comparison of Test 5 and Test 6	156
Figure 5.120: Test 6 Load History to Max Strength Capacity	156
Figure 5.121: Test 5 Load History to Max Strength Capacity	157
Figure 5.122: Activation of Bar Bending (a) One Side of Joint (b) Both Sides of Joint	159

Figure 5.123: Cracking Perpendicular to the Joint (a) Test 1b (b) Test 2 (c) Test 3 (d) Test 4 (e) Test 5 (f) Test 6	160
Figure 5.124 Diagonal Cracking (a) Test 1b (b) Test 2 (c) Test 3 (d) Test 4 (e) Test 5 (f) Test 6.....	161
Figure 5.125 Failure of Grouted Joint (a) Test 1b (b) Test 2 (c) Test 3 (d) Test 4 (e) Test 5 (f) Test 6.....	162
Figure 5.126: Cover Concrete Spalling (a) Test 1b (b) Test 2 (c) Test 3 (d) Test 4 (e) Test 5 (f) Test 6.....	163
Figure 5.127 Rebar Fracture (c) Test 3 (d) Test 4 (e) Test 5 (f) Test 6.....	164
Figure 5.128: Existing Connection Free Body Diagram	167
Figure 5.129: Alternate Connector Option 1 (a) Plan View (b) Elevation View	168
Figure 5.130: Alternate Connector Option 2 (a) Plan View (b) Elevation View	169
Figure 5.131: Alternate Connector Option 3 (a) Plan View (b) Elevation View	169
Figure 5.132: Alternate Connector Option 4 (a) Plan View (b) Elevation View	170
Figure 5.133: Alternate Connector Option 5 (a) Plan View (b) Elevation View	170
Figure 5.134: Alternate Connector Option 6 (a) Plan View (b) Elevation View	171
Figure 5.135: Alternate Connector Option 7 (a) Plan View (b) Elevation View	171
Figure 5.136: PCI Handbook Truss Mechanism	172
Figure 5.137: Sketch of eccentrically loaded weld	173
Figure 6.1: Test 7 Displacement History.....	175
Figure 6.2: Test 7 Load History	176
Figure 6.3: Test 7 Force-Displacement Response.....	176
Figure 6.4: Test 7 Rigid Body Rotation	177
Figure 6.5: Test 7 Left Side Grouted Shear Key with Applied Load = 0 kips	179
Figure 6.6: Grouted Shear Key with Applied Load = 174 kips (a) Left Side (b) Right Side	179

Figure 6.7:	Test 7 Grouted Shear Key with Applied Load = -174 kips (a) Left Side (b) Right Side.....	180
Figure 6.8:	Test 7 Left side of Grouted Shear Key with Applied Load = 232 kips	180
Figure 6.9:	Test 7 Grouted Shear Key – Significant Strength Loss (a) Left Side (b) Right Side.....	181
Figure 6.10:	Test 7 Right Side of Grouted Shear Key – Δ_{c1} –Third Cycle	182
Figure 6.11:	Test 7 Grouted Shear Key – Δ_{c2} –Third Cycle	182
Figure 6.12:	Test 7 Right Side of Grouted Shear Key – Δ_{c3} –First Cycle.....	183
Figure 6.13:	Test 7 Damage to Right Side Shear Connector Insert at Δ_{c6} – First Cycle.....	184
Figure 6.14:	Test 7 Left Side Shear Connector Pocket at Δ_{c6} – Second Cycle	184
Figure 6.15:	Test 7 Grouted Shear Key – Δ_{c8} –Third Cycle	185
Figure 6.16:	Test 7 Damage to Left Side Shear Connector Insert at Δ_{c6} –Third Cycle	185
Figure 6.17:	Test 7 Test 6 Removed Shear Connector Plate (a) Top View Left Connector (b) Bottom View Left Connector (c) Top View Right Connector (d) Bottom View Right Connector	186
Figure 6.18:	Variance in Surface Preparation of the Shear Key	187
Figure 6.19:	Alternate Shear Connector Detail 1 (a) Side View (b) Shear Connector Inserts.....	188
Figure 6.20:	Test 8 Displacement History.....	189
Figure 6.21 :	Test 8 Load History	189
Figure 6.22:	Test 8 Force-Displacement Response.....	190
Figure 6.23:	Test 8 Rigid Body Rotation	190
Figure 6.24:	Test 8 Grouted Shear Key with Applied Load = 0 kips (a) Left Side (b) Right Side.....	192
Figure 6.25:	Test 8 Right Side of Grouted Shear Key with Applied Load = 48 kips	192
Figure 6.26:	Test 8 Left Side of Grouted Shear Key with Applied Load = -96 kips	193

Figure 6.27:	Test 8 Grouted Shear Key with Applied Load = 144 kips (a) Left Side (b) Right Side.....	193
Figure 6.28:	Test 8 Grouted Shear Key with Applied Load = 240 kips (a) Left Side (b) Right Side.....	195
Figure 6.29:	Test 8 Grouted Shear Key – Significant Strength Loss (a) Left Side (b) Right Side.....	196
Figure 6.30:	Test 8 Grouted Shear Key $-\Delta_{c1}$ –First Cycle.....	197
Figure 6.31:	Test 8 Grouted Shear Key $-\Delta_{c1}$ –Third Cycle	198
Figure 6.32:	Test 8 Grouted Shear Key Δ_{c2} –First Cycle	199
Figure 6.33:	Test 8 Right Shear Connector Δ_{c2} –Second Cycle.....	199
Figure 6.34:	Test 8 Damage to the Right Shear Connector $-\Delta_{c2}$ –Second Cycle	200
Figure 6.35:	Test 8 Damage to Right Shear Connector Δ_{c3} –Third Cycle	201
Figure 6.36:	Test 8 Left Side of Grouted Shear Key $-\Delta_{c3}$ –Third Cycle	201
Figure 6.37:	Test 8 Grouted Shear Key Δ_{c3} - Third Cycle	202
Figure 6.38:	Test 8 Test 8 Removed Shear Connector Plate (a) Top View Left Connector (b) Bottom View Left Connector (c) Top View Right Connector (d) Bottom View Right Connector	203
Figure 6.39:	Comparison of Damage at $\Delta \approx 0.5$ in. (a) Test 2 (b) Test 4 (c) Test 5 (d) Test 8.....	205
Figure 6.40:	Force-Displacement Response Comparison of Test 4 and Test 8 (Rotated)	206
Figure 6.41:	Alternate Shear Connector Detail 2 (a) Side View (b) Shear Connector Inserts	208
Figure 6.42:	Test 9 Displacement History.....	209
Figure 6.43:	Test 9 Load History	209
Figure 6.44:	Test 9 Force-Displacement Response.....	210
Figure 6.45:	Test 9 Rigid Body Rotation	210

Figure 6.46: Test 9 Grouted Shear Key with Applied Load = 0 kips (a) Left Side (b) Right Side.....	212
Figure 6.47: Test 9 Right Side of Grouted Shear Key with Applied Load = 156 kips	212
Figure 6.48: Grouted Shear Key with Applied Load = -206 kips (a) Left Side (b) Right Side	213
Figure 6.49: Grouted Shear Key with Applied Load = 260 kips (a) Left Side (b) Right Side	214
Figure 6.50: Grouted Shear Key – Significant Strength Loss (a) Left Side (b) Right Side	214
Figure 6.51: Grouted Shear Key at $-\Delta_{c1}$ –Third Cycle	216
Figure 6.52: Grouted Shear Key at $-\Delta_{c2}$ –First Cycle	217
Figure 6.53: Right Side of Grouted Shear Key at Δ_{c2} – Second Cycle.....	217
Figure 6.54: Grouted Shear Key at Δ_{c3} –First Cycle	218
Figure 6.55: Grouted Shear Key at Δ_{c3} –Second Cycle	218
Figure 6.56: Grouted Shear Key at $-\Delta_{c3}$ –Second Cycle.....	219
Figure 6.57: Right Side Shear Connector Insert at $-\Delta_{c3}$ –Third Cycle.....	220
Figure 6.58: Grouted Shear Key at $-\Delta_{c3}$ - Third Cycle	220
Figure 6.59: Right Side of Grouted Shear Key at $-\Delta_{c4}$ - First Cycle	221
Figure 6.60: Right Side of Grouted Shear Key at $-\Delta_{c4}$ - Third Cycle.....	222
Figure 6.61: Grouted Shear Key at $-\Delta_{c4}$ - Third Cycle	222
Figure 6.62: Test 9 Removed Shear Connector Plate (a) Top View Left Connector (b) Bottom View Left Connector (c) Top View Right Connector (d) Bottom View Right Connector	223
Figure 6.63: Test 10 Displacement History.....	225
Figure 6.64: Test 10 Load History	226
Figure 6.65: Test 10 Force-Displacement Response.....	226

Figure 6.66:	Test 10 Rigid Body Rotation	227
Figure 6.67:	Test 10 Grouted Shear Key with Applied Load = 0 kips (a) Left Side (b) Right Side.....	228
Figure 6.68:	Test 10 Right Side of Grouted Shear Key with Applied Load = -107 kips	229
Figure 6.69:	Test 10 Grouted Shear Key with Applied Load = -262 kips (a) Left Side (b) Right Side.....	229
Figure 6.70:	Test 10 Grouted Shear Key with Applied Load = 312 kips (a) Left Side (b) Right Side.....	230
Figure 6.71:	Test 10 Grouted Shear Key with Applied Load = 364 kips (a) Left Side (b) Right Side.....	231
Figure 6.72:	Test 10 Grouted Shear Key with Applied Load = 300 kips.....	232
Figure 6.73:	Test 10 Grouted Shear Key with Applied Load = 391 kips.....	232
Figure 6.74:	Test 10 Damage to the Right Grouted Shear Key with Applied Load = 391 kips.....	233
Figure 6.75:	Test 10 Grouted Shear Key – Significant Strength Loss (a) Left Side (b) Right Side.....	234
Figure 6.76:	Test 10 Grouted Shear Key at $-\Delta_{c1}$ – First Cycle.....	236
Figure 6.77:	Test 10 Right Side of Grouted Shear Key at $-\Delta_{c1}$ – Second Cycle	236
Figure 6.78:	Test 10 Grouted Shear Key at Δ_{c2} – Third Cycle.....	237
Figure 6.79:	Test 10 Damage to the Right Grouted Shear Key at Δ_{c2} – Third Cycle	237
Figure 6.80:	Test 10 Grouted Shear Key at Δ_{c3} – First Cycle	238
Figure 6.81:	Test 10 Right Side Shear Connector Insert at $-\Delta_{c3}$ –First Cycle.....	239
Figure 6.82:	Test 10 Grouted Shear Key at $-\Delta_{c3}$ - Second Cycle	239
Figure 6.83:	Test 10 Grouted Shear Key at $-\Delta_{c3}$ - Third Cycle.....	240
Figure 6.84:	Test 10 Grouted Shear Key at $-\Delta_{c4}$ – Third.....	241
Figure 6.85:	Test 10 Damage to Right Side of Grouted Keyway from Underneath.....	241

Figure 6.86:	Test 10 Test 10 Removed Shear Connector Plate (a) Top View Left Connector (b) Bottom View Left Connector (c) Top View Right Connector (d) Bottom View Right Connector	242
Figure 6.87:	Force-Displacement Response Comparison of Test 6 and Test 10	244
Figure 6.88:	Comparison of Damage at $\Delta \approx 0.2$ in. (a) Test 6 (b) Test 10.....	244
Figure 6.89:	Force-Displacement Response Comparison of Test 6 and Test 10	245
Figure 6.90:	Cracking Perpendicular to the Joint (a) Test 7 (b) Test 8 (c) Test 9 (d) Test 10.....	247
Figure 6.91	Diagonal Cracking (a) Test 7 (b) Test 8 (c) Test 9 (d) Test 10	248
Figure 6.92	Failure of Grouted Joint (a) Test 7 (b) Test 8 (c) Test 9 (d) Test 10	249
Figure 6.93:	Cover Concrete Spalling (a) Test 7 (b) Test 8 (c) Test 9 (d) Test 10	250
Figure 6.94	Rebar Fracture (a) Test 7 (b) Test 8 (c) Test 9 (d) Test 10.....	251
Figure 7.1:	Sub-Assembly Computational Model Schematic	254
Figure 7.2:	Test 4. Analytical Model Force-Displacement Response.....	255
Figure 7.3:	Test 9. Analytical Model Force-Displacement Response.....	255
Figure 7.4:	Global Computational Bridge Model.....	258
Figure 7.5:	Displaced Shape Comparison with Theoretical Zero Composite Action when $K_{spring}=0.001k/in$ (a) Displaced Shape (b) Error.....	260
Figure 7.6:	Shear Flow when $K_{spring}=0.001k/in$	261
Figure 7.7:	Displaced Shape Comparison with Theoretical Full Composite Action when $K_{spring}=10000k/in$ (a) Displaced Shape (b) Error	262
Figure 7.8:	Shear Flow Comparison with Theoretical Full Composite Action when $K_{spring}=10000k/in$ (a) Shear Flow (b) Error.....	263
Figure 7.9:	Six Girder Displaced Shape Comparison with Theoretical Full Composite Action when $K_{spring}=2555k/in$ (a) Displaced Shape (b) Error.....	265
Figure 7.10:	Six Girder Shear Flow Comparison with Theoretical Full Composite Action when $K_{spring}=2555k/in$ (a) Shear Flow (b) Error	266

Figure 8.1:	Slab Bridge Yield Curvature vs Width	269
Figure 8.2:	Slab Bridge Yield Curvature vs Depth	269
Figure 8.3:	Slab Bridge Yield Curvature vs $f'c$	270
Figure 8.4:	Slab Bridge Yield Curvature vs ρ	270
Figure 8.5	Slab bridges Non-Dimensional Coefficients C' and C	271
Figure 9.1:	Elevation View (a) Alternate Connector 1(b) Alternate Connector 2	274

EXECUTIVE SUMMARY

This report describes the research performed to establish the baseline characteristics of bridges with longitudinal shear keys loaded in the transverse direction. An experimental program was conducted in which 10 large scale tests were performed on a unit length of a common used longitudinal joint found in bulb-tee girder bridges.. The experimental program was separated into Phase I and Phase II. Phase I focused on monotonic and cyclic loading, grout strength and polyester polymers. While Phase II examined bond strength, alternate connectors and the use of polyester polymer with an alternate connector.

A subassembly computational model was developed to represent the experimental test setup. A 2D global computational model was developed using OpenSEES that used springs to represent the longitudinal shear keys.. The model was subjected to uniformly distributed static loading applied to the girders. Elastic beam elements were used to represent the girders, while zero length springs in the longitudinal direction represented the longitudinal shear key. Rigid links and springs in the transverse direction were utilized to enforce compatibility. Based on the case study, it is recommended that if the expected shear flow is below the capacity of the joint, the joint should be treated as acting in full composite action until more computational studies are done.

Moment curvature analysis was used to develop equations for first yield and nominal yield curvature of slab superstructures. The yield curvature can be used for design to define a superstructure yield limit state. Two yield limit state were defined, first yield and equivalent yield. While equivalent yield has been used in the past for displacement based design, first yield may be more appropriate for superstructures which should remain elastic. Future work is still needed for a wider range of bridge superstructure types.

CHAPTER 1 INTRODUCTION

1.1 Background

Bulb-tee prestressed precast girder bridges are used in the Northwestern United States because of their benefits associated with reliability and short construction time. Compared to traditional cast in place bridge decks, bulb-tee girder decks are of higher quality because they are constructed offsite in a controlled environment. They reduce the amount of construction steps and therefore require less time on site to build. Additionally the bulb-tee girder's predecked surface reduces construction risks, allowing workers to operate on the flanges. The bulb-tee girders are connected with longitudinal keyway joints that consist of a diamond-shaped shear key that extends the length of the girder and a discrete shear connector that repeats itself every four feet. A typical longitudinal keyway joint can be seen in Figure 1.1. The shear connectors are installed first to align adjacent girders and adjust for differential camber. Grout is then poured into the shear key and shear connector pockets to increase connectivity between bulb-tee girders and distribute vertical loads.

Bulb-tee girder bridges with longitudinal joints date back to the 1960's. Adjustments to their design over the last 50 years have been based upon field observations of existing joints,. Past research on bridges with longitudinal keyway joints have focused on longitudinal vertical load distributions including the effects of diaphragms, the development of new joints, and constructability. No known research has focused on the transverse response, which can be initiated from earthquake induced excitation, impact loading, ice drifts, wind gusts, and tsunamis. Some similar connections in precast diaphragms have been studied, such as parking decks, but none that match the popular connection seen in Figure 1.1.

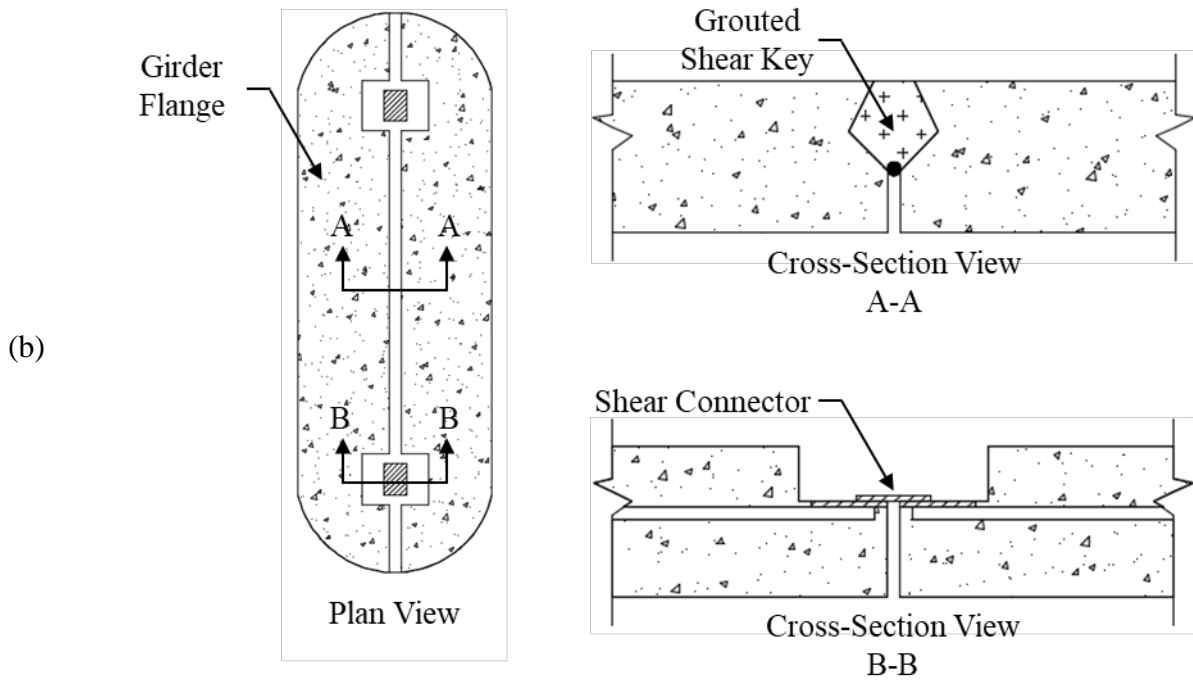
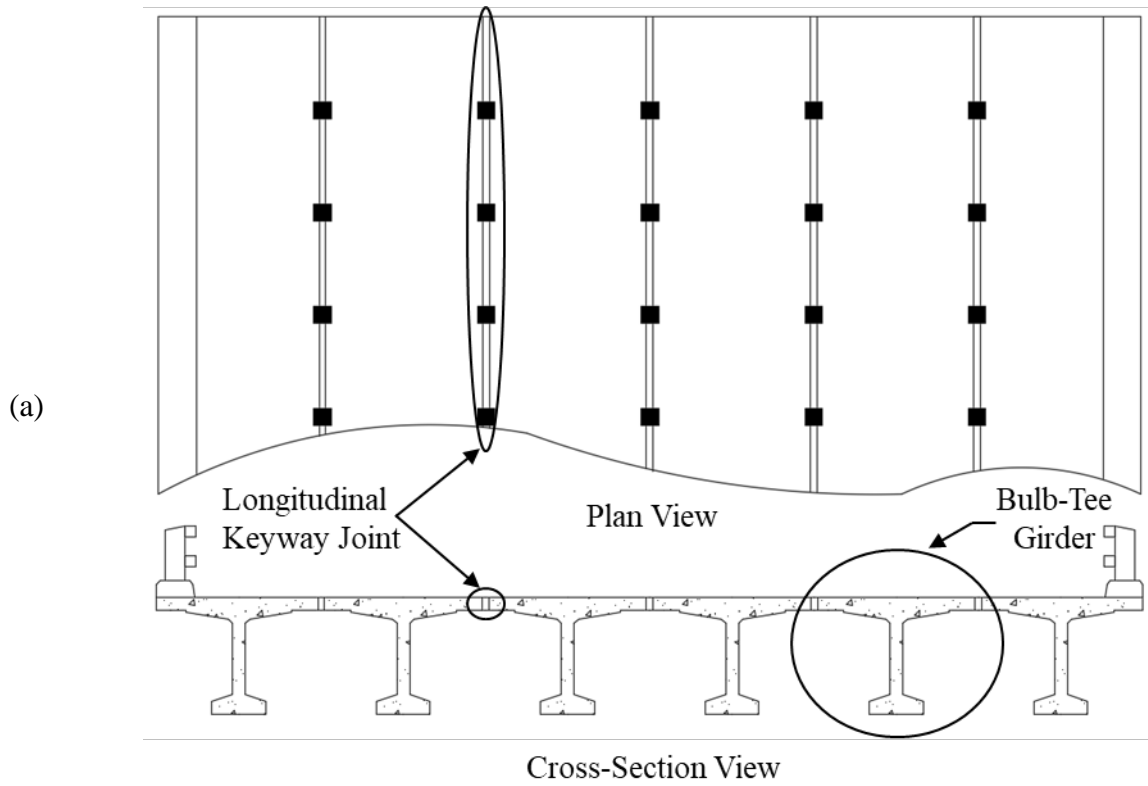


Figure 1.1: Typical Longitudinal Keyway Joint (a) Global View (b) Local View.

Alaska is a good representation of the Northwest United States because a majority of their bridge inventory is composed of bulb-tee girder bridges with longitudinal joints, starting with the Carlanna Creek Bridge in 1973, and extending to the Klehini River Bridge in 2017. Alaska is also located near to the Pacific Plate and North American Plate boundary and is considered a highly hazardous seismic region. Therefore, bridges with longitudinal keyway joints have a high probability of experiencing earthquake induced excitation. Despite Alaskan bulb-tee girder bridges dating back to the 1970s, the last major earthquake was The Great Alaska Earthquake, occurring on March 27, 1964. One case study exists where an ice drift imposed a transverse load on the Safety Sound Estuary Bridge. The ice drift caused one of the piers to displace and damaged the longitudinal keyway joint as shown in Figure 1.2.

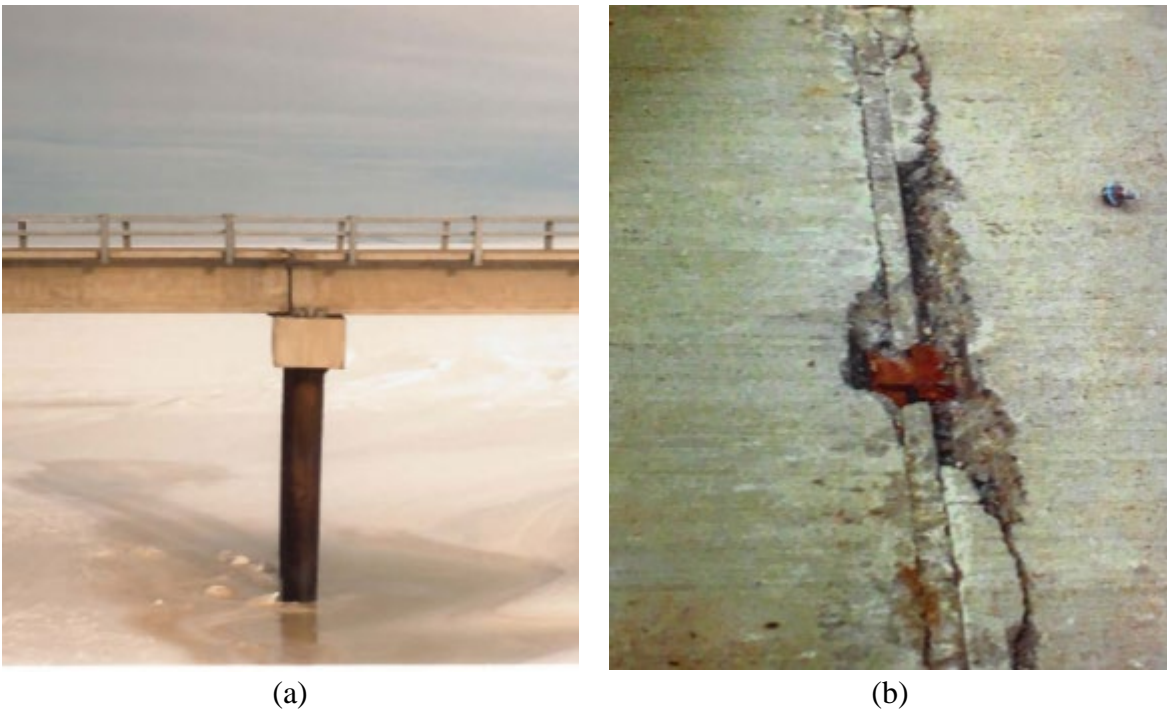


Figure 1.2: Safety Sound Estuary Bridge (a) Damaged Pier (b) Damaged Longitudinal Keyway Joint.

1.2 Motivation

Due to lack of data, it has been common practice for designers to model bridge superstructures with longitudinal keyway joints in the transverse direction one of two ways. One assumption is to model the joint as providing full composite action, i.e. the girders act as one monolithic cross section. The other assumption is to model the joint as providing zero composite action, i.e. the girders act independent of one another with individual strain profiles. Full composite action when compared to zero composite action will provide a greater stiffness and a reduced displaced shape as seen in Figure 1.3. It is probable that the global response of the superstructure will not behave as either assumption, but rather the connectivity provided by the longitudinal keyway joint between girders will be somewhere in between.

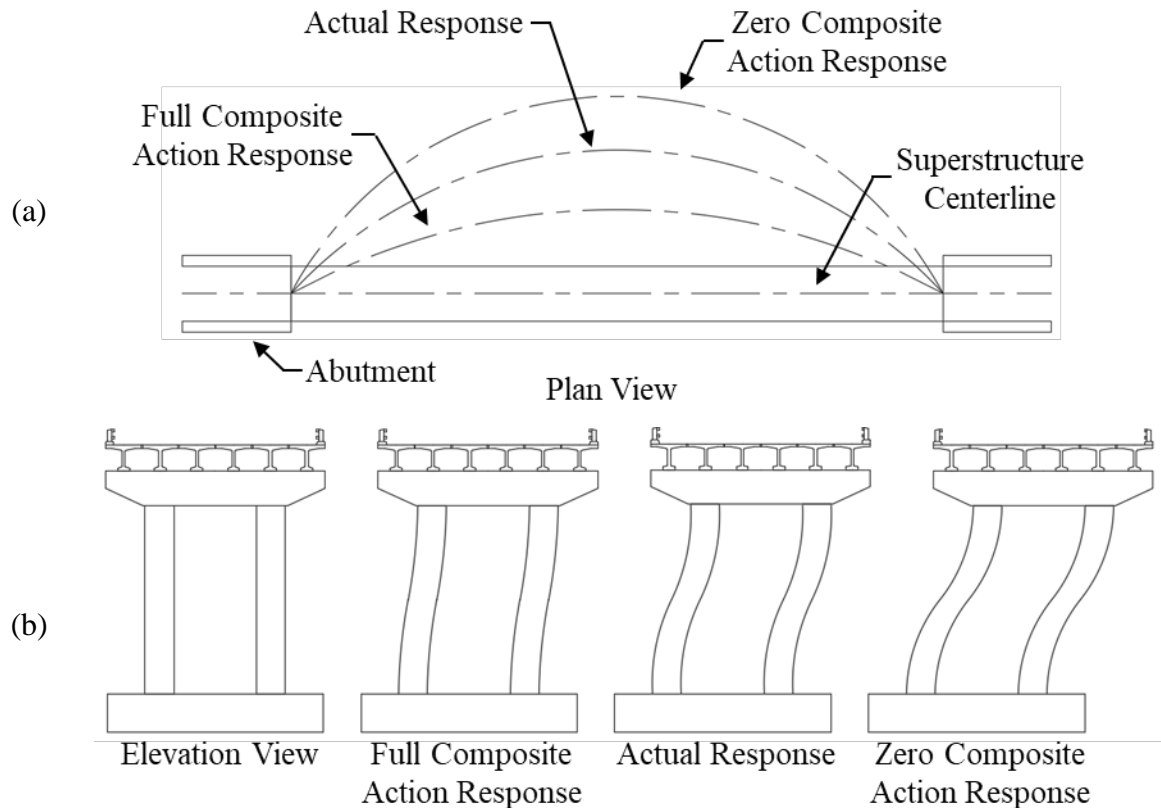


Figure 1.3: Bridge Response (a) Global Superstructure Response (b) Pier Response.

The problem lies in choosing the correct stiffness. Overestimation of superstructure stiffness leads to higher than expected displacements along the length of the bridge, resulting in higher demands at the piers. Conversely, underestimation of superstructure stiffness leads to an underestimation of abutment strength demand. Because of the possibility of undesirable outcomes, there is a need to study the longitudinal joint connectivity.

1.3 Scope and Layout

The scope of this research report is to determine the behavior of the existing longitudinal shear key and provide design recommendations for modeling the joint under transverse loading. Chapter 2 is a literature review that informs the reader of past research on bridges with longitudinal joints and similar joints in precast structures. Chapter 3 highlights the gap in the literature and presents objectives to fill the gaps. The experimental methods follow in Chapter 4. Chapter 5 and 6 go over the experimental results for Phase I and II of the project, respectively. The global computational bridge model used to determine the effective stiffness provided by the longitudinal shear key in the transverse direction is presented in Chapter 7. Chapter 8 presents the methods and evaluation of bridge superstructure yield limit states. The summary, recommendation, and future work are presented in Chapter 9.

CHAPTER 2 LITERARY REVIEW

2.1 Bulb-Tee Girder Bridges with Longitudinal Keyway Joints

The first record of research that examined precast girder bridge systems with keyway joints was part of an NCHRP project that looked at the distribution of forces between panels of bridges comprised of stemmed members in the 1980s (Stanton & Mattock, 1987). Finite element analysis was used to determine the effects of diaphragms, skew angle, load positioning, and member geometry on the load distribution between girders. In the study, three types of diaphragms were examined to determine the effects of load distribution factors. Of the three, concrete cast in place diaphragms were the most effective in distributing forces between members. Steel diaphragms were also shown to improve the distribution of forces, however, concrete precast diaphragms that are attached to the structure by welding showed to have almost no effect on force distribution.

Further work was done on live-load distribution and connector forces, which involved the field testing of eight bridges and a finite element analysis parametric study (Z. Ma, Chaudhury, Millam, & Hulsey, 2007). Four pairs of bridges that represented different geometries were selected. Pairs with similar geometry ensured redundancy and provide verification of the instrumentation. Each bridge was equipped with twenty-four strain gauges to measure shear and flexural strains under two loading conditions that employed large dump trucks: (1) static loading and (2) continuous loading.

Finite element models for the bridges were calibrated using the strain data collected from the eight field tests. This was followed by parametric studies that assessed the impact of shear connectors and intermediate diaphragms on force distribution. Shear connector spacing showed to have little effect on vertical shear forces, however maximum horizontal forces increased as the spacing increased. Nonetheless, the total horizontal shear force across the joint remained constant regardless of connector spacing. The main factor impacting shear connector force was the location of loading. Intermediate diaphragms were shown to drastically reduce the non-uniformity of horizontal shear forces and maximum horizontal shear forces across the joint with just one diaphragm placed at center span. The use of five intermediate diaphragms showed a reduction in maximum horizontal shear forces across the joint when compared to a single

diaphragm. These results can be clearly seen in Figure 2.1 which depicts maximum horizontal shear forces in the shear connectors. WOISD represents no intermediate diaphragms, WISD represents five intermediate diaphragms, and WISD-Center represents one intermediate diaphragm at mid-span. Shear connector spacing was based upon using seven, fourteen and twenty-eight shear connectors along the joint and load was applied on either G1, the outside girder, or G3, the middle girder, of the five girder superstructure bridge identified as W100NB. The load condition was either 1, where the load was applied a distance equal to the height of the girder from the abutment, or 3, where the load was applied at mid-span.

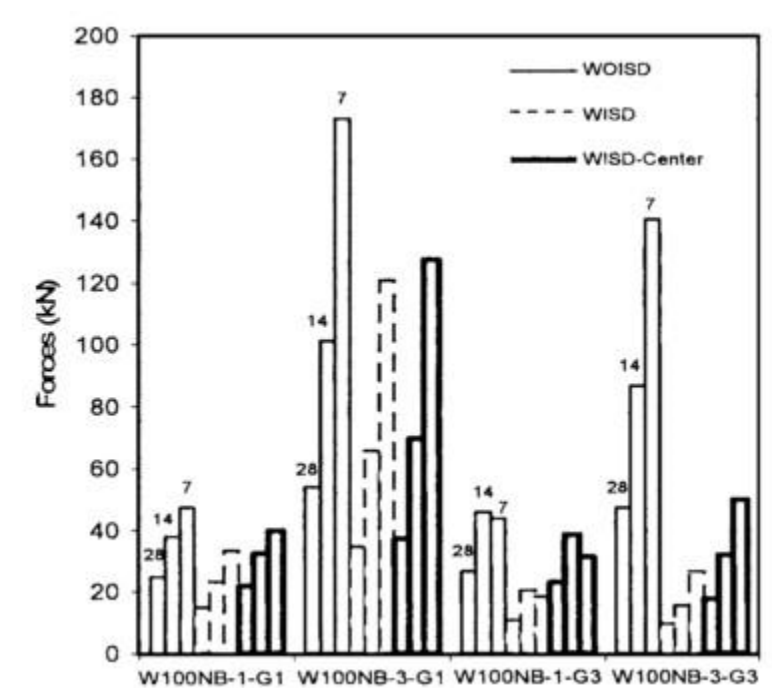


Figure 2.1: Maximum Horizontal Shear Force (Z. Ma, Chaudhury, Millam, & Hulsey, 2007)

Additional research was performed to investigate the impact of steel and concrete intermediate diaphragms on bulb-tee girder bridges (Li & Ma, 2010). Five finite element models were developed and calibrated based upon the eight previously mentioned field tests. The five models consisted of three bridges with steel diaphragms, one bridge with a concrete diaphragm at mid-span and one bridge without diaphragms. Of the three steel diaphragm bridges, the first had five intermediate diaphragms and the other two had only one intermediate diaphragm whose

cross sectional area varied. Model 1 refers to the bridge model with five intermediate diaphragms with a cross sectional area of 2,110 mm², Model 2 refers to the bridge model with one steel intermediate diaphragm with a cross sectional area of 2,839 mm², Model 3 refers to the bridge model with one steel intermediate diaphragm with a cross sectional area of 1,361 mm², Model 4 refers the bridge model with one concrete intermediate diaphragm with a thickness of 229mm and Model 5 refers to the bridge model without any intermediate diaphragms.

The results showed that the effect of the diaphragms on flexural strains, displacements and moments at mid-span was dependent on the location of the loading. When the load was placed at mid-span on the middle girders, the flexural strains, displacements and moments at mid-span were lower and a more uniform distribution observed when compared to the loading located at mid-span on the edge girder. These results are reflected in Figure 2.2, which compares flexural strain at mid-span with the load placed on three different girders with the five different models. It was observed that the diaphragms could significantly reduce the maximum moment on individual girders. There was no effect on shear distribution between girders with any of the diaphragm configurations. The same analysis was repeated for bridges with half the span length of the original. It was found that intermediate diaphragm effects were also based on span length. The shorter the span length, the higher the effect on mid-span deflections and the lower the effect on mid-span bending moments.

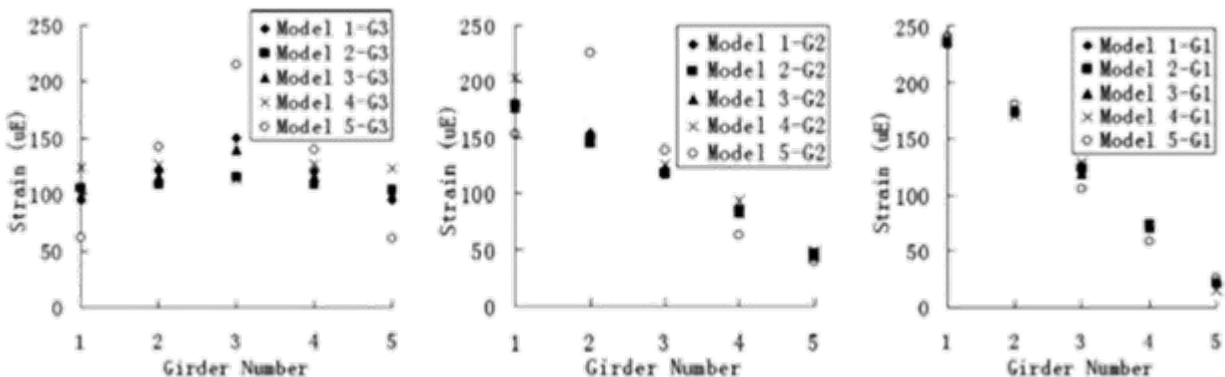


Figure 2.2: Comparison of Deflections (a) Loading G3; (b) Loading G2; (c) Loading G1 (Li & Ma, 2010)

Other researchers also looked at the effects of intermediate diaphragms and skew angle on longitudinal load distribution factors (Smith, Yue Li, & Bulleit, 2011). They used finite element analysis to conduct a parametric study that considered shear plate size, skew angle and intermediate diaphragms. The diaphragms were either placed at mid-span or at thirds along the bridge. The analysis performed only considered the shear plate (modelled as elastic springs) for the joint model.

The models were subjected to AASHTO vehicle loading and the spring forces and moments that modeled the joint were examined along the length of the bridges. The maximum moments and forces in all directions were related to strains. It was found that plate spacing and size had little effect on forces experienced by the plates and stresses stayed well below yield for the AASHTO vehicle loading. However, as skew angle increased the transverse moment and transverse axial stress increased. Deflections at quarter lengths along the bridge were compared for the different diaphragm configurations, where it was noted that adding one diaphragm decreased the deflection by up to fifty percent but two diaphragms showed no further impact.

The first experiments performed on the connection between girders looked at the effect of shear plate location, geometry of the grouted shear key, and the interaction between the grout keys and shear plates (Stanton & Mattock, 1987). Five foot-long, six-inch thick slabs were created with two varying keyways and two varying shear connectors that were commonly used in practice. Figure 2.3 depicts the keyway and connector details employed. The slabs were connected and load was applied at two points, twenty inches apart, to represent wheel loading on one slab seven inches from the joint centered on either side of the shear connector. The results at service loading showed that the grout resisted most of the transfer force. Failure was found to occur in the slab rather than the grout key itself. In order to optimize the keyway, the widest point was recommended to be at mid-depth of the slab.

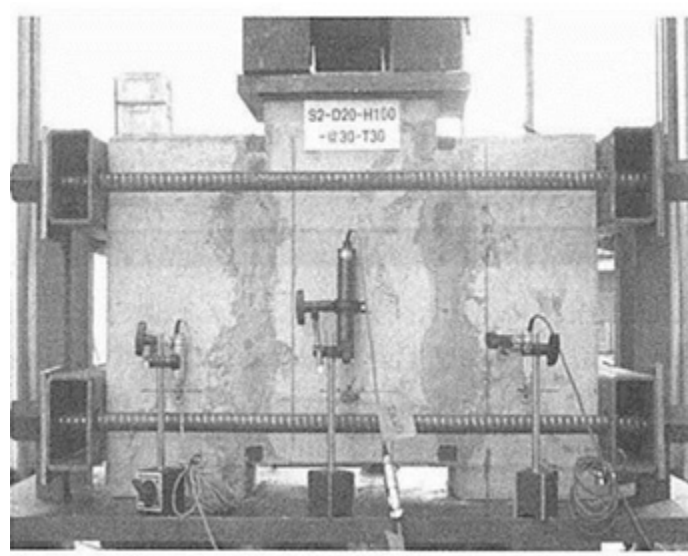


Figure 2.4: Test Setup (H.-Y. Kim et al., 2013)

Shear-transfer mechanisms were examined using five different shear connector systems in over-hang deck panel bridge systems (Y. H. Kim & Trejo, 2014). The goal of this research was to obtain a better understanding of the effects of confinement on shear connector systems and develop design equations to obtain an adequate number of shear connectors. Five different systems with three specimens each were tested in push off tests. One specimen used hooped rebar with no confinement to transfer shear, the rest used threaded rods and couplers with varying levels of confinement. One had no confinement, one had confinement inside the shear pocket, one had confinement outside the shear pocket and the last one had both inside and outside confinement. Confinement details can be seen in Figure 2.5. It was seen in these tests that there were four steps to shear failure. First was loss adhesion, second was shear key action, third was the failure of the shear key action, and fourth was sustained dowel action. Also, equations were developed for shear at initial adhesion loss, peak shear strength and the sustained shear strength.

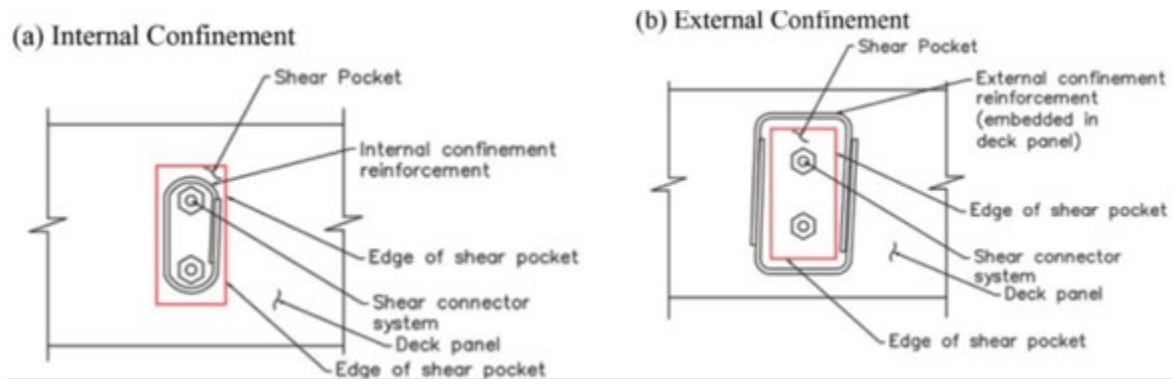


Figure 2.5: Confinement Systems (Y. H. Kim & Trejo, 2014)

Later experiments were performed to study the constructability and structural behavior of precast bridge deck slabs systems (Issa, Anderson, Domagalski, Asfour, & Islam, 2007). A full-scale bridge was designed, built and tested at the University of Illinois at Chicago. The bridge consisted of two forty-foot long spans comprised of eleven full-depth precast slab panels with transverse joints that were installed on three W18x86 steel girders with full composite action provided by shear pockets. Constructability was taken into account, thus the panels and transverse joints were constructed to simulate typical field practice. Static testing was performed that simulated AASHTO vehicle loading under three cases: service load, overload and ultimate load. The prototype bridge was found to have acceptable results with no stress above the cracking stress under both the negative and positive moment. Nonlinear finite element analysis confirmed experimental results and the assumption of full composite action. The FEA model also confirmed post tensioning was necessary to ensure live load induced tensile stress on the transverse joints did not exceed that of the bond stress.

Since the first tests on keyway joints, it has been perceived that current joints are not durable due to their limitation in transferring moment and the formation of cracks along the joint. Thus further research was performed looking at different possible joints that would eliminate the concerns of durability (Li, Ma, Griffey, & Oesterle, 2010). Some of the first research looked at three unique longitudinal joint details that considered constructability and cost. The three details explored were a U-bar detail, a headed bar detail, and a spiral bar detail which can be seen in Figure 2.6. A survey was given to practicing professionals about the three details. Results from the survey showed concern with the spiral and U-bar detailing, and suggested a welded wire

reinforcement detailing. Thus only the studded head method and welded wire reinforcement method were adopted.

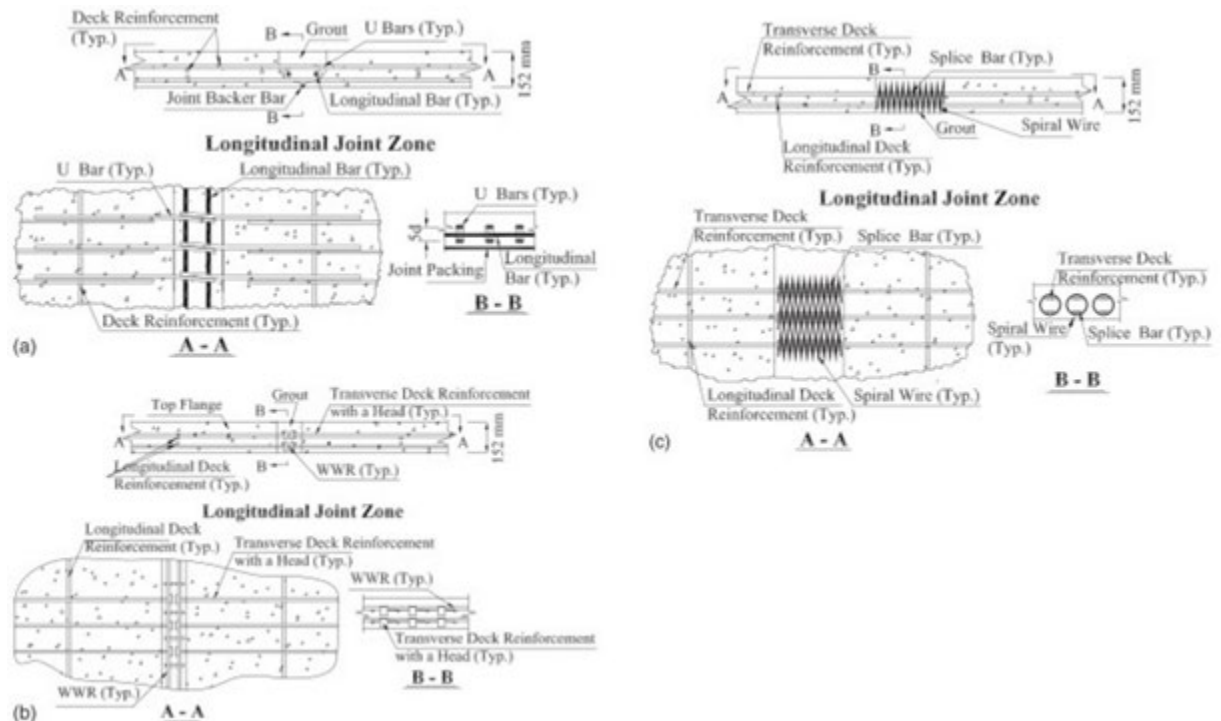


Figure 2.6: Proposed New Joint Details (Li, Ma, Griffey, et al., 2010)

Specimens were created for the studded head, the welded wire reinforcement, and a control specimen with dimensions of two feet wide, ten feet long and six inches deep and cast monolithically to remove the interaction of the grout. The experiments studied the lap length and reinforcement spacing. Specimens were tested using four-point bending to impose maximum moment across the joint. It was found that the welded wire reinforcement was not an adequate design due to sudden failure during testing. The optimal detailing was a studded head design with six inches of lap space to develop the bars and provide substantial ductility.

The detail was then examined further to determine the feasibility for use in decked precast prestressed concrete girder bridge systems (Li, Ma, & Oesterle, 2010). In order to determine the range of forces that would be applied to test specimens in static and fatigue experiments, seven finite element bridge models representing different geometries and skew angles with the studded bar joint detail were developed. The models were calibrated with the

same eight bridges previously mentioned and subject to different load conditions using ASHTTO design specifications.

Four full-scale deck slabs were created with a studded head joint detail, each slab consisted of two panels grouted together with dimensions six feet wide, sixty-four inches long and six inches deep. It should be noted that each panel had the joint along two edges so it could be used to make two different slabs. SET 45 HW was chosen as joint grout because the setting time would be desirable for field use. A flexure static test (four-point bending), a flexure-shear test static (three-point bending), a flexure fatigue and a flexure-shear fatigue test were performed on the slabs. The loads used were taken from the computational study. Cyclic testing did not reduce the loading capacity of the joint but it did reduce the development of the plastic hinge in the flexural tests. The flexural-shear test specimens failed in shear. It was found that the studded bar joint was sufficient in transferring forces between girders and would be a viable detail.

The U-bar detailing was reexamined as an alternative joint for decked precast prestressed concrete girder bridge systems with the idea to keep the bends as tight as possible to minimize the size of the joint (Zhu, Ma, & French, 2012). The range of forces that were used in the reexamination were determined using finite element models of two-span and three-span continuous bridges under ASHTTO bridge design specification loading. Four full-scale specimens were created with the U-bar detail, two used an overnight cure, SET 45 HW, and two used a seven-day cure, HPC mix 1, as the grout mixture. The specimens consisted of two panels with dimensions fifteen inches wide, thirty-six inches long and seven and a quarter inches deep. Static tension and fatigue tension tests seen in Figure 2.7 were performed to simulate the tensile forces from negative moment. The results showed that all specimens reached the service load but only the HPC mix 1 specimens reached calculated tensile capacity. It was found that the U-bar's in the joint reached yielding stresses and that the joint could be assumed to act as continuous reinforcement. Therefore the joint's strength came from the interaction of the closure-pour and the U-bars. The strength of the closure-pour had some effect on the stiffness and capacity of the joint. However fatigue loading had negligible effects on the joint's strength.

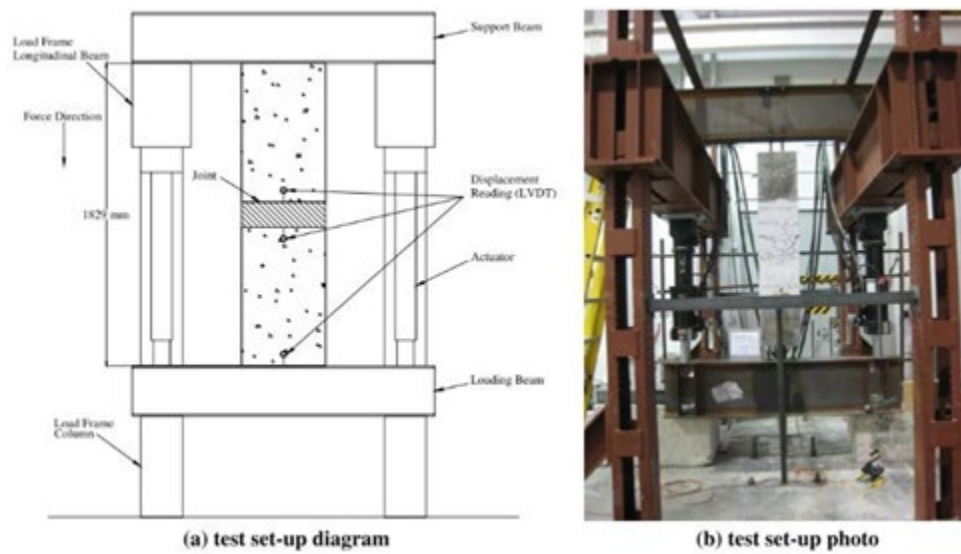


Figure 2.7: Test Set Up (Zhu, Ma, Cao, & French 2012)

Researchers then looked at both the studded head detailing and the U-bar detailing to determine which detail is more viable for decked precast prestressed concrete girder bridge systems since both joints were considered suitable (Z. J. Ma, Cao, Chapman, Burdette, & French, 2012). Strut-and-tie models were created to predict the capacity of the joints. Three specimens were created, one studded head and two U-bar specimens. The U-bar joint was considered with both deformed wire reinforcement and stainless steel since a ductile material was needed to make the 3db loop diameters for the U-bars. Each detail had the same depth, the same rebar spacing and the same overlap distance. It was found that the U-bar joint detail with deformed wire reinforcement hoops provided the greatest tensile capacity as well as produced the smallest cracks under service loads. Thus three more specimens with the deformed wire reinforcement were created with varied loop bar spacing, concrete strength and overlap length. After tensile testing was performed to failure, it was seen that reducing the concrete strength reduced the total tensile strength and the capacity but less than expected. It was seen that reducing the lapping distance resulted in a reduction in the capacity more than expected and increasing the spacing between bars showed a capacity above the expected capacity. A strut-and-tie model was then developed that was able to predict the capacity of the joint to within fifteen percent of the experimental ultimate load.

Researchers then developed design equations for the U-bar joint detail (He, Ma, Chapman, & Liu, 2013). The goals were to minimize the width and ensure that the joint reaches full moment capacity. Four parameters that were taken into consideration in the design were spacing of U-bars, overlap length, diameter of the lacer bar and grout strength. Past experimental results demonstrated that section analysis was valid for capacity assessment with the assumption that the U-bars are continuous (Z. J. Ma et al., 2012). However, since the U-bars are not continuous, a strut-and-tie model was developed and compared with past data and showed to have a consistent prediction of moment capacity.

Additionally four other joint details were examined in order to enhance durability (Sennah & Afefy, 2015). In particular, two moment connections and two bolted connections were designed using AASHTO design specifications. The two moment connections were based on work done by the Ontario Ministry of Transportation. The two bolted connections were identical except that one connection had a plate welded to the anchor rods. Figure 2.8 depicts the joints mentioned above. The theoretical strengths for each joint were estimated using punching shear capacity, yield lines and code-specified equations. Five specimens were created and tested, one specimen for each new joint and one duplicate of the moment connection with overlapped hooks (Afefy, Sennah, Tu, Ismail, & Kianoush, 2015). Load was applied monotonically until failure. In the moment connection without overlapping hooks, failure was observed due to flexure in the joint. In the moment connection with overlapped hooks, failure was due to flexure in the slab. In the two bolted specimens, failure was caused by de-bonding of the dowel bolts. The connection with the plate welded to the anchor rod had a more ductile de-bonding. It was concluded that the moment connection with overlapping bars preformed best. It was found that all joints were able to satisfy both the AASHTO and CHBDC specifications for wheel loads. Additionally, the moment resisting joints provided more capacity than the bolted connections and it was noted that the bolted connections should be treated as solely shear connections.

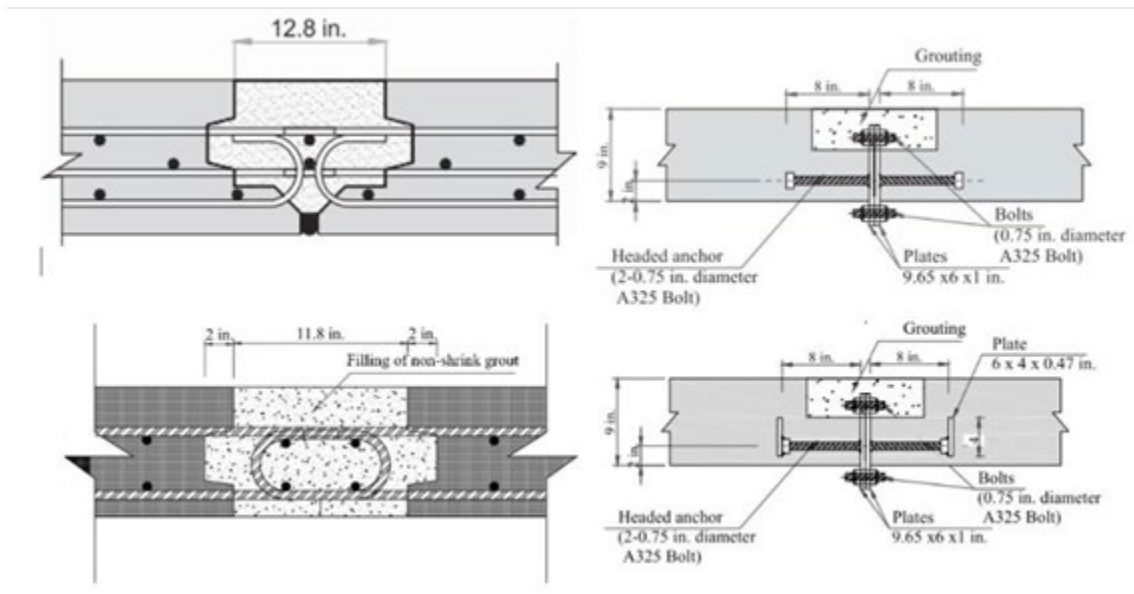


Figure 2.8: Proposed New Joint Details (Sennah & Afefy, 2015)

2.2 Shear connectors in Prestressed Diaphragms

Connections common in precast roof and floor systems are similar to those found in bridges with longitudinal keyway joints. In the case of precast floors, the connections serve the purpose to transfer forces across beams and maintain diaphragm action. Due to major damage in these systems after the 1994 Northridge earthquake there has been a new focus on these types of structures and connections (Fleischman, Sause, Pessiki, & Rhodes, 1998; Wood, Stanton, & Hawkins, 2000). The methodology and design philosophy of diaphragms were reexamined (Fleischman, Restrepo, Ghosh, Naito, & Sause, 2005). It was concluded that the assumption to use a beam detailing methodology for internal forces did not match complex diaphragm forces in reality. Another flaw was that deformation in the joints of the diaphragms were not considered in design, which resulted in overloading conditions on connectors instead of allowing for load redistribution. Thus research was needed at the diaphragm level, joint level and detail level to improve behavior through diaphragm action.

Some of the earliest research examined two different types of hairpin rebar shear connectors used to create diaphragm action in T-beams (Venuti, 1970). The research was used to define failure characteristics and determine capacity of the connections. The first connection consisted of a pocket with a bent rebar that had legs at forty-five degree angles embedded into

the flange of a T-beam. A rebar was then welded to the embedded rebar and the pocket is filled with grout. The second was similar to the first but the embedded rebar has a plate welded at sixty degrees from the contact point of the connection. Figure 2.9 depicts the two different connections. Sixty-four full size specimens were created and tested under in-plane shear loading with varying leg angles, bar sizes, weld lengths, numbers of bars and types of toppings. It was found that in-plane shear failure was caused by yielding of the embedded rebar and that shear failure was not abrupt. Bar size, number of bars and topping all had positive effects on the shear strength along the connection. For example, it was found that #5 embedded bars provided fifty percent more strength than #4 embedded bars.

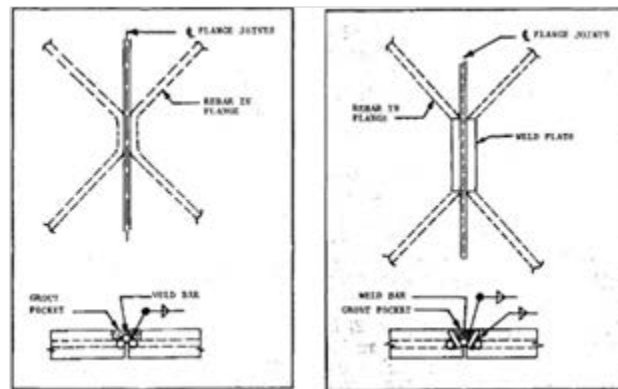


Figure 2.9: Shear Connectors (Venuti, 1970)

In addition to shear, tension and multiaxial loading for hairpin connectors has also been studied (Jose A. Pincheira, Oliva, & Kusumo-Rahardjo, 1998). Tests for each case were performed under monotonic and cyclic conditions for a total of ten specimens. The detail of the connection consisted of a plate welded at 10 degrees off the vertical line of a rebar with forty-five degree legs and embedded twelve inches into a two-inch flange (see Figure 2.10). Depending on the loading type, different mechanisms were observed. Pure shear relied on bearing of the concrete, friction between the plate and the concrete and axial forces of the anchor bars. Tension relied on the bending of the plate and bending of the embedded bar. Compression relied on bearing of the plate. When subject to biaxial stresses, results were dependent on whether tension or compression was being applied. Tension weakened the response by removing the bearing mechanism in shear, while compression enhanced the response of the shear

mechanisms by enhancing friction. Using a truss model to model the rebar provided conservative results ranging from fifteen to eighty percent higher than predicted values for both shear and tension but did not provide conservative results considering them occurring at once.

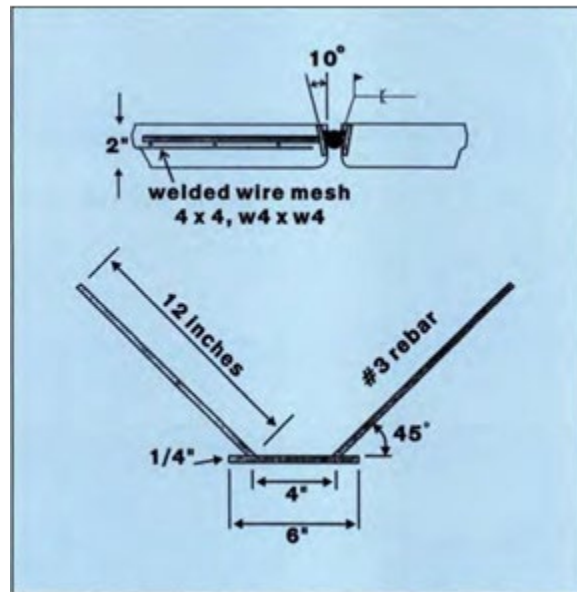


Figure 2.10: Hairpin Connector (Jose A. Pincheira et al., 1998)

Two new shear vector connectors were tested under shear, tension and multiaxial loading (Fattah Shaikh & Feile, 2004). The vector connectors were made from a single plate of either A36 steel or stainless steel (see Figure 2.11). The plate was bent to provide a vertical face at the connection and two forty-five degree embedded legs. Twenty-nine, four-foot by four-foot by four-inch specimens were cast with the specified detail and used for testing under monotonic and cyclic loading for each load case. It was found that the stainless steel showed a more ductile response, with almost four times the yield displacement as the A36 steel, but overall failure modes and loads achieved were similar between the two steels. Under monotonic horizontal shear and biaxial loading, which included both horizontal shear and tension forces, failure was due to pull out of the tension leg of the connector. In the multiaxial load case, tension was applied to the joint until a one inch gap was measured and then shear loading was applied. Under cyclic horizontal shear and biaxial loading, rupture of the plate was observed. Under monolithic vertical shear loading, failure occurred from failure of the concrete. Under monolithic tensile

loading all failure occurred in the failure of the weld. All results were consistent throughout testing.



Figure 2.11: Vector Connector (Fattah Shaikh & Feile, 2004)

Ninety-five more tests were performed evaluating seven additional connectors used to connect T-beam diaphragm systems (José A. Pincheira, Oliva, & Zheng, 2005). Connection types included a hairpin connector, a stud welded plate, a vector connector, a bent wing connector, mesh and angle connector, a structural tee connector, and a bent plate connector (see Figure 2.12). Depending on the connector, four-foot by four-foot specimens were made with two or four inches thick slabs. Specimens were then loaded both in-plane and out of plane shear as well as tension, both monotonically and cyclically. The bent plate showed brittle behavior and was not considered a viable connection. Six different failure modes were observed due to different configurations and loadings. Those modes were fracture of the anchor, pullout of the anchor, fracture of the plate, fracture of the weld, crushing of the concrete, and concrete shear cracking. It was seen that in-plane shear ductility was reduced in all specimens subjected to cyclic loading and depended on the type of connection. Volume change was especially important as noted in an example where a bent wing connector loaded cyclically under in-plane shear with a quarter inch gap had nearly a reduction factor of three when compared to the monotonic counterpart. In the end it was decided that the bent wing and the vector connector provided the best results in terms of dependable strength, ductility, and observed failure modes even though they had a relatively low strength of about twelve kips under in-plane shear loading when compared to some of the other connectors that had strength of up twenty-five kips per connector.

The bent wings failed through ductile fracture of the legs and the vectors failed through either fracture or pull out of the legs. It was considered that pull out failure could be avoided in the vector if an anchorage wire was threaded through the legs like the bent wing.

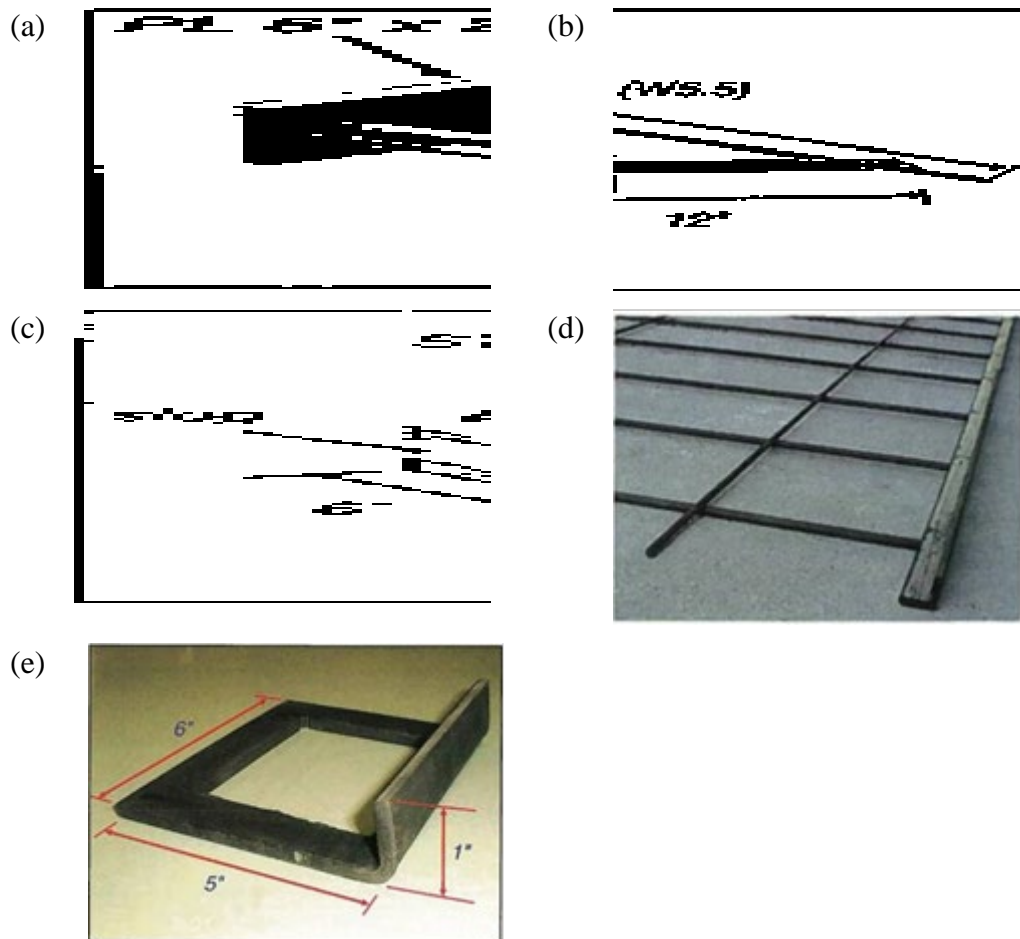


Figure 2.12: (a) Stud Welded Plate, (b) Bent Wing Connector, (c) Structural Tee Connector, (d) Mesh and Angle Connector, (e) Bent Plate Connector (José A. Pincheira et al., 2005)

Additionally six common shear connectors in Figure 2.13 were subject to monotonic shear and tension loading, as well as cyclic loading for shear and a combination of shear and tension for a combined total of thirty tests (Cao & Naito, 2009; Naito, Pao, & Peter, 2009). The reinforcing details used are prevalent in precast diaphragm structures including toppings, chords and shear connectors. Monotonic backbone envelopes were developed for each connector in both tension and shear loading. The backbones are defined by the yield point, peak load and failure

load. These characteristics were then used in a Phase II, which consisted of full-scale testing of shear connector groups and connections between precast members. Scaled panel joints monotonically tested were used to inform 3-D finite element models of parking deck structures, which in turn were used for parametric studies.

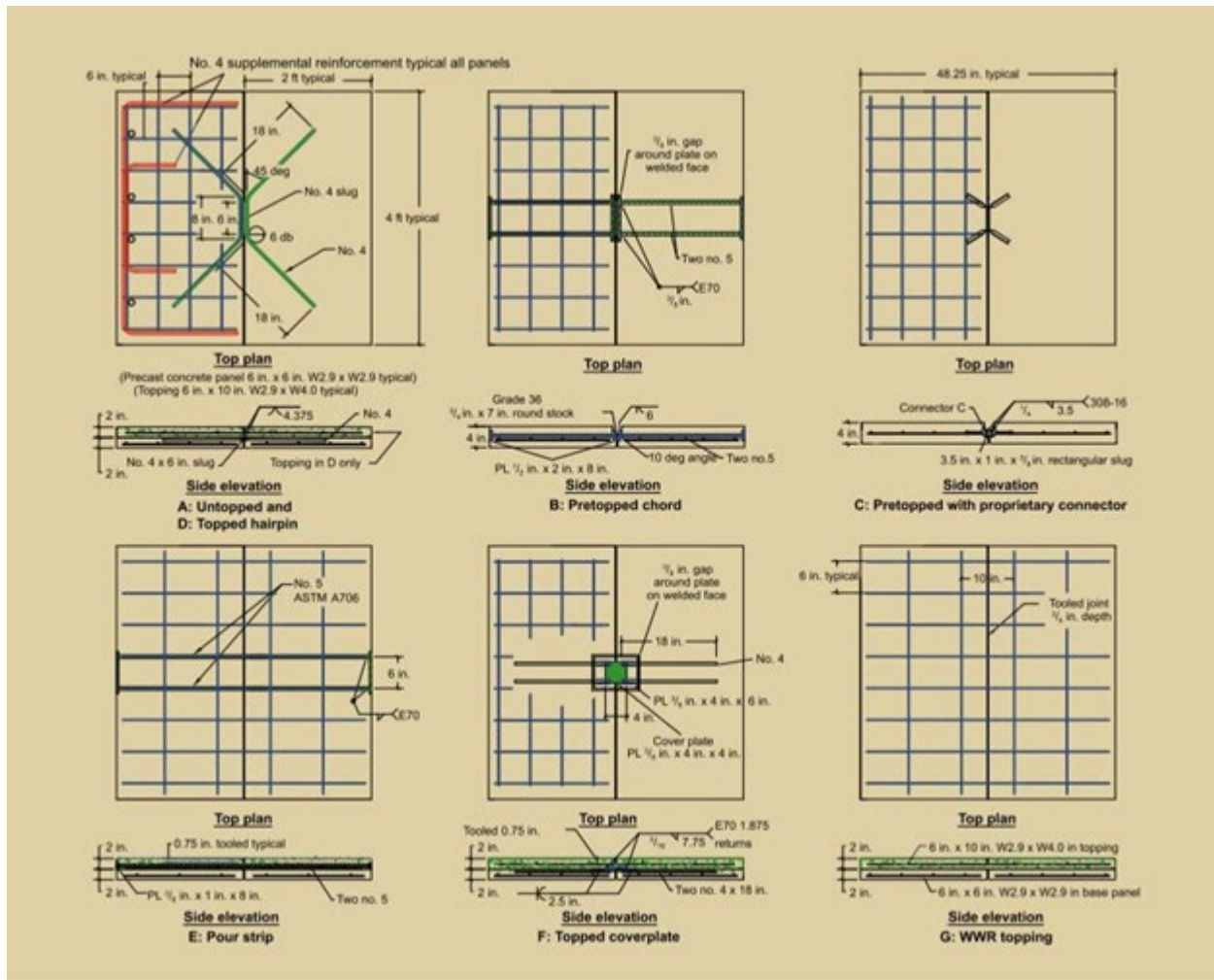


Figure 2.13: Shear Connectors (Cao & Naito, 2009; Naito et al., 2009)

Loose welded plate connections in precast concrete panels under cyclic loading were also examined to determine the force-displacement relationship (Hofheins, Reaveley, & Pantelides, 2002). Each assembly consisted of three hollow-core wall panels and four welded joint connectors, two in each joint. The wall panels were enclosed in a steel belt that allowed a hydraulic actuator to apply load on panels at the upper corner of the assembly. The load was

applied cyclically and the welded connections failed. Test results showed that the size of the loose plates had no effect on maximum load and displacement. It was shown that the connections can resist high shear loads up to thirty-one kips, but have little ductility around thirty percent above yield, thus the connections should be designed as elastic. The observed failure mechanism consisted of anchor bars tearing from the embedded angles in the connection due to loss of concrete around the angles and high eccentric loads on the connection. It was also found that current design, using a truss analogy, for the connections provided a conservative result.

2.3 Modeling of Joints between Precast Members

Initial modelling efforts on the keyway joint focused on calibration of load distribution factors between girders (Stanton & Mattock, 1987). Finite element analysis was performed on bridges with constant span, depth and width but a varying number of girders ranging from four to eight. The joints were modeled as either continuous or hinged. When the outside girder was loaded, the hinged joint provided a more uniform distribution of moment at mid-span across girders when compared to a continuous joint. When the middle girder was loaded, the opposite was observed.

Since the main purpose of these keyway joints is to transfer shear forces and not moment between girders, other researchers have since used hinges when modeling keyway joints (Z. Ma et al., 2007). Alternatively eight node shell elements have also been used for the connection (Li & Ma, 2010). The eight node element restrains all displacement and rotational degrees of freedom unlike the hinge element, which only restrains the displacement. The analysis was validated by comparing flexural strains at mid-span and shear strains near the abutments with data from field tests. It was determined that both the eight node element and the hinge element closely matched the strains seen in the field and thus the plate element could be used.

The possibility of using springs instead of either hinges or eight node shell elements was also examined for modelling of the longitudinal keyway joint (Smith et al., 2011). In particular, only the steel plate shear connectors were examined. Finite element models of composite superstructure bridges were created with varying levels of skew and intermediate steel diaphragms. The diaphragms were either placed at mid-span or at thirds along the bridge. The shear plate connectors were modeled as springs with transverse axial, transverse moment,

vertical shear and horizontal shear stiffness based on the cross sectional area and length of the plates (which were assumed to remain elastic). It should be noted that no element was used to model the grout. The use of springs was shown to be feasible and allowed for the possibility to represent a large range of connectors, as well as grout.

Precast joints in parking structures have also used springs to model the intermediate shear connectors that tie together girders and create diaphragm action (Fleischman, Restrepo, et al., 2005). Inelastic spring properties were based on experimental results where the joint force-slip relationship was tested under tension and shear. The inelastic springs were able to represent multiple joint details.

CHAPTER 3 STUDY PLAN

3.1 Research Gap

Previous experimental and analytical research has reviewed vertical load distribution for keyway joint bridges (He et al., 2013; Li & Ma, 2010; Smith et al., 2011; Stanton & Mattock, 1987). It has been noted that the typical keyway joint is sufficient for transferring forces at service loads and that intermediate diaphragms enhance load distribution. Additionally, forces experienced by shear connectors in keyway joints are not based on the number of connectors but their location with respect to loading (Z. Ma et al., 2007). To date, no research has been performed on the transverse response of bridges with longitudinal keyway joints. Additionally there is a need to study the effects of other parameters on the bridge such as intermediate diaphragms and end support conditions.

The performance of prestressed floor and roof systems after the 1994 Northridge earthquake demonstrated significant vulnerabilities. In response, research has been performed on these systems, focusing on the shear connectors that transfer the diaphragm force between elements (Djazmati & Pincheira, 2004; Fattah Shaikh & Feile, 2004; Fleischman, Naito, et al., 2005; Jose A. Pincheira et al., 1998; José A. Pincheira et al., 2005). Various connector systems have been tested under shear, tension, and multiaxial loading. Force-slip relationships have been developed and failure mechanisms have been examined. Similar shear-slip relationships must be established considering the interaction between grout and steel plate connectors that make up keyway joints in bridges. The relationships can then be modeled as inelastic springs as shown in the literature (Fleischman, Naito, et al., 2005) to appropriately incorporate the joint's influence on the superstructure.

Researchers have also identified concerns over the ability of the connections to transfer moment (Afefy et al., 2015; Li, Ma, Griffey, et al., 2010; Zhu et al., 2012). As a consequence, alternative joints that could transfer moment and allow the joint to act as a continuous section between girders have been studied. If it is found that the current joint configuration employed in longitudinal keyways results in unacceptable performance, other joints may be considered as part of this research project.

3.2 Objectives

The main objective of this research is to determine the influence of longitudinal keyway joints on the transverse response of bridges with bulb-tee girders. More specifically the goals of the project are listed below:

1. Develop a model for the shear-slip relationship of the joint interface. This will allow for characterization of composite action provided by the joint. Additionally, the research will provide designers with limit states of the current joint.
2. Consider and implement alternative joints if the existing joint demonstrates unfavorable behavior.
3. Evaluate bridge superstructure lateral displacement profiles and variables that impact its calculation, such as superstructure stiffness, substructure stiffness, end support conditions, and intermediate diaphragms.
4. Determine deformation limit states for systems with longitudinal keyway joints.
5. Develop modeling guidelines for bulb-tee girder bridges with longitudinal keyway joints. I.e. effective stiffness of the superstructure.

CHAPTER 4 EXPERIMENTAL PROGRAM

The amount of composite action that longitudinal keyway joints provide is based on their ability to resist shear flow. In order to evaluate the effectiveness of shear flow resistance, the shear slip relationship was examined through an experimental program. The program looked at both monotonic and cyclic behavior of the keyway joint currently used in Alaska. The experimental results will be used to calibrate non-linear springs that will be used in analytical bridge models for evaluation of joint connectivity. This section is limited to the experimental program that will support the analytical portion of the project. The analytical studies are described in 7.1 and Chapter 7.

The experimental program consisted of large scale unit length deck panel tests. Two phases were planned and executed, the results are presented in Chapter 5 and Chapter 6. The first phase consisted of six panels with a focus on examining the shear slip relationship of a popular as built connection typical of Alaska bridges. The second phase considered alternate connections in effort to improve the serviceability of the joint. The experimental program for the ten tests are presented in Table 4.1.

Table 4.1: Experimental Program

Test ID	Connection	Load History
1a	Shear Connectors	Monotonic
1b	Grouted Shear Key	Monotonic
2	Existing Connection	Monotonic
3	Existing Connection	Cyclic
4	Existing Connection	Cyclic
5	Existing Connection with Lower Bound Grout Strength	Cyclic
6	Existing Connection with PPC 1121	Cyclic
7	Existing Connection with Reduced Bond	Cyclic
8	Alternate Connection 1	Cyclic
9	Alternate Connection 2	Cyclic
10	Alternate Connection 1 with PPC 1121	Cyclic

4.1 Test Conceptualization

To better understand the forces imposed on the keyway joints, it is important to understand where the forces come from. A visual representation assuming Euler–Bernoulli Beam Theory is presented in Figure 4.1. As a transverse load is imposed to the superstructure of a bridge, the superstructure will deflect inducing bending moment and bending normal stresses seen in Section A. In order for the bridge to act monolithic as assumed, the longitudinal keyway joints will need to resist the shear flow in the joints. The shear flow is generated from the variation of the bending normal stresses along the cross section as seen in Section B. Thus the joint will be need to resist shear flow.

The test setup used for the experimental portion recognized that the longitudinal keyway joint resists shear stress through the flanges of the bulb-tee girders. Therefore the test setup

emulated shear loading through the joint while maintaining the same detail as the joints and surrounding flange. Figure 4.2 depicts the area of interest and the proposed test specimen that simulated the area of interest.

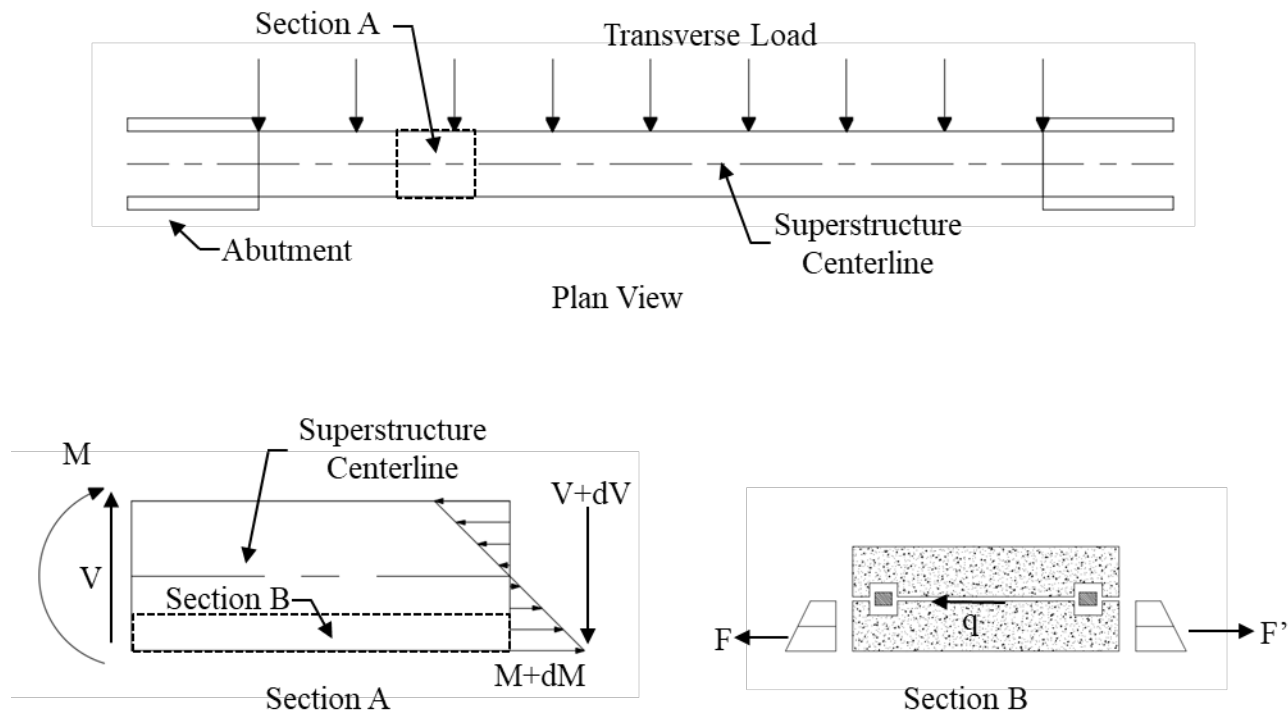


Figure 4.1: Induced Shear Flow through Longitudinal Joints

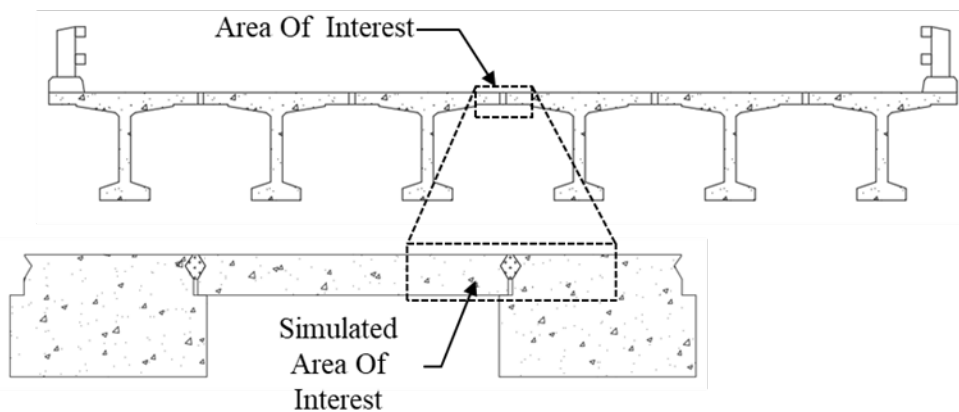


Figure 4.2: Conceptualization of the Specimen

4.2 Experimental Test Setup

The conceptual view and a photo of the actual test setup can be seen in Figure 4.3 and Figure 4.4 respectively. The test setup consisted of a 440 kip compression/300 kip tension load capacity, 40 inch stroke capacity actuator fastened horizontally to a reaction block. On the other end of the actuator was connected to the test specimen using a load spreader which consisted of a sandwich of two 8 in. x6 in. x0.5 in. Hollow Structural Section (HSS) and one 33 in. x24 in. x1 in. plate on each side of the specimen. The HSS tubes ran vertically and were spaced to match the hole configuration of the actuator ram. The HSS's transferred force to the steel plates, which in turn bore on the specimen through half-inch neoprene pads, which provided a more even distribution of stresses. The plates and HSS's were held together with four threaded rods and were hand tightened to the actuator. This setup ensured that the load was transferred through bearing in both the push and pull directions of the actuator. To take vertical load off the test specimen, the actuator head connected to the specimen rested on a Teflon sliding pad. The specimen was connected to side blocks on either side that are secured to the strong floor through post-tensioning.

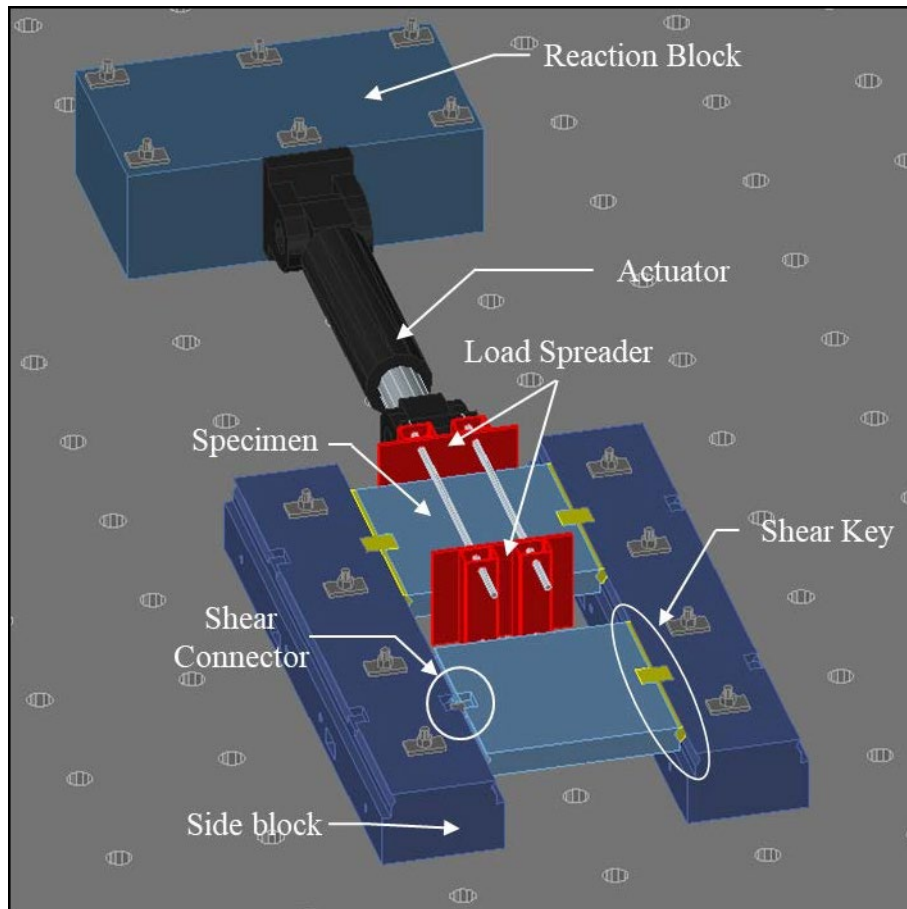


Figure 4.3: Test Setup Conceptual View



Figure 4.4: Test 3 Setup in CFL at NC State

4.3 Instrumentation

The specimen was instrumented with: (1) infrared LED markers, (2) string potentiometers, (3) electrical resistant strain gage rosettes and (4) Linear Variable Differential Transformers (LVDTs). Figure 4.5 shows the schematic of the instrumentation. It should be noted that load for the system was obtained from an internally integrated load cell inside the actuator ram.

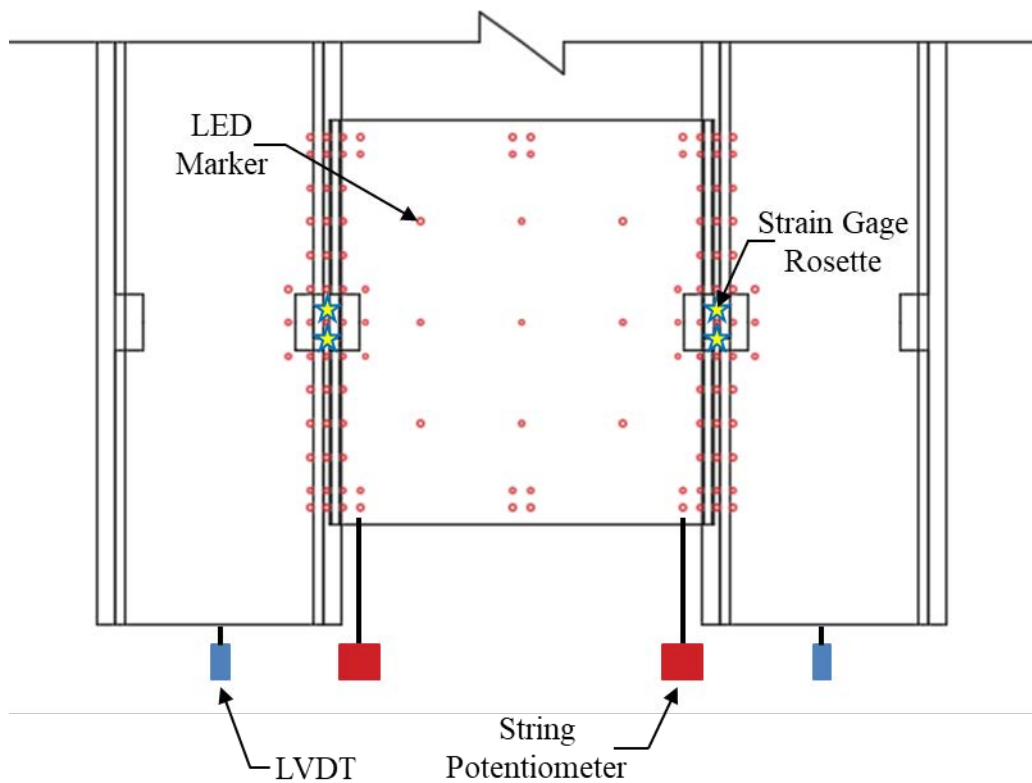


Figure 4.5: Instrumentation of Test Specimen

The 3-D position of infrared LED markers were monitored using the Optotrack Certus HD system (Northern Digital Inc., 2019). The system can provide an accurate measurement of displacement of the specimen of up to 0.006 inches at the given range. Additionally, rigid body rotation of the specimen was calculated using the LED positions. LEDs were deployed along both joints at a spacing of four inches in the longitudinal direction and a spacing of two inches in

the transverse direction. Additionally a twelve inch grid was placed about the center of the specimen.

As a redundant means of measurement, two string potentiometers were used to monitor the displacement of the joint on either side of the specimen. The difference between measurements were also used to calculate the rotation of the specimen. The string potentiometers were attached to the specimen such that they aligned with an LED in the direction of loading. But due to the nature of the damage propagation during testing, the string potentiometer would often detach from the specimen, providing inaccurate readings in later cycles of the test.

For all but one test, the grout poured into the shear key would conceal the shear connector below. Simple hand calculations showed shear failure of the connector plate, connecting the embedded shear connector inserts, to be the critical component. Due to this, the connector plates were instrumented with electrical resistant strain gage rosettes. Two rosettes placed on the longitudinal center line of the joint, half an inch from either free face as shown in Figure 4.6. The rosettes would allow the measurement of principal strains in the plate.



Figure 4.6: Electrical Resistant Strain Gage Rosettes Applied to Connector Plate

To ensure that all deformation was accounted for, linear potentiometers were placed in the center line at the base of the side blocks to monitor any lateral slip that occurred. Slip and rotation of the side blocks could thus be calculated and eliminated from the overall response of the specimen.

4.4 Specimen Detailing

The specimens were constructed to be consistent bulb tee girders from the Alaska Bridge and Structures Manual (AKDOT, 2017). The geometry of each slab was 6 in. x 48 in. x 45.75 in. corresponding to the as built slab height of six inches, the unit length of the joint of forty-eight inches and a width that matches the geometry of the CFL strong floor. The reinforcement of the slabs consisted of one #5 rebar mat and one #4 rebar mat and can be seen in Figure 4.7.

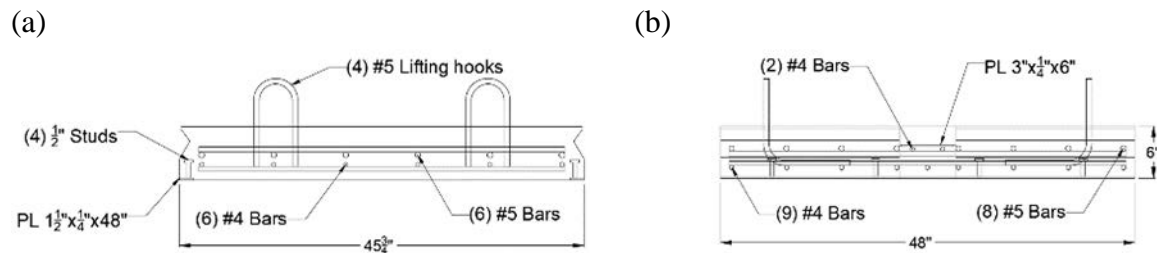


Figure 4.7: Specimen Detailing Plan (a) Front View (b) Side View

The side blocks were 29 inches wide, 18 inches tall, and 144 inches long and can be seen in Figure 4.8. The top six inches of the side blocks had reinforcement consistent with the six-inch slab test specimens, one #5 rebar mat and one #4 rebar mat of reinforcement. Along the length of the block the same diamond keyway geometry ran the entire length. Each block had two pockets on each side to allow each block to participate in four tests. The specimen were then connected to the side blocks through either welding a shear connector plate to the embedded plates in specimen and side blocks or through grouting the keyways and open pockets with high-strength, non-corrosive, non-shrink grout, or both. To prevent possible damage of the lab equipment after failure of the joint, the specimens rested on a 2-inch lip of the side blocks. To ensure that friction was minimized, the contact between the specimen and the side blocks was steel. This was done with embedded plates in the specimens and embedded angles in the side blocks. To further reduce the frictional forces, the steel was grinded clean of any rust and residue and then greased.

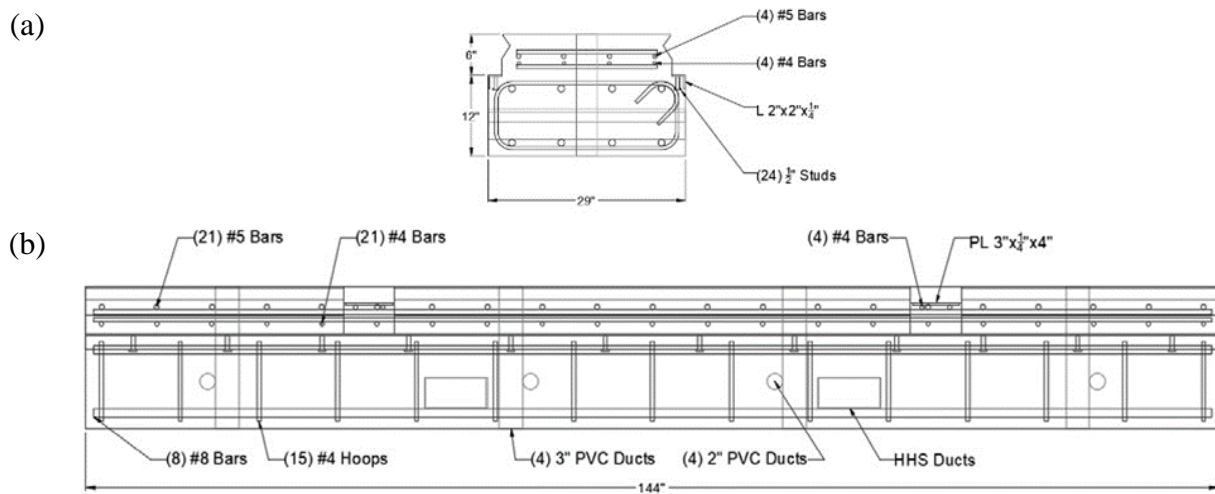


Figure 4.8: Side Block Detailing Plan (a) Front View (b) Side View

The reaction block was used to transfer force from the actuator to the strong floor. The block was 27 in. x 84 in. x 48 in. in size and used six post tensioning bars to secure to the strong floor. Two 27 in. x 18 in. x 1/2 in. plates provided a flat bearing surface for the actuator and actuator connection. The actuator was connected using four 1 1/2 in. threaded rods that pass through the 2 in. duct in the block to the knuckle of the actuator. The rods were hand fastened with a washer plate and a nut. The reinforcement of the block consisted of ten pairs of U-bars that were tied together to create a closed hoop, where U-bars were placed in line with the direction of loading. Sixteen #8 bars make up the reinforcement in the orthogonal direction. The detailing can be seen in Figure 4.9.

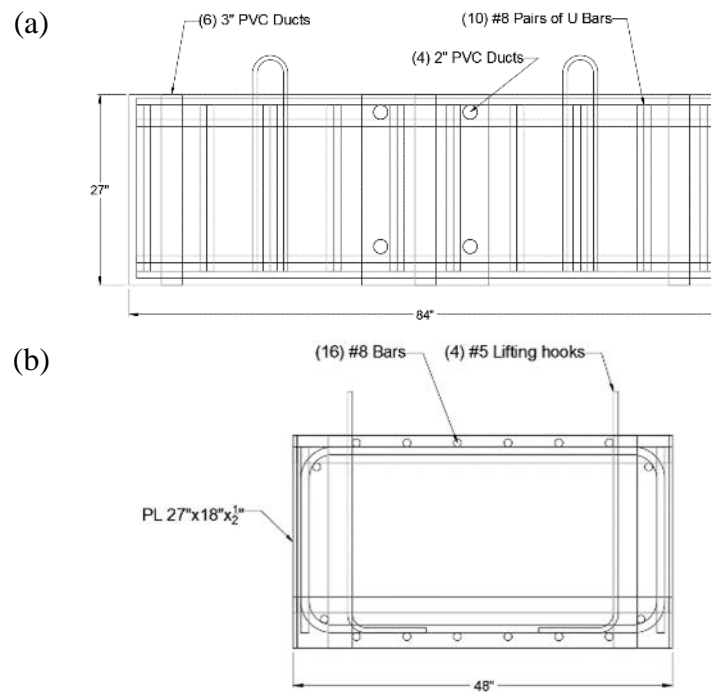


Figure 4.9: Reaction Block Detailing Plan (a) Front View (b) Side View

4.5 Specimen Construction

All concrete elements were constructed at the Constructed Facility Laboratory on North Carolina State University's Centennial Campus Raleigh. Steel cages and mats used for the specimens and side blocks were tied using templates to ensure uniform spacing. Once each component of steel was tied, they were placed into forms. Steel-Ply forms were used for the side blocks and reaction block, but due to the unique dimensions of the specimens, specimen forms were constructed out of plywood and dimension lumber. Construction of each element prior to pouring concrete is visible in in Figure 4.8.

Once the specimen forms were assembled, the keyway block outs were placed. Custom birch trim was used to construct the block out which allowed for easy instillation and structural integrity. The forms were sprayed with form release solution and allowed to dry before steel was inserted. The steel mats were placed in the forms with the steel connector imbeds on top of the mats. Rectangular wood blocks covered the steel connector insert plates and blocked out the shear pocket.

The side block formwork was first sprayed with form release and allowed to dry. Then the steel cages that make up the bottom section of the side block element were placed. The horizontal duct work were then inserted which comprised of HSS ducts and 2 in. PVC ducts. The steel angles were bolted to the side of the forms to make up the side block lip. The key block out was assembled, sprayed and inserted on top of the steel angles, which included adding two inches of additional block out. Next the steel mats were placed in the forms with the steel connector imbeds on the top of the mats. Rectangular wood blocks covered the steel connector insert plates and blocked out the shear pocket. Lastly the horizontal duct work was placed.

The reaction block formwork was first sprayed with form release and allowed to dry. The steel plates were then fastened to the forms. The steel U bars pairs were assembled prior to placing them in the formwork. Once placed the steel cage was tied inside the forms. The horizontal and vertical ductwork were installed.



Figure 4.10: Specimen Construction (a) Specimen (b) Side Block (c) Reaction Block

4.6 As Built Joint Detailing

The as built joint detailing was based on Alaska Bridge 663. The joint detailing consisted of two components; the steel connector and the grouted keyway, both of which will be discussed in this section. This detailing is consistent with the detailing found in Tests 1-7.

4.6.1 Steel Connector

The steel connector was comprised of an A36 3 in. x 1/4 in. x 4 in. connector plate that was field welded to the embedded shear connector insert present in both the side block and specimen. The 3/16 in. fillet weld wrapped around all outside edges of the connector plate. The details of the embedded shear connector insert can be seen in Figure 4.11 and Figure 4.12. To ensure that there was no offset from the centerline of the specimens and side blocks, the plates were welded to both ends of the rebar. The length of rebar for the specimens was 44 3/4 in. based on geometry and the length for the side blocks was 24 in. based on the embedment length used for Alaska Bridge 663, as seen in Figure 4.13.

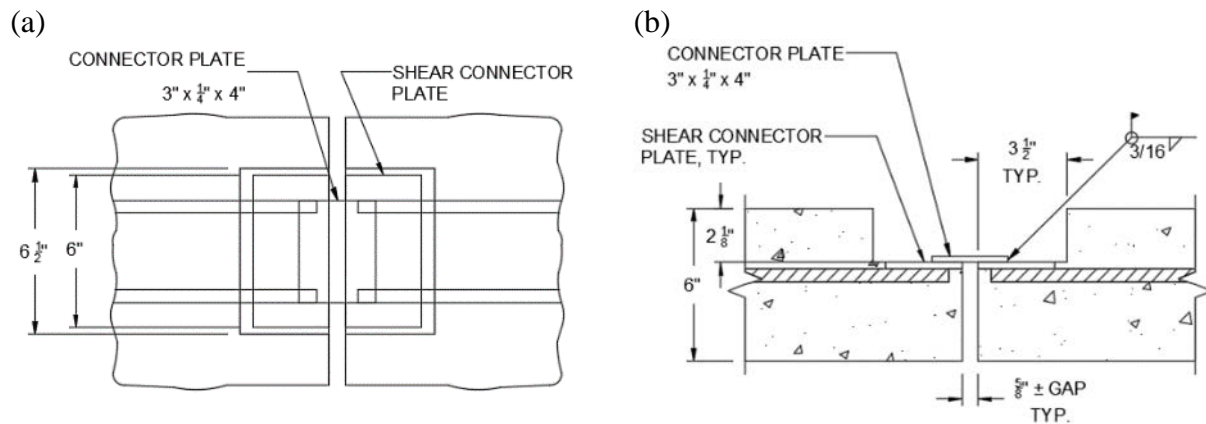


Figure 4.11: Shear Connector (a) Top View (b) Side View

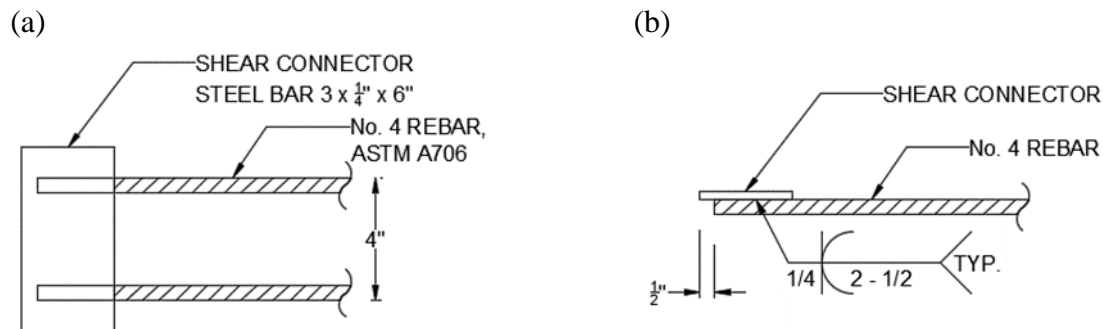


Figure 4.12: Shear Connector Inserts (a) Top View (b) Side View



Figure 4.13: Shear Connector Inserts (a) Specimen (b) Side Block

4.6.2 Longitudinal Shear Key

The detailing of the grouted keyway can be seen in Figure 4.14. This detailing varies from Alaska bridge 663's detail such that the top of the key did not end at a point but rather a $\frac{1}{4}$ in. rectangle. The alteration was done to avoid stress concentrations at the top of the keyway and avoid chipping. The shear key was a $3 \frac{5}{8}$ inch tall by 3 inch wide diamond shaped void that was filled with grout to connect the specimen to the side blocks on either side through compatibility. The block out used during construction for the shear key is presented in Figure 4.15. After forms were removed, the surface of the keyway was prepared to remove any loose concrete and expose the aggregate.

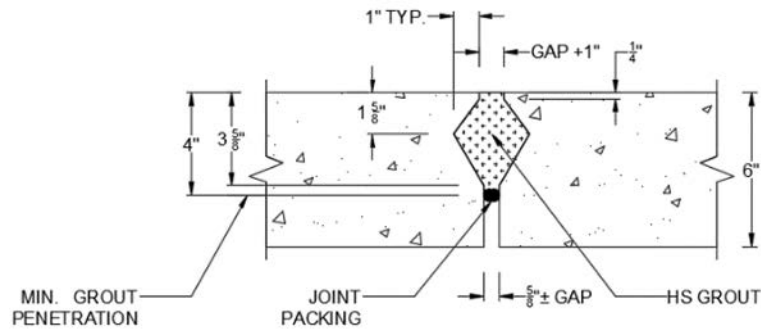


Figure 4.14: Longitudinal Shear Key

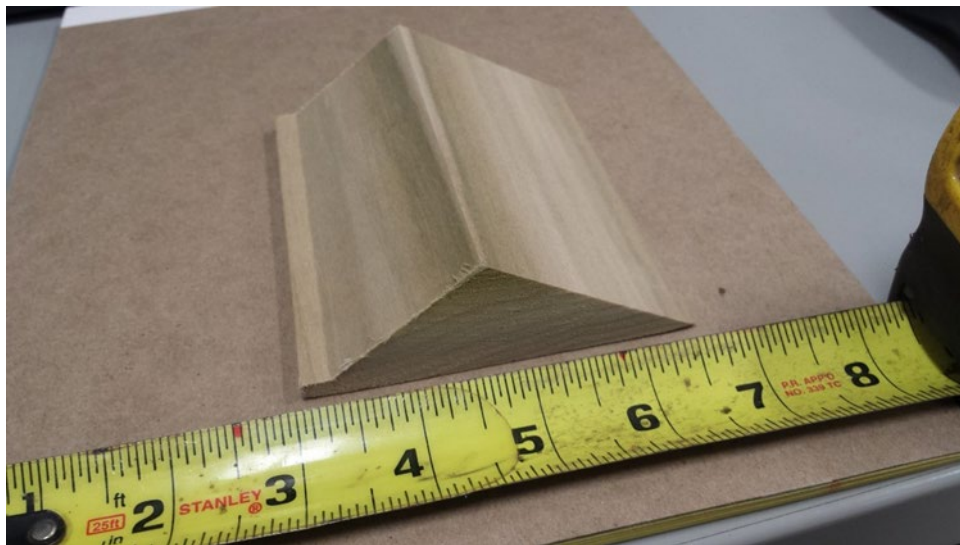


Figure 4.15: Longitudinal Shear Key Block Out

4.7 Material Properties

4.7.1 Concrete

Concrete compressive strength was specified as 6,750 psi at 28 days which matched strength specifications for bulb-tee girders in recent Alaska bridge 663 drawings. The mix was designed and produced locally. All concrete elements were poured from the same batch. After casting, a water-based concrete curing and sealing compound was applied on the surface. The elements were left to cure in their formwork for the next seven consecutive days. Cylinders were cast to verify the required compressive strength and to determine compressive stress on specimen testing day. Compressive strength was determined in accordance with ASTM C39, (2016). A sample of a tested cylinder is presented in Figure 4.16. The average concrete compressive strength for each specimen is detailed in Table 4.2.



Figure 4.16 ASTM C39 Cylinder Test

Table 4.2: Average Concrete Compressive Strength

Specimen	f'_c (7 Day) [ksi]	f'_c (28 Day) [ksi]	f'_c (Test Day) [ksi]
S1			8.59
S2			10.88
S3			10.08
S4	5.72	7.50	9.74
S5			10.43
S6			10.93
S7			7.08
S8			7.55
S9		6.41	8.11
S10			8.46

4.7.2 Steel

All longitudinal and transverse reinforcement used during construction of the concrete elements was ASTM A706 Grade 60 black steel. While all plates and angles were ASTM A36 Steel. Tension tests were conducted for each phase using ASTM 370, (2014). For the first phase, coupons were constructed out of the ¼ in. bar and #4 rebar used to create the shear connector inserts. For the second phase, coupons were constructed out of the #4 rebar, ¼ in. bar, and the 1 in. bar used to construct the shear connector inserts. The yield stress, yield strain, ultimate stress and ultimate strain are summarized in Table 4.3 through Table 4.7. While the tension tests showed relatively consistent results, it should be noted that the yield stress for the ASTM A36 steels were at least 150% higher than the design value.

Specimens were placed in an MTS high-force test system (Figure 4.17) and loaded at a maximum rate of 0.5 in/min during the elastic portion of testing and a maximum of 1.0 in/min during the inelastic portion of testing. Strains during the tension tests were predominantly captured with a two inch extensometer placed mid-height of the specimen. The exception was the #4 rebar in phase one, which used the Optotrack Certus HD system in conjunction with

infrared LEDs to capture displacements and back calculate strains. The LEDs had a gage length of two inches.

Table 4.3: Phase I Material Properties of A706 #4 Rebar

Rebar Tensile Test ID	Properties at Yield Stress		Properties at Maximum Stress	
	Stress [ksi]	Strain [in/in]	Stress [ksi]	Strain [in/in]
1	67.95	0.0032	99.37	0.1154
2	66.94	0.0033	99.00	0.1130
3	66.98	0.0033	98.95	0.1136
Average	67.29	0.0033	99.11	0.1140

Table 4.4: Phase II Material Properties of A706 #4 Rebar

Rebar Tensile Test ID	Properties at Yield Stress		Properties at Maximum Stress	
	Stress [ksi]	Strain [in/in]	Stress [ksi]	Strain [in/in]
1	64.11	0.0027	98.69	0.1190
2	67.46	0.0030	99.01	0.1094
3	64.60	0.0028	98.74	0.1162
Average	65.39	0.0028	98.81	0.1149

Table 4.5: Phase I Material Properties of A36 ¼ in. Steel Plate Coupons

Coupon Tensile Test ID	Properties at Yield Stress		Properties at Maximum Stress	
	Stress [ksi]	Strain [in/in]	Stress [ksi]	Strain [in/in]
1	57.19	0.0019	74.11	0.1737
2	54.51	0.0018	73.81	0.1754
3	55.13	0.0022	73.83	0.1712
Average	55.61	0.0020	73.92	0.1734

Table 4.6: Phase II Material Properties of A36 ¼ in. Steel Plate Coupons

Coupon Tensile Test ID	Properties at Yield Stress		Properties at Maximum Stress	
	Stress [ksi]	Strain [in/in]	Stress [ksi]	Strain [in/in]
1	56.58	0.0023	78.74	0.1589
2	57.44	0.0022	79.53	0.1536
3	60.07	0.0023	78.69	0.1592
Average	58.03	0.0023	78.99	0.1572

Table 4.7: Phase II Material Properties of A36 1 in. Steel Plate Coupons

Coupon Tensile Test ID	Properties at Yield Stress		Properties at Maximum Stress	
	Stress [ksi]	Strain [in/in]	Stress [ksi]	Strain [in/in]
1	59.04	0.0022	75.05	0.1229
2	59.10	0.0023	74.93	0.1376
3	56.88	0.0032	74.28	0.1399
Average	58.34	0.0026	74.75	0.1335



Figure 4.17: ASTM 370 Tension Test

4.7.3 Grout

In accordance with Alaska Department of Transportation (Alaska DOT) practices, the grout used in longitudinal shear keys must be a non-shrink, non-metallic/non-corrosive, high-strength grout with at least a 28 day compressive strength of 9,000 psi. Alaska DOT provided three commercially available grouts used in recent projects that meet the requirements, Dayton

Superior Sure-Grip High Performance Grout, Dayton Superior 1107 Advantage Grout, and Sakrete Non-Shrink Construction Grout. Along with the three provided grouts, BASF Master Flow 928 Grout was examined of its strength and durability. More details in the study can be found in Section 4.7.3.1. The study showed that Dayton Superior Sure-Grip High Performance Grout as meeting both strength and durability requirements, thus it was used for the experimental tests.

Test specimens were prepared as per manufacturer recommendations, with the surface saturated four hours prior to pouring the grout into the keyway and shear connector pocket. The water content used in the mix for all the tests was 6.6 pounds of water per 50 pounds of mix. After the grout was poured, it was moist cured for three days using a layer of plastic followed by a layer of moist cloth followed by one more layer of plastic (Figure 4.18). To acquire material properties for test day prediction, ASTM C109,(2010). Tests were performed on 2x2x2 inch cubes on the day of the test, with results shown in Table 4.8.

In addition to conventional grout, a Polyester Polymer Concrete (PPC) was used for two of the tests. The material was prepared and applied with the guidance of a company representative. Prior to use, a material test study was performed with results in section 4.7.3.2.



Figure 4.18: Moist Curing of Grouted Specimen

Table 4.8: Average Grout Compressive Strength

Specimen	Age [Days]	f _c (Test Day) [ksi]
S1	4	7.55
S2	12	10.21
S3	30	12.01
S4	72	11.79
S5	7	7.16
S6*	6	7.10
S7	15	8.92
S8	10	5.74
S9	9	7.10
S10*	17	7.34

*polyester polymer concrete

4.7.3.1 High Strength Grout Material Study

While strength was the main focus of this study, durability of the grout was desirable for the longevity of the connection. To determine grout properties, each underwent compressive strength testing (ASTM C109-10; ASTM C39-16), splitting tensile strength testing (ASTM C496-17), and resistance to freezing and thawing/ durability testing (ASTM C666-03). Grout was prepared using motorized concrete mixer and the appropriate water content given by the grout data sheet.

Compressive strength tests were performed at ambient temperature on cubes and cylinders at 3, 7, 28, and 90 days. The results are presented in Table 4.9 through Table 4.12. All grouts except Sakrete Non-Shrink Construction Grout met the 28 day compressive strength requirement of 9.0 ksi in both cylinder and cube compression tests. BASF Master Flow 928 provided the highest strength followed by Dayton Superior Sure-Grip High Performance Grout. Split tension strength tests were performed at ambient temperature on cylinders at 28 and 90 day strength. The results can also be found in Table 4.9 through Table 4.12. The same trend in compressive strength was seen in the split tensile strength with BASF Master Flow 928 providing the highest strength followed by Dayton Superior Sure-Grip High Performance Grout.

Durability testing was also performed for all four grouts by another researcher and can be found elsewhere (Jayaprakash, Nau, Pour-Ghaz, and Kowalsky,2019). The preliminary results showed consistent and satisfactory results for, Dayton Superior Sure-Grip High Performance Grout and Dayton Superior 1107 Advantage Grout. Satisfactory results are defined as grout prisms maintaining a minimum elastic modulus of 60% of the original modulus after being exposed to 300 repeated freezing and thawing cycles. BASF Master Flow 928 showed inconsistency in meeting these requirements.

With results from the strength and durability tests, Dayton Superior Sure-Grip High Performance Grout was selected to be used as the grout in the experimental program. Dayton Superior Sure-Grip High Performance Grout had the second highest strength in both the strength compressive tests and the split tensile tests while meeting the ASTM C666 specifications for durability.

Table 4.9: Material Properties of Dayton Superior Sure-Grip High Performance Grout

Age [Days]		Stress [ksi]		
		4x8 Cylinder	2x2x2 Cube	Split Tension
3	Average	8.10	10.21	
	Std. Dev.	0.10	0.46	
7	Average	8.91	10.41	
	Std. Dev.	0.25	0.33	
28	Average	9.86	10.41	0.63
	Std. Dev.	0.29	0.88	0.04

Table 4.10: Material Properties of Dayton Superior 1107 Advantage Grout

Age [Days]		Stress [ksi]		
		4x8 Cylinder	2x2x2 Cube	Split Tension
3	Average	7.16	7.18	
	Std. Dev.	0.29	0.15	
7	Average	8.04	8.93	
	Std. Dev.	0.29	0.35	
28	Average	9.05	9.91	0.61
	Std. Dev.	0.21	0.53	0.01
90	Average	9.61	10.44	0.44
	Std. Dev.	0.44	1.00	0.16

Table 4.11: Material Properties of Sakrete Non-Shrink Construction Grout

Age [Days]		Stress [ksi]		
		4x8 Cylinder	2x2x2 Cube	Split Tension
3	Average	5.60	6.47	
	Std. Dev.	0.13	0.69	
7	Average	7.42	7.15	
	Std. Dev.	0.15	0.84	
28	Average	8.43	8.60	0.50
	Std. Dev.	0.38	0.81	0.16
90	Average	9.44	10.66	0.32
	Std. Dev.	0.34	0.77	0.10

Table 4.12: Material Properties of BASF Master Flow 928 Grout

Age [Days]		Stress [ksi]		
		4x8 Cylinder	2x2x2 Cube	Split Tension
3	Average	7.84	8.44	
	Std. Dev.	0.21	0.45	
7	Average	8.80	10.20	
	Std. Dev.	0.02	0.26	
28	Average	10.60	11.47	0.68
	Std. Dev.	0.70	0.81	0.21
90	Average	11.04	12.27	0.61
	Std. Dev.	0.76	0.51	0.12

4.7.3.2 Polyester Polymer Concrete Material Study

A substitution of a conventional grout for a PPC was motivated from the benefits associated with a reduced curing time, allowing a bridge to carry load as early as four hours after installation. AKDOT currently utilizes PPCs for bridge overlays to increase the longevity of bridge decks. KwikBond Polymers, LLC PPC 1121 has had been used on past bridge Alaska Bridge projects and was thus selected for this study.

Preliminary testing was performed to determine the suitability of the PPC. These tests included compressive strength testing (ASTM C579-01, method B & C), splitting tensile strength testing (ASTM C496-17), length change testing (ASTM C490, 2017), and Differential Scanning Calorimetry (DSC) testing (ASTM E1356-08). Kwikbond provided all material used to cast the specimens. Materials were mixed in 5 gallon buckets using an electric double-paddle hand mixer. Materials were proportioned and mixed following the Kwikbond product data sheet. The mix was comprised of 2 parts graded sand, 1 part graded rock, PPC binder resin at 12% of aggregate weight, DDM 9 catalyst at 2% of resin weight, and Z Cure additive at 2% of catalyst weight. Forty 2x2x2 inch cubes, eighteen 4x8 inch cylinders and three 1x1x1¼ inch prisms were made from a total of five batches cast in a 22°C controlled environment.

Compressive strength tests were performed at ambient temperature on cubes and cylinders at 3, 7, 28, and 90 day strength. To determine if low temperature effects the compressive strength, compressive strength tests were performed on cubes at -20°C at 3, 7, and 28 day strength. Split tension tests were performed on cylinders at 28 and 90 day strength. It should be noted that one of the batches used to cast fifteen of the forty cubes had cured before proper consolidation was achieved leading to those fifteen specimens being discarded. The results from the compressive strength test are shown below in Table 4.13. Figure 4.19 compares the compressive strength between the cylinders and cubes tested at ambient temperature. The results show little difference between methods, with no significant change in strength after seven days. Figure 4.20 compares the compressive strength between cubes tested at ambient temperature and cubes tested at -20°C. The cubes tested at -20°C had 160% more strength than cubes tested at ambient temperature. When comparing the split tension test between PPC and the grout used in the previous tests, the PPC had 130% greater capacity.

To assess high temperature effects, DSC was used to determine the glass transition temperature, T_g , of the polyester. Three samples were tested. The first sample had a mass of 10.9

mg and used a heat rate of 10°C/min to go from 0°C to 300°C. No clear location for T_g could be determined. The rate of loading was decreased from 10°C/min to 1°C/min for the second sample, which had a mass of 12.0 mg and went from 0°C to 250°C. Still no clear location of T_g was evident. The third sample rate of loading was 1°C/min from 0°C to 500°C with a mass of 9.6 mg. The third sample showed signs of evaporation but still no clear indication of a glass transition point. Thus the efforts to determine the T_g were discontinued.

The early age shrinkage of the PPC was monitored using two 1x1x1 1¼ inch prisms. It should be noted that the third prism broke upon demolding of the specimen. Samples were monitored for two weeks (Figure 4.21). The average recorded strain 24 hours after casting was 294×10^{-6} in/in. At the end of two weeks the average strain was measured to be 324×10^{-6} in/in.

It was determined that PPC would be a suitable material, despite having a lower compressive strength (although the split tension strength was higher than the conventional high strength grouts). Additionally, while the coefficient of thermal expansion provided by KwikBond Polymers, LLC (8.4×10^{-6} in/in/°F) is higher than that of a conventional grout such as BASF Master Flow 928 (6.5×10^{-6} in/in/°F), the amount of early age shrinkage is substantially lower in the PPC. Where early age shrink BASF Master Flow 928 was experimentally found to be 173×10^{-6} (the difference between the early age shrinkage divided by the difference in the coefficient of thermal expansion is 79.5, meaning a 79.5°F variation in temperature would provide equal strain from shrinkage between the PPC and the conventional grout). More detail on early age shrinkage of BASF Master Flow can be found in the report on Durability of the Grouted Shear Stud Connection in Cold Climates.

Table 4.13: Material Properties of PPC 1121

Day	Stress [ksi]			
	2x2x2 Cube	4x8 Cylinder	2x2x2 Cube [-20°C]	Split Tension
3	5.93	6.20	10.58	
	6.84	6.20	12.14	
	6.68	6.34	9.68	
Average	6.48	6.25	10.80	
7	6.98	6.56	11.83	
	7.10	7.03	11.94	
	7.25	6.47	12.19	
Average	7.11	6.69	11.99	
28	7.02	5.88	11.20	
	6.66	6.45	10.48	0.81
	7.22	6.12	10.82	0.82
Average	6.96	6.15	10.83	0.82
90	6.73	6.57		
	6.68	6.42		0.89
	5.73	6.88		0.87
Average	6.38	6.62		0.88

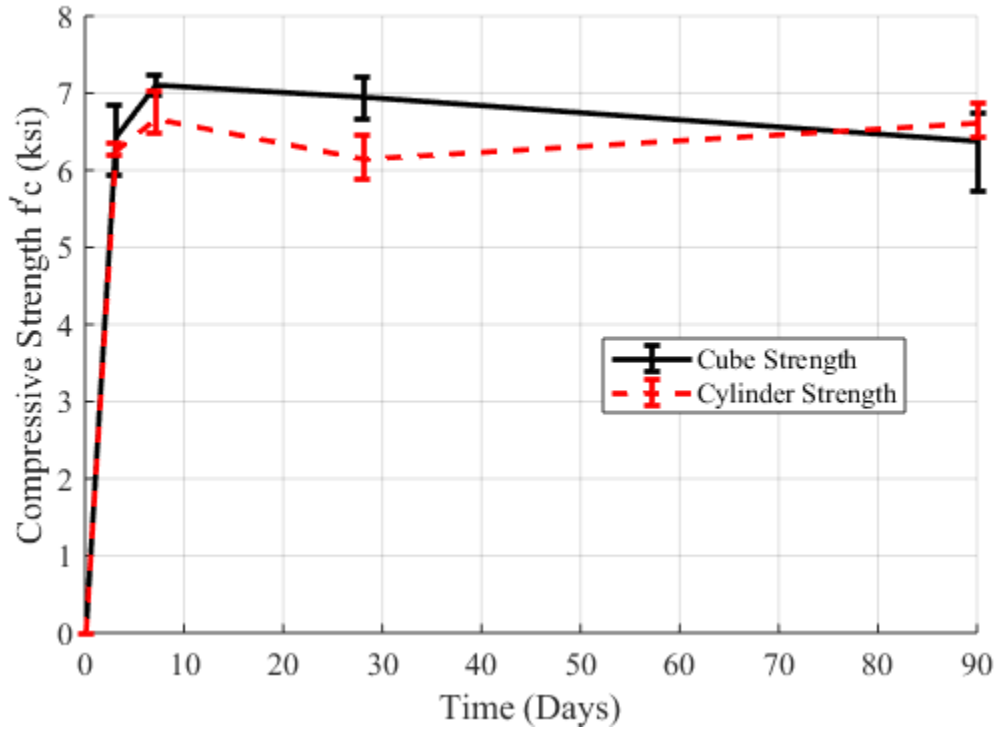


Figure 4.19: PPC 1121 Compressive Strength Comparison of Cube and Cylinders

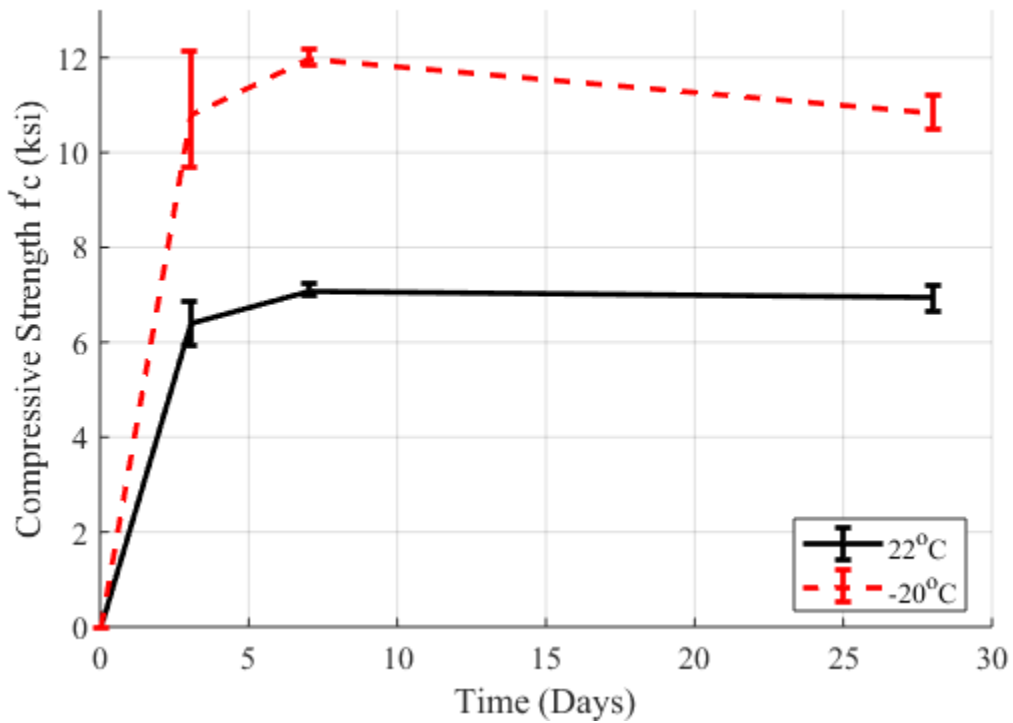


Figure 4.20: PPC 1121 Cube Compressive Strength f'c Variation due to Temperature

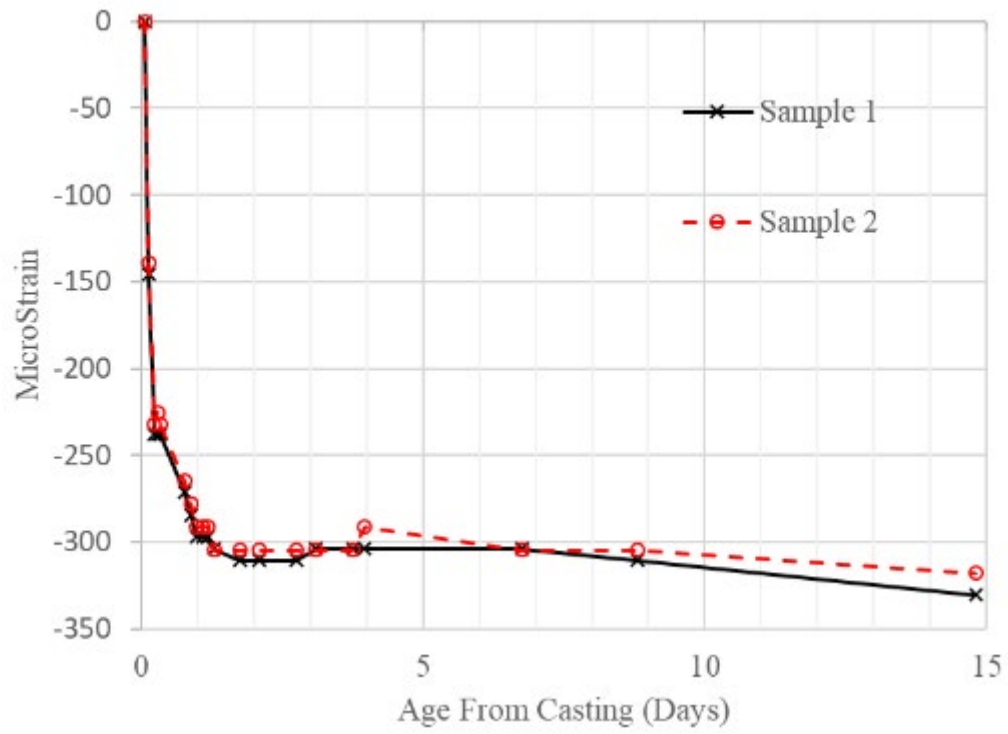


Figure 4.21: PPC 1121 1x1x11¼ Prism Shrinkage Strain

4.8 Loading Protocol

A monotonic push-over scheme was used for the initial loading protocol for testing specimens. The scheme was implemented for the first three tests; Test 1a., Test 1b., and Test 2. Loading was performed in terms of force at quarter increments of the expected capacity up until a reduction in force was observed. Then the load was applied in terms of displacements up until significant damage or rotation was evident. Monotonic loading was applied in quarter increments of the expected capacity of the test.

Test 1a. only examined the shear connector portion of the existing connection. The maximum capacity estimation was based on capacity calculations of the shear connector. The calculations determined the connection was controlled by shear yielding in the 3 in. x 4 in x ¼ in shear connector plate. Test 1b. only examined the grouted shear key portion. The maximum capacity estimation was based on the AASHTO LRFD tension stress limit equation for components subject to moderate or lower corrosion conditions as given by Equation 4.1. For all successive tests, maximum capacity was estimated, using the results for the two prior tests. The grouted shear key max strength was derived using Equation 4.1 and assuming a cracked displacement equal to the displacement observed in Test 1b (grouted shear key only). The force component of the steel shear tab at the maximum anticipated strength was based on the force displacement response of Test 1a. (steel shear tab only) and the cracking displacement of the grout.

$$f_t = 0.19 \sqrt{f'_c} \text{ (ksi) or } f_t = 6\sqrt{f'_c} \text{ (psi)} \quad \text{Equation 4.1}$$

A monotonic loading protocol is helpful to determine the upper bound performance of the connection but a cyclic loading protocol was desired due to the nature of earthquake induced loading. Since it was unclear what the expected demand of the joint would be, a parametric study was performed to determine maximum shear flow between girders in bulb tee superstructures up to controlling limit states. The study is presented in in section 4.8.1. It was determined that continuous bridges could expect maximum shear flows ranging from 0.2 k/in to 54 k/in upon reaching a design limit states. With knowledge that the monotonic test on the existing joint provided a capacity to withstand an average shear flow of 2.7k/in before significant

strength loss, the joint is expected to withstand maximum demands below and above its strength capacity.

The outcome was a loading protocol that captured shear flow levels typical of bridge geometries considered. Force was applied cyclically in three cycle sets. Starting with an average shear flow along the joint equal to 0.1 k/in and increasing with increments of 0.1k/in until 1.0k/in. The increment then increased to 0.2k/in. Load would be applied until a significant strength loss occurred in the specimen at which point, a displacement control protocol was applied. Displacements were applied in three cycle sets based on increments of displacement proportional to the displacement of significant strength loss (denoted as Δ_c). The loading protocol is graphically displayed in Figure 4.22 and Figure 4.23.

Test 3, the first cyclic test, showed that no significant damage accumulation occurred prior to the maximum force capacity due to cyclic loading. Therefore, the force portion of the loading protocol was switched to single cycle sets at quarter increments of the maximum anticipated strength, calculated as mentioned above, until strength loss occurred.

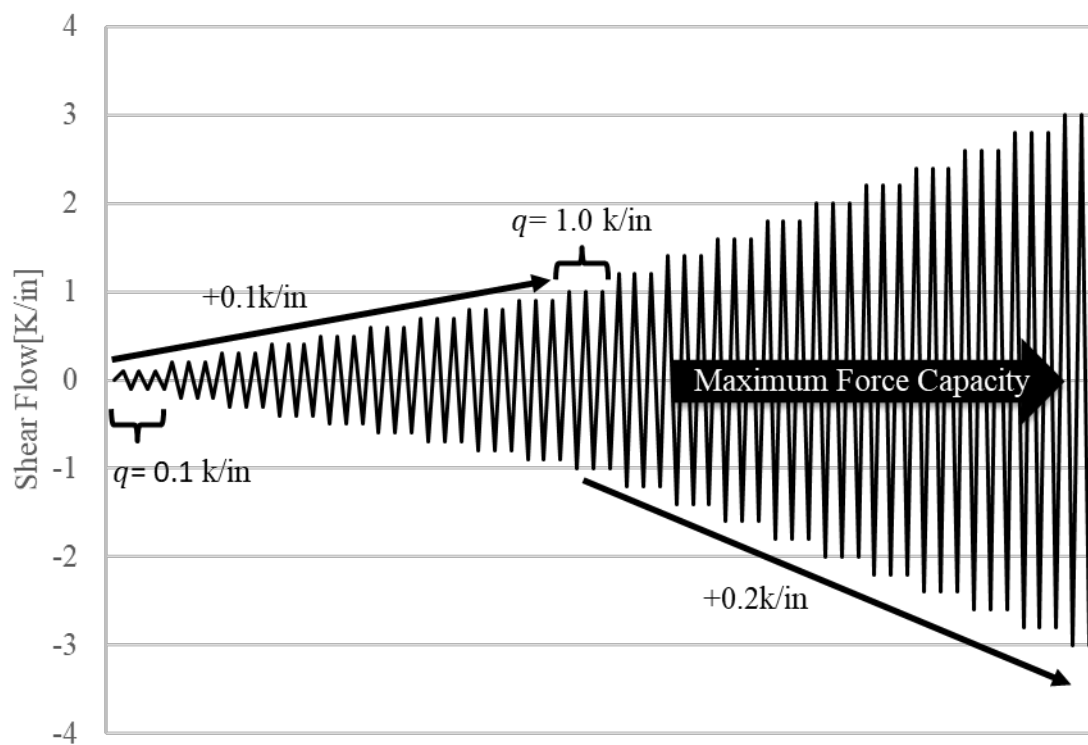


Figure 4.22: Cyclic Force Loading Protocol

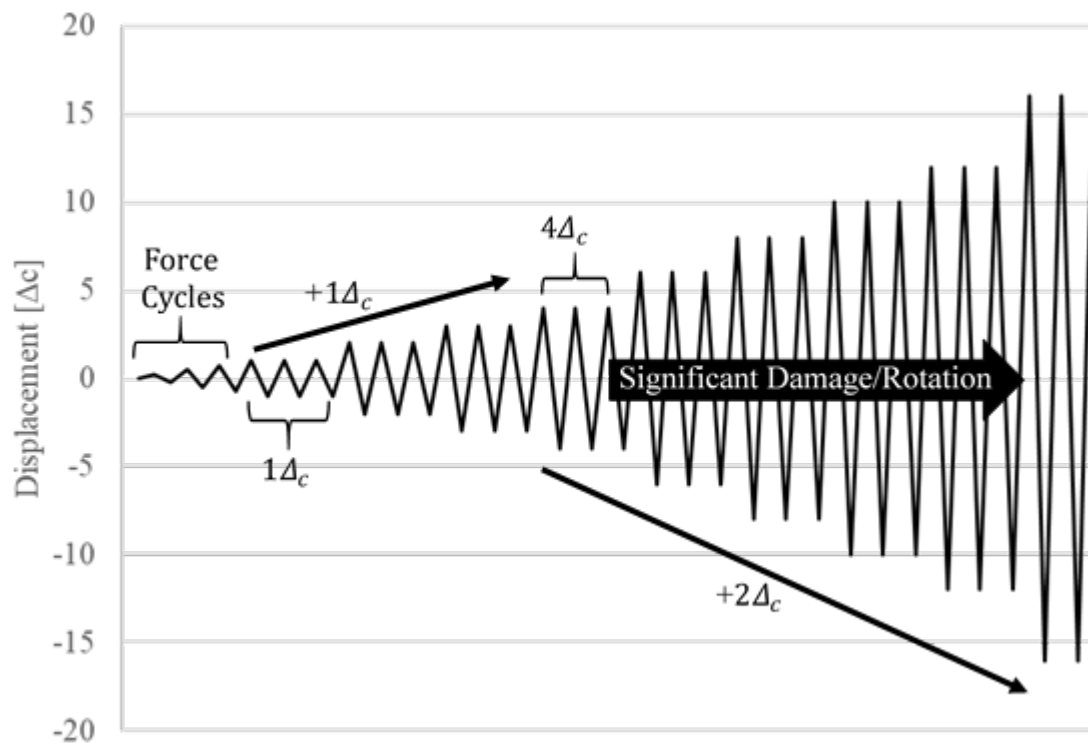


Figure 4.23: Cyclic Displacement Loading Protocol

4.8.1 Maximum Shear Flow Parametric Study

A parametric study was performed to estimate the maximum shear flow that would occur between girders in bulb tee superstructures based on various displacement limit states. The parametric study assumed pinned abutment conditions, uniform column height, zero column stiffness, and a continuous symmetric superstructure. The lesser of two displacement limits were found at a point 'x' along the bridge where x is the distance to the center bridge column. The first displacement limit state, $\Delta_{5\%}$, was based on five percent column drift using Equation 4.2. Where h_c is the column height. The second displacement limit state, Δ_ϕ , was based on the yield curvature of the superstructure, ϕ_y , length of the superstructure, l , and the length along the superstructure, x , using Equation 4.6 ϕ_y is defined in Equation 4.3, where ε_y is the yield strain of longitudinal rebar (assumed to be 0.002 in/in) and w_{ss} is the superstructure width. A uniform load, w , was then calculated using the lesser of the two displacement limit states using Equation 4.5 where E_{ss} is the modulus of elasticity of the superstructure and I_{ss} is the moment of inertia of the superstructure about the transverse direction. The uniform load was then used to calculate the maximum shear force as seen in Equation 4.6 where Q_{ss} , is the first moment of area of the superstructure to the closest longitudinal joint to the centroid and b is the thickness of the joint. Consequently the maximum shear flow through the joint can be calculated using Equation 4.7.

$$\Delta_{5\%} = 0.05h_c \quad \text{Equation 4.2}$$

$$\phi_y = \frac{2\varepsilon_y}{w_{ss}} \quad \text{Equation 4.3}$$

$$\Delta_\phi = \phi_y \frac{l^3 - 2lx^2 + x^3}{3l^2} x \quad \text{Equation 4.4}$$

$$w = \Delta(x) \frac{24E_{ss}I_{ss}}{x(l^3 - 2lx^2 + x^3)} \quad \text{Equation 4.5}$$

$$\tau_{max} = \frac{wlQ_{ss}}{2I_{ss}b} \quad \text{Equation 4.6}$$

$$q_{max} = \tau_{max}b \quad \text{Equation 4.7}$$

To get the values for the parametric study, Alaska bridge drawings 505, 537, and 547 were used. This provided three different column heights, three different supper structure geometries (w_{ss} , I_{ss} , Q_{ss}) and three different bridge lengths for a total of twenty seven different combinations of bridges. An example of one calculation is provided below for Alaska Bridge 537. The elevation view in Figure 4.24 (a) provides a span length of 356'-4 in. Using Figure 4.24 (b) and (c), the elevations for bottom and top of the columns can be used to estimate the column height, h_c , as 36 feet. Figure 4.24 (c) and (d) can then be used to calculate cross sectional properties w_{ss} , I_{ss} and Q_{ss} , where Q_{ss} is to the closest joint to the centroid of the cross section. w_{ss} , I_{ss} and Q_{ss} were calculated to equal 45 feet, 8819 ft⁴, and 291 ft³ respectively. A uniform distributed load of 69.4 k/ft was calculated using Equation 4.5 to provide $\Delta\phi$ equal to 7.2 in. at 125'-6 in. along the bridge. This equated to a maximum shear flow of 24.0 k/in along the keyway joint. The complete results of the parametric study can be seen in Table 4.14 sorted from lowest to highest maximum shear flow. The study resulted in maximum shear flows ranging from 1.1 k/in to 25.9 k/in.

A broader parametric study was done on the range of expected geometries for Alaska Bridges. Parameters in the study were bridge lengths of 150 feet to 900 feet. at increments of 150 ft., column heights of 10 feet to 80 feet at increments of 15 feet and bridge widths of 32 and 64 feet for a total of 60 cases using the girder geometry from Alaska Bridge 547. The study results produced maximum shear flows ranging 0.2 k/in to 54 k/in, which captured the subset of shear flows seen in the first study. The same trends were observable for both studies as can be seen in Table 4.14. At lower levels of maximum shear flow, the controlling limit is the column displacement limit. But as the column height increases, and/or the bridge width increases, and/or bridge length decreases, the controlling limit tends towards the yield curvature displacement limit. But before the yield curvature displacement limit controls, maximum shear flow values reach levels above the average shear flow levels sustained by Test 2 (2.7 k/in) (the complete connection of both the welded steel connector plate and grouted keyway under monotonic loading). In Table 4.14, the last entry before the shear flow is above 2.7 k/in is Entry 9 which coincidentally is the value for Alaska Bridge 505.

Table 4.14: Maximum Shear Flow Parametric Study Results

Entry	Parameters			Limits		Demand		
	h_c [ft]	w_{ss} [ft]	l [ft]	$\Delta_{5\%}$ [in]	Δ_ϕ [in]	w [k/ft]	τ_{max} [ksi]	q_{max} [k/in]
1	36	38	896	21.6	109.3	0.7	0.18	1.1
2	44.3	38	896	26.6	109.3	0.9	0.22	1.3
3	46.24	38	896	27.7	109.3	0.9	0.23	1.4
4	36	45	896	21.6	92.3	1.3	0.26	1.6
5	36	42.6	896	21.6	97.5	1.2	0.27	1.6
6	44.3	45	896	26.6	92.3	1.6	0.32	1.9
7	44.3	42.6	896	26.6	97.5	1.5	0.33	2.0
8	46.24	45	896	27.7	92.3	1.6	0.34	2.0
9*	46.24	42.6	896	27.7	97.5	1.6	0.34	2.1
10	46.24	38	356	27.7	14.9	23.0	2.27	13.6
11	36	38	356	21.6	14.9	23.0	2.27	13.6
12***	44.3	38	356	26.6	14.9	23.0	2.27	13.6
13	46.24	45	356	27.7	12.6	34.5	2.82	16.9
14	36	45	356	21.6	12.6	34.5	2.82	16.9
15	44.3	45	356	26.6	12.6	34.5	2.82	16.9
16	46.24	42.6	356	27.7	13.3	34.7	3.04	18.2
17	36	42.6	356	21.6	13.3	34.7	3.04	18.2
18	44.3	42.6	356	26.6	13.3	34.7	3.04	18.2
19	46.24	38	251	27.7	8.6	46.3	3.22	19.3
20	36	38	251	21.6	8.6	46.3	3.22	19.3
21	44.3	38	251	26.6	8.6	46.3	3.22	19.3
22	46.24	45	251	27.7	7.2	69.4	3.99	24.0
23**	36	45	251	21.6	7.2	69.4	3.99	24.0
24	44.3	45	251	26.6	7.2	69.4	3.99	24.0
25	46.24	42.6	251	27.7	7.6	69.8	4.31	25.9
26	36	42.6	251	21.6	7.6	69.8	4.31	25.9
27	44.3	42.6	251	26.6	7.6	69.8	4.31	25.9

* Alaska Bridge 505, **Alaska Bridge 537, ***Alaska Bridge 547

CHAPTER 5 EXPERIMENTAL PHASE I

This chapter presents a summary of the experimental results of Phase I of the experimental program. The aim of these tests are to evaluate the existing connection and determine any deficiencies. These tests are used to inform the variables studied in the second phase of the experimental testing.

5.1 Test 1a

Test 1a., conducted at the CFL at NC State on June 21, 2017, was a monotonic pushover test of the steel shear connector plate portion of the commonly used keyway joint for precast prestressed bulb-tee girders. The loading protocol was based on the anticipated shear yielding of the steel connector plate from the tensile tests above. Since the anticipated displacements would be relatively small compared to the tolerances of the 40 inch stroke actuators, the actuator was controlled in force control. Loads were applied at the anticipated quarter increments of the yield capacity of the plate, which was calculated to be 16.3 kip increments. The applied load vs displacement at the center of the panel can be seen in Figure 5.1. The rigid-body rotation as a function of the displacement at the center of the specimen can be seen in Figure 5.2.

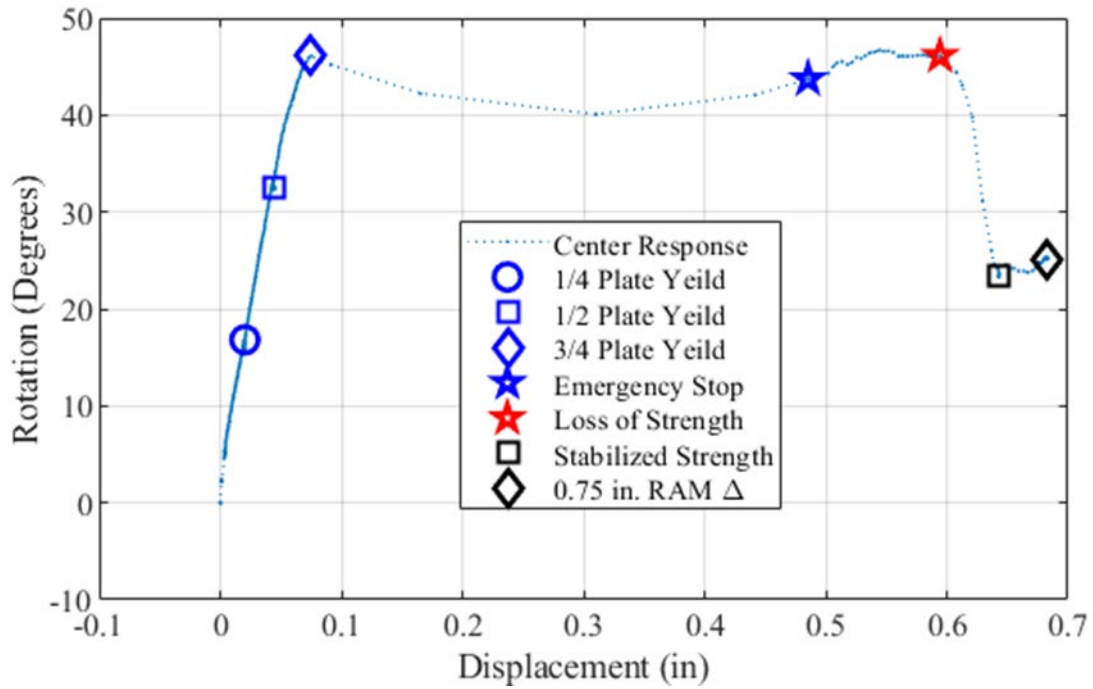


Figure 5.1: Test 1a Force-Displacement Response

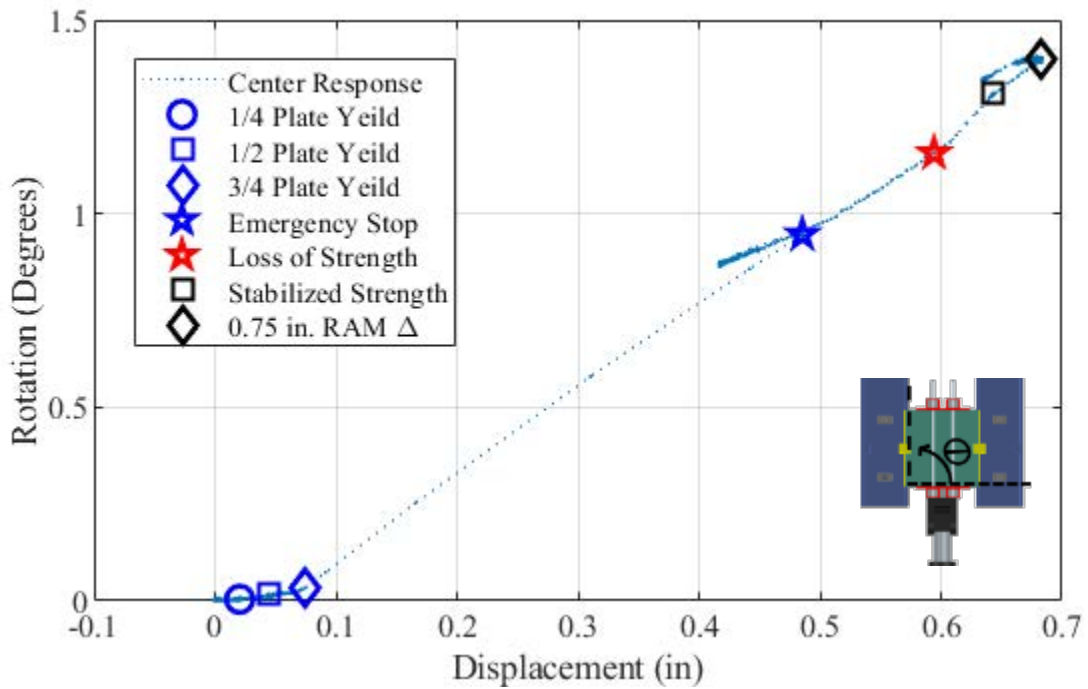


Figure 5.2: Test 1a Rigid Body Rotation

5.1.1 Test 1a Summary

The first loading cycle resulted in a force of 16.8 kips and a displacement of 0.020 inches measured at the center of the specimen. This equated to a rigid body rotation of 0.004° . No damage or slip through the keyway joint was visible. Figure 5.3 shows the left and right shear connector pocket. The load of the specimen was then increased to 32.6 kip, which caused the center of the specimen to displace 0.044 inches in total. No damage was visible at this point either. Figure 5.4 shows the left and right shear connector pocket. The rigid body rotation of the specimen increased to 0.016° .

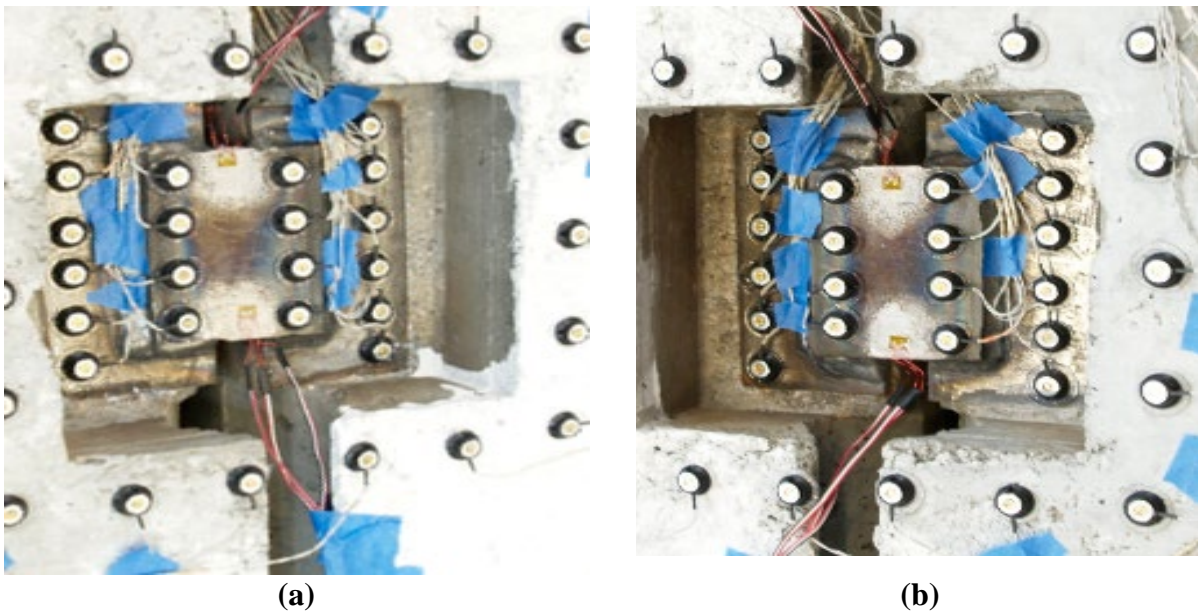


Figure 5.3: Test 1a Connector Plate Pocket at $\frac{1}{4}$ Plate Yield (a) Left Side (b) Right Side

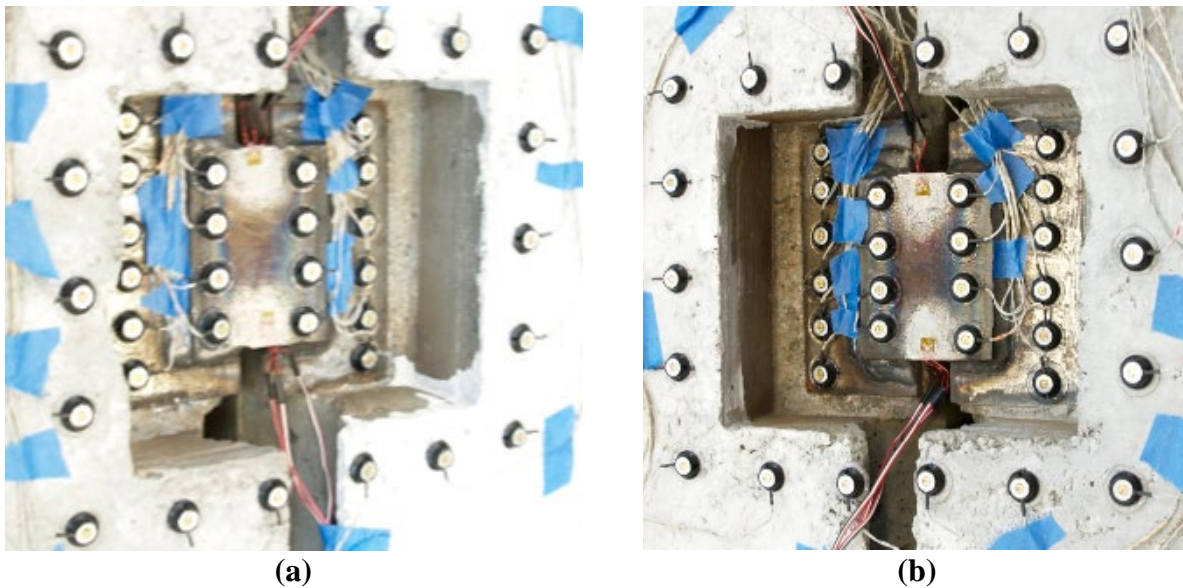


Figure 5.4: Test 1a Connector Plate Pocket at $\frac{1}{2}$ Plate Yield (a) Left Side (b) Right Side

On the way to 49 kips, $\frac{3}{4}$ plate yield, the connection deformed dramatically, only reaching a load of 46.1 kips. Just prior to this large deformation, the displacement was 0.075 inches with a rigid body rotation of 0.034° at the center of the specimen. The condition of the connections can be seen in Figure 5.5. Because the actuator was on load control, the actuator continued to push for five seconds until the emergency stop was hit. This led to a load of 43.7 kips and a displacement of 0.485 inches at the center of the specimen. It was clear that most of the deformation occurred in the right pocket and that the specimen rotated. The rotation at the center of the specimen was 0.946° . As the displacement occurred, the concrete surface surrounding the embedded plates began to spall off and the embedded plates began to separate from the concrete. This likely occurred due to the yielding of the embedded rebar that is welded to the plates. In the left pocket, which can be seen in Figure 5.6 (a) only slight spalling and separation of the plate embedded in the side specimen occurred before the plate began to bear against the side of the pocket and cause a crack to appear. In the right pocket, which can be seen in Figure 5.6 (b), clear spalling occurs on concrete surfaces surrounding both embedded plates. The plate embedded into the specimen un-bonded and separated from the concrete surface. Clear rotation was visible as the plate began to bear against the side of the pocket. The plate embedded in the side block had significant spalling that occurred on the surface with the plate but also some

spalling visible in the pocket face. Separation of the embedded plate was visible from underneath, but little rotation was visible.

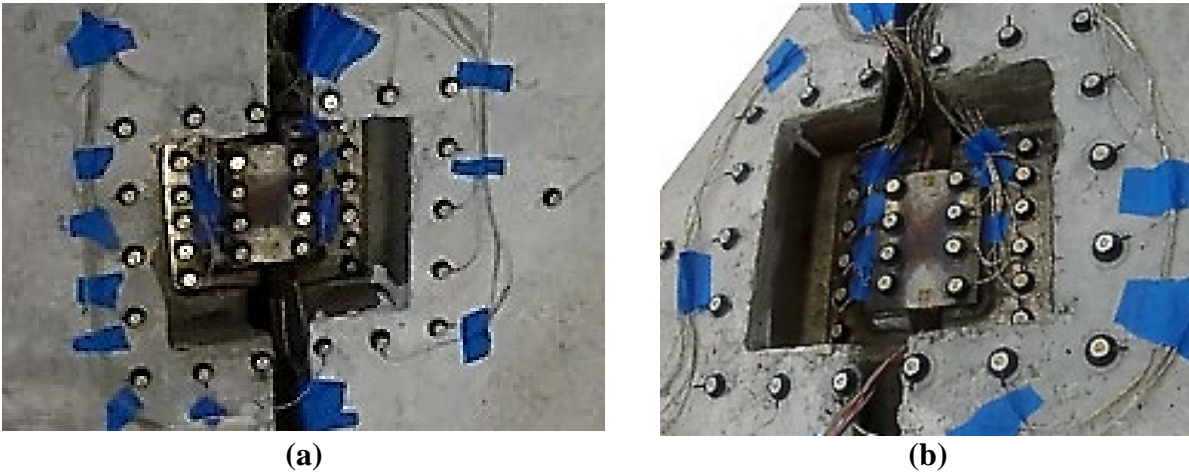


Figure 5.5: Test 1a Connector Plate Pocket on the way to $\frac{3}{4}$ Plate Yield (a) Left Side (b) Right Side

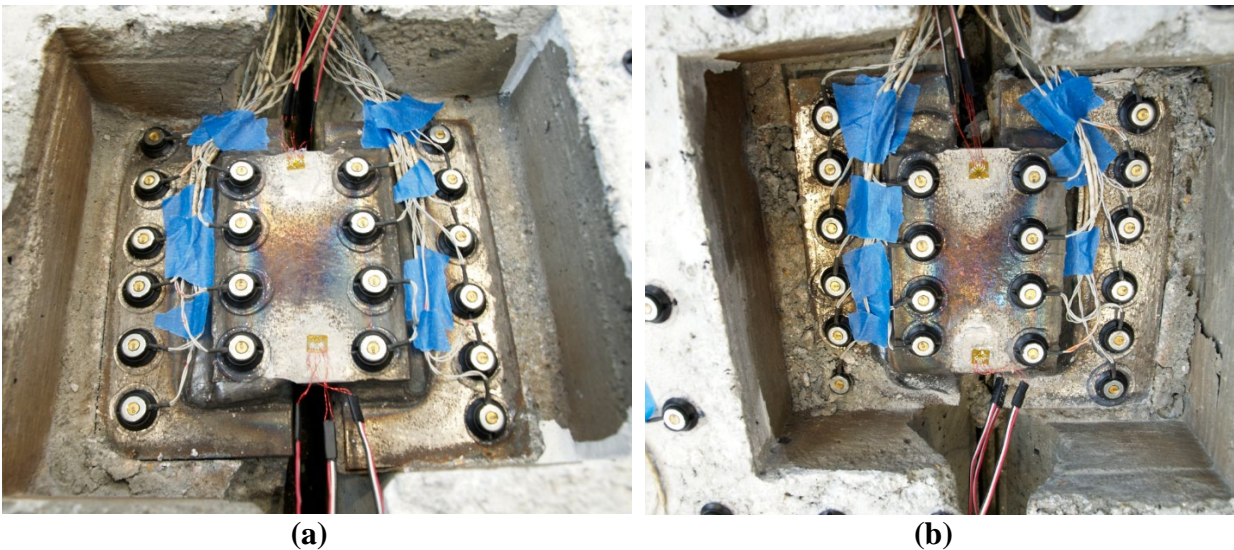


Figure 5.6: Test 1a Connector Plate Pocket at Emergency Stop (a) Left Side (b) Right Side

After damage was noted and pictures were taken, the actuator was switched to displacement control and the specimen was pushed another 0.25 inches. At a displacement of 0.594 inches and a rigid body rotation of 1.156° at the middle of the specimen, a significant drop of strength occurred. Just prior to the large drop in strength, the load applied by the actuator was 46.2 kips. After the drop, the load was 23.4 kips with a center specimen displacement of 0.643

inches corresponding to a rigid body rotation of 1.310° . Figure 5.7 shows the condition of the pockets just prior to the drop in strength. The left pocket continued to show little deformation, while the right pocket had more spalling as the embedded plate in the specimen continued to bear onto the pocket. This appeared to cause cracking along the longitudinal keyway. As the displacement continued, the strength decreased as the crack along the longitudinal keyway widened and a second crack appeared on a face in the pocket, which can be seen in Figure 5.8 (b). After the crack formed, the strength leveled out and displacement was applied until the middle of the specimen was at 0.683 inches with a load of 25.4 kips, which corresponds to a rigid body rotation of 1.398° .

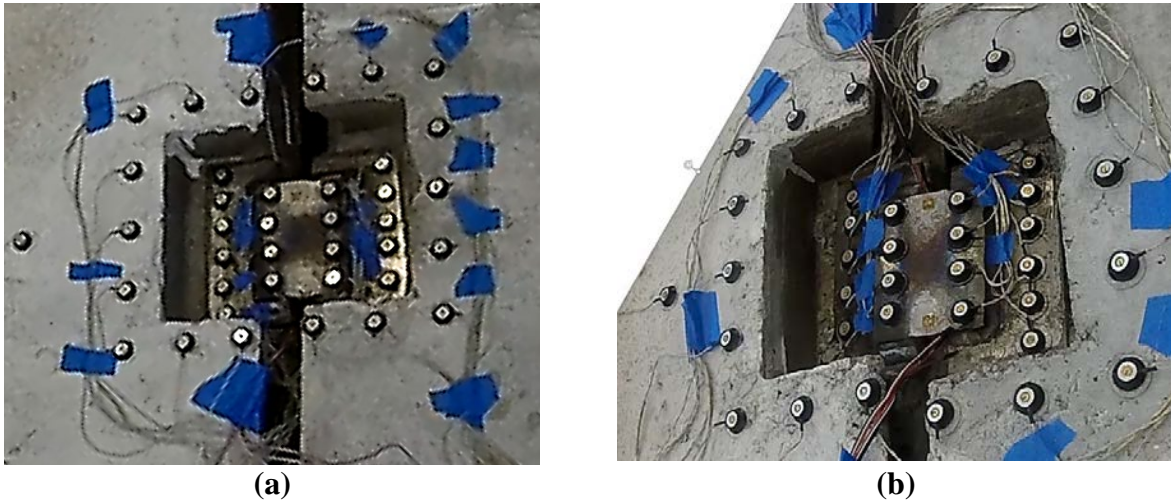


Figure 5.7: Test 1a Connector Plate Pocket Prior Strength Loss (a) Left Side (b) Right Side

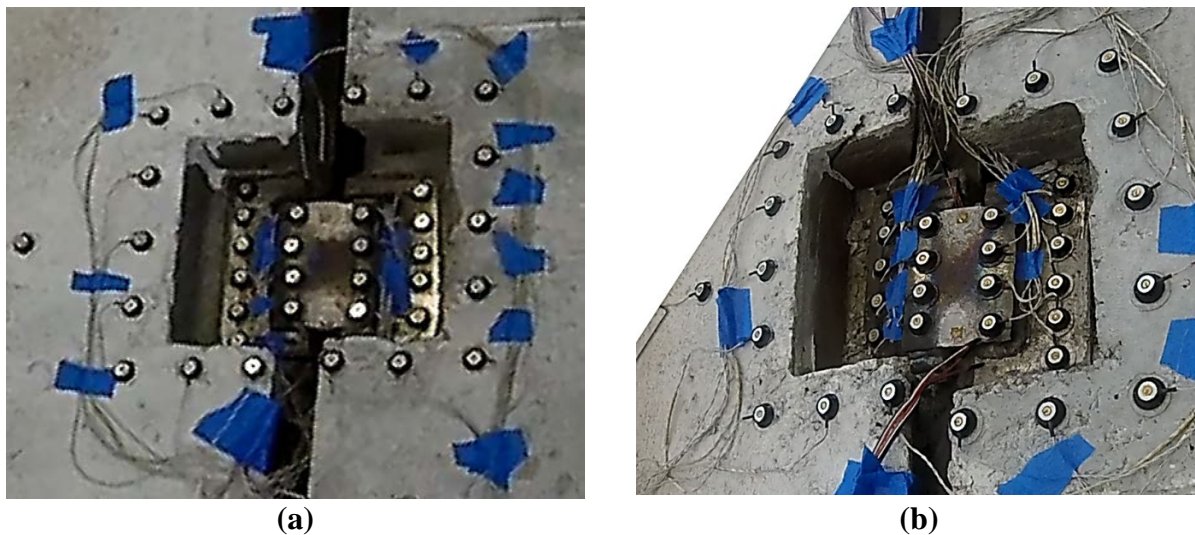


Figure 5.8: Test 1a Connector Plate Pocket After Strength Loss (a) Left Side (b) Right Side

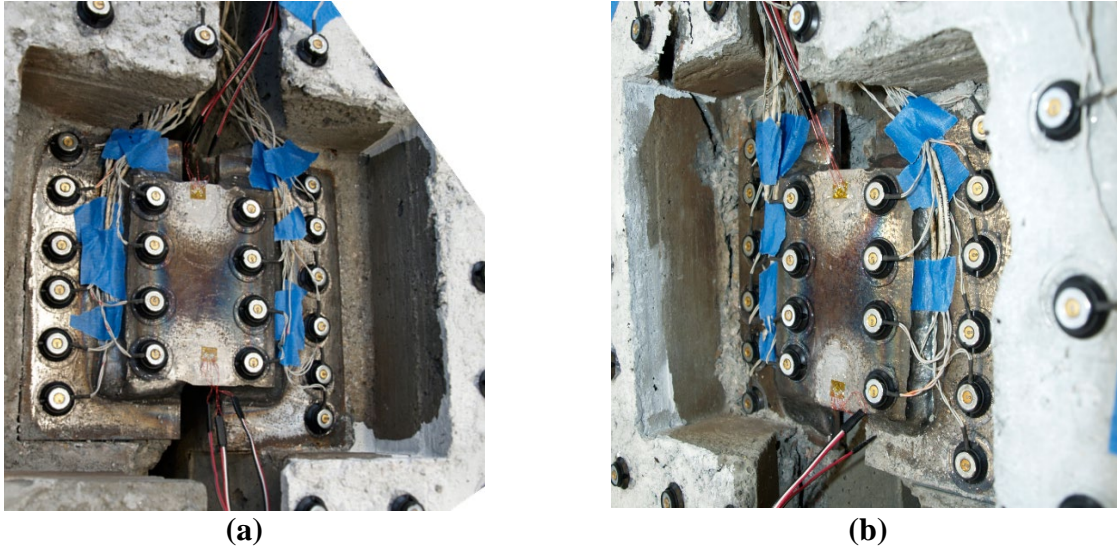


Figure 5.9: Test 1a Connector Plate Pocket at End of Test (a) Left Side (b) Right Side

At the end of the test, no new significant damage was observed, rather, only existing cracks widened and more rotation occurred across the specimen. As can be seen in Figure 5.9 (a), minor damage occurred to the left pocket. In contrast with the right pocket, it can be seen in Figure 5.9 (b) that significant cracking occurred on the specimen. One large crack occurred through the keyway where the embedded steel plate was bearing and a second crack occurred along the concrete surface across the pocket base and side onto the top of the slab. Upon further inspection, it was found that the two large cracks were connected leading to one large piece of concrete chipping away from the top of the unreinforced section of the slab and revealing the bent embedded rebar as seen in Figure 5.10. It is most likely that the specimen first failed due to embedded rebar crushing the concrete that it was bearing against. This led to unsupported rebar, which in turn led to large demands and deformation of the plate until it was able bear against the pocket. Eventually, from plate bearing, the concrete cracked and created one large area of damage.

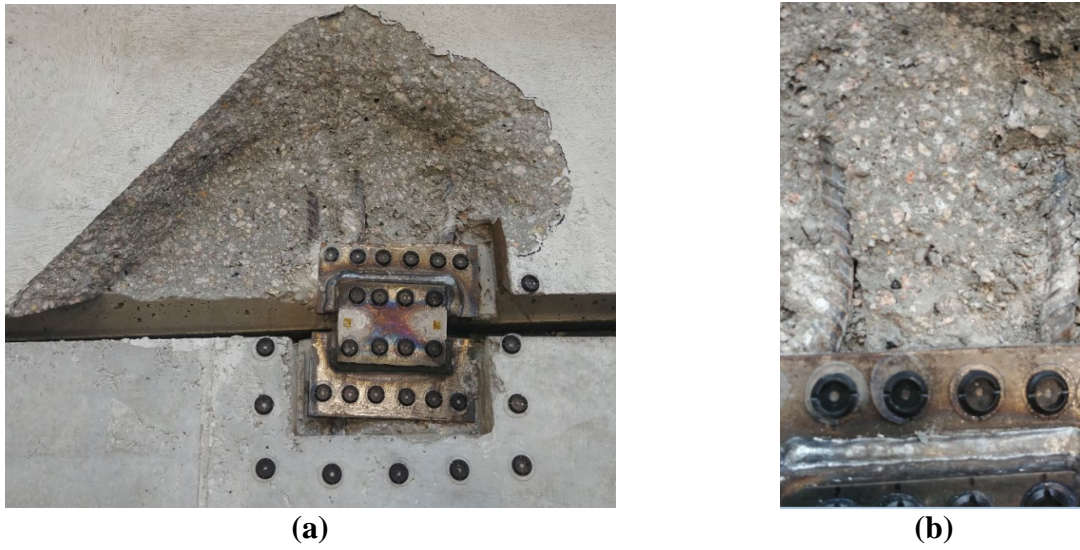


Figure 5.10: Test 1a Damage to the Shear Connector Pocket (a) Concrete Pocket (b) Embedded Rebar

A simple check shown below in Figure 5.11 indicates that the resistance of the specimen was more than that attributed solely to the unsupported rebar. Using the bar diameter, d_{bar} , equal to 0.5 inches, the plastic section modulus of the bar, Z_{circle} , can be calculated using Equation 5.1. Where Z_{circle} is the section modulus of a circle in which the yield stress of the section has been reached through the entire section on both sides of the neutral axis. The plastic moment, M_p , which is the moment needed to generate yield stress throughout the entire section can be calculated with the yield stress of the steel, f_y , equal to 60 ksi and Z_{circle} as seen in Equation Equation 5.2. M_p , can then be compared with the moment of one bar just before the specimen experienced large deformations. Assuming that the rebar is in double bending, and the clear length of the rebar is about two inches, the moment can be calculated using the force experienced by one bar. This was 11.5 kips just prior to large deformations, multiplied by the half the clear length of the bar, which can be seen in Figure 5.11 (about one inch). It can be seen that M_p , equal to 1.25 k-in, and the moment in the bar, equal to 11.5 k-in, are off by a magnitude of about 10. Thus, concrete is influencing the response by changing the boundary conditions of the rebar. In pure shear, the capacity of one #4 bar is approximately 7 kips, implying that under full restraint, bar fracture in shear may define the lower bound strength.

$$Z_{circle} = \frac{d_{bar}^3}{6} = \frac{(0.5 \text{ in})^3}{6} = 0.0208 \text{ in}^3 \quad \text{Equation 5.1}$$

$$M_P = f_y Z_{circle} = 60 \text{ ksi} (0.0208 \text{ in}^3) \\ = 1.25 \text{ kin} \quad \text{Equation 5.2}$$



Figure 5.11: Plastic Moment of Embedded Rebar

No rupture was observed in the 3/16th field fillet welds around the connector plate. In order to check the welds of the embedded plates, the plates were cut out with a torch. Inspection of the welds showed no damage occurred. This can be seen in Figure 5.12.



Figure 5.12: Test 1a Welds of Embedded Plates

5.1.2 Test 1a Conclusion

Test 1a. provided a unique insight to the behavior of the joint that only includes the steel connector plate. An unexpected failure mode occurred through bending of the rebar and large

rotations of the specimen. Most of the damage occurred in one of the shear pockets of the joint. It is most likely that the specimen first failed due to embedded rebar crushing the concrete that it was bearing against. This led to unsupported rebar, which in turn led to large demands and deformation of the plate until it was able bear against the pocket. Once the concrete stress was sufficiently high from the plate bearing, the concrete cracked causing a large area of concrete to spall off as visible in Figure 5.13. Since the presence of grout would prevent additional rotation, it was decided that a cyclic test of just the steel connector plate would not likely yield useful results.

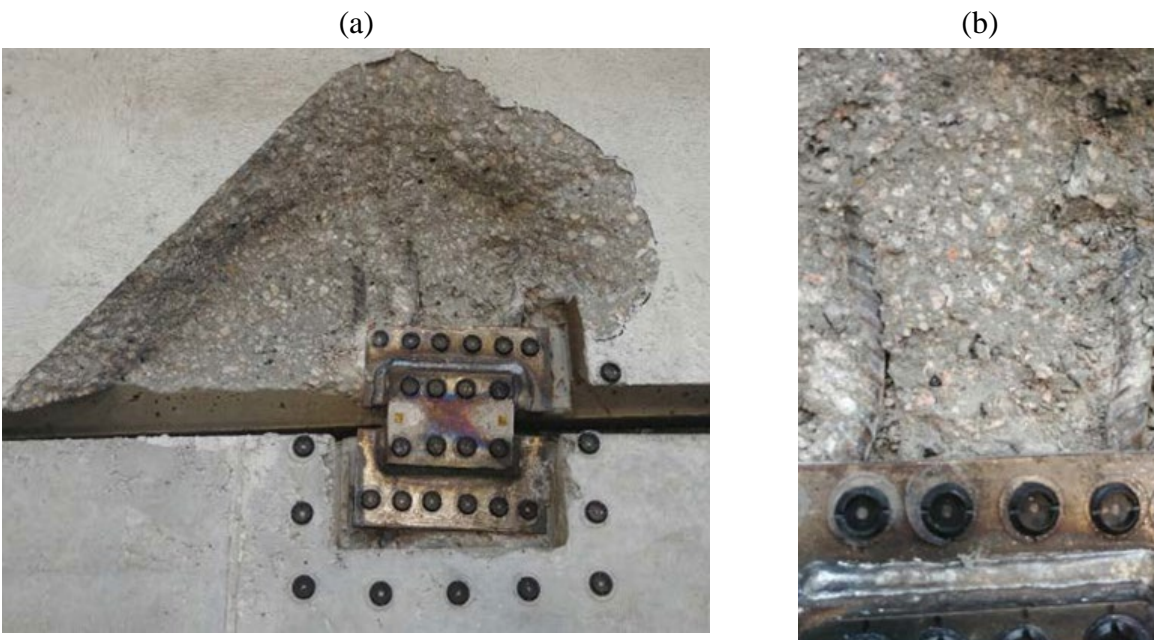


Figure 5.13: Test 1a. Damage to the Shear Connector Pocket (a) Concrete Pocket (b) Embedded Rebar

5.2 Test 1b

Test 1b. was conducted on June 30, 2017 and was a monotonic pushover test of the grouted shear key portion of the commonly used keyway joint on the same specimen. The loading protocol was based on the anticipated tensile stress of the grout based on the compressive tests above. Since the anticipated displacements compared to the 40-inch stroke actuator tolerance is relatively small, the actuator was controlled in force control with a 0.25inch displacement limit. Loads were applied at quarter increments of the tensile strength of the grout, which was calculated to be 45.3 kip increments. The complete load-displacement response of the specimen measured at the center can be seen in Figure 5.14. The rigid-body rotation in terms of displacement of the center of the specimen can be seen in Figure 5.15.

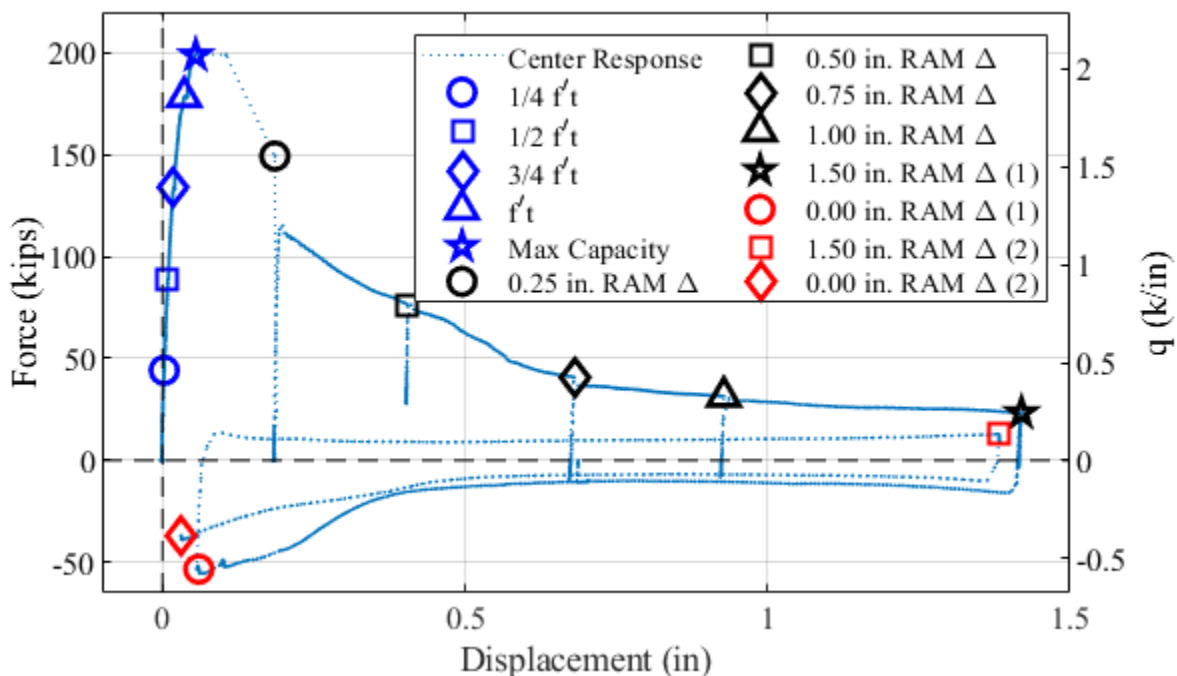


Figure 5.14: Test 1b Force-Displacement Response

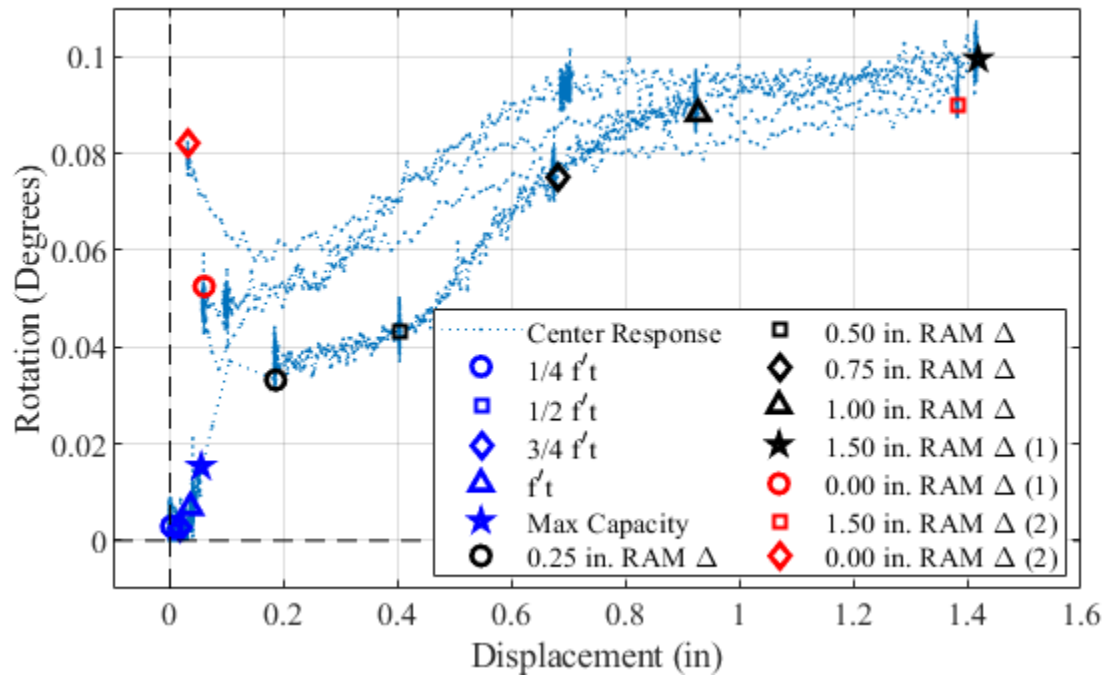


Figure 5.15: Test 1b Rigid Body Rotation of Specimen vs Displacement

5.2.1 Test 1b Summary

The first load increment provided a force of 44.4 kips and a displacement of 0.003 inches at the center of the specimen. No damage or relative displacement was visible as seen in Figure 5.16. The load on the specimen was then increased to 89.2 kips, which caused the center of the specimen to displace 0.009 inches in total. The rigid body rotation of the center of the specimen was 0.002° and as shown in Figure 5.17, no damage was visible.

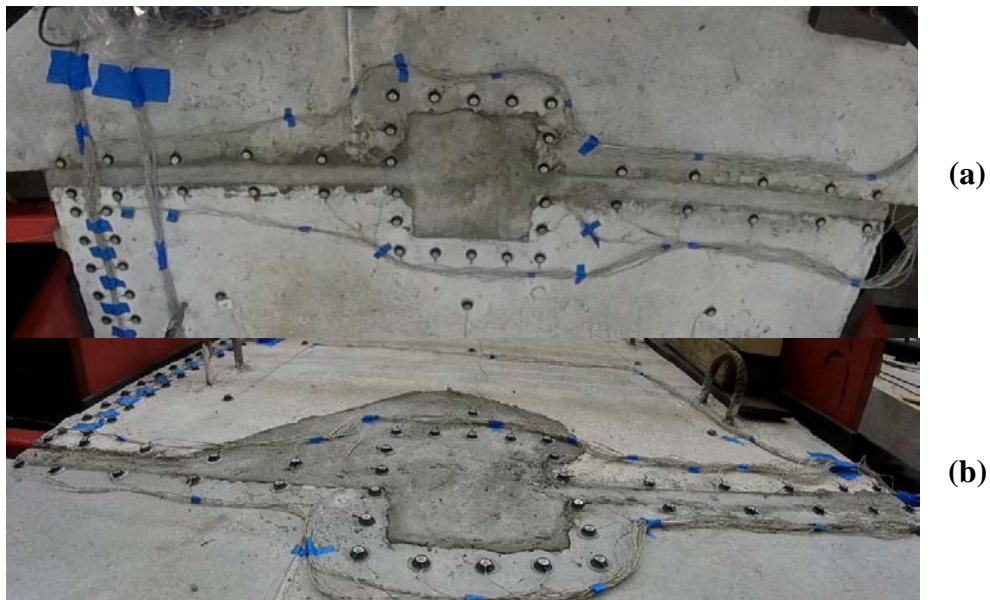


Figure 5.16: Test 1b Grouted Shear Key at $\frac{1}{4}$ f't (a) r Side (b) Right Side

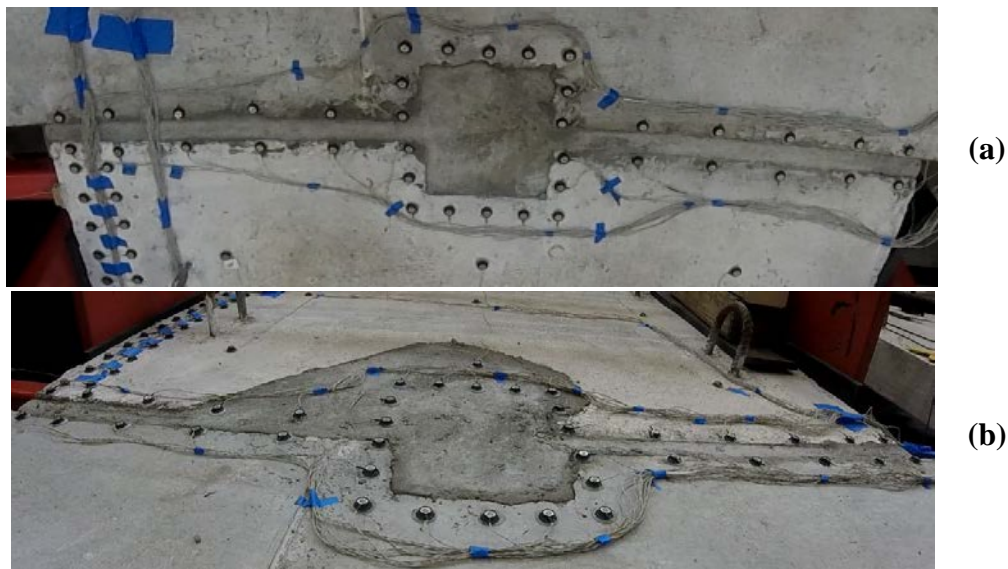


Figure 5.17: Test 1b Grouted Shear Key at $\frac{1}{2}$ f't (a) Left Side (b) Right Side

The first signs of cracks appeared at the next increment of loading, with a load of 133.6 kips and a displacement of 0.0182 inches at the center of the specimen. The rigid body rotation of the specimen was 0.003° . The left side in Figure 5.18 (a) had cracks form along the edge of the joint as well as through the joint near both ends of the shear pocket. The right side only had minor cracks along the joint as seen in Figure 5.18 (b). At 178.4 kips, which was the expected strength of the grout, the strength continued to increase with a displacement of 0.0358 inches.

More cracks start to appear on both joints of the specimen. The specimen experienced a rigid body rotation of displacement of 0.007° . The left pocket developed two large diagonal cracks in the shear connector pocket and increasing cracks lengths along the joint, which is presented in Figure 5.19 (a). The right side had cracks forming along and across the joint and one crack that formed through the shear pocket and into the specimen as seen in Figure 5.19 (b).

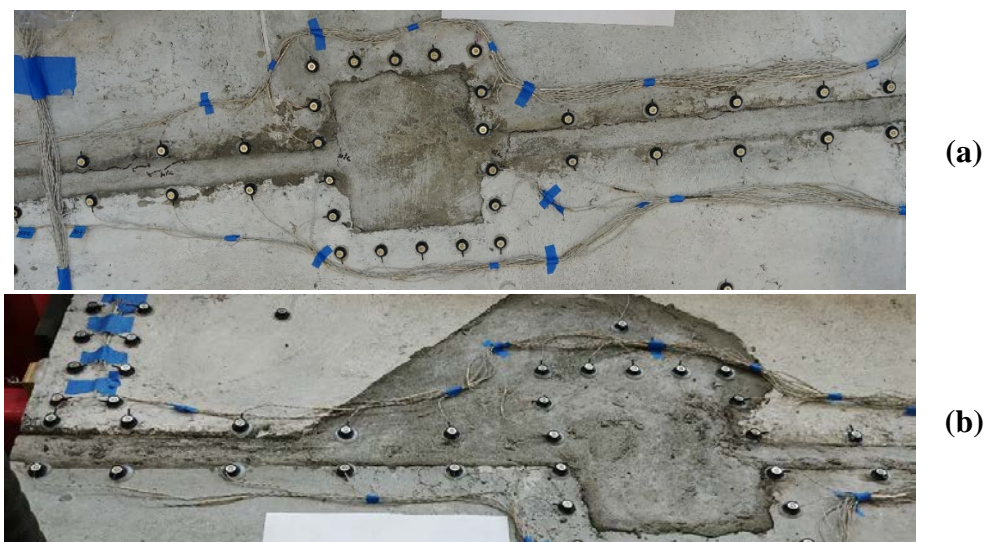


Figure 5.18: Test 1b Grouted Shear Key at $3/4 f't$ (a) Left Side (b) Right Side

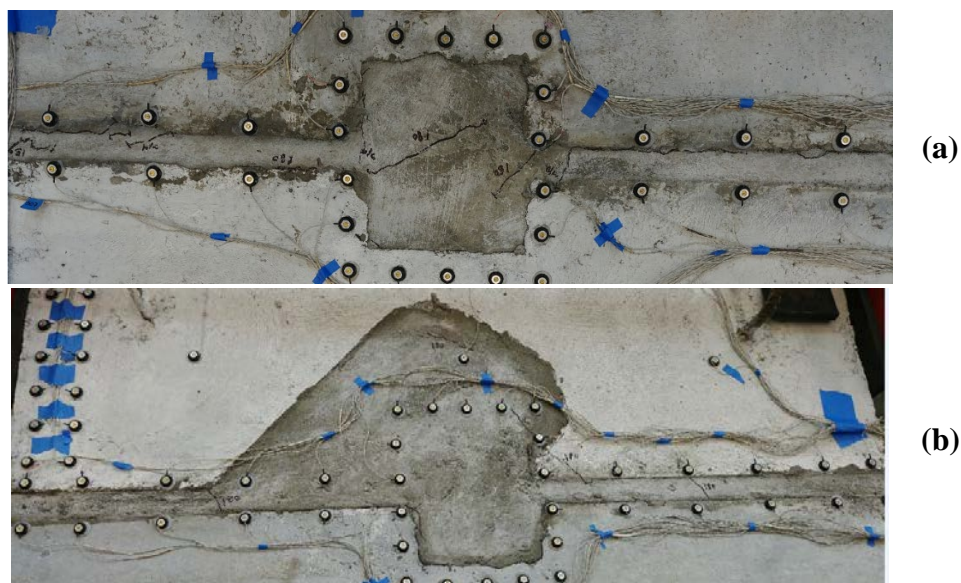


Figure 5.19: Test 1b Grouted Shear Key at $f't$ (a) Left Side (b) Right Side

Because loss of strength was not achieved in the last increment of loading, another 44.4 kip increment was applied, however, the specimen did not reach that level before the load rapidly degraded. The maximum load sustained was 199.2 kips (the maximum predicted load based on the tensile strength of the concrete was 178kips). At this point, the displacement of the center of the specimen was 0.0559 inches with a rigid body rotation of 0.015° . On the left side a new large diagonal crack formed across the shear connector pocket, while prior diagonal cracks increased in size. Cracks also formed in the specimen close to where the hydraulic actuator was applying pressure through the load spreader. It should be noted that this behavior was seen on both sides of the load spreader plate and cracks disconnected the string potentiometers monitoring the joint displacement on both sides of the specimen. The right side experienced similar damage as the left joint and damage of both joints can be seen in Figure 5.20. Large diagonal cracks formed in the shear connector pocket and continued into both the specimen and the side block. Once the force dropped, the actuator stopped at the preset 0.25 inch actuator displacement limit. The force rapidly declined, the cracks widened, and some spalling of grout at the surface of the joint was noted. With the actuator at 0.25 inches, the load was 149.3 kips with a displacement of 0.186 inches at the center of the specimen (this is different from the 0.25-inch limit, which was for the actuator rather than specimen displacement). The rigid body rotation was 0.033° . The damage can be seen in Figure 5.21.

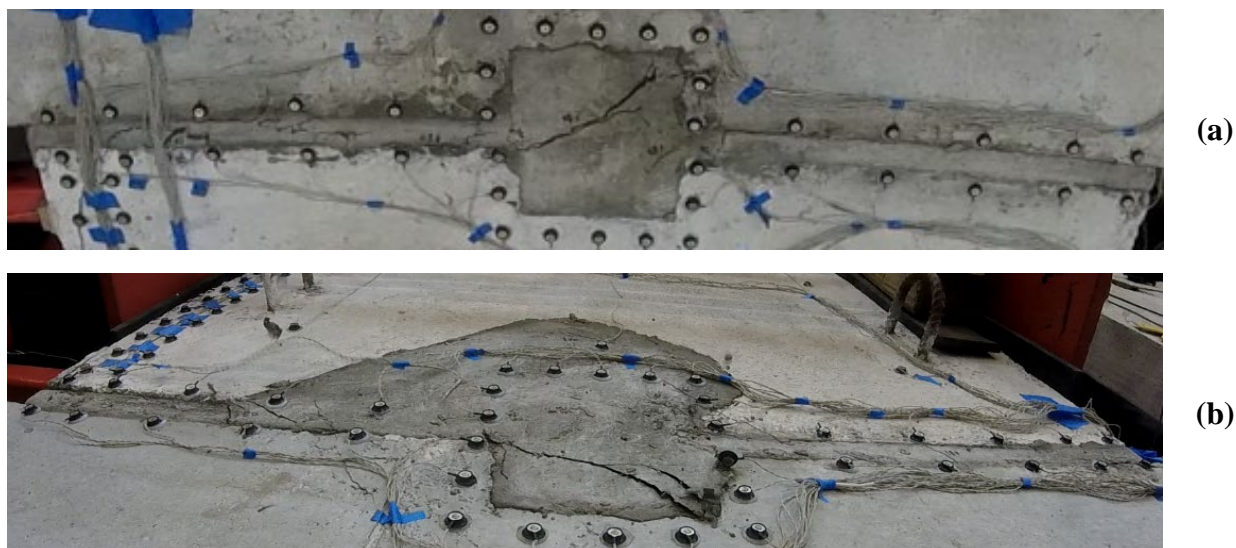


Figure 5.20: Test 1b Grouted Shear at Key Max Capacity (a) Left Side (b) Right Side

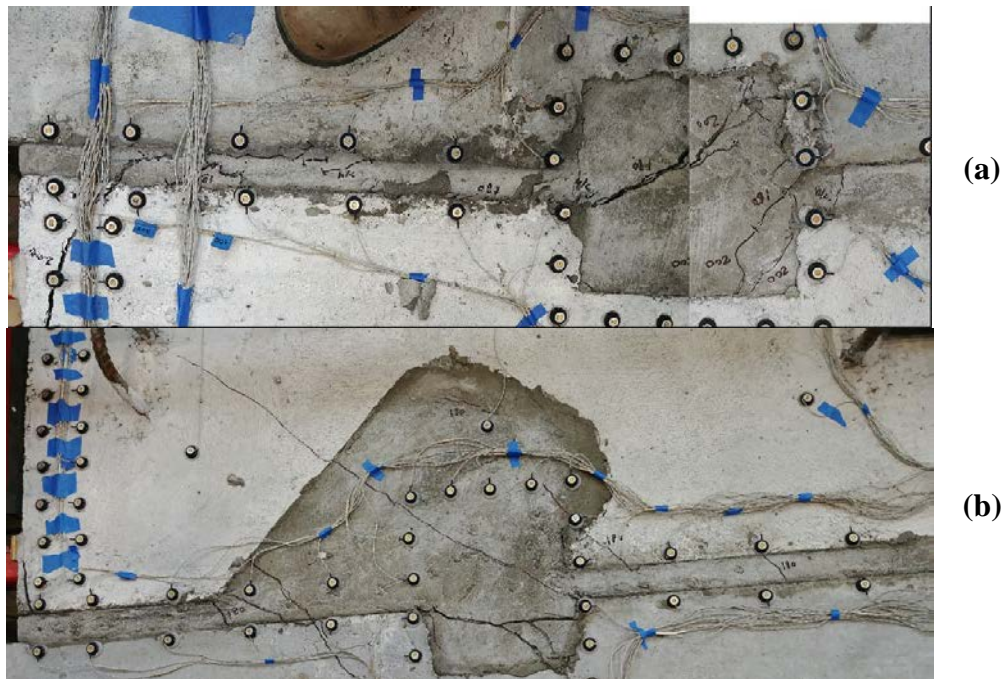


Figure 5.21: Test 1b Grouted Shear Key at 0.25 in. RAM Δ (a) Left Side (b) Right Side

At this point the actuator was switched to displacement control and an increment of an additional 0.25 inches was imposed. The strength continued to drop as the actuator reached 0.50 inches. The corresponding load was 75.6 kips and a displacement of 0.406 inches was measured at the center of the specimen with a rigid body rotation of 0.043° . Figure 5.22 (a) depicts the damage in the left joint, which consisted of widening cracks. Figure 5.22 (b) depicts the damage of the right joint, which mainly consisted of widening cracks with some new diagonal cracks that formed in the right shear connector pocket. An additional 0.25 inch increment was applied, with the corresponding load of 40.8 kips and a displacement of the center of the specimen of 0.680 inches. The left joint did not form any new cracks, rather, the cracks widened and the high strength grout started to push up out of the joint. Similar behavior was seen in the right joint, damage of both joints can be seen in Figure 5.23.

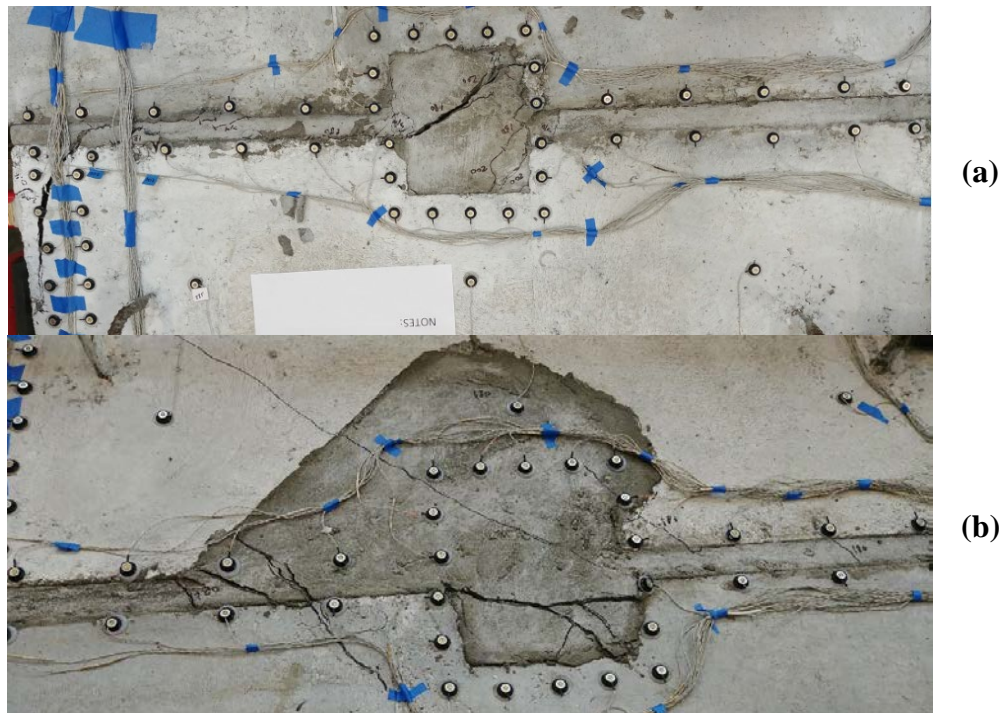


Figure 5.22: Test 1b Grouted Shear Key at 0.50 in. RAM Δ (a) Left Side (b) Right Side

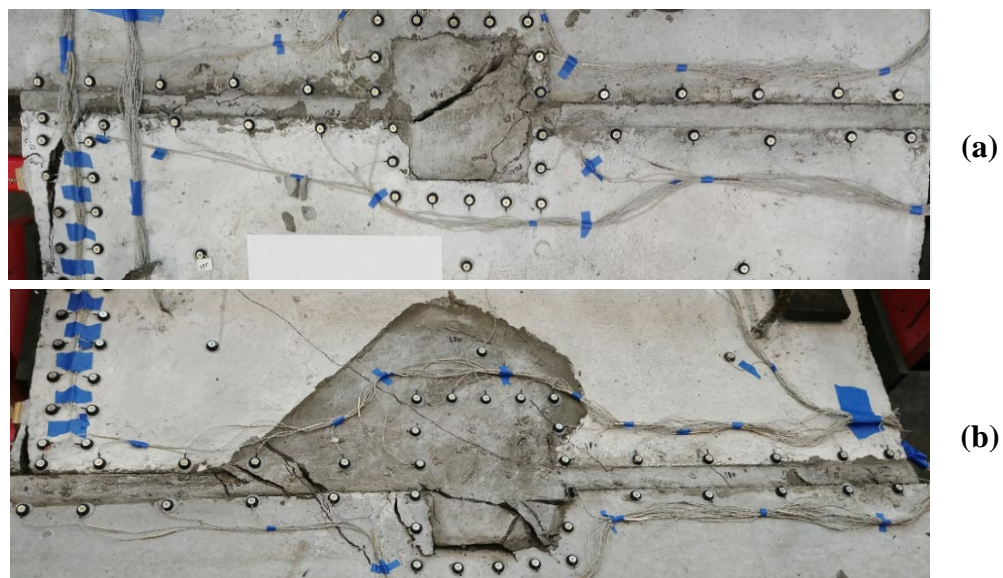


Figure 5.23: Test 1b Grouted Shear Key at 0.75 in. RAM Δ (a) Left Side (b) Right Side

This continued to be the trend as the force stabilized. An additional 0.25 increment led to a total actuator displacement of 1.00 inch and a load of 31.4 kips, with the displacement and rigid body rotation measured at the center of the specimen to be 0.928 inches and 0.088° respectively. Damage can be seen in Figure 5.24. An additional 0.50 increment was then applied (total of 1.5

inch actuator displacement), with a corresponding load of 23.4 kips which led to a displacement at the center of the specimen of 1.42 inches and a rigid body rotation of 0.100° . The damage can be seen in Figure 5.25. Some additional cracks on the left joint appeared. The cracks went into the side specimen midway between the load spreader and the shear connector pocket.

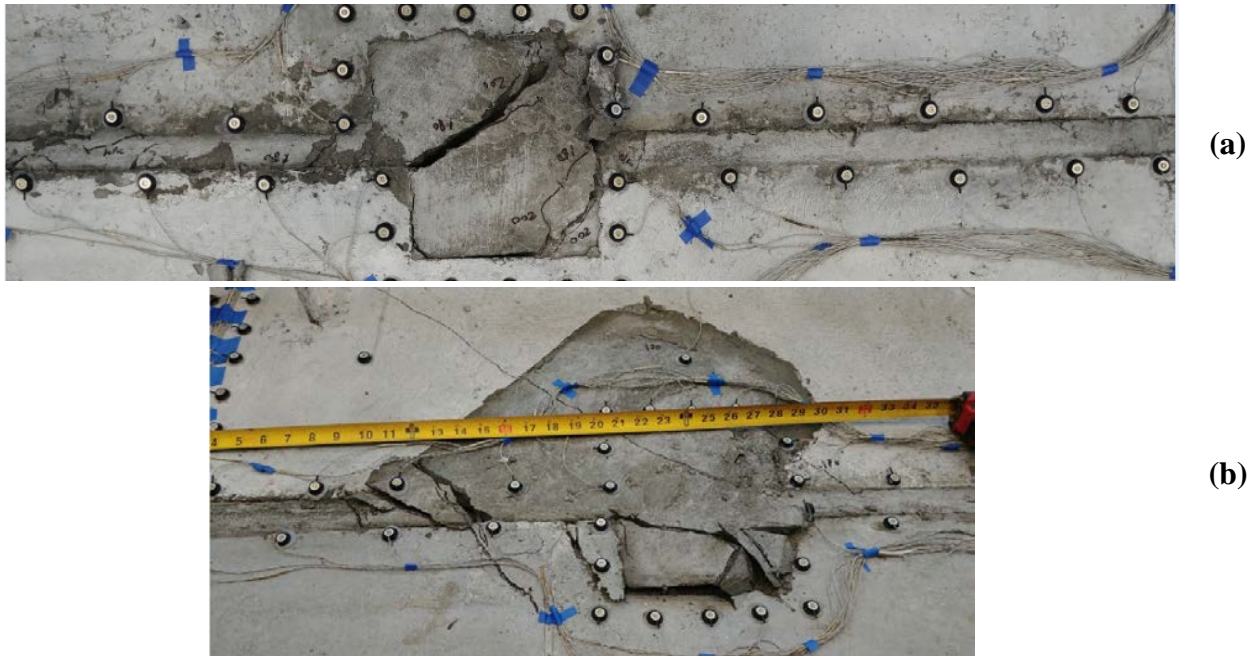


Figure 5.24: Test 1b Grouted Shear Key at 1.00 in. RAM Δ (a) Left Side (b) Right Side



Figure 5.25: Test 1b Grouted Shear Key at 1.50 in. RAM Δ (1) (a) Left Side (b) Right Side

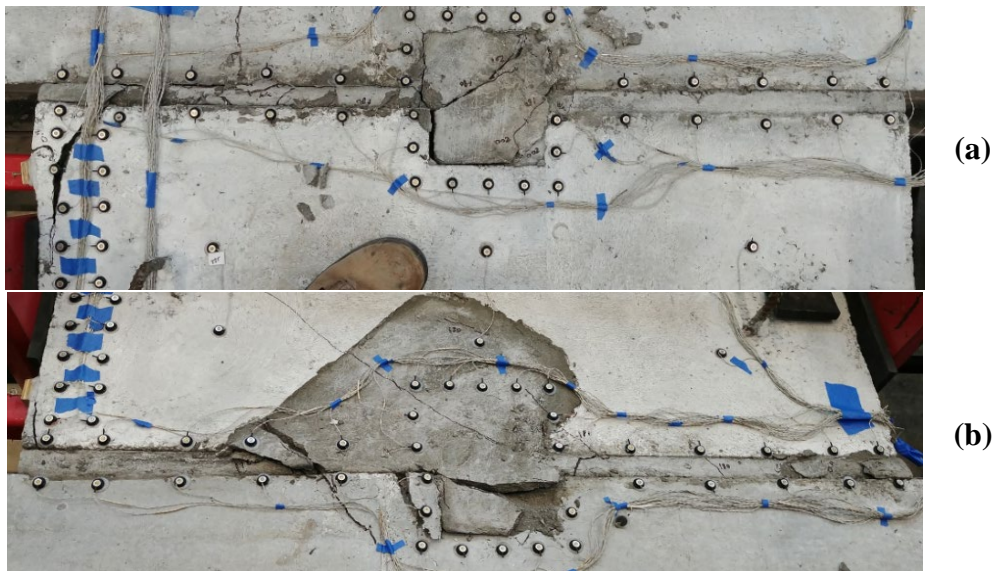


Figure 5.26: Test 1b Grouted Shear Key at 0.00 in. RAM Δ (1) (a) Left Side (b) Right Side



Figure 5.27: Test 1b Grouted Shear Key at 1.50 in. RAM Δ (2) (a) Left Side (b) Right Side

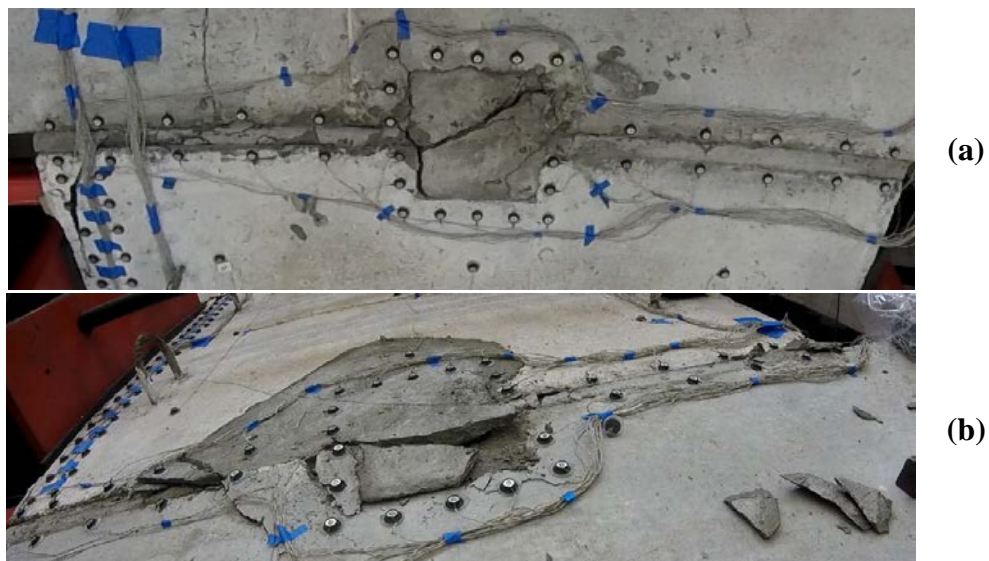


Figure 5.28: Test 1b Grouted Shear Key at 0.00 in. RAM Δ (2) (a) Left Side (b) Right Side

After pushing with the actuator to 1.50 inches, it seemed that the response of the joint was relatively stable and that the monotonic backbone was established. Thus, it was decided to perform a reversal back to zero displacement. To prevent crushing instrumentation, the actuator was taken to a displacement just before zero. Upon reversal, the load dropped from 23.4 kips to -

15.9 kips and stabilized to -11 kips for the majority of the reversal, picking up strength around 0.4 inches. The strength peaked at -53.4 kips at an absolute displacement of 0.060 inches at the center of the specimen with a rigid body rotation of 0.053° . The damage can be seen in Figure 5.26. On the left side it was observed that cracks closed but no new cracks formed. The same could be said about the right side except that some of the grout that was pushed out previously continued to be pushed out of the joint. The specimen was then pushed back to an actuator displacement of 1.50 inches. Upon reversal, the load steadily dropped to 14.4 kips at a displacement of 0.395 inches. The load was maintained for the remainder of the cycle where the specimen reached a displacement of 1.382 inches corresponding to a load of 12.9 kips. No new cracks formed, the only observable change was larger crack widths, which can be seen in Figure 5.27. The rigid body rotation of the specimen was measured as 0.090° . To finish testing the actuator was taken back to zero displacement. Upon reversal, the load dropped from 12.9 kips to -9.7 kips and maintained that strength for the majority of the reversal, picking up strength around 0.4 inches, similar to the first reversal. The strength peaked at -38.2 kips at an absolute displacement of 0.031 inches at the center of the specimen. Similar observations to the first reversal were observed, where no new cracks formed but cracks closed, which can be seen in Figure 5.28.

Some new damage was observed when removing the grout from the keyway in preparation to remove the specimen. The grout was removed using a hammer drill to degrade the grout such that it could be removed by hand. In doing so, three locations had large sections of unreinforced concrete detach with little persuasion from the hammer drill. This damage likely occurred from the test as the grout pushed the unreinforced keyway putting tension into the concrete. Some indication of these large cracked sections were visible but the cracks at the time were not considered significant. The large areas of damage can be seen in Figure 5.29(a). Two large areas of damaged concrete formed on the left side joint. The damage on the specimen was a continuation of the crack that made the string potentiometer obsolete near the spreader plate while the damage on the side block had small portions of the crack visible at max capacity. The large damaged area that formed on the right side joint occurred in the side block, starting from one of the cracks in the shear pocket and continuing about a foot past the specimen. Due to these sections un-bonding, some shear key grout was able to be removed and can be seen in Figure

5.29 (b). A notable observation of the grout was that some concrete was still bonded to the sides where the needle scalar could clean the joint prior to the pour but not present on the unscaled sections. On the prepared section, grinding between the interface of the shear key and grout was also noted. It was also observed that most of the spalling grout on top of the joint seen during the test did not penetrate into the grout section but rather was localized to the top of the grout.

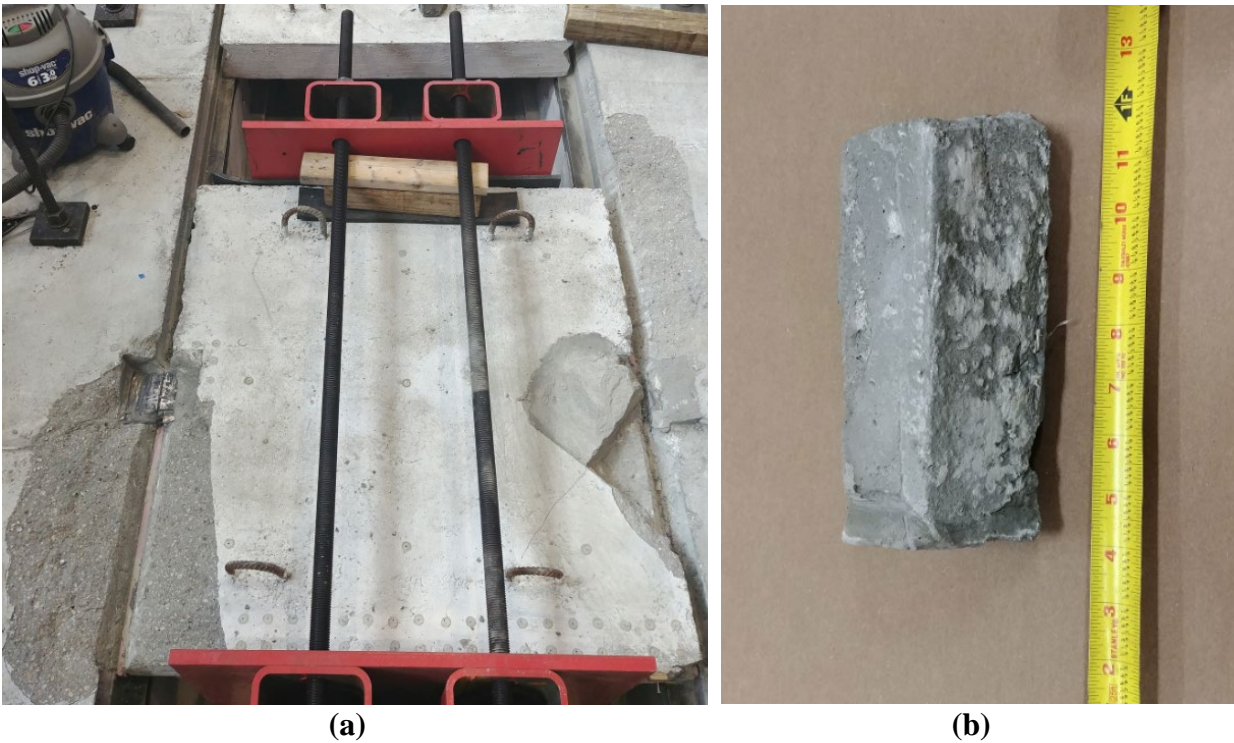


Figure 5.29: Post Test 1b. Damage (a) Test Specimen and Side Blocks (b) Shear Key Grout

5.2.2 Test 1b Conclusion

In order to be economical, the same specimen was used for test 1a. and test 1b. This was possible because much of the damage from test 1a. was focused in the shear connector pocket and not the shear key. The shear connector plates from Test 1a were torched off such that they would not contribute to the response. Grout was poured into the joint and damaged section of the specimen. Test 1b, although not an exact test of the grout's response because of the residual damage from Test 1a, behaved well with limited rotation of the specimen. It was observed that most of the force in the joint will be transferred by the grout due to its relatively large force and low displacement when compared to the steel in Test 1a. Overall, the 'grout only' behavior was

better than expected, with numerous distributed cracks occurring as viewed in Figure 5.30. Additionally the use of Equation 4.1 closely predicted the maximum capacity of the joint with a ratio of the maximum recorded load over the expected maximum load equal to 1.12.

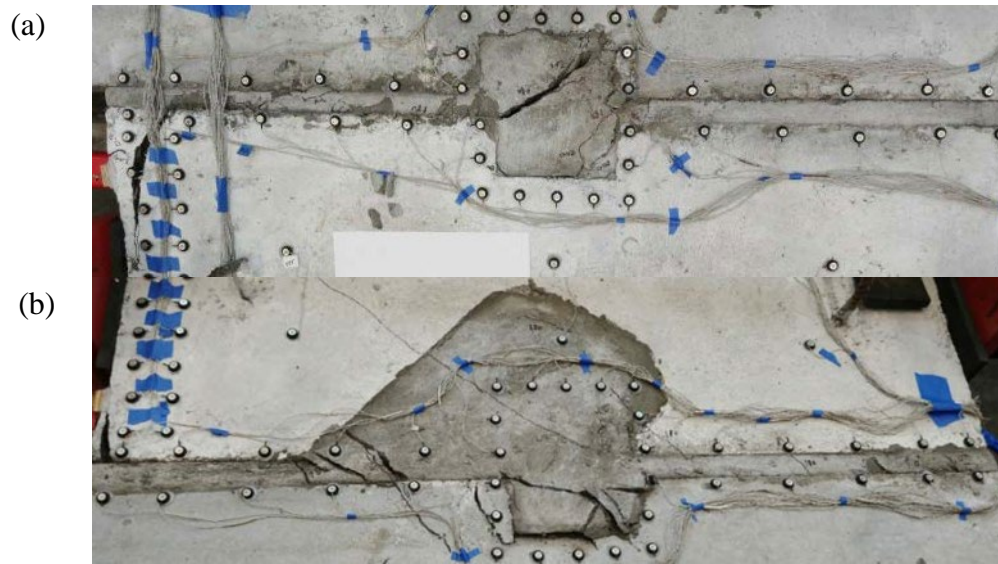


Figure 5.30: Test1b. Grouted Shear Key at 0.75 in. of displacement (a) Left Side (b) Right Side

5.3 Test 2

Test 2 was performed on August 9, 2017 at the CFL at NCSU. This section presents the overall response of the specimen and then discusses experimental procedures, results and observations in chronological order. Following the loading protocol, the complete unaltered load-displacement response of the specimen measured at the center can be seen in Figure 5.31. The rigid-body rotation in terms of displacement of the center of the specimen can be seen in Figure 5.32.

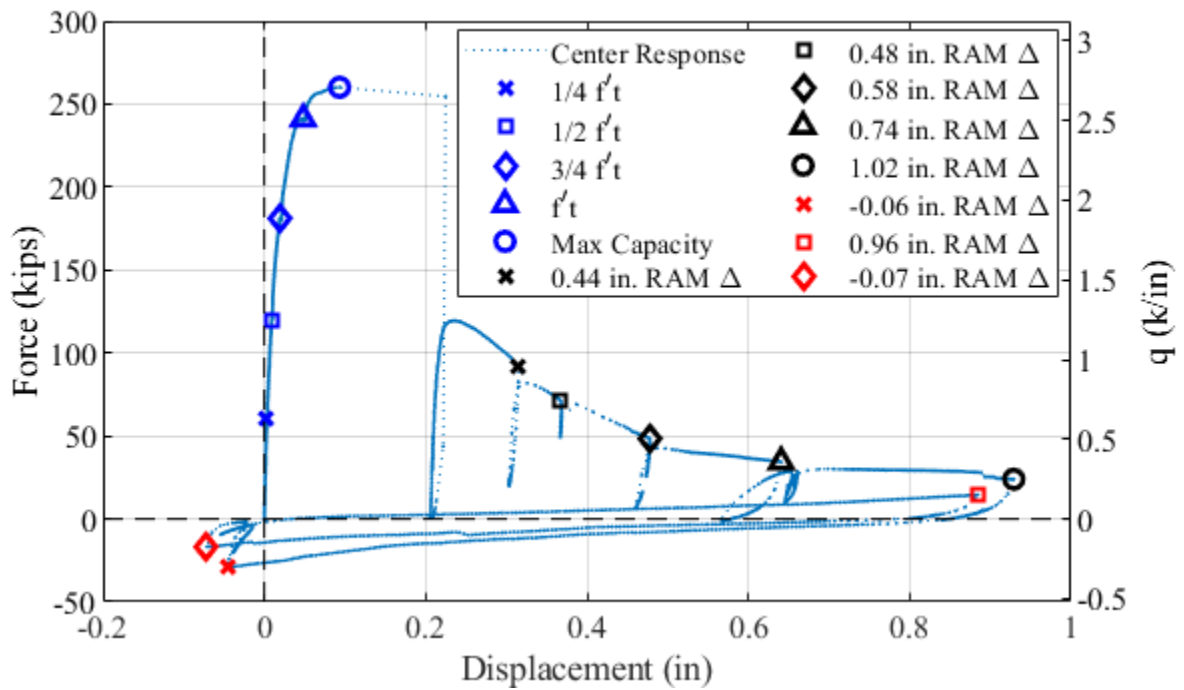


Figure 5.31: Test 2 Force-Displacement Response

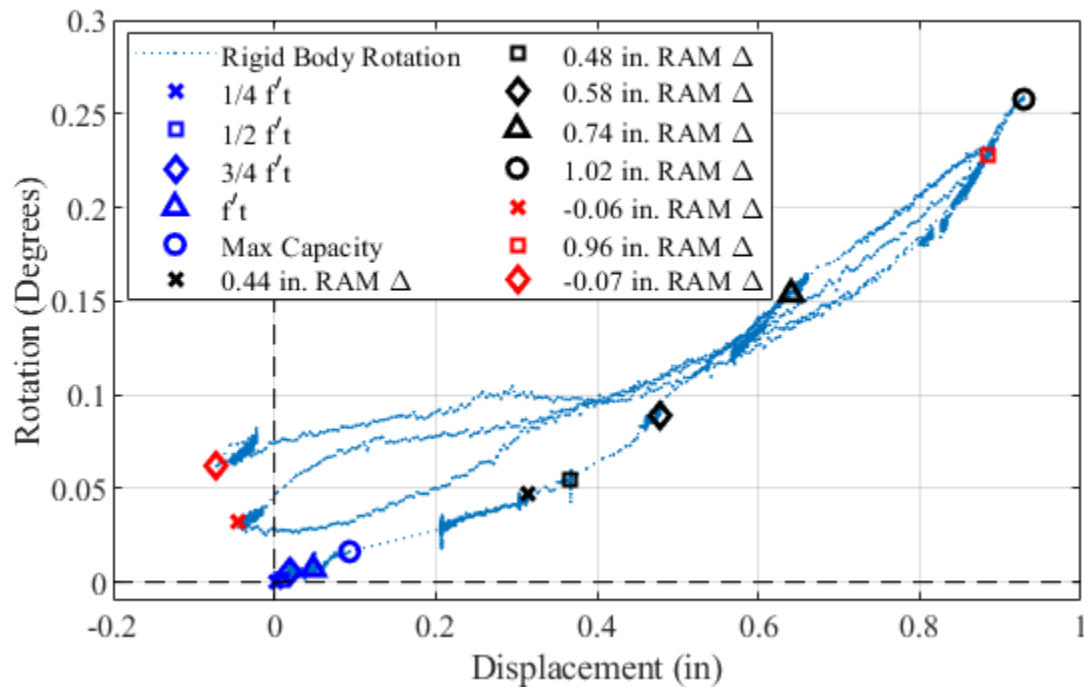


Figure 5.32: Test 2 Rigid Body Rotation of Specimen vs Displacement

5.3.1 Test 2 Summary

The first load increment provided a force of 60.2 kips and a displacement of 0.003 inches at the center of the specimen. No damage or relative displacement was visible. The specimen was then loaded to 119.9 kips, which caused the center of the specimen to displace 0.009 inches in total, no rigid rotation was noted. At this force, cracks were visible along the interface of the grout and the specimen and across the keyway as seen in Figure 5.33.

At the next increment of loading, the load was 180.8 kips and the displacement at the center of the specimen was 0.019 inches. Visible cracks started to appear outside the joints, with a crack forming in the side block on the left side and a crack forming in the specimen on the right side. Some new cracking in the grouted pockets is visible along with cracks along the joint. The described damage can be seen in Figure 5.34.

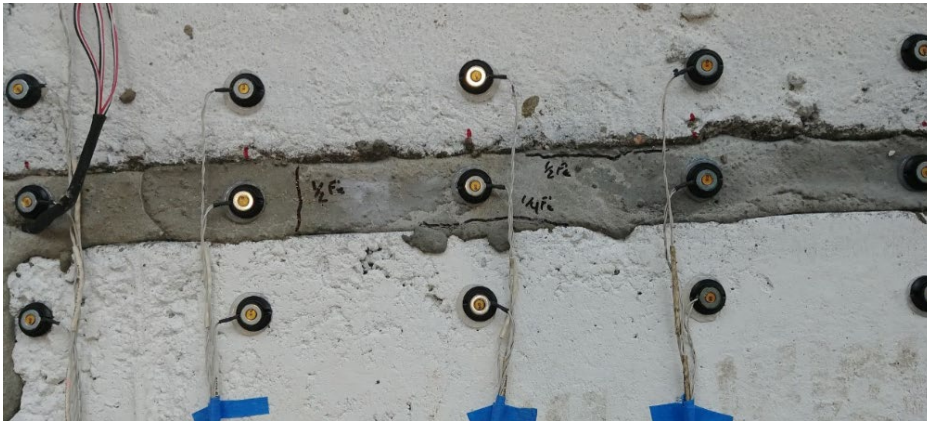


Figure 5.33: Test 2 Right Side of Grouted Shear Key at $\frac{1}{2} f't$

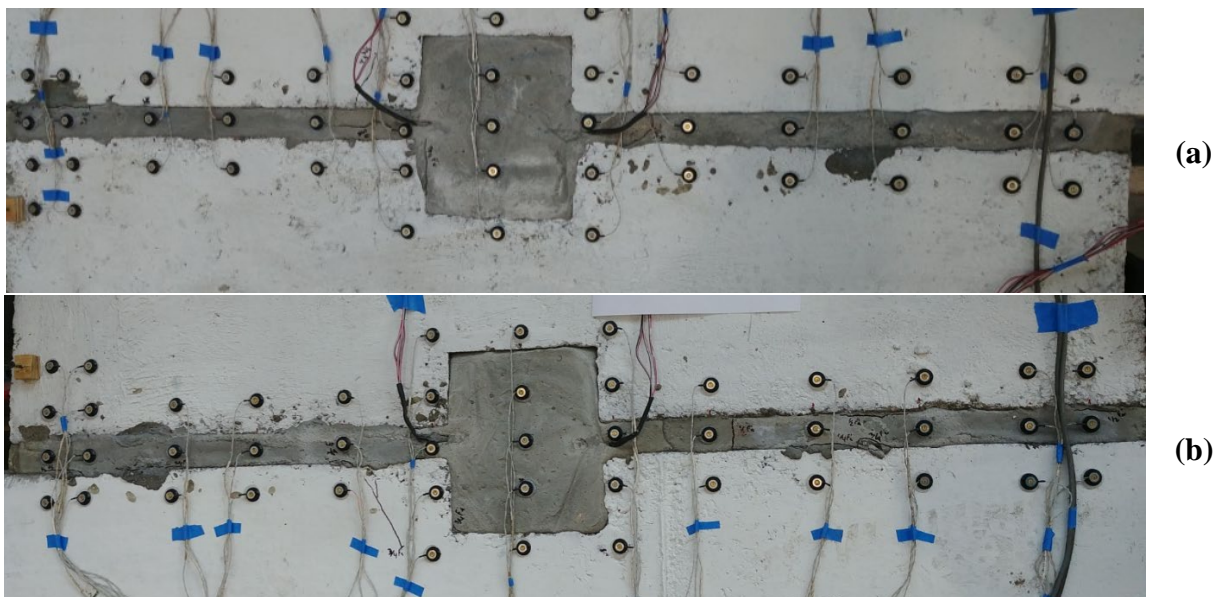


Figure 5.34: Test 2 Grouted Shear Key at $\frac{3}{4} f't$ (a) Left Side (b) Right Side

At 241.1 kips, which was 98% of the expected joint max strength, the strength continued to increase with a displacement of 0.048 inches with a rigid body rotation of 0.007° . More cracks start to appear on both of the side blocks and on the specimen in a diagonal direction pointing towards the actuator (Figure 5.35). Because loss of strength was not achieved in the last increment of loading, another 61.3 kip increment was applied; however, the specimen did not reach that level before the load rapidly degraded. The maximum load sustained was 260.0 kips (the maximum predicted load was 245.3 kips). At this point, the displacement of the center of the specimen was 0.093 inches with a rigid body rotation of 0.016° . As the strength decreased, the

actuator continued to push until it reached a limit of 0.35 inches. At this point similar damage was seen on both sides of the specimen. Already present diagonal cracks grew in length and new ones formed in the side block and specimen. Spalding and loose grout was visible along the joint with cracks in the grouted pocket propagating. New cracks also appeared on the right side joint close to the loading plate and potentiometer. The damage is presented in Figure 5.36. It was noted that some crushing of the concrete was present on the interface of the loading plate and the specimen.

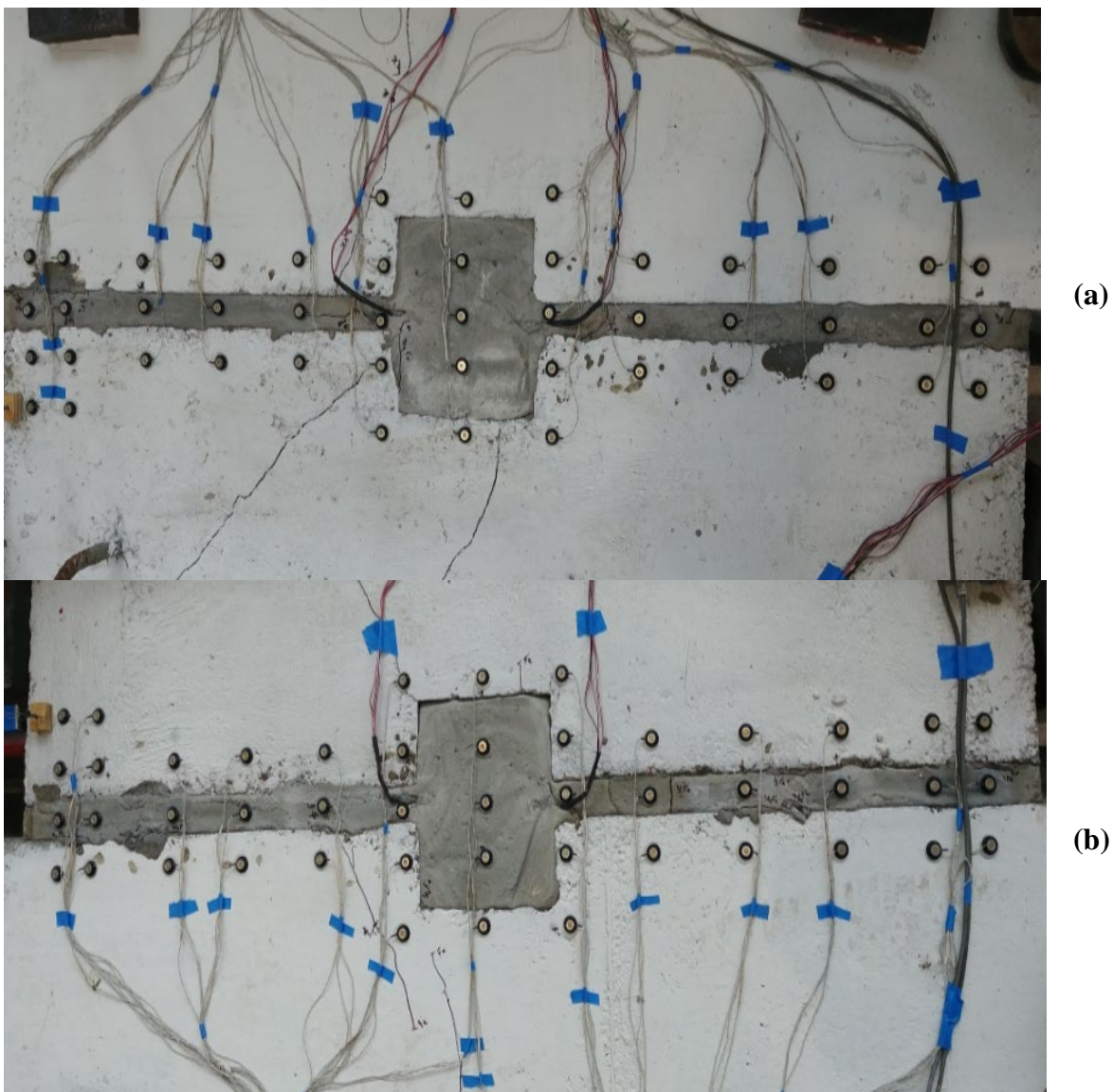


Figure 5.35: Test 2 Grouted Shear Key at f'_t (a) Left Side (b) Right Side

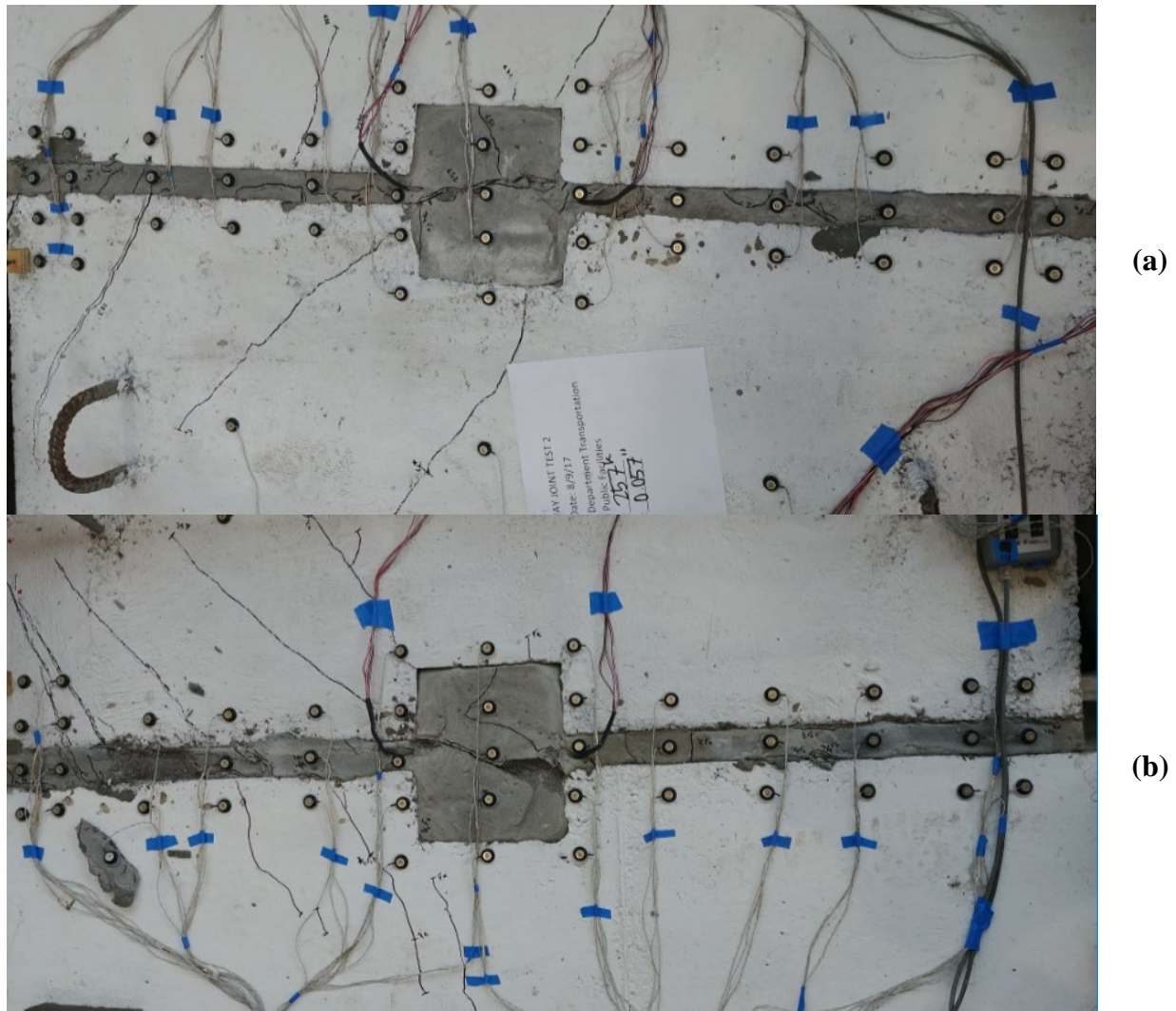


Figure 5.36: Test 2 Grouted Shear at Key Max Capacity (a) Left Side (b) Right Side

A new displacement limit was set for 0.50 inches and the loading protocol was switched from force control to displacement control at increments of 0.10 inches of actuator ram displacement. At the first increment the total actuator displacement was equal to 0.44 inches corresponding to a load of 92.3 kips. The displacement at the center of the specimen reached 0.315 inches with a rigid body rotation of 0.048° . Figure 5.37 (a) and Figure 5.37 (b) depicts the damage of the left and right joint respectively, which mainly consisted of widening cracks with two cracks lengthening on the right side specimen that are associated with cover concrete spalling.

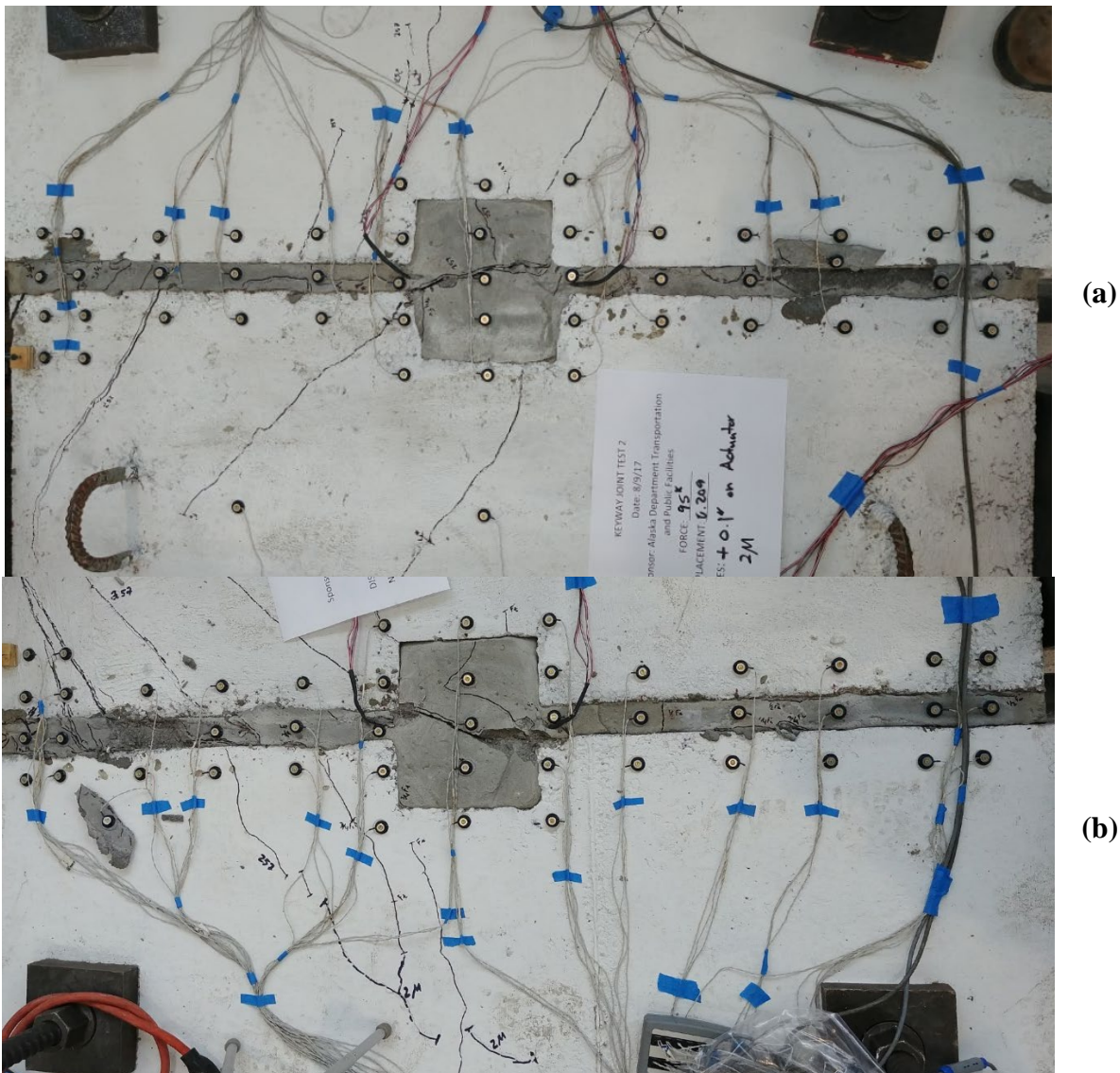


Figure 5.37: Test 2 Grouted Shear Key at 0.44 in. RAM Δ (a) Left Side (b) Right Side

An additional 0.10 inch increment was planned but the 0.50 inch limit was reached corresponding to a total actuator displacement 0.48 inches and a load of 71.8 kips. The center of the specimen reached a displacement of 0.366 inches. Both the left joint and right joint formed one new crack branching off an existing crack as seen in Figure 5.38. Displacement limits were reset to 0.75 inches and an additional 0.10 increment of displacement was applied leading to a total actuator displacement of 0.58 inches and a load of 47.8 kips, with a corresponding displacement at the center of the specimen of 0.478 inches and a rigid body rotation of 0.089° . New damage was only concentrated in the right joint. New cracks formed, connecting to old

ones in the side block resembling damage associated with large spalling of cover concrete. Additionally, loose concrete was removed from the specimen close to the loading plate. Damage can be seen in Figure 5.39.

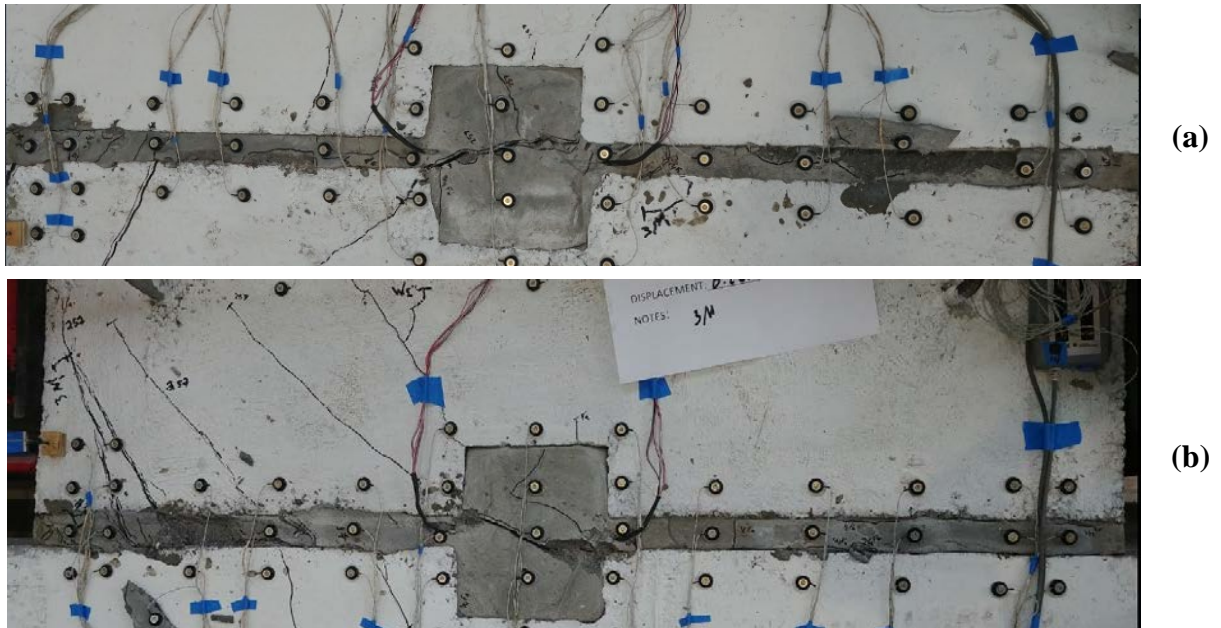


Figure 5.38: Test 2 Grouted Shear Key at 0.48 in. RAM Δ (a) Left Side (b) Right Side

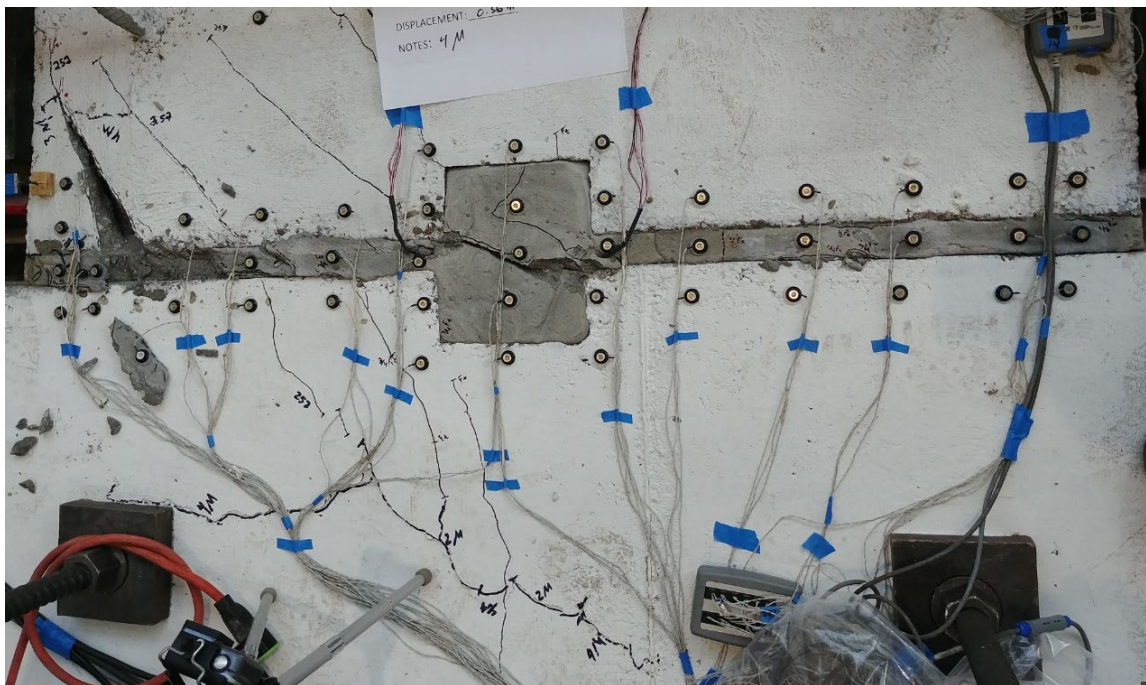


Figure 5.39: Test 2 Right Side Grouted Shear Key at 0.58 in. RAM Δ

An additional 0.1 increment of displacement was applied for a total of 0.74 inch actuator displacement and a load of 34.4 kips. The displacement at the center of the specimen was 0.641 inches. The displacement of the left keyway joint was 0.580 inches and the right joint was 0.702 inches. The damage can be seen in Figure 5.40. Notable damage occurred on the side block of the left joint. A large single piece of cover concrete on the end of the side block farthest from the actuator displaced upwards creating large cracks in the side block and a gap between the grouted joint and the concrete lip of the shear key. Additionally, on the right side, large connected cracks appeared on the specimen resembling damage associated with spalling cover concrete.

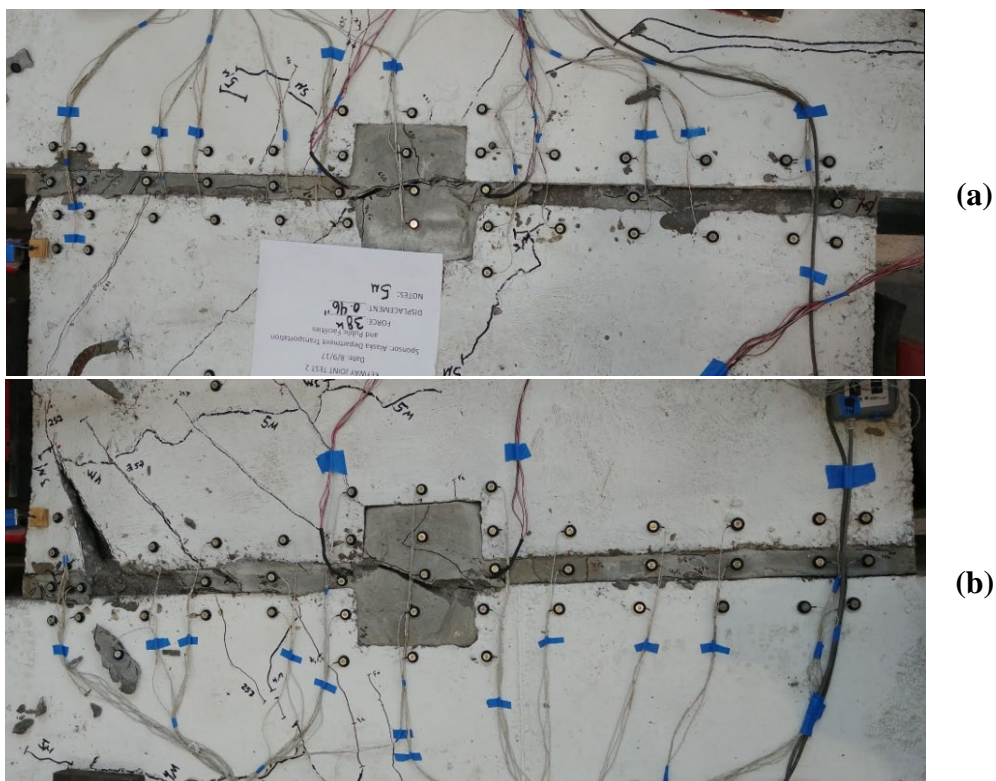


Figure 5.40: Test 2 Grouted Shear Key at 0.74 in. RAM Δ (a) Left Side (b) Right Side

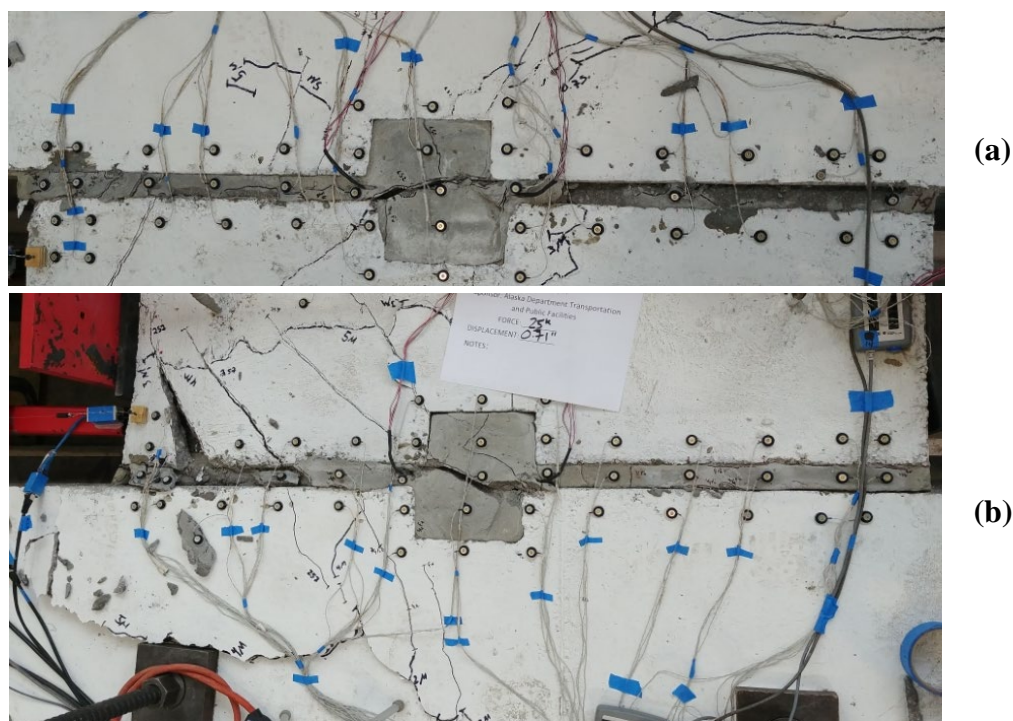


Figure 5.41: Test 2 Grouted Shear Key at 1.04 in. RAM Δ (a) Left Side (b) Right Side

It was decided that the force was stabilizing and thus the increment of actuator ram displacement was increased to 0.25 inches. Upon loading, the 0.75 inch actuator displacement limit was reached, but because the change in actuator displacement was low, no observations were taken. The displacement limit was removed and an increment of 0.25 inches displacement was applied to the actuator for a total actuator displacement of 1.04 inches and a load of 23.9 kips. The center of the specimen displacement was recorded at 0.929 inches with a rigid body rotation of 0.258° . Damage can be seen in Figure 5.41. The gap between the concrete lip and the grouted joint on the left side block continued to grow as the cover concrete was pushed up causing a crack to form at the vertex of the keyway faces. Similar behavior was observed on the right side block. Minor new cracks appeared and old crack widths widened.

After pushing with the actuator to 1.04 inches, it seemed that the response of the joint was relatively stable and that the monotonic backbone was established. Thus, it was decided to perform a reversal back to zero displacement. Before the reversal, the load relaxed from 23.4 kips to 0.1 kips. Upon the reversal the force gradually increased to a peak of -29.1 kips at an absolute displacement of -0.060 inches of the actuator. This corresponded to a -0.045in displacement at the center of the specimen and a rigid body rotation of 0.032° . Two small cracks

appeared perpendicular to the face of the pocket on specimen's left side. A significant crack appeared on the right side block opposite in direction of the other cracks but similar in nature as it was pointing to the loading. The damage can be seen in Figure 5.42.

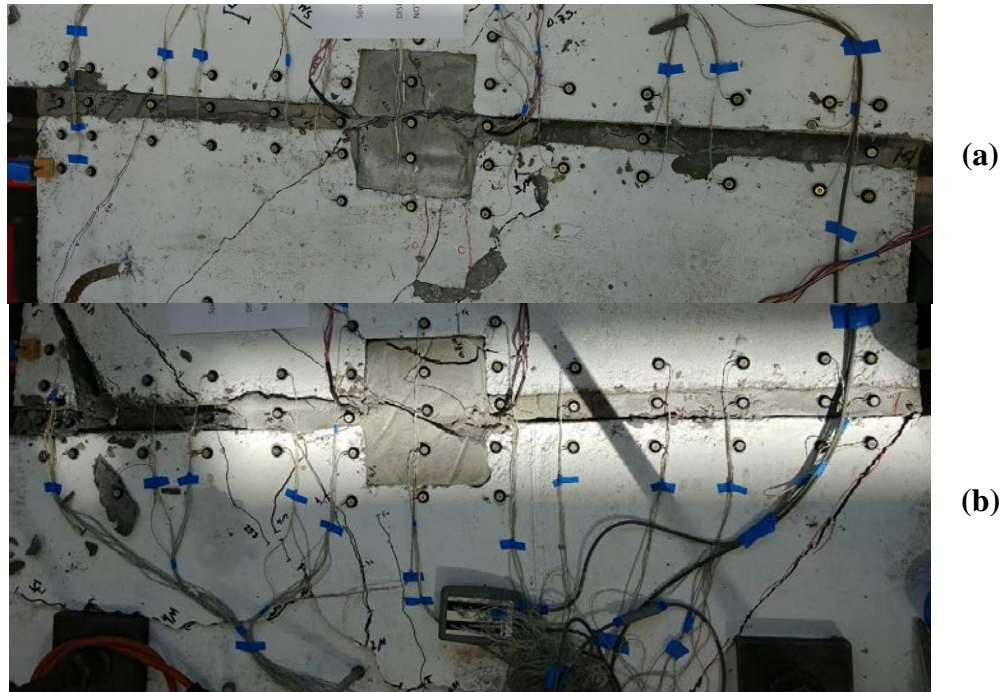


Figure 5.42: Test 2 Grouted Shear Key at -0.06 in. RAM Δ (a) Left Side (b) Right Side

The specimen was then pushed back to an actuator displacement of 0.96 inches. Upon reversing, the load dropped from -29.1 kips to -2.85 kips, and then gradually increased to 14.5 kips. This corresponded to a 0.884 inch displacement and rigid body rotation of 0.228° at the center of the specimen. Minor cracks formed on the left side block but no new cracks formed on the right joint side. Damage of the left side block can be seen in Figure 5.43. To finish testing the actuator was taken back to -0.07 inches of displacement. Upon reversal, the load dropped from 14.5 kips to 0.3 kips and gradually increased to -16.8 kips. This corresponded to an absolute displacement of 0.071 inches at the center of the specimen. Two new minor cracks formed, one on the left side block and one on the right side of the specimen. Damage can be seen in Figure 5.44.

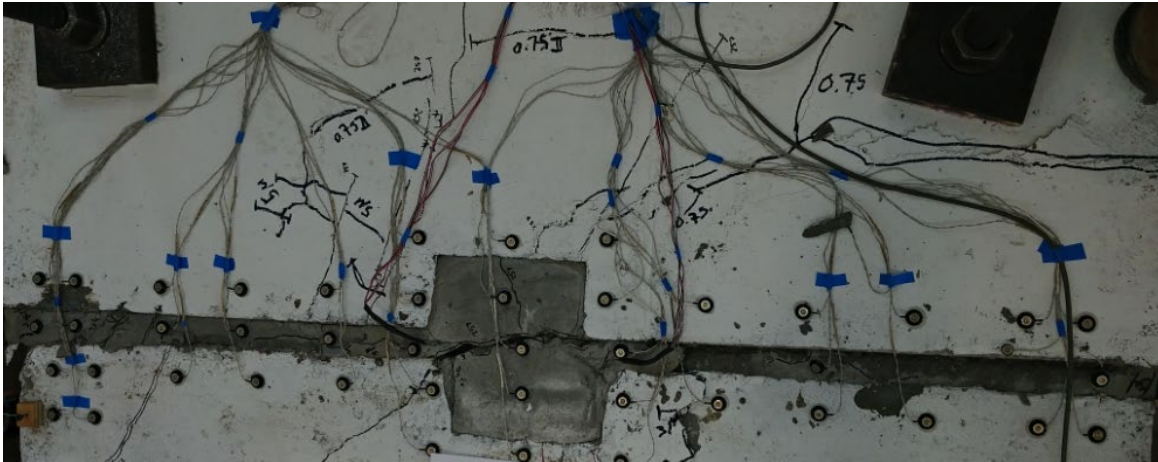


Figure 5.43: Test 2 Left Side Grouted Shear Key at 0.96 in. RAM Δ

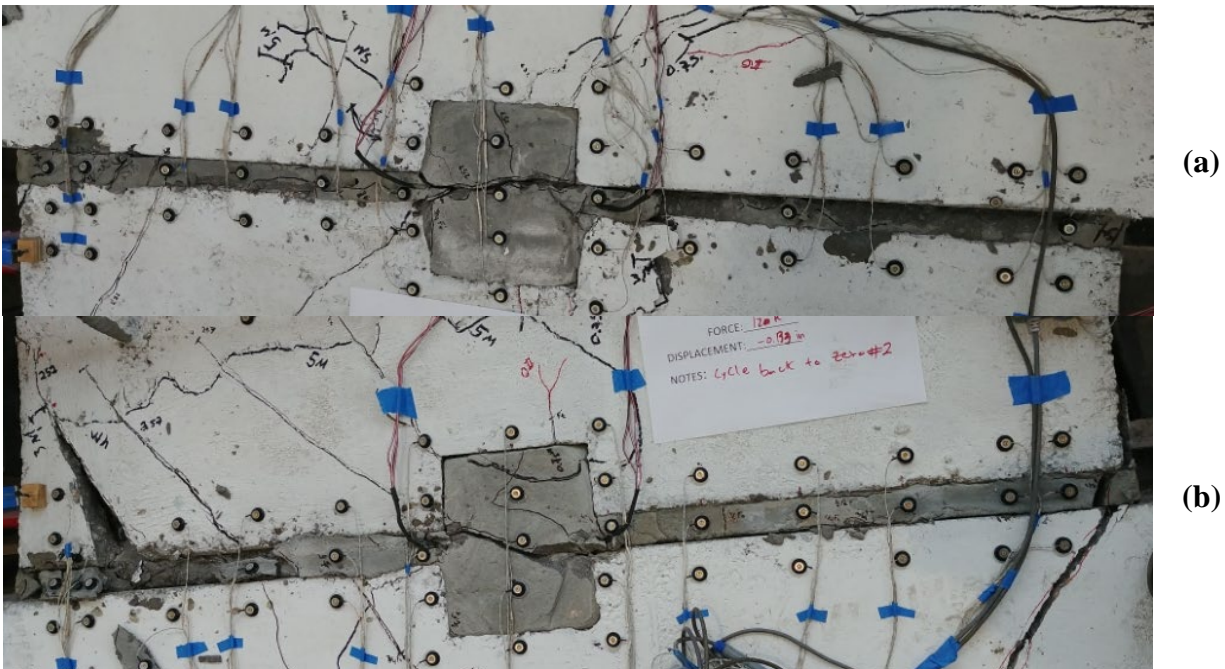


Figure 5.44: Test 2 Grouted Shear Key at -0.07 in. RAM Δ (a) Left Side (b) Right Side

In order to remove the specimen for disposal, it first must be detached from the side blocks along the joint. Figure 5.45 (a) shows the specimen prior to detachment. Figure 5.45 (b) shows the specimen disconnected from the side blocks. Upon detaching the specimen, it was observed that most of the cracked concrete could be removed by hand in large pieces. Pieces removed by hand for the left and right joint respectively are shown in Figure 5.46 (a) and Figure 5.46 (b) respectively. These large concrete pieces were a part of the cover concrete of the specimen and predominantly had a fracture along the vertex of the keyway faces. Removing the

loose concrete and grout revealed the shear connectors below. The connectors behaved similarly to Test 1a, where the embedded plates pryed upward and created a gap between the concrete and the plates. Damage was concentrated in the rebar portion of the shear connector inserts. Figure 5.47 shows that no damage could be seen in any of the welds. The embedded rebar crushed the surrounding concrete that it was bearing against, leading to new boundary conditions and relatively large unsupported lengths in the rebar, causing bending in the rebar as well as translation and rotation in the plates.

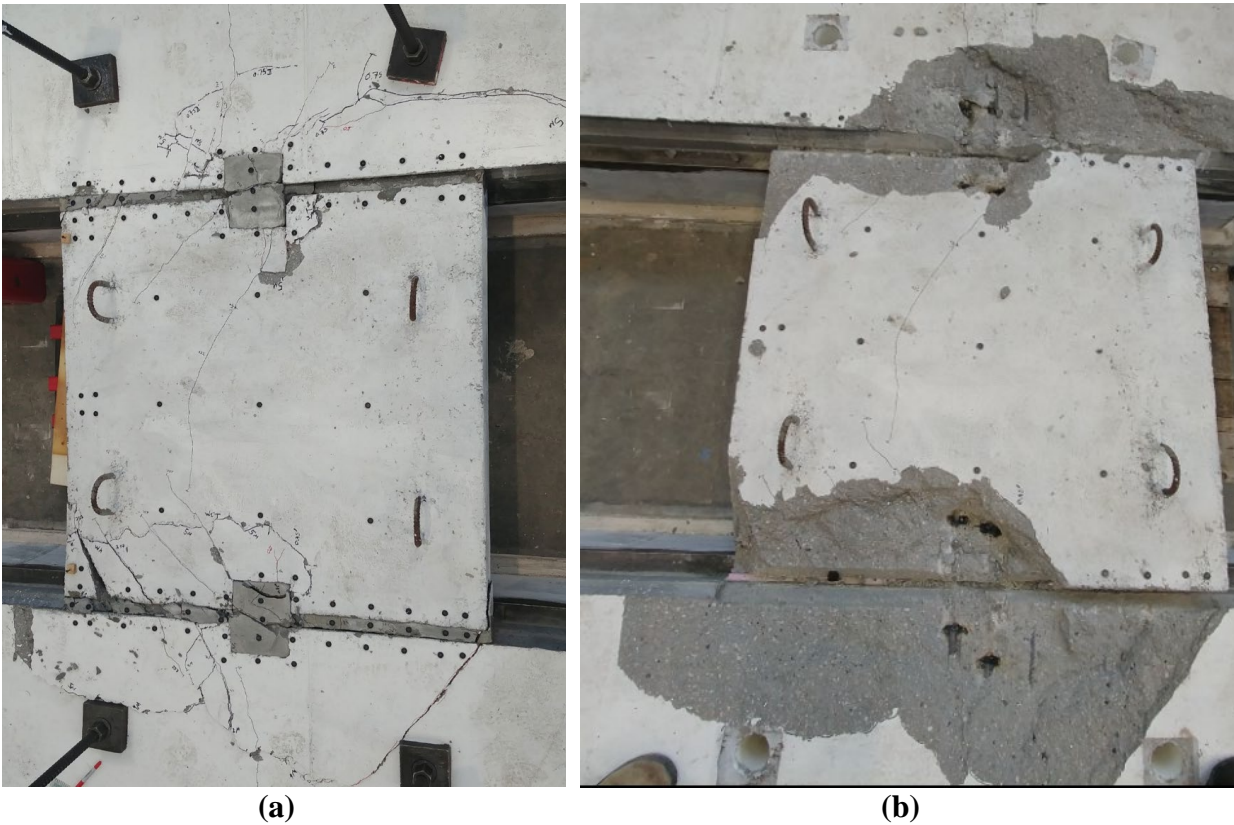


Figure 5.45: Test 2 Post Damage (a) Undetached Test Specimen (b) Detached Test Specimen

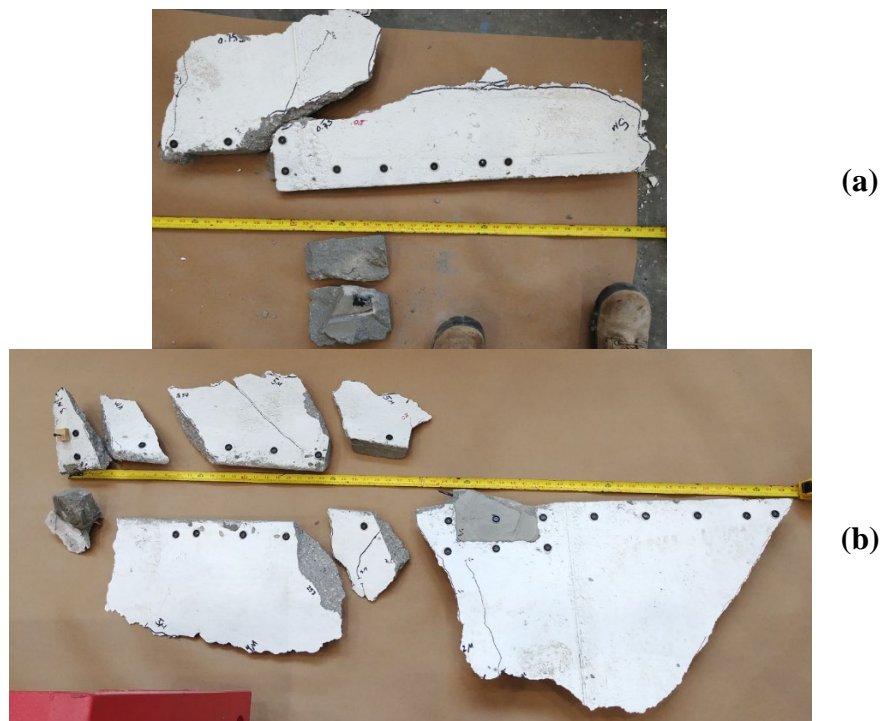


Figure 5.46: Test 2 Post Damage (a) Left Joint (b) Right Joint

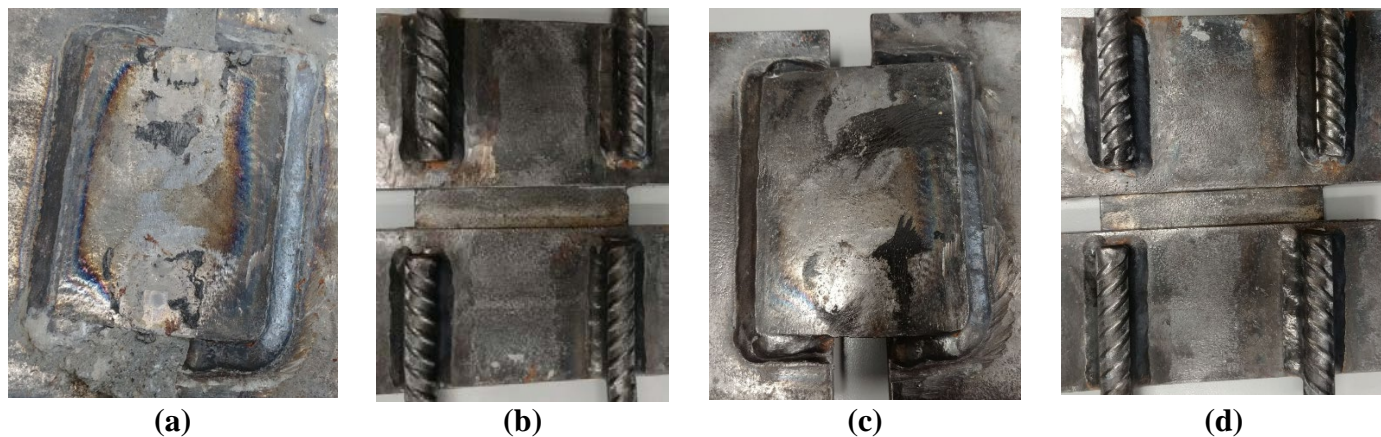


Figure 5.47: Test 2 Plate Welds (a) Left Shear Tab (b) Left Embedded Plate (c) Right Shear Tab (d) Right Embedded Plate

5.3.2 Test 2 Conclusion

Test 2 was a monotonic pushover test of the commonly used keyway joint for precast prestressed bulb-tee girders. Test 2 performed similar to what was expected after Test 1a and Test 1b. The maximum strength of the joint could be closely estimated using the maximum grout tension stress with consideration of the steel shear tab to achieve a ratio of the maximum

recorded load over the expected maximum load of 1.06. Numerous distributed diagonal cracks appeared along both the specimen and side block. The diagonal cracks pointed toward the direction of the applied load leading to fracture of large pieces of the cover concrete in the joint along the vertex of the keyway faces and significantly reduced the strength of the joint.

5.4 Test 3

Test 3 was performed at the CFL at NCSU starting on October 18, 2017, and ending on November 29, 2017. This section presents the overall response of the specimen and then discusses experimental procedures, results and observations in chronological order. The displacement history measured at the center of the specimen is displayed in Figure 5.48. Complementary to the displacement history, the specimen load history is presented in Figure 5.49. The complete unaltered load-displacement response of the specimen measured at the center of the specimen can be seen in Figure 5.50. Figure 5.51 provides a close up of the hysteretic response of the specimen prior to significant strength loss. Complementary to the force displacement response, the rigid body rotation of the specimen versus displacement of the center of the specimen can be seen in Figure 5.52.

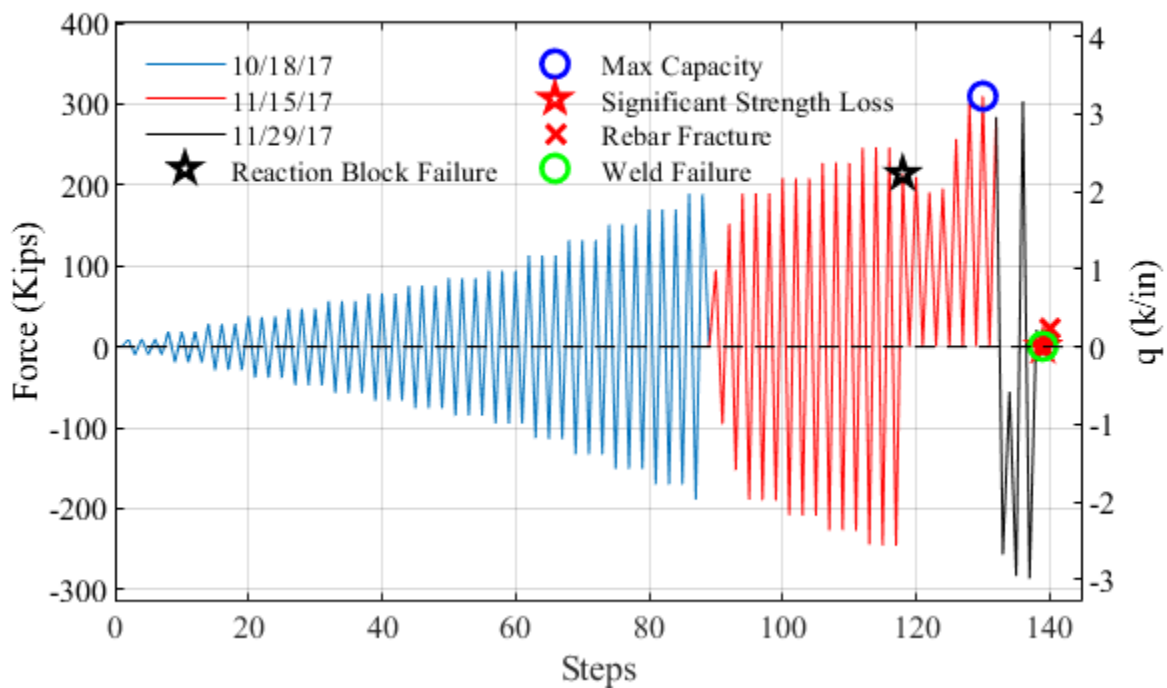


Figure 5.48: Test 3 Force History

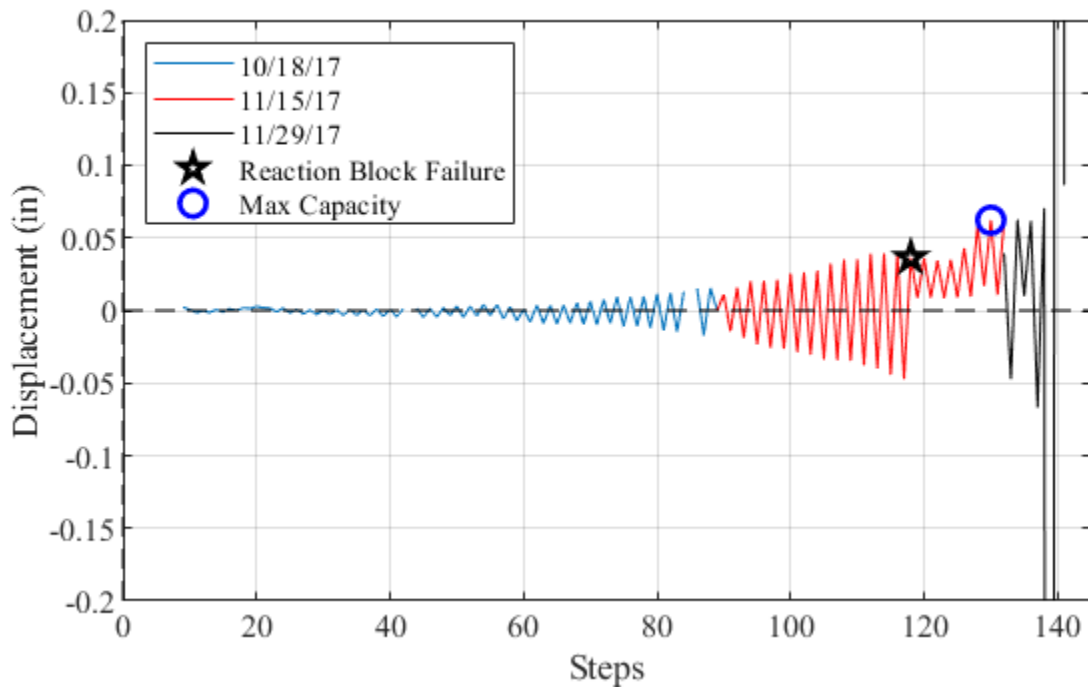


Figure 5.49: Test 3 Displacement History

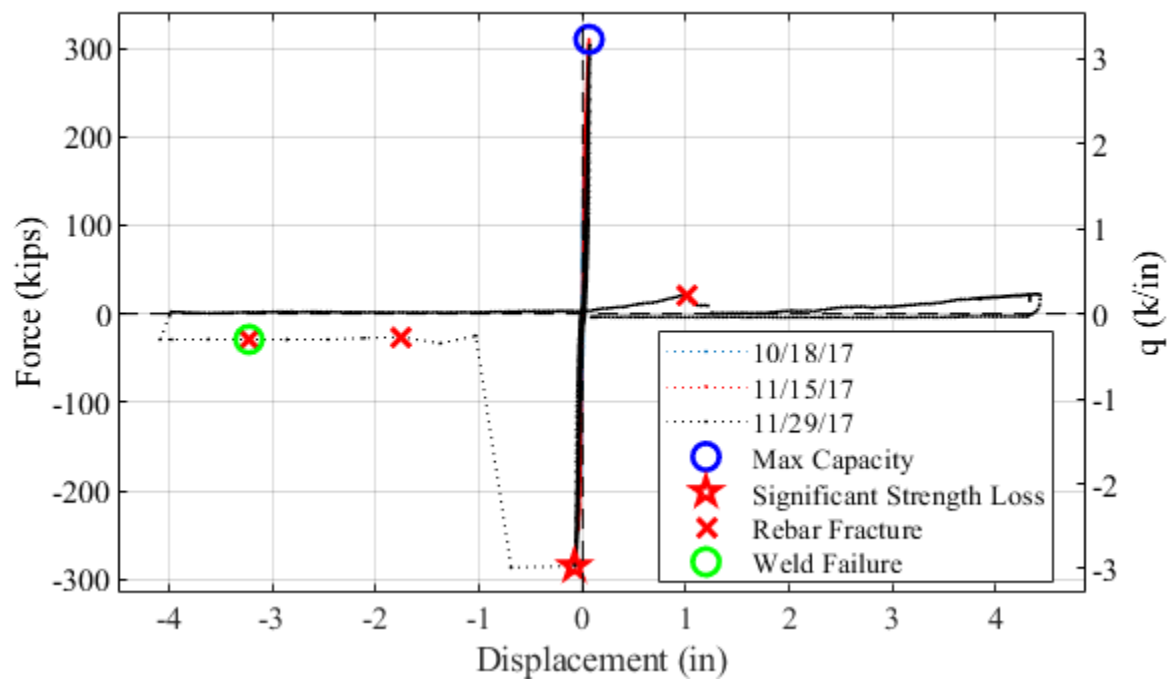


Figure 5.50: Test 3 Force-Displacement Response

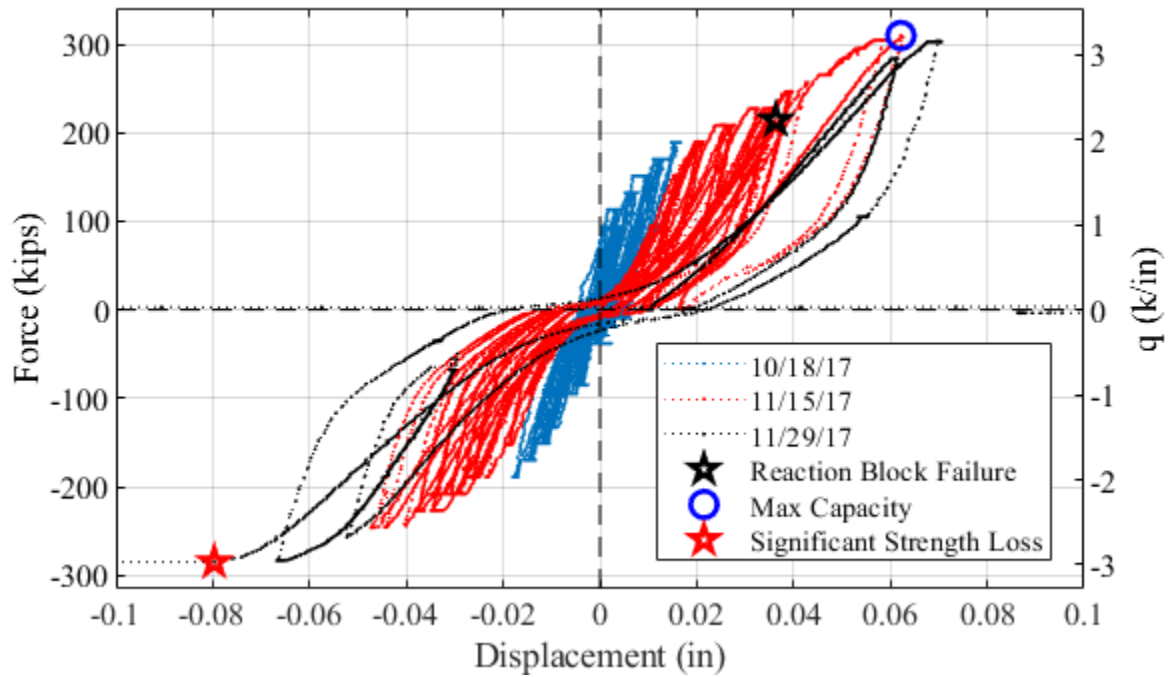


Figure 5.51: Test 3 Force-Displacement Response Prior to Significant Strength Loss

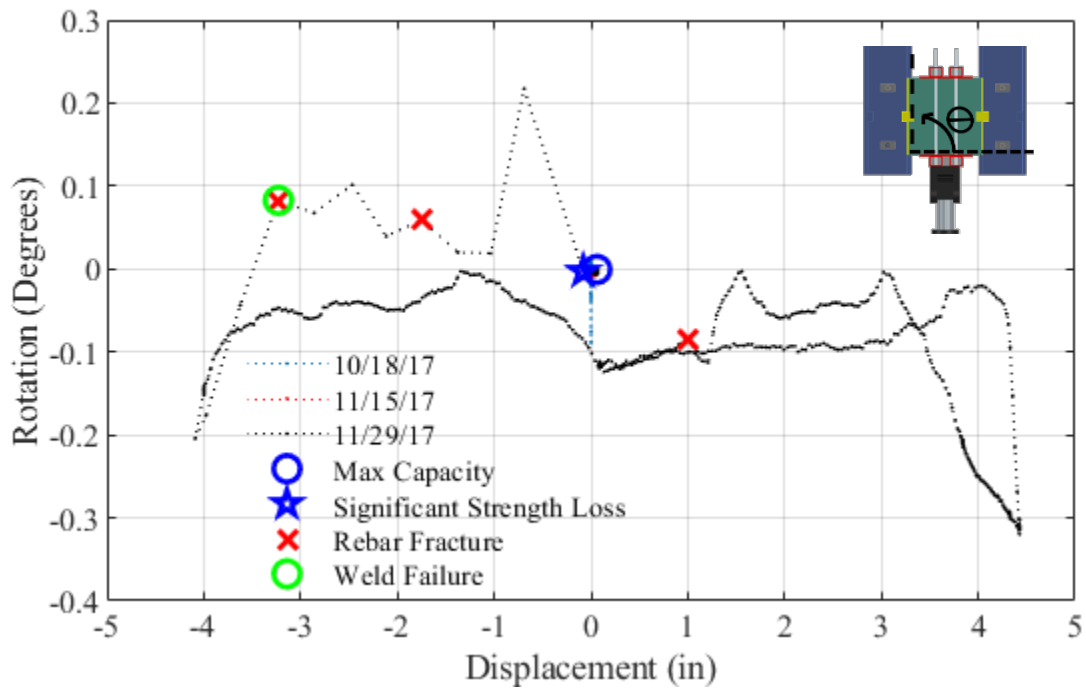


Figure 5.52: Test 3 Rigid Body Rotation

5.4.1 Test 3 Summary

The first part of Test 3 took place on October 18, 2017. Force was applied cyclically in three cycle sets, starting with increments of 9.6 kips. This load is associated with an average shear flow along the joint equal to 0.1 k/in. Loading progressed in increments of an average shear flow of 0.1 k/in until the load reached 1.0k/in (96 kips). Minor surface cracking was visible parallel to the boundaries of the joint and perpendicular to the joint at low levels of force. The progression of cracks can be seen in Figure 5.53 and Figure 5.54, where Figure 5.53 is prior to any loading and Figure 5.54 is the third cycle at an average shear flow equal to 1.0k/in. The first visible cracks outside of the grout occurred at an average shear flow of 0.3k/in on the right side block perpendicular to the pocket associated but the damage was induced from previous tests on the side block. The crack can be seen in Figure 5.54 (b). The max positive and negative displacement of the center of the specimen at $q_{\text{average}}=1.0\text{k/in}$ was -0.004 in. and -0.013 in. with an associated rigid body rotation of -0.002° and -0.003° respectively.

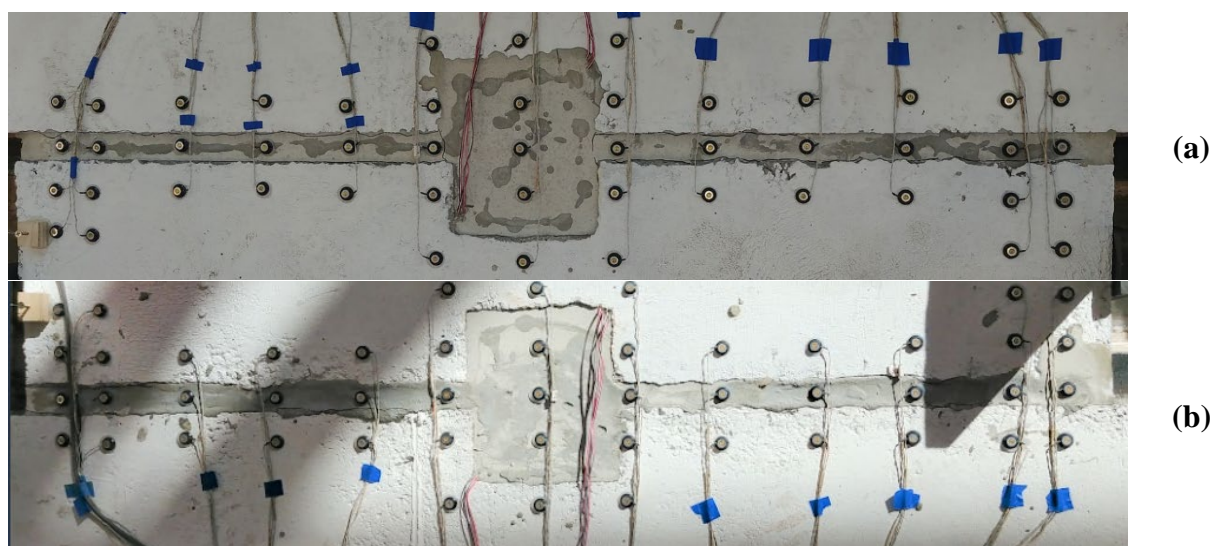


Figure 5.53: Test 3 Grouted Shear Key $q_{\text{average}}= 0.0\text{k/in}$ (a) Left Side (b) Right Side





Figure 5.54: Test 3 Grouted Shear Key $q_{\text{average}} = 1.0\text{k/in}$ (a) Left Side (b) Right Side – Third Cycle

The increments of loading applied to the specimen increased to 19.2 kips or $q_{\text{average}} = 0.2\text{k/in}$. No new cracks were observed until a crack perpendicular to the pocket occurred on the left side block at $q_{\text{average}} = 1.6\text{k/in}$. The crack continued to propagate at $q_{\text{average}} = 1.8\text{k/in}$ and can be seen in Figure 5.55. When the load reached -189 kips ($q_{\text{average}} = -2.0\text{k/in}$), unexpected localized yielding was observed in the HSS's that make up the load spreader. After one more push cycle, the test was terminated. The maximum positive and negative displacement of the center of the specimen at $q_{\text{average}} = 2.0\text{k/in}$ was 0.011 in. and -0.022 in. with an associated rigid body rotation of -0.002° and -0.004° respectively. Upon termination it was found that the data acquisition system was not recording and only optical tracking system data and hand written data was available. The localized yielding in the HSS's was resolved using $1\frac{1}{4}$ in. plates to transfer rod forces to the HSS walls and inserting 4 in. x 4 in. x $\frac{3}{8}$ in. HSS tubes to change boundary conditions of the original HSS faces. The pre-altered and post-altered test setup can be seen in Figure 5.56.

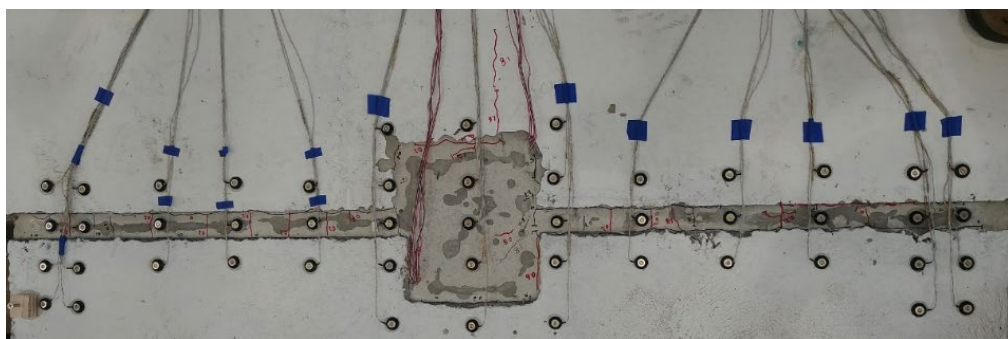


Figure 5.55: Test 3 Left Side of Grouted Shear Key $q_{\text{average}} = 1.8\text{k/in}$ – Third Cycle



Figure 5.56: Test 3 HSS Load Spreader (a) Pre-Altered Test Setup (b) Post-Altered Test Setup

After the test setup was altered, the test was resumed on November 15, 2017. One cycle of $q_{\text{average}} = 1.0\text{k/in}$ and $q_{\text{average}} = 1.6\text{k/in}$ was repeated to compare with the available data from the previous segment of Test 3. This led to a minor crack propagating in the right joint pocket and some cracking in the patched section of the right side block. The original loading protocol was then continued at $q_{\text{average}} = 2.0\text{k/in}$ to $q_{\text{average}} = 2.6\text{k/in}$ (246 kips) at which point, large cracks began to form diagonally in the specimen, starting around the pockets and propagating towards the applied load as seen in Figure 5.57. Prior to completion of the first cycle of $q_{\text{average}} = 2.8\text{k/in}$, the reaction block bond failed and the reaction block slipped at 214 kips, triggering a displacement limit. Since the predicted strength of the specimen was 264 kips, we continued pushing the specimen in an attempt to reach maximum strength capacity. With the specimen experiencing significant strength loss the test could continue using three cycle sets based on the displacement of significant strength loss. The reaction block slipped six more times and the test was terminated. During the last push, the specimen reached a load of 310 kips with a center of specimen displacement of 0.057 in. and a rotation of -0.001° . No new visible damage was observed.

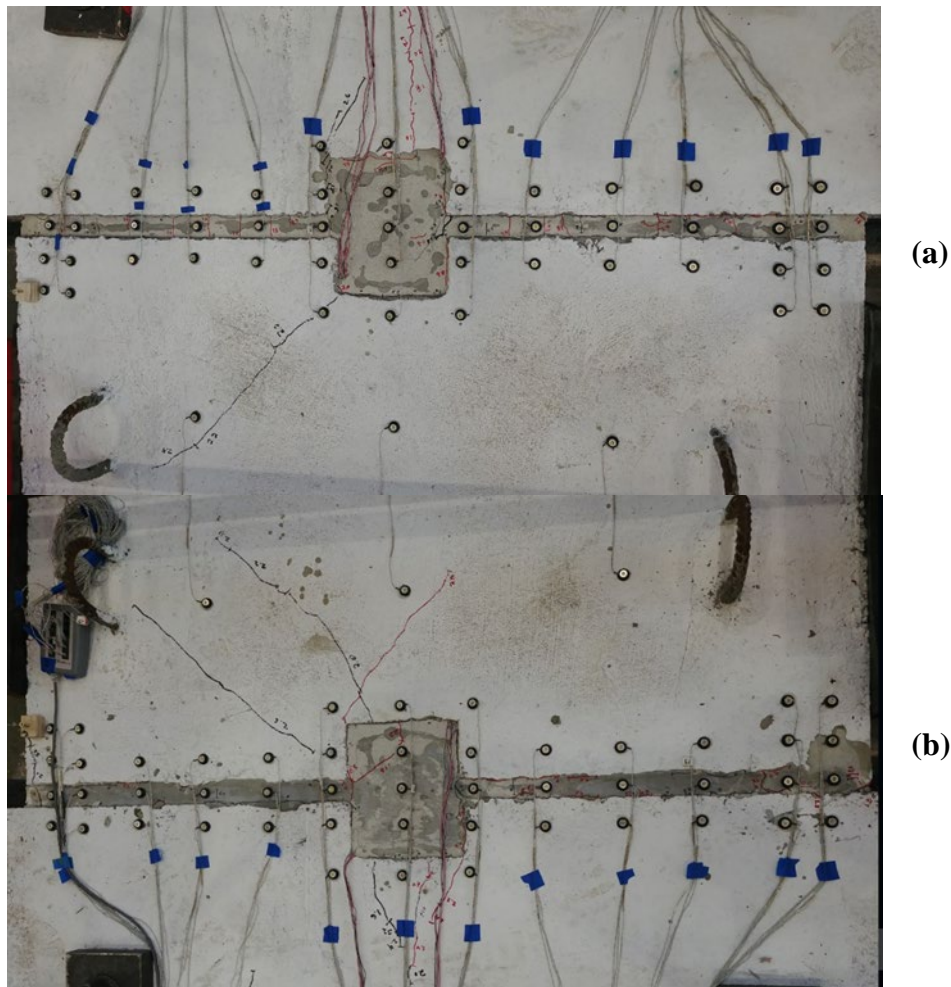


Figure 5.57: Test 3 Grouted Shear Key Pocket $q_{\text{average}} = 2.6\text{k/in}$ (a) Left Side (b) Right Side– Third Cycle

The test was resumed on November 29, 2017 after the reaction block was restored. The loading protocol was switched from three cycle to single cycle sets until significant strength loss occurred to ensure that the reaction block would not slip again. The test continued from $q_{\text{average}} = 2.8\text{k/in}$, the load cycle that the reaction block originally slipped at. During $q_{\text{average}} = 3.0\text{k/in}$, new diagonal cracks appeared in the specimen. At $q_{\text{average}} = 3.2\text{k/in}$ (303 kips), diagonal cracks could be seen in both joint pockets (Figure 5.58). The displacement at the center of the specimen was 0.065 in with no measurable rotation. On the reversal, the load reached -286 kips when the grout in the longitudinal joint cracked. The center of the specimen displacement became -0.085 in. with a rigid body rotation of -0.003° .

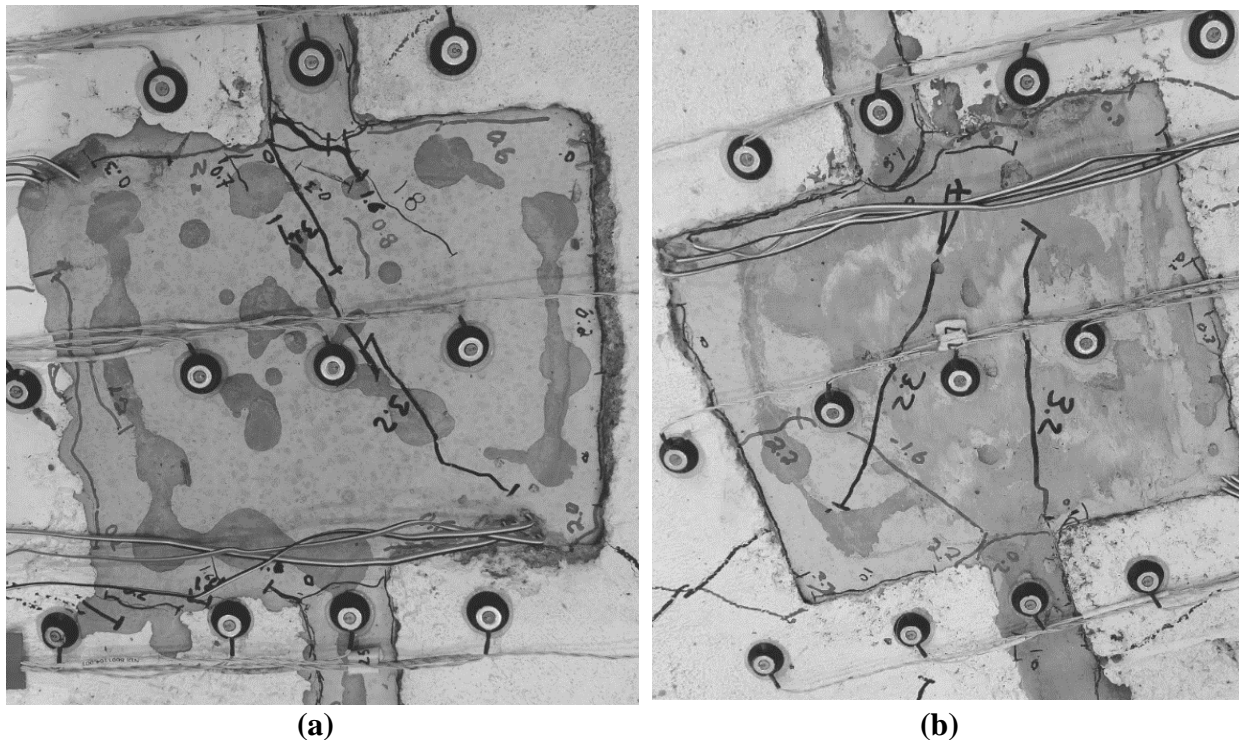


Figure 5.58: Test 3 Grouted Shear Key Pocket $q_{average} = 3.2\text{k/in}$ (a) Left Side (b) Right Side– Third Cycle

As grout cracked, the displacement limit was reached but the actuator controller was not updating live displacements. This meant that the actuator displacements were not getting compared with the limit and thus the limit was never triggered to turn off the actuator. By the time this was realized and the actuator was stopped manually, eleven seconds had passed since the grout cracked. The displacement of the center of the specimen reached -4.093 in. with a rotation of -0.204° and a force of -29 kips . The resulting damage can be seen in Figure 5.59. As seen in previous tests, numerous cracks occurred in cover concrete of the specimen and side blocks. These cracks resulted in the ability to remove large pieces of cover concrete and grout. The removed material can be seen in Figure 5.60. Upon removing the material, the shear connectors were revealed. Bending of the embedded rebar connected to the plates along with translation and rotation of the shear connectors was observed and can be seen in Figure 5.61. During this monotonic load cycle, two of the embedded rebar that make up the shear connector inserts fractured and one embedded rebar weld failed. The first fracture occurred on the shear connector insert embedded in the right side block at a center of specimen displacement of 1.758 in. and force of 26 kips . The second fracture occurred on the shear connector insert in left side

block immediately followed by failure of weld in the other rebar in the same shear connector insert. The damage can be seen in Figure 5.62. The recorded displacement was -3.234 inches with a force of 29.09 kips.

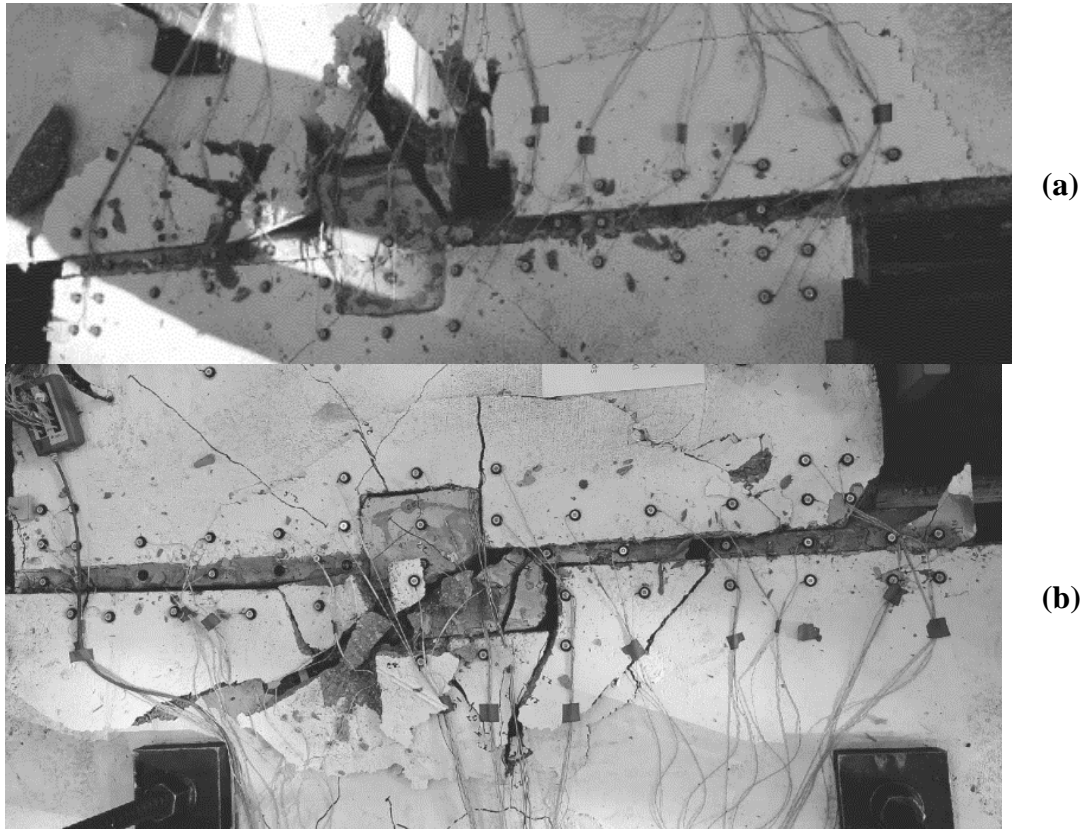


Figure 5.59: Test 3 Grouted Shear Key $\Delta = -4.093$ in. (a) Left Side (b) Right Side

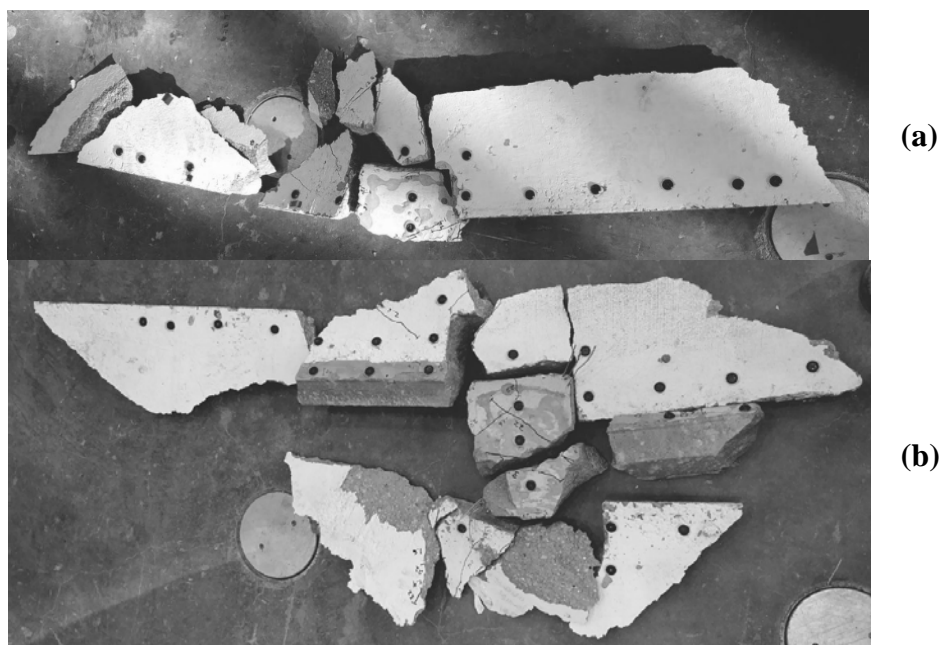


Figure 5.60: Test 3 Removed Material (a) Left Side (b) Right Side

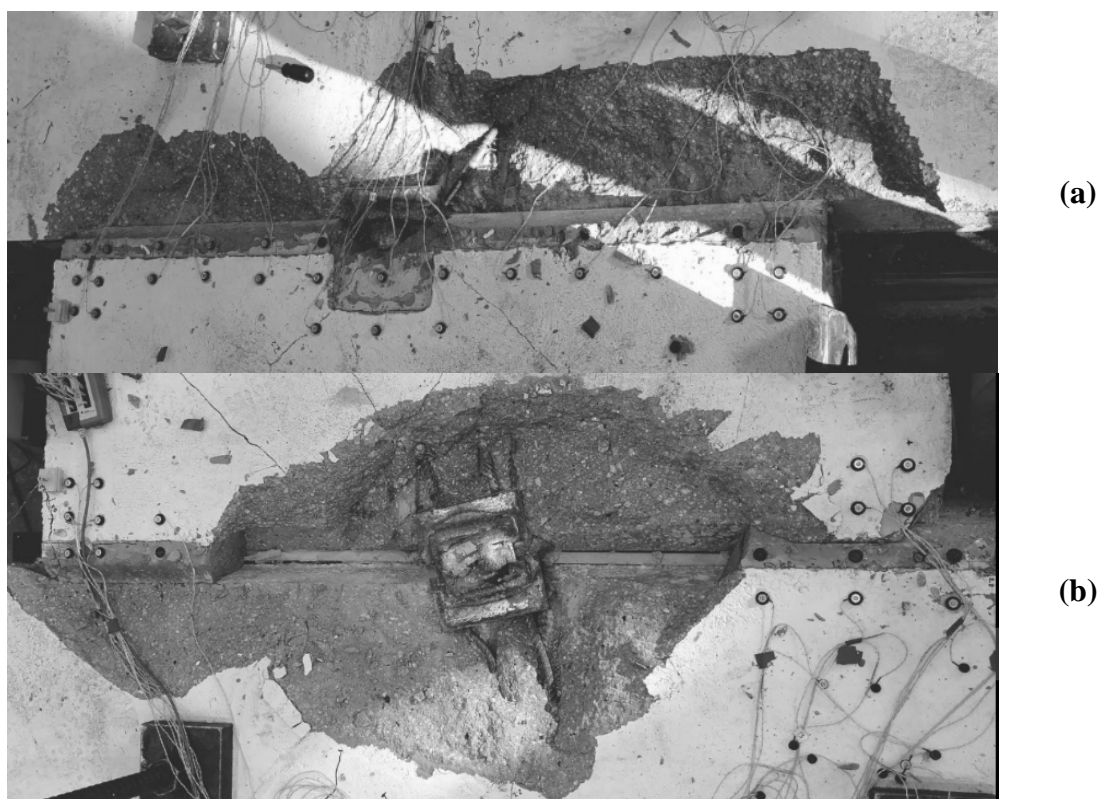


Figure 5.61: Test 3 Grouted Shear Key $\Delta = -4.093$ in. with Material Removed (a) Left Side (b) Right Side

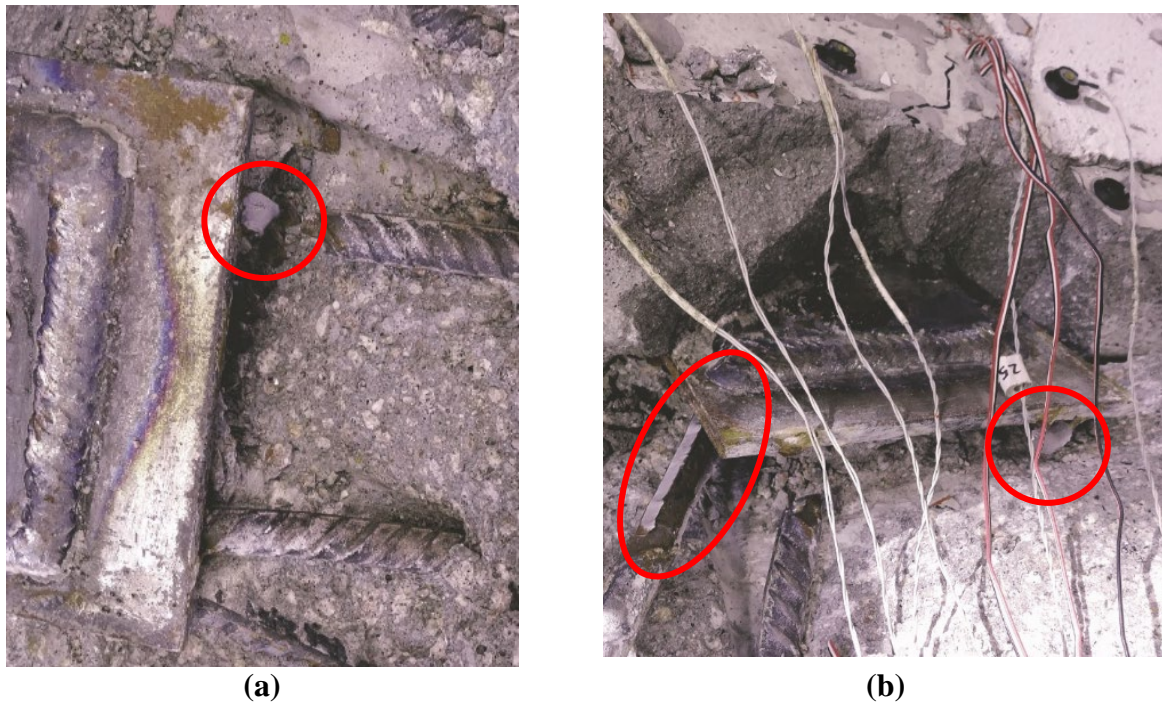


Figure 5.62: Test 3 Damage to Shear Connector Inserts at $\Delta = -4.093$ in. (a) Left Side
(b) Right Side

It was decided to apply an equal positive displacement in case there was remaining strength in the positive direction. Little strength was observed up until a center of specimen displacement of 0.069 in. The strength then began to steadily increase from 3 kips to 20 kips. At this point the rebar welded to the shear connector insert embedded in the right side specimen fractured at a displacement of 0.997 in. The fracture can be seen in Figure 5.63. The strength then decreased to 0 kips and steadily increased to 21 kips at a center of specimen displacement of 4.423 in and a rotation of -0.314° . No more damage was observed. The specimen was then brought back to a zero displacement with center of specimen displacement of 0.082 in. During that duration no more observable damage occurred as seen in Figure 5.64 and the strength did not increase beyond -4 kips. The test was then terminated. The welds of the shear connectors can be examined in Figure 5.65. While unintended, the loading history resembled multiple low level cycles, followed by a large monotonic push (similar to a velocity pulse).



Figure 5.63: Test 3 Damage to Right Side Shear Connector Inserts at $\Delta = 4.423$ in.

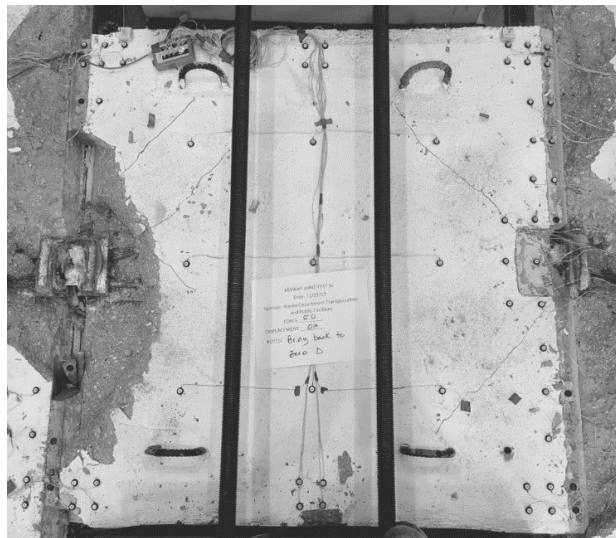


Figure 5.64: Test 3 Test Specimen 3 at $\Delta = 0.082$ in.

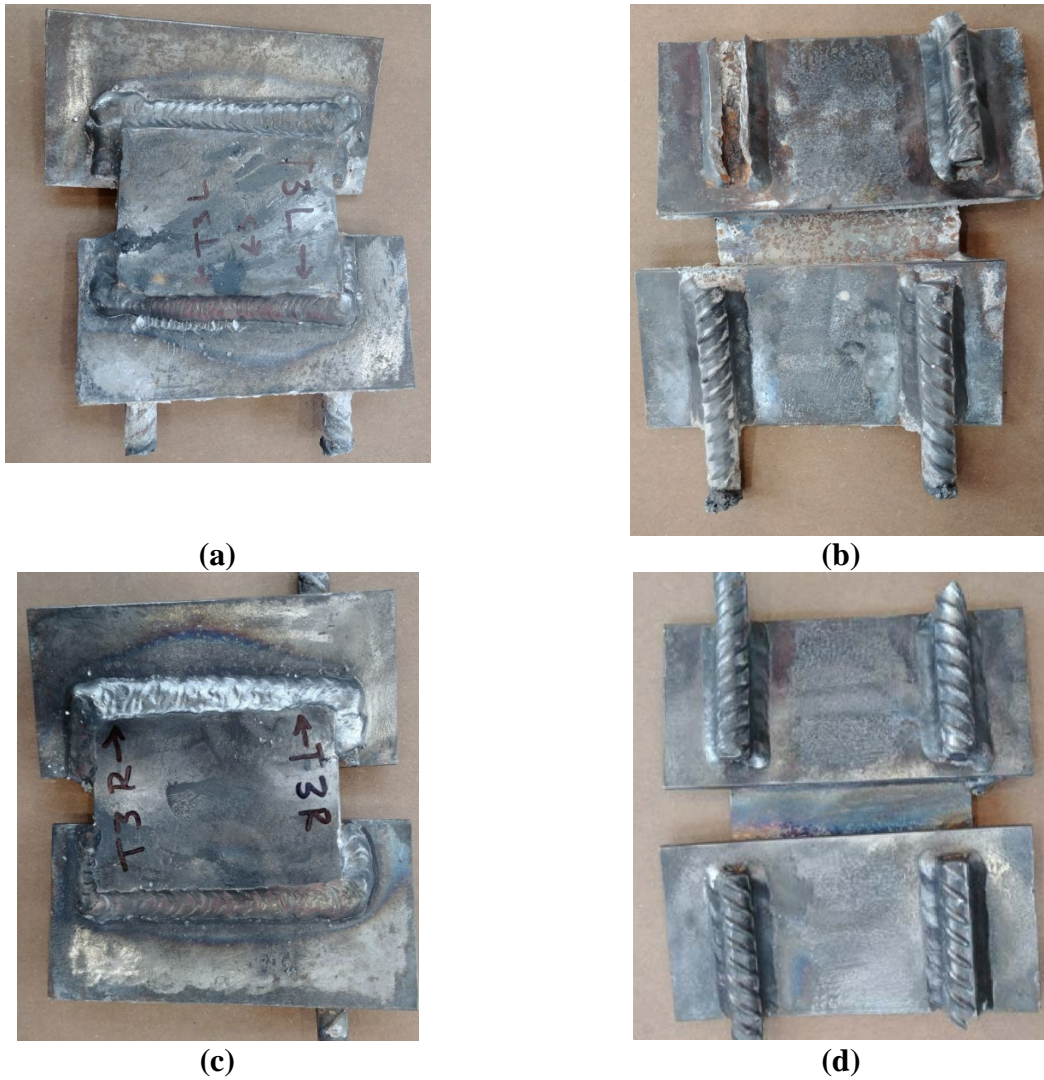


Figure 5.65: Test 3 Removed Shear Connector Plate (a) Top View Left Connector (b) Bottom View Left Connector (c) Top View Right Connector (d) Bottom View Right Connector

5.4.2 Test 3 Conclusion

Test 3 was a three-cycle cyclic test of a commonly used keyway joint for precast prestressed bulb-tee girders. The applied force was based on an analytical study described in Section 4.8.1. The study showed that realistic shear flow in transverse joints could range from 0.2 k/in to 54 k/in. Thus, loading started with an average shear flow along the joint equal to 0.1 k/in and increasing with increments of 0.1 k/in until 1.0 k/in. The increment then increased to 0.2 k/in. The joint provides a high stiffness that slowly reduces while the number of cycles and or load increases. The joint was expected to reach a strength of 263 kips, but instead reached a maximum strength of 310 kips, 1.20% of the anticipated capacity.

As the joint reached maximum capacity, due to human error, after cracking the controller actuator could not read the displacement limit and led to a monotonic loading of approximately 4 inches of displacement. During this monotonic load, two of the embedded rebar that make up the shear connector inserts fractured and one embedded rebar weld failed revealing a new limit state. Similar damage to the cover concrete as seen in Test 2 was noted in Test 3.

5.5 Test 4

Test 4 was performed at the CFL at NCSU starting on December 19, 2017, and ending on December 20, 2017. This section presents the overall response of the specimen and then discusses experimental procedures, results and observations in chronological order. The displacement history measured at the center of the specimen is displayed in Figure 5.66. Complementary to the displacement history, the specimen load history is presented in Figure 5.67. Additionally the complete unaltered load-displacement response and rigid body rotation versus displacement of the specimen measured at the center of the specimen can be seen in Figure 5.68 and Figure 5.69, respectively.

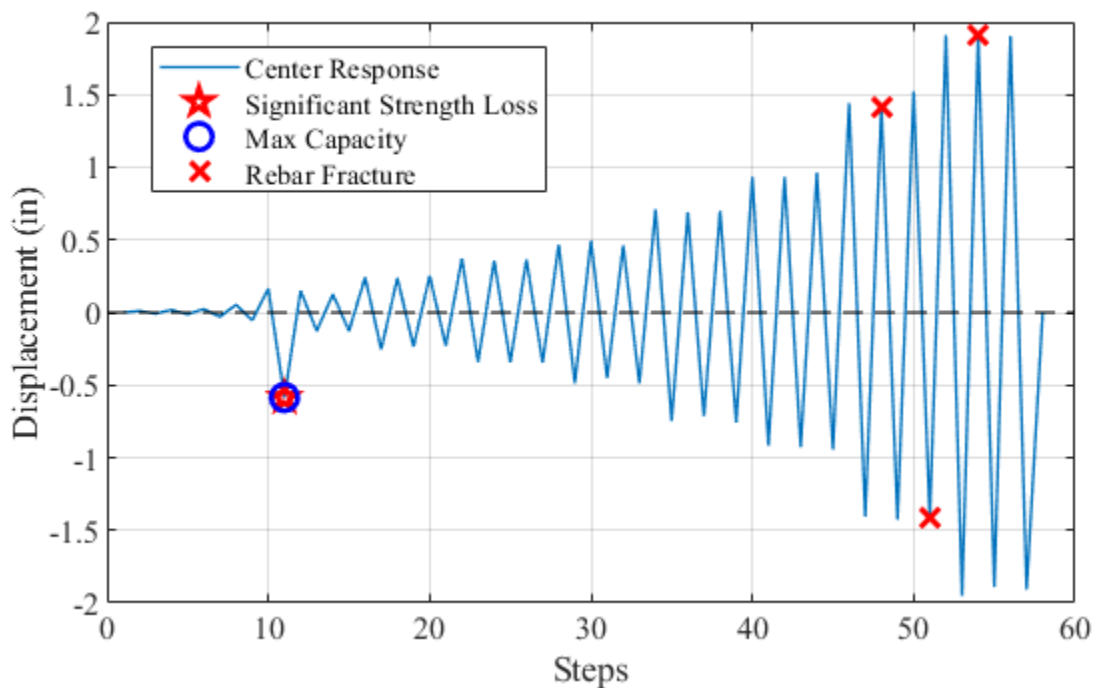


Figure 5.66: Test 4 Displacement History

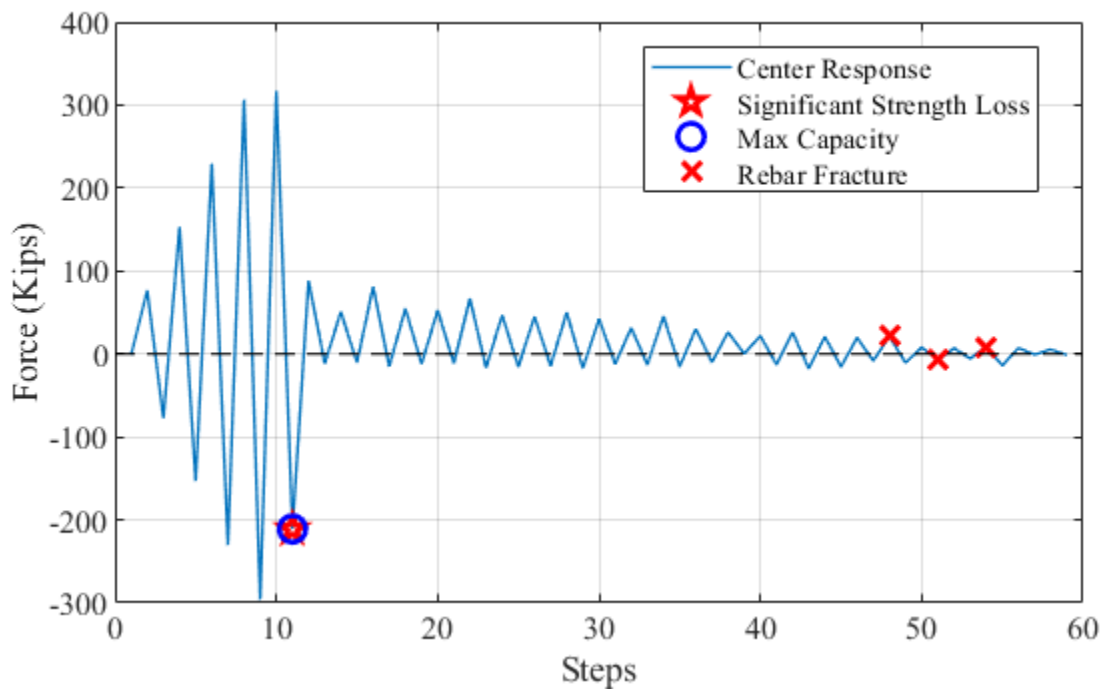


Figure 5.67: Test 4 Load History

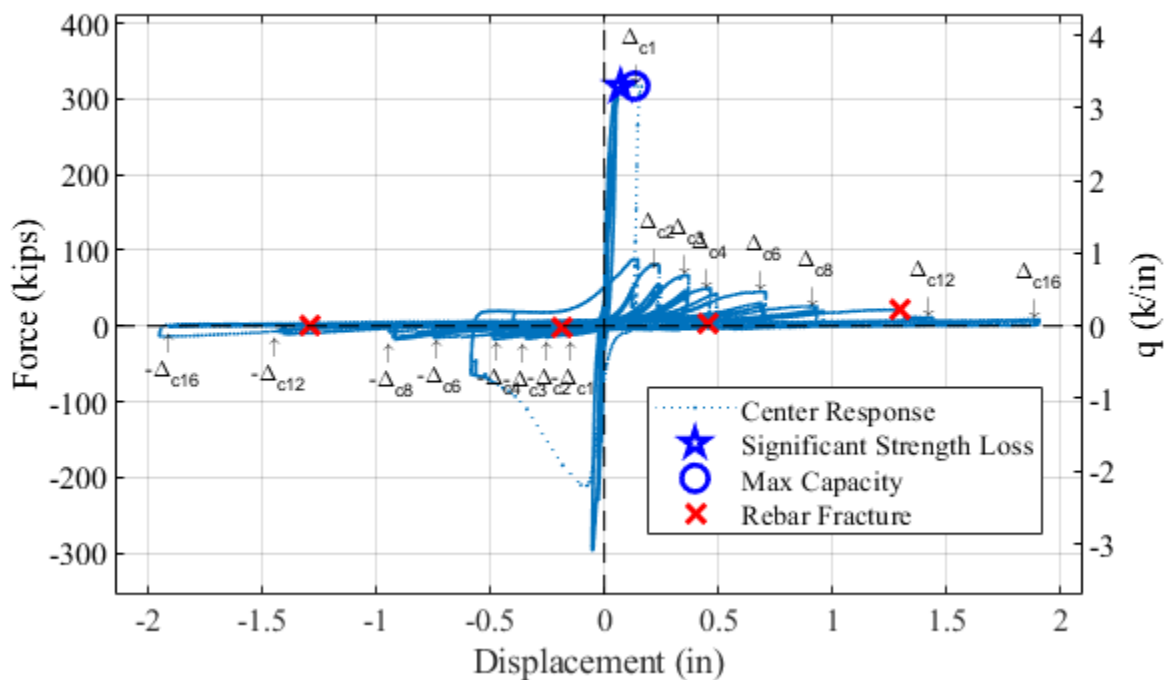


Figure 5.68: Test 4 Force-Displacement Response

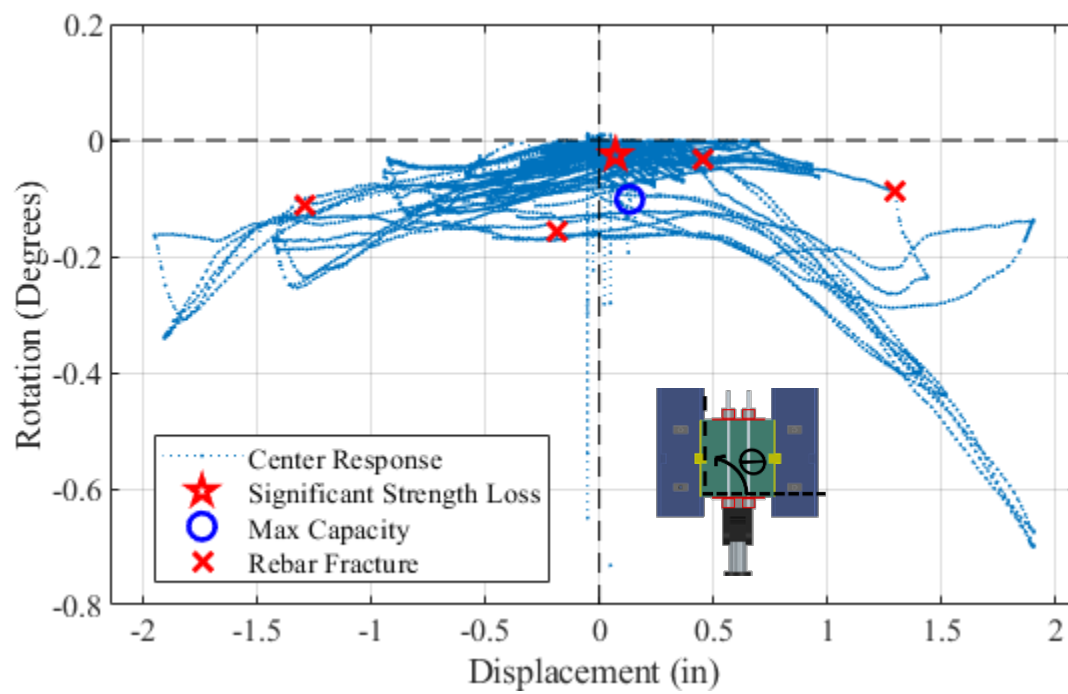


Figure 5.69: Test 4 Rigid Body Rotation

5.5.1 Test 4 Summary

Force was applied cyclically in single cycle sets, at increments of 78 kips ($q_{\text{average}} = 0.8\text{k/in}$). Only minor surface cracking was visible parallel to the boundaries of the joint and perpendicular to the joint during the first two increments of loading. The progression of the cracks can be seen in Figure 5.70 and Figure 5.71, where Figure 5.70 is prior to any loading and Figure 5.71 is the damage in the right joint under -153 kips of loading. The first visible cracks outside of the grout occurred in the third increment of loading (229 kips). Cracks started around the pockets and propagated towards the applied load with the exception of one minor crack propagating into the right side block. The associated displacement and rigid body rotation at this level of loading was 0.023 in. and -0.010° respectively. As the loading increased to 306 kips, more large cracks began to form diagonally in the specimen and the first visible cracks perpendicular to the grout pocket appeared as seen in Figure 5.72. The max positive and negative displacement of the center of the specimen at $q_{\text{average}} = 3.2\text{k/in}$ was 0.053 in. and -0.053 in. with an associated rigid body rotation of -0.008° and -0.005° respectively.

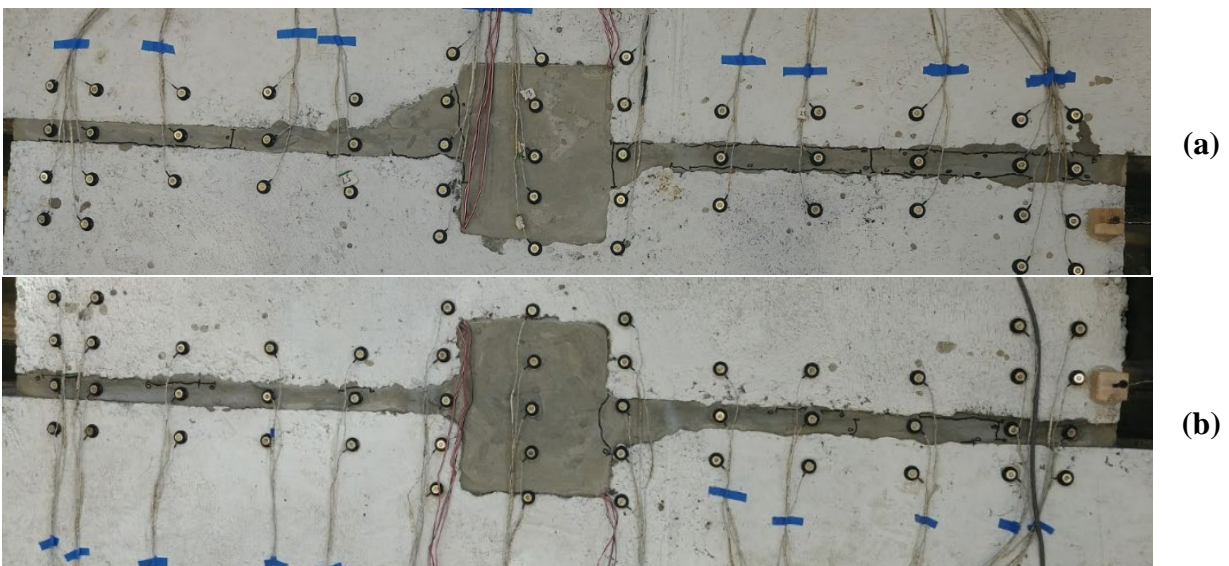
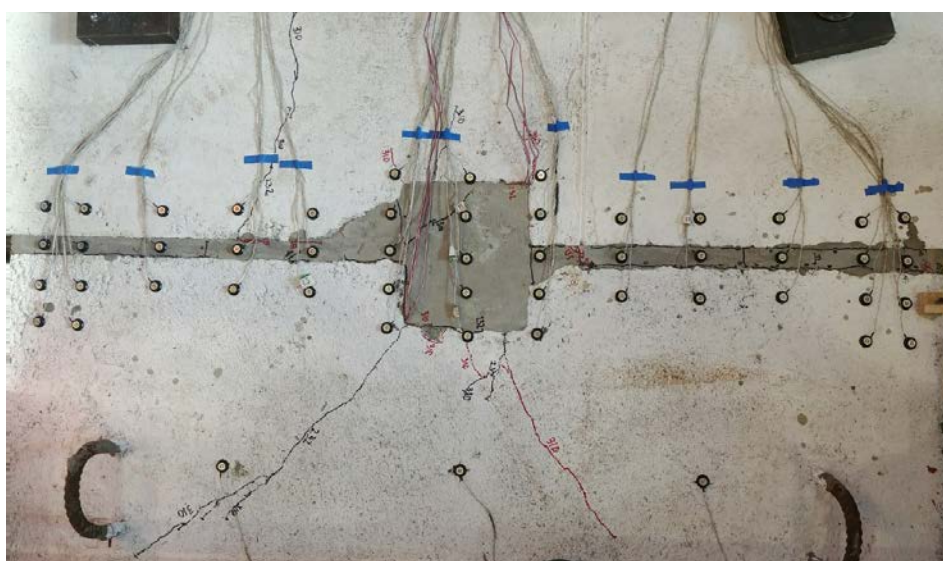


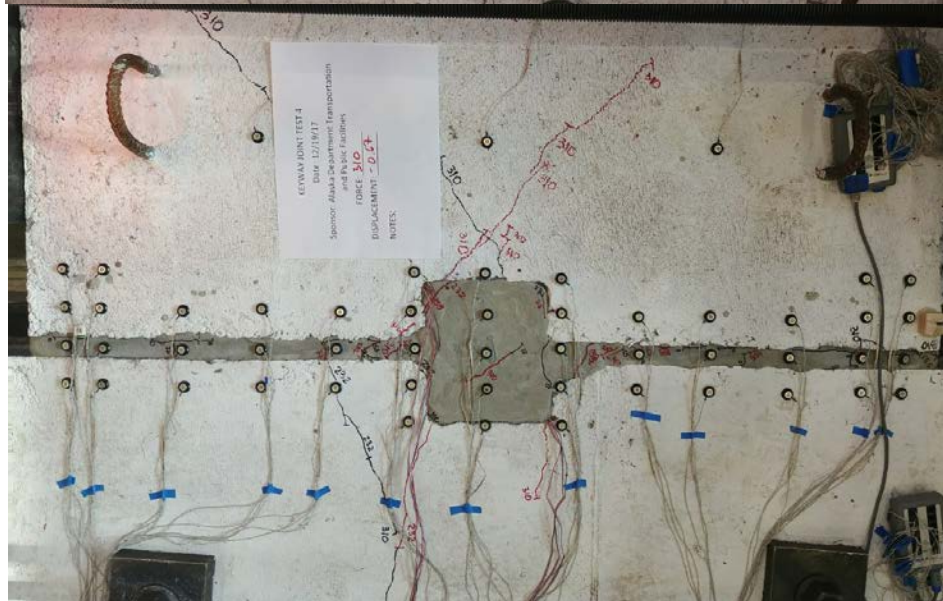
Figure 5.70: Test 4 Grouted Shear Key with Applied Load = 0 kips (a) Left Side (b) Right Side



Figure 5.71: Test 4 Right Side of Grouted Shear Key with Applied Load = -153 kips



(a)



(b)

Figure 5.72: Test 4 Grouted Shear Key with Applied Load = -306 kips (a) Left Side (b) Right Side

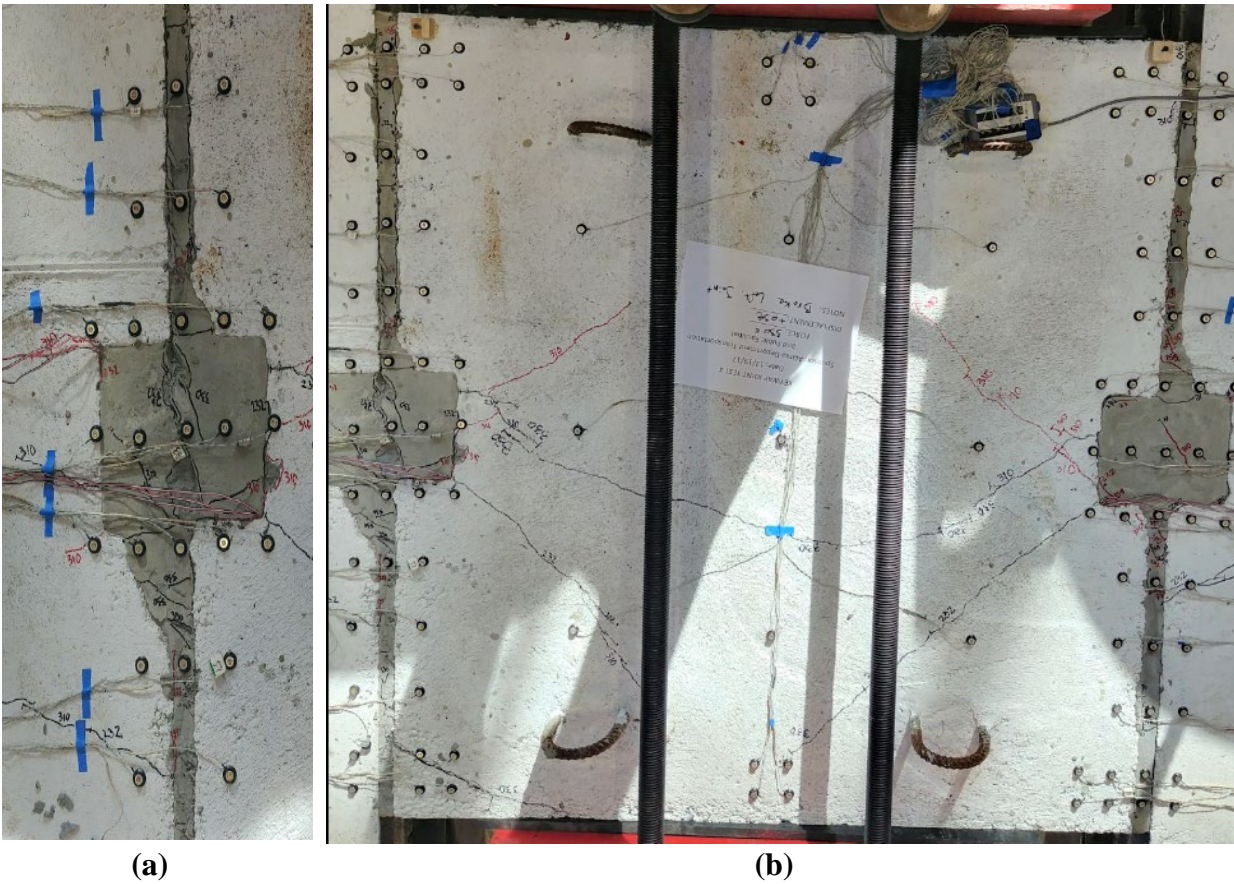


Figure 5.73: Test 4 Grouted Shear Key Δ_{c1} (a) Left Side (b) Overall View –First Cycle



Figure 5.74: Test 4 Left Side of Grouted Shear Key Cracking Δ_{c1} –First Cycle

Since loss of strength was not achieved in the last increment of loading, another 78 kip increment was applied, however, the specimen did not reach that level before the load rapidly degraded. The maximum load sustained was 317 kips (the maximum expected load based on Test 3 was 310 kips). At this point, the displacement of the center of the specimen was 0.134 inches with a rigid body rotation of -0.102° . As the displacement limit was reached, the forces on the specimen relaxed and the displacement reduced to 0.110 inches. This was thought to be the displacement of significant strength loss of the joint used to define the increments of displacement, Δ_{c1} . Significant observable damage occurred as seen in Figure 5.73 and Figure 5.74. The grout in the left joint cracked down the length of the joint. A large crack also formed at the vertex of the keyway faces at the specimen face in which load was being applied. The diagonal cracks propagating from the pockets increased in size, with one pair of cracks connecting from one pocket to another.

The actuator was then switched to displacement control. Using the previous actuator displacement of -0.65 in, which provided a specimen displacement of -0.053 in., an actuator displacement of -0.72 was estimated to reach a specimen displacement of -0.110 in ($-\Delta_{c1}$). But with the lower strength, less elastic shorting was present in the system and the first reversal at $-\Delta_{c1}$ led to a center of specimen displacement of -0.586 in. and rotation of -0.058° with a load of -64 kips. A local maximum load of -211 kips occurred at -0.074 in. with a rotation of -0.015° . Similar observable damage produced in the push direction was seen in the pull direction as seen in Figure 5.75. The right joint cracked down the length similar to the left joint resulting in formation of more diagonal cracks around the pocket and propagation towards the applied force. Existing diagonal cracks increased in size with one crack spanning across the entire specimen surface. On the left side, diagonal cracks formed near the face of the specimen in which the load was applied and continued into the side block. The grouted pocket on the left side was also damaged to the point in which a piece of the grout in the pocket along with the surrounding cover concrete could be removed.

Due to the unpredictability of using the actuator displacement, the rate of loading was reduced and the displacement of the center of the specimen was monitored manually to conclude the loading for each cycle. By the end of the third cycle of Δ_{c1} , only a few new diagonal cracks formed as seen in Figure 5.76. Cycles continued manually at scalars of Δ_{c1} . After the second push cycle at Δ_{c3} (0.357 in.) the cover concrete surrounding the left pocket was completely debonded and free to remove by hand. As subsequent cycles progressed, no significant observable damage occurred up until the first pull cycle of Δ_{c6} (-0.747 in.), which can be seen in Figure 5.77. On the left side, more debonded cover concrete was removed by hand. While on the right side cover concrete began to rise up near the pocket in the right side block. Both pockets had loose grout that was also removed by hand. It should be noted that grout within the shear key began to debond and pry up along the left joint. As the test continued, the first fracture occurred in the shear connector embedded in left pocket of the specimen during the first push cycle of Δ_{c12} at a displacement of 1.296 in and a force of 21 kips. The fracture was not observed until the second cycle and can be seen in Figure 5.78 (a). Additional cover concrete of the specimen spalled off on the left side allowing for a majority of the grout in the shear key to be removed as shown in Figure 5.79. During the second cycle of Δ_{c12} another fracture occurred in the shear connector embedded in the right side block pocket at a displacement of -0.187 in. and a force of -1 kip. The fracture can be seen in Figure 5.80 (b). By the completion of the third cycle of Δ_{c12} , the cover concrete on the right side block surrounding the pocket was removed and a majority of the grout was also removed from both pockets as seen in Figure 5.81. Additionally a third fracture was observed on the shear connector embedded in the right side block pocket at a displacement of 0.453 in and a force of 4 kips. The fracture left the specimen connected only through grout on the right side. The fractured bar can be seen in Figure 5.82 The final three cycle set, Δ_{c16} , was conducted. During the second cycle, a fourth rebar fractured at a displacement of -1.294 in. and force of -1 kip. The rebar was part of the shear connector in the left pocket, embedded into the specimen. This resulted in no connectivity between the side blocks and the specimen through the shear connectors. The response was now strictly grouted shear key. No significant cracking was observed past the last fracture. After three cycles at Δ_{c16} the specimen was brought back to zero displacement and terminated. The welds of the shear connectors can be examined in Figure 5.84.



Figure 5.77: Test 4 Grouted Shear Key Δ_{c3} –Second Cycle

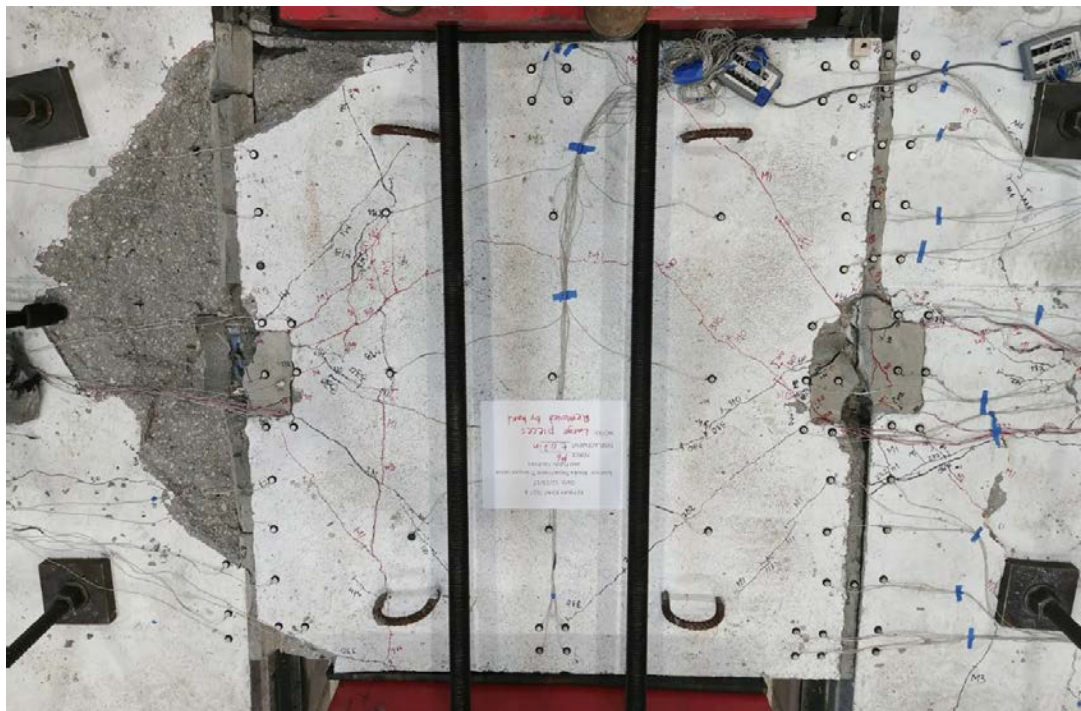


Figure 5.78: Test 4 Grouted Shear Key $-\Delta_{c6}$ –First Cycle



Figure 5.79: Test 4 Grouted Shear Key - Δ_{c12} –First Cycle



(a)



(b)

Figure 5.80: Test 4 Damage to Shear Connector Inserts at Δ_{c12} (a) Left Connector (b) Right Connector –Second Cycle



Figure 5.81: Test 4 Grouted Shear Key $-\Delta_{c12}$ –Third Cycle



Figure 5.82: Test 4 Damage to Right Side Shear Connector Insert at Δ_{c12} –Third Cycle



Figure 5.83: Test 4 Damage to Left Side Shear Connector Insert at Δ_{c16} –Second Cycle

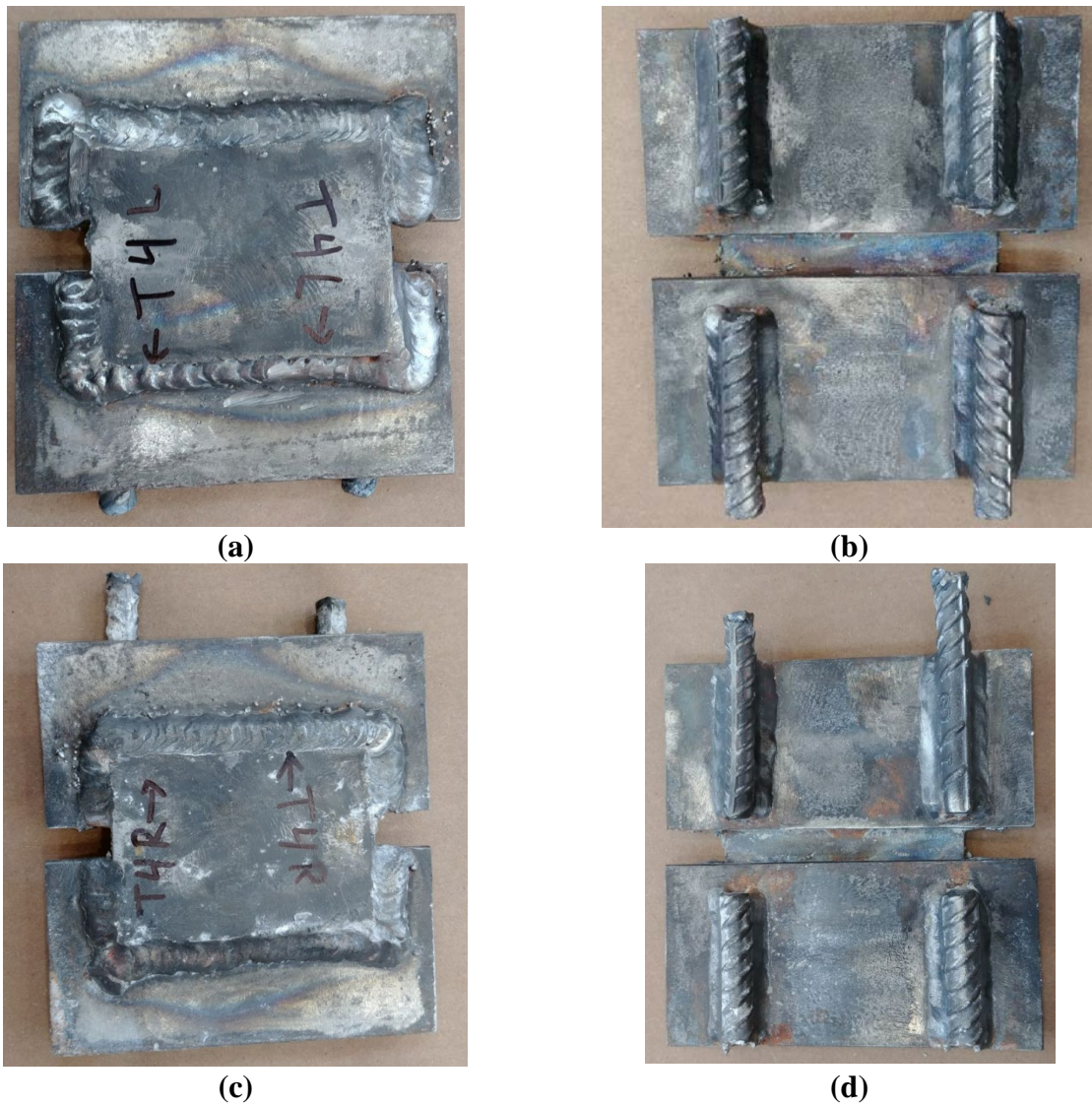


Figure 5.84: Test 4 Removed Shear Connector Plate (a) Top View Left Connector (b) Bottom View Left Connector (c) Top View Right Connector (d) Bottom View Right Connector

5.5.2 Test 4 Conclusion

Test 4 was a three-cycle cyclic test of the commonly used keyway joint for precast prestressed bulb-tee girders conducted at the CFL. Since Test 3 provided insight into the cyclic response of the joint prior to significant strength loss, the cyclic behavior of the joint after significant strength loss was investigated. As a consequence, for Test 4, loading up until maximum strength consisted of single cycle increments of force (25%, 50%, 75%, and 100% of expected maximum strength) were followed by three cycle sets at increments of the displacement at maximum force. Test 3 was used to inform the expected strength of joint, since they were poured from the same batch and had similar grout strengths on the day of testing. Loading stopped after two embedded rebar from each shear connector insert fractured leaving only shear resistance due to aggregate interlock. Similar damage to the cover concrete as seen in Test 2 and Test 3 was visible. One important thing to note is that the number of 'low shear flow cycles' did not reduce the maximum strength of the joint as Test 4 sustained a load just 3% higher than Test 3.

5.6 Test 5

Test 5 was performed at the CFL at NCSU starting on July 5, 2018, and ending on July 6, 2018. This section presents the overall response of the specimen and then discusses experimental procedures, results and observations in chronological order. The displacement history measured at the center of the specimen is displayed in Figure 5.85. Complementary to the displacement history, the specimen load history is presented in Figure 5.86. Additionally the complete unaltered load-displacement response and rigid body rotation versus displacement of the specimen measured at the center of the specimen can be seen in Figure 5.87 and Figure 5.88 respectively.

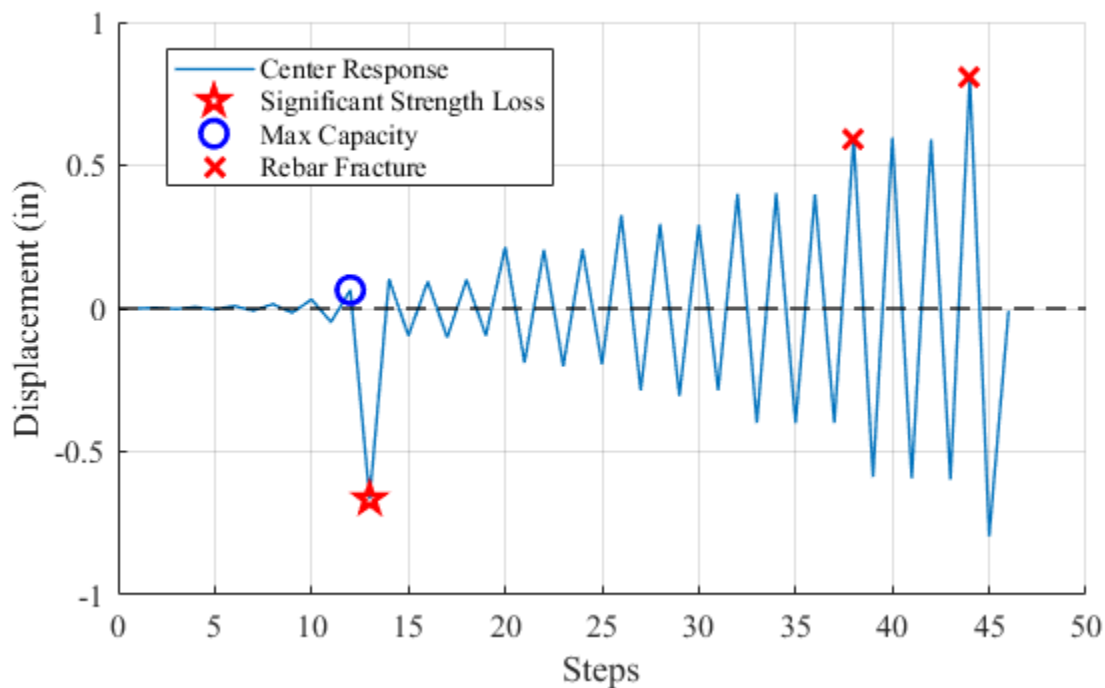


Figure 5.85: Test 5 Displacement History

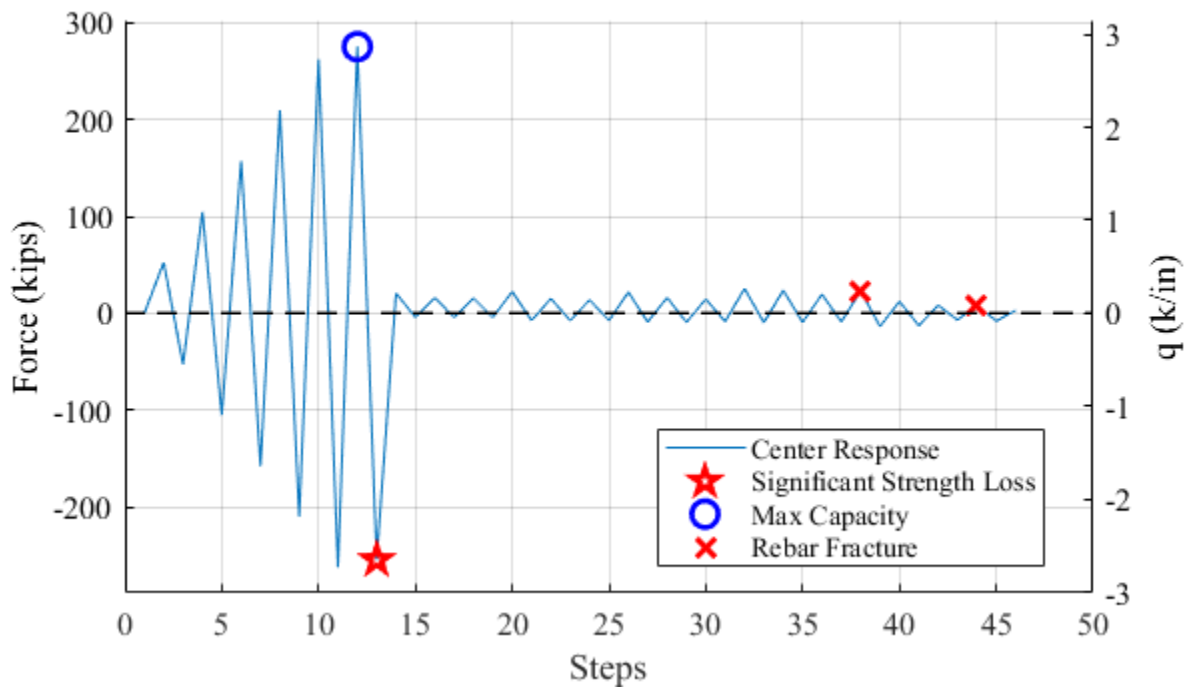


Figure 5.86: Test 5 Load History

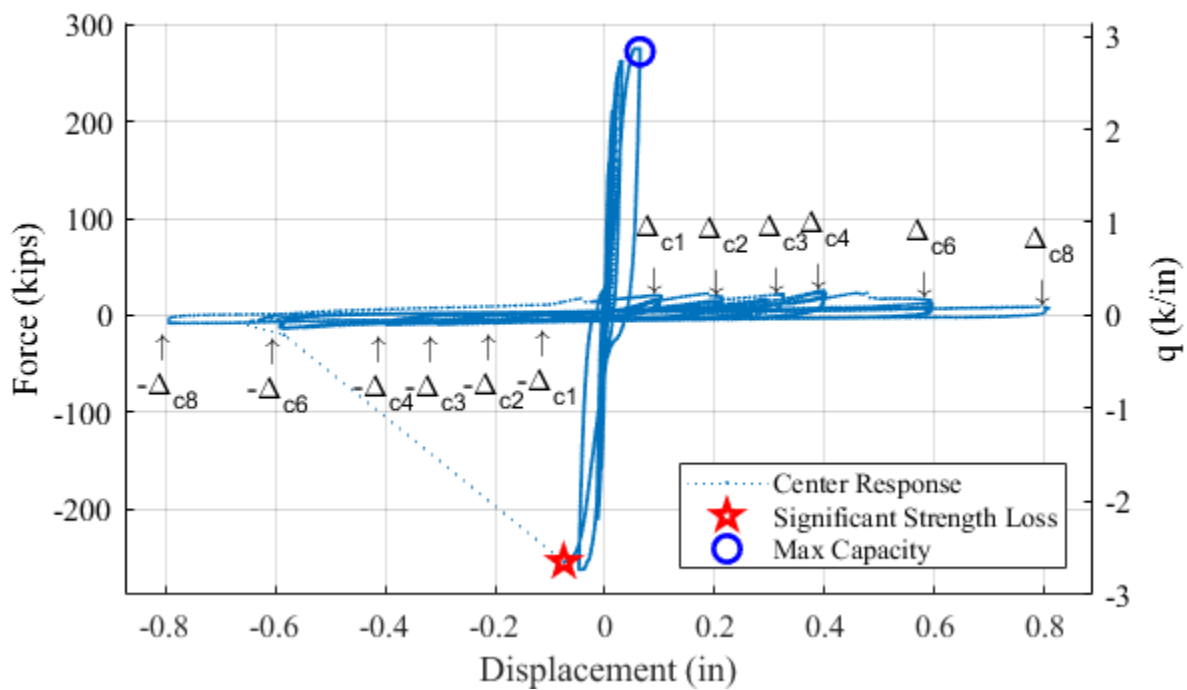


Figure 5.87: Test 5 Force-Displacement Response

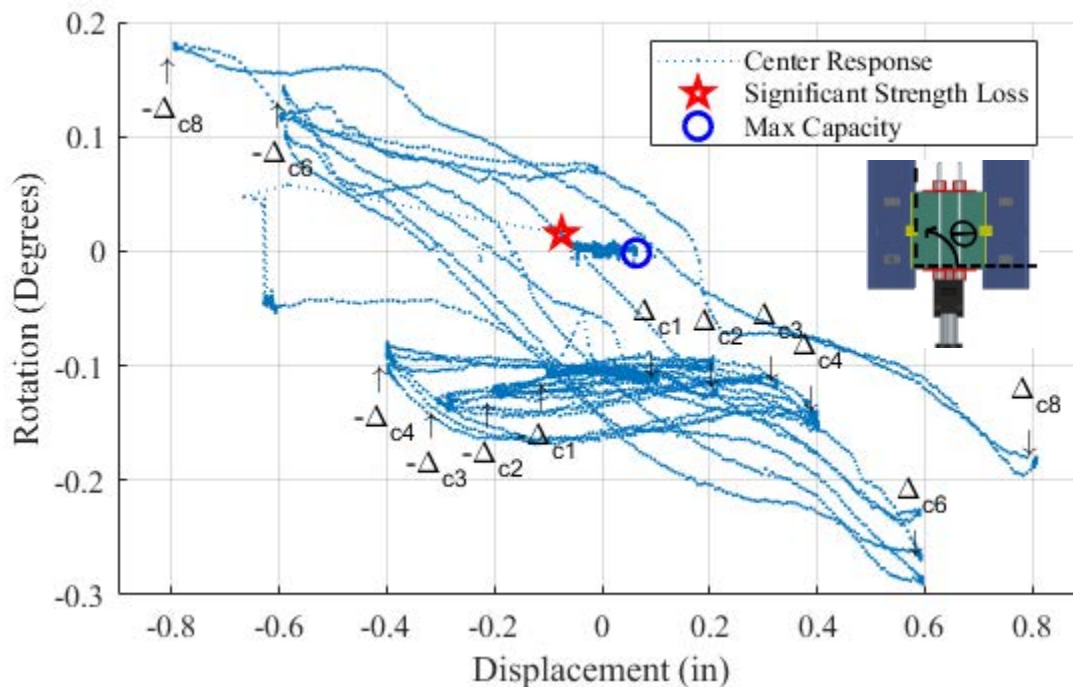


Figure 5.88: Test 5 Rigid Body Rotation

5.6.1 Test 5 Summary

Test 5 took place on July 05, 2018. Force was applied cyclically in single cycle sets, at increments of 53 kips ($q_{\text{average}} = 0.6\text{k/in}$). Surface cracks were highly prevalent prior to any load application due to the higher ratio of water to grout mixture and consequently more shrinkage as seen in Figure 5.89. Additionally, the top surface of the grouted joint was white with a chalky texture that could be scratched. As load was applied, minor surface cracking similar to the shrinkage cracks propagated through the joint up until the maximum anticipated strength of the connection, 213 kips ($q_{\text{average}} = 2.2\text{k/in}$), as evident in Figure 5.90 and Figure 5.91. The max positive and negative displacement of the center of the specimen at 213 kips was 0.015 inches and -0.015 inches with an associated rigid body rotation of 0.004° and -0.002° respectively. Since maximum strength of the specimen was not achieved, another increment of loading was applied resulting in the first visible crack outside of the grout at 266 kips ($q_{\text{average}} = 2.8\text{k/in}$). The crack formed in the specimen on the right side, near the pocket and propagated diagonally towards the applied load with an associated center of specimen displacement of 0.031 inches and rigid body rotation of -0.004° . Additionally surface cracks began to appear parallel to the boundaries of the joint at the grout and concrete interface. On the reversal, four similar diagonal

cracks formed in the specimen in the opposite direction and one crack perpendicular to the joint at the pocket formed in the right side block (Figure 5.92). This was accompanied by a center of specimen displacement of -0.048 inches and rigid body rotation of 0.005° .

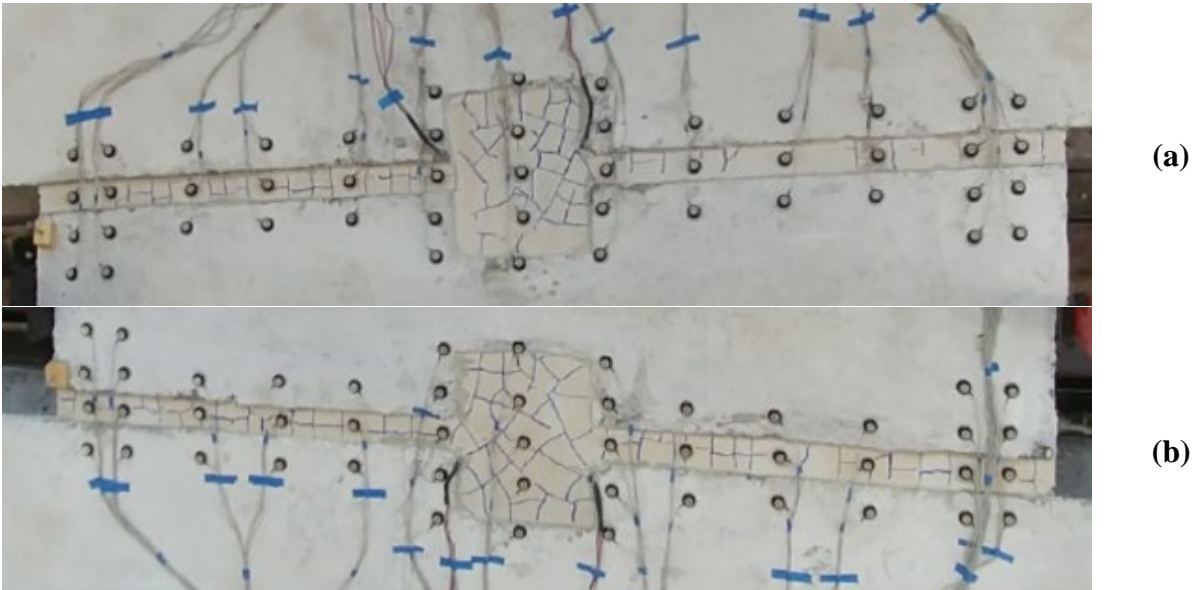


Figure 5.89: Test 5 Grouted Shear Key with Applied Load = 0 kips (a) Left Side (b) Right Side

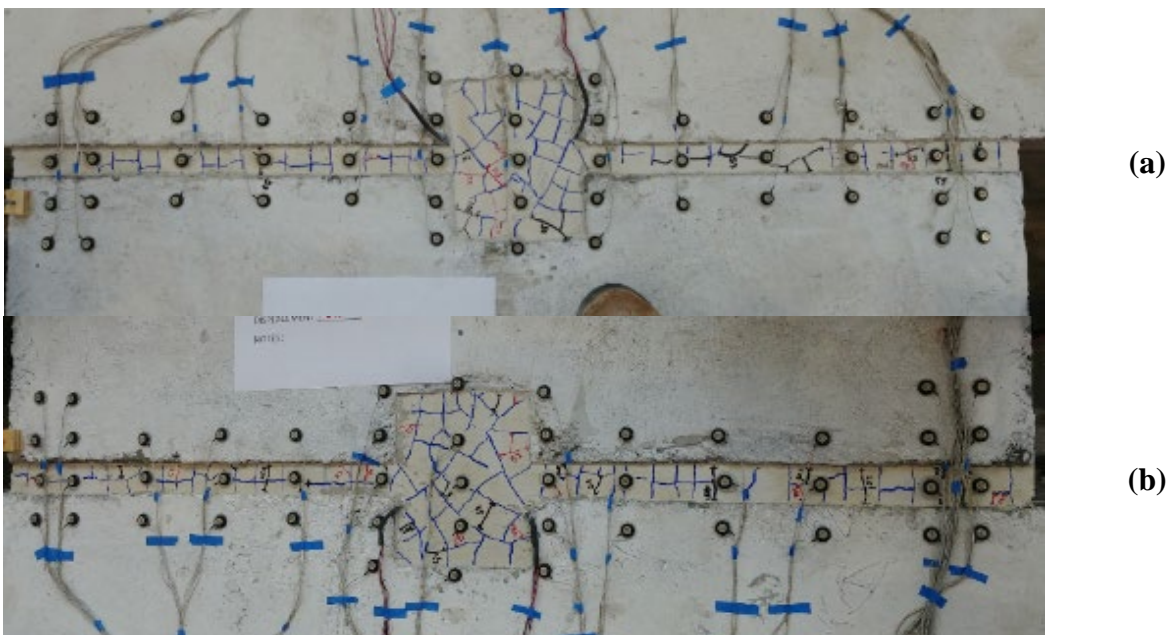


Figure 5.90: Test 5 Grouted Shear Key with Applied Load = 106 kips (a) Left Side (b) Right Side



Figure 5.91: Test 5 Grouted Shear Key with Applied Load = -213 kips

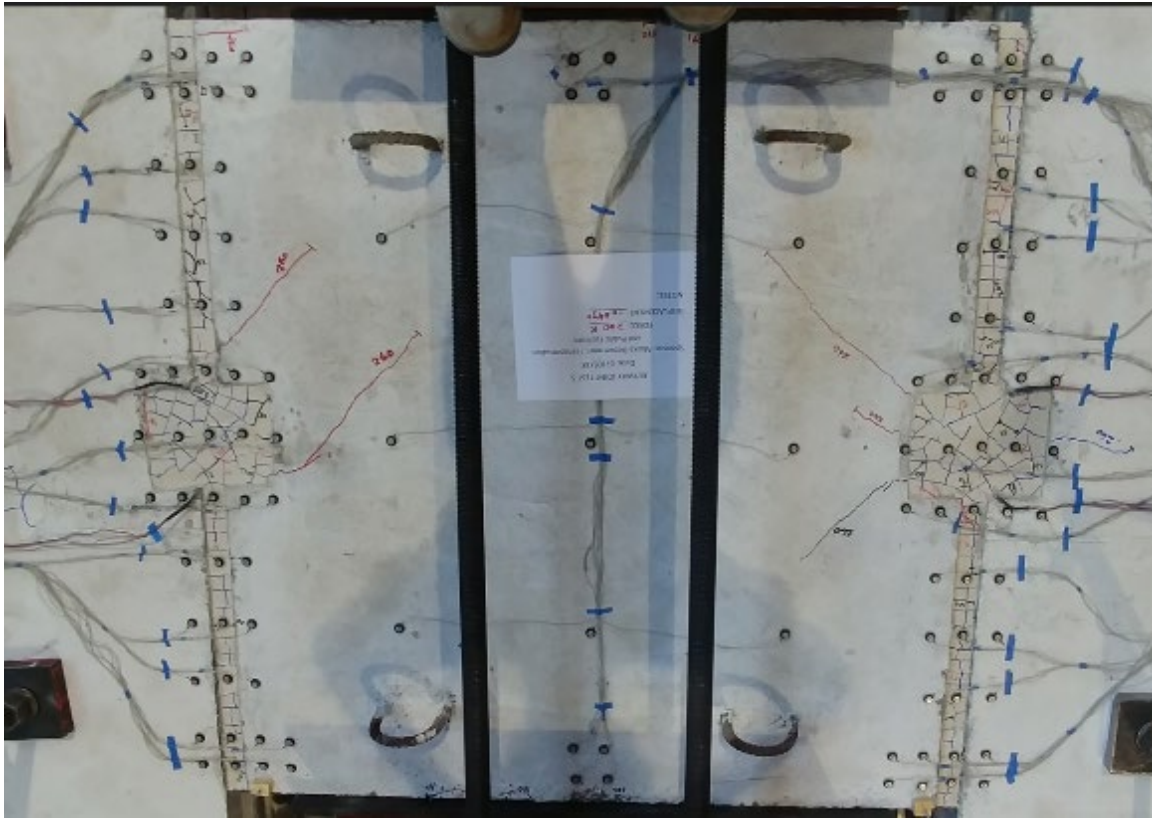


Figure 5.92: Test 5 Grouted Shear Key with Applied Load = -266 kips

In an attempt to minimize the actuator displacement limit increase and therefore additional damage at failure, the increment of loading was reduced to 13 kips, a quarter of the original increment. The specimen was then loaded to 280 kips with a center of the specimen displacement of 0.064 inches and negligible rigid body rotation. While existing cracks lengthened, three new diagonal cracks formed in the specimen and three new diagonal cracks formed in the side blocks (Figure 5.93). The load was reversed to -280 kips, however, the specimen only reached 256 kips at a displacement of -0.075 in and rigid body rotation of 0.015 before the load rapidly degraded. As the joints ability to resist the load decreased, the actuator was able to retract to its full limit of -0.62 inches bringing the specimen along with it (for reference, -266 kips, resulted in an actuator displacement of -0.52 inches). The 0.62 in. limit was needed in order to achieve the force in the pull direction while accounting for the experimental takeup that is concentrated in the threaded rods. There is substantially less takeup in the push direction, and future tests aimed to fracture the specimen first in the push direction.

At this point in the test, the displacement of the center of the specimen was 0.665 inches with a rigid body rotation of 0.047° with significant damage to the longitudinal joint as seen in Figure 5.94. Damage was focused in the side blocks. Cracks formed in both side blocks along the vertex of the keyway faces leading to the removal of large pieces of cover concrete. Removing the unbonded cover concrete by hand revealed the shear connector plates and embedded rebar depicted in Figure 5.95.



Figure 5.93: Test 5 Grouted Shear Key with Applied Load = 280 kips



Figure 5.94: Test 5 Grouted Shear Key – Significant Strength loss



Figure 5.95: Test 5 Grouted Shear Key – Significant Strength Loss (a) Left Side (b) Right Side

The actuator was then switched to displacement control. The displacement at significant strength loss was estimated at 0.100 inches, which was used to define the displacement of significant strength loss of the joint, Δ_{c1} . Demand was applied in three cycle sets at increments proportional to Δ_{c1} . Due to the unpredictability of using the actuator displacement, the rate of loading was reduced and the displacement of the center of the specimen was monitored manually to conclude the loading for each cycle. Little damage was accumulated through cycles Δ_{c1} to Δ_{c4} . The deformation and therefore the associated damage occur only at the exposed embedded rebar. As the rebar deformed only minor spalling of concrete surrounding the rebar occurred. Figure 5.96 and Figure 5.97 show the accumulated damage from Δ_{c1} to Δ_{c4} . During the first push cycle of Δ_{c6} (0.594 in.), bar fracture was observed in the right shear connector insert shown in Figure 5.98. Successively, the first Δ_{c6} pull cycle (-0.588 in.) led to damage to the right and left embedded shear connectors. Instead of bar fracture, the embedded rebar appeared to be failing at the weld as seen in Figure 5.99 and Figure 5.100 for the right and left side respectively. No significant observable damage occurred for the remainder of the Δ_{c6} cycles. Upon the first push cycle of Δ_{c8} instead of weld failure, the remainder of the exposed rebar fractured leaving no connectivity between the side blocks and the specimen through the shear connectors. The fractured rebar can be seen in Figure 5.101. With only the grout providing the response, no notable additional damage occurred with little residual strength (+/- 8kips). Only the first full cycle was completed before the test was concluded and the specimen was returned to zero displacement.



Figure 5.96: Test 5 Grouted Shear Key - Δ_{c1} –Third Cycle



Figure 5.97: Test 5 Grouted Shear Key - Δ_{c4} –Third Cycle



Figure 5.98: Test 5 Damage to Right Side Shear Connector Insert at Δ_{c6} –First Cycle

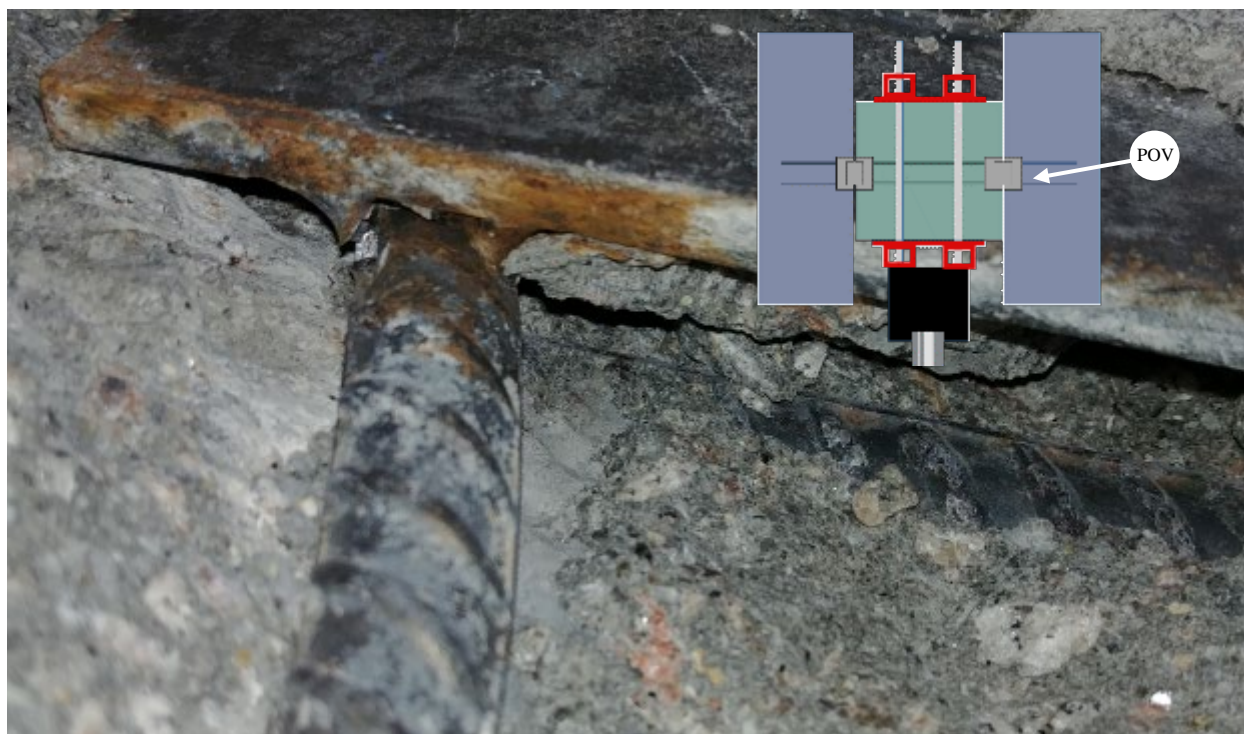


Figure 5.99: Test 5 Damage to Right Side Shear Connector Insert at $-\Delta_{c6}$ – Frist Cycle



Figure 5.100: Test 5 Damage to Left Side Shear Connector Insert at $-\Delta_{c6}$ – First Cycle



(a)



(b)



(c)



(d)

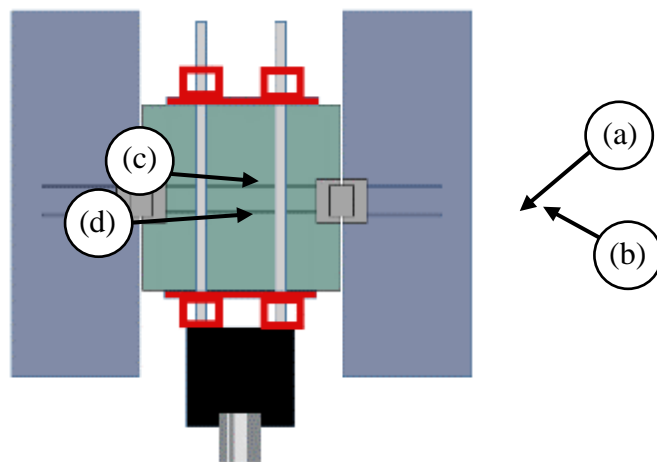


Figure 5.101: Test 5 Damage to Shear Connector Insert at Δ_8 –First Cycle

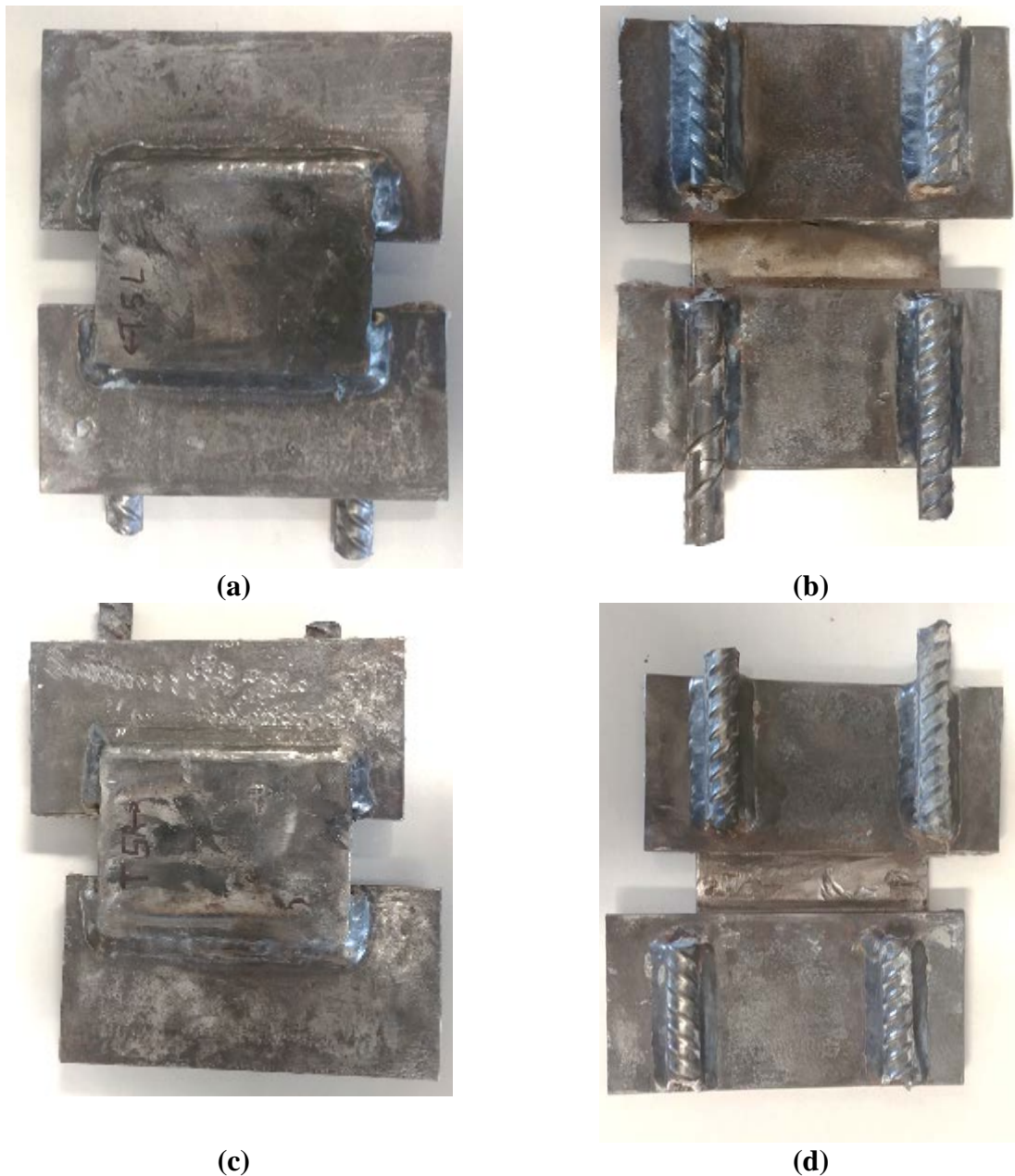


Figure 5.102: Test 5 Removed Shear Connector Plate (a) Top View Left Connector (b) Bottom View Left Connector (c) Top View Right Connector (d) Bottom View Right Connector

The specimen was then removed with no additional induced damage. The shear connector plates were removed from the specimen to reveal the welds as seen in Figure 5.102. All of the welds were undamaged except for minor damage near the ruptured rebar. Upon removing the plates, sections of grouted shear key were also exposed. As seen in Figure 5.103,

there was clear segregation in the grout inside the joint. There was about an inch to an inch and a half of color variation on top of the surface, which was true for both sides of the joint.

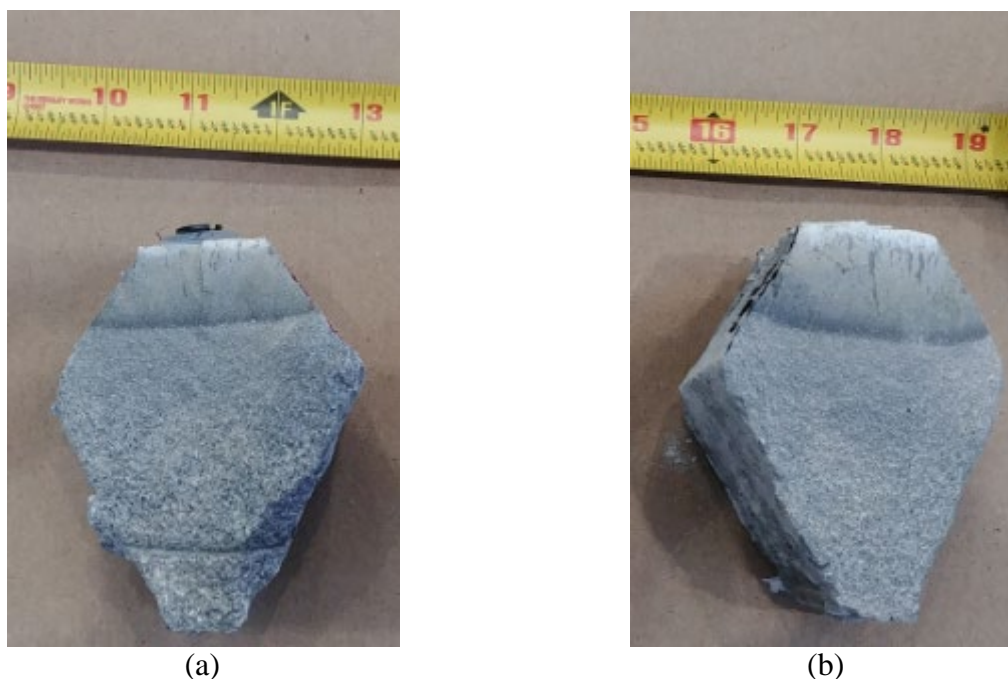


Figure 5.103: Test 5 Removed Grouted Shear Key (a) Left Side (b) Right Side

5.6.2 Test 5 Conclusion

Test 5 examined the shear slip response of a lower bound compressive strength grout. The objective of the experiment was to determine the consequences of accepting a grout compressive strength below the Alaska DOT minimum requirement of 9,000 psi at 28 days. Thus a compressive strength of 6,000 psi was targeted using 9 pounds of water per 50 pounds of bagged mix and testing after 10 days. A 7,160 psi strength was achieved. The first notable consequence was segregation between the aggregate and the water while pouring the grout into the joint. This was later confirmed after the experiment upon examining grout extracted from the shear key (Figure 5.103). The segregation led to significant cracking and low strength at the surface. Despite segregation, the joint's strength was higher than expected. With an assumed strength of 213 kips, the joint reached a maximum strength of 275 kips, 1.29% of the anticipated capacity.

The response of the joint was similar to the previous tests. Due to the large displacement at rapid strength loss coupled with significant damage to the cover concrete, little residual strength remained. Upon removing the spalled cover concrete and grout, the entire shear key in both joints were exposed. It is important to note that the damage was concentrated only in the side blocks. The damage only exposed the embedded shear plate rebar in the side blocks, consequently insuring that the weak link and concentration of deformation occurred only in these exposed rebar. When compared with Test 4, the displacement at which the first rebar fractured was about half of what was seen previously, $\Delta c6$ in Test 5 and $\Delta c12$ in Test 4. Additionally the displacement in which all rebar fractured was also doubled, $\Delta c8$ in Test 5 and $\Delta c16$ in Test 4. This could be attributed to only one side of the embedded shear connector plate contributing to the damage and consequently the displacement as opposed to both sides in Test 4.

5.7 Test 6

Test 6 was performed at the CFL at NCSU on August 27, 2018. This section presents the overall response of the specimen and then discusses experimental procedures, results and observations in chronological order. The displacement history measured at the center of the specimen is displayed in Figure 5.104. Complementary to the displacement history, the specimen load history is presented in Figure 5.105. Additionally the complete unaltered load-displacement response and rigid body rotation versus displacement of the specimen measured at the center of the specimen can be seen in Figure 5.106 and Figure 5.107 respectively.

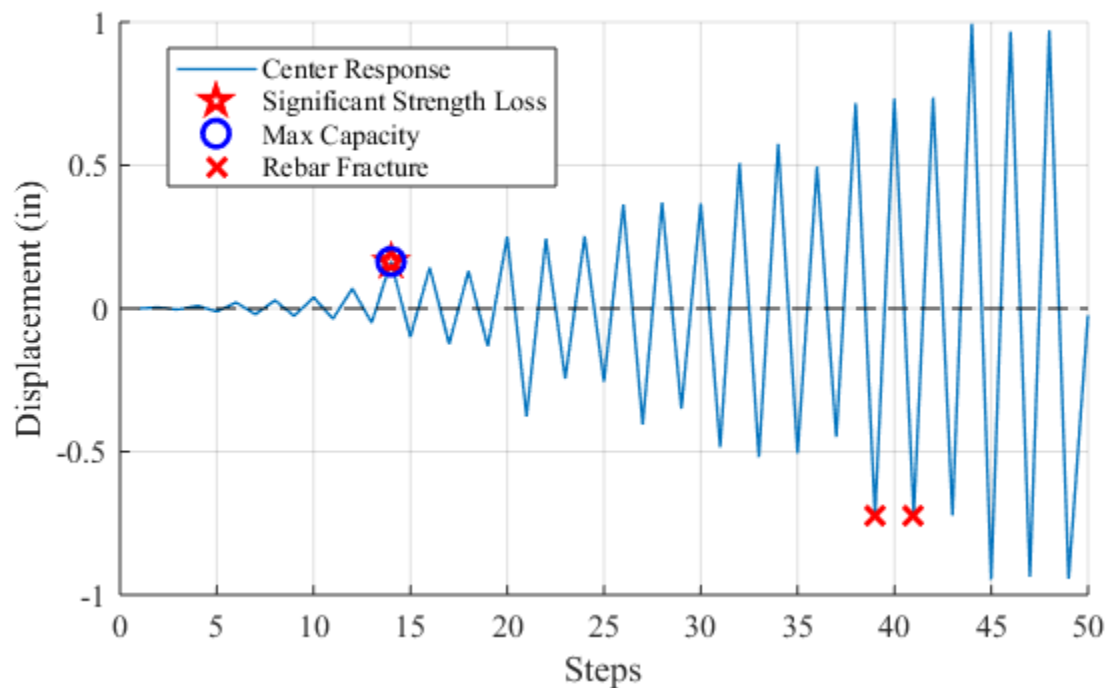


Figure 5.104: Test 6 Displacement History

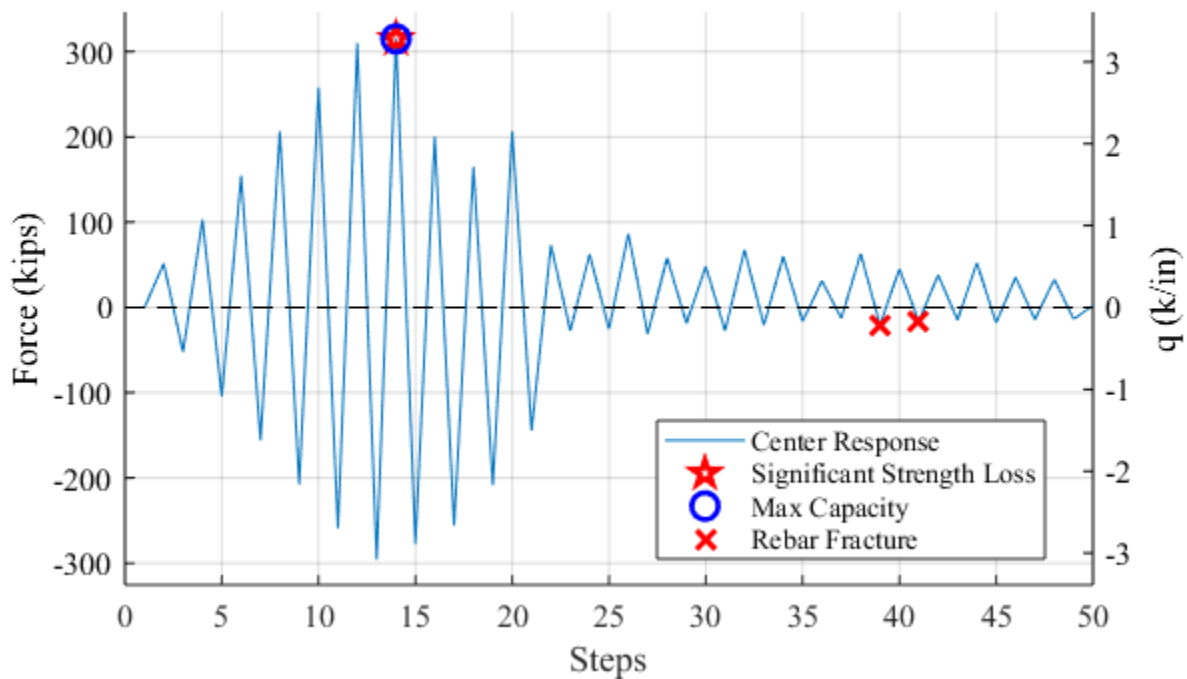


Figure 5.105: Test 6 Load History

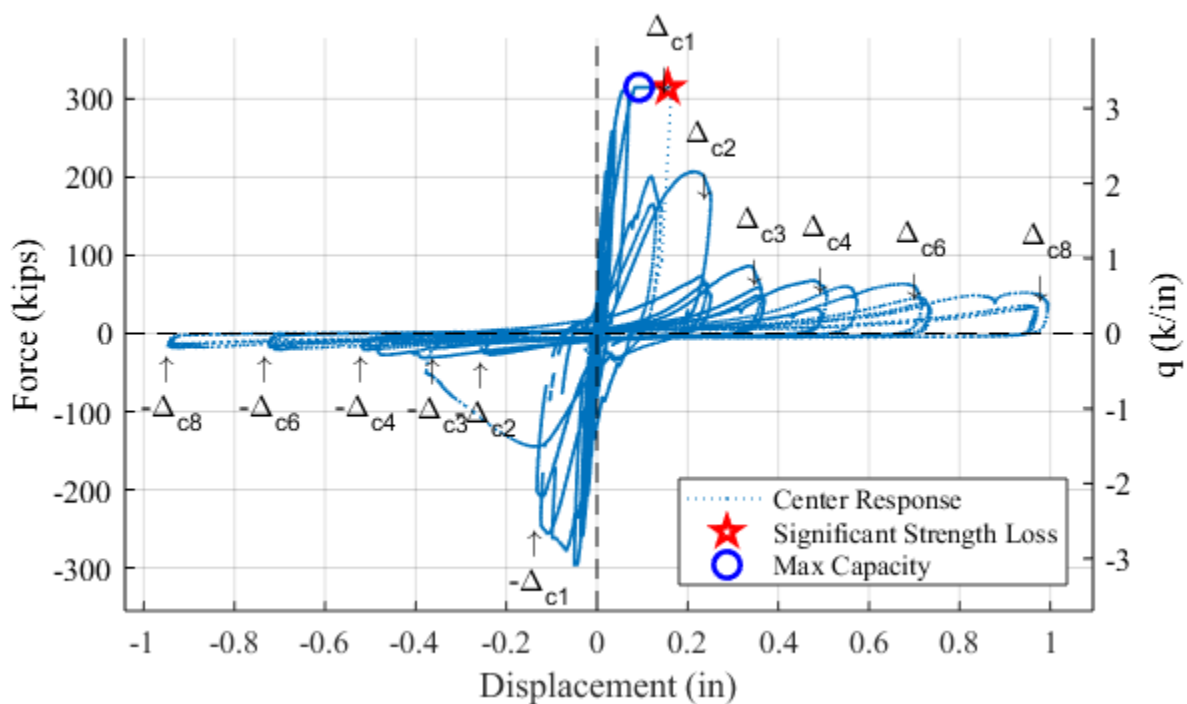


Figure 5.106: Test 6 Test 6 Force-Displacement Response

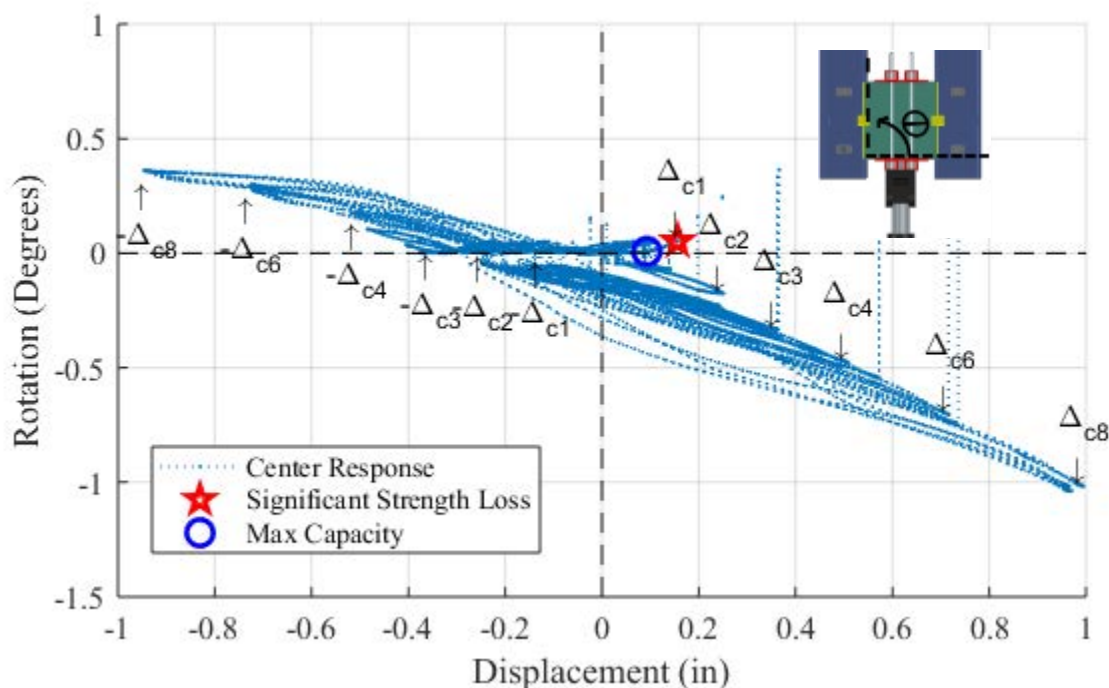


Figure 5.107: Test 6 Rigid Body Rotation

5.7.1 Test 6 Summary

Force was applied cyclically in single cycle sets, at increments of 52.5 kips ($q_{\text{average}} = 0.5 \text{ k/in}$). Prior to loading, only one preexisting crack was visible that was not associated with the patched sections of the side blocks. The crack was located on right side block and ran perpendicular to the joint (Figure 5.108). As load was applied, no visible damage occurred during the first four increments of loading, although it was noticed that the specimen displacement increased as force was being held as early as 105 kips. At the anticipated capacity of the joint, 210 kips, the max positive and negative displacement at the center of the specimen was 0.028 inches and -0.026 inches with an associated rigid body rotation of 0.000° and -0.003° respectively. Force increments continued to increase at 52.5 kips. Upon the next load increment, an associated force of 263 kips ($q_{\text{average}} = 2.7 \text{ k/in}$), the first visible crack appeared in the specimen running diagonal from the shear pocket to the joint as seen in Figure 5.109. The max positive and negative displacement of the center of the specimen was 0.039 inches and -0.036 inches with an associated rigid body rotation of 0.000° and -0.003° respectively. The load was then increased to 315 kips ($q_{\text{average}} = 3.3 \text{ k/in}$) in the push direction and -300 kips ($q_{\text{average}} = 3.1 \text{ k/in}$) in the pull direction due to the actuator capacity in tension. The loading resulted in formation of diagonal

cracking which propagated toward the applied load in both directions. Cracks formed in both the specimen and the side blocks as seen in Figure 5.110. The max positive and negative displacement of the center of the specimen was 0.062 inches and -0.047 inches with an associated rigid body rotation of -0.001° and -0.003° respectively. The push load was then increased to 320 kips ($q_{\text{average}} = 3.3\text{k/in}$). The specimen reached a center specimen displacement of 0.093 inches with a rigid body rotation of 0.008° . Upon holding the load, the specimen drifted to 0.156 inches with a rigid body rotation of 0.056° before the sustained load began to drop. Damage was evident with significant diagonal cracking appearing in the specimen and the left side block. Additionally longitudinal cracks appeared on the joint interface between the concrete and the PPC parallel to the joint. Damage can be seen in Figure 5.111. The actuator was then switched to displacement control. The displacement at significant strength loss was estimated at 0.120 inches, which was used to define the displacement of significant strength loss of the joint, Δ_{c1} . Demand was applied in three cycle sets at increments proportional to Δ_{c1} . Due to the unpredictability of using the actuator displacement, the rate of loading was reduced and the displacement of the center of the specimen was monitored manually to conclude the loading for each cycle.

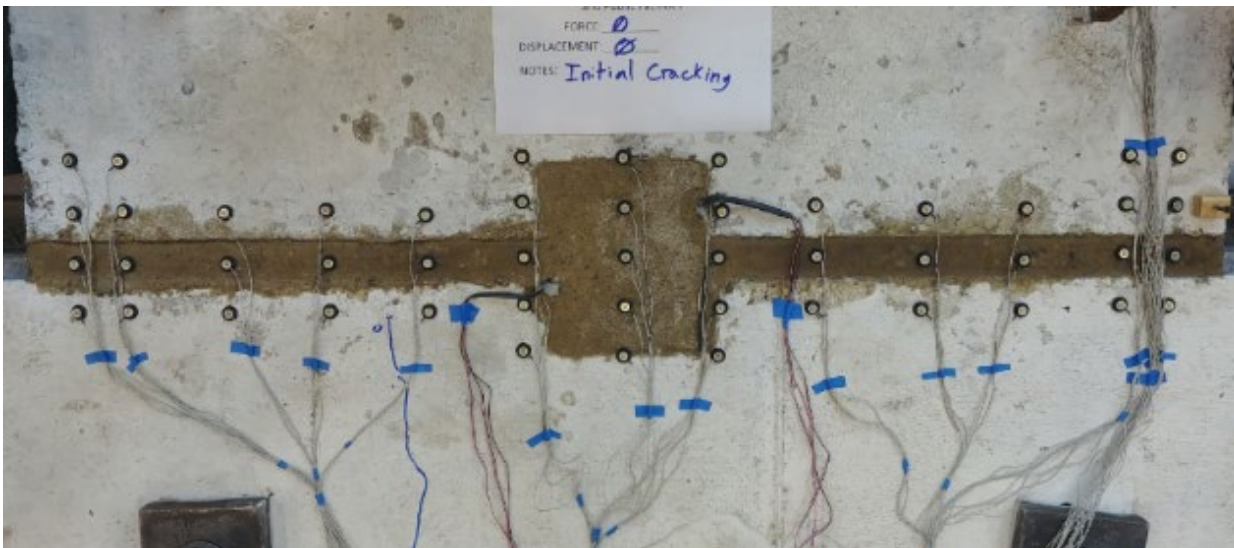


Figure 5.108: Test 6 Right Side Grouted Shear Key with Applied Load = 0 kips



Figure 5.109: Test 6 Right Side Grouted Shear Key with Applied Load = 260 kips



Figure 5.110: Test 6 Grouted Shear Key with Applied Load = -300 kips



Figure 5.111: Test 6 Grouted Shear Key with Applied Load = 320 kips

On the reversal, the specimen was taken to a displacement of -0.099 inches, $-\Delta_{c1}$, with a force of 260 kips and a rigid body rotation 0.023° . More diagonal cracks began to propagate in the specimen and side blocks in the opposite direction. By the end of the third cycle of Δ_{c1} the force dropped to 165 kips and -208 kips with a rigid body rotation of -0.080° and 0.012° for the push and pull directions respectively. Damage from Δ_{c1} is visible in Figure 5.112. Cracks formed diagonally across the left longitudinal joint, while one crack formed in the pocket of the right longitudinal joint. Additionally, old diagonal cracks lengthened and new diagonal cracks formed inside both the specimen and the side blocks. A longitudinal crack also appeared in the right longitudinal joint opposite of the existing longitudinal crack.

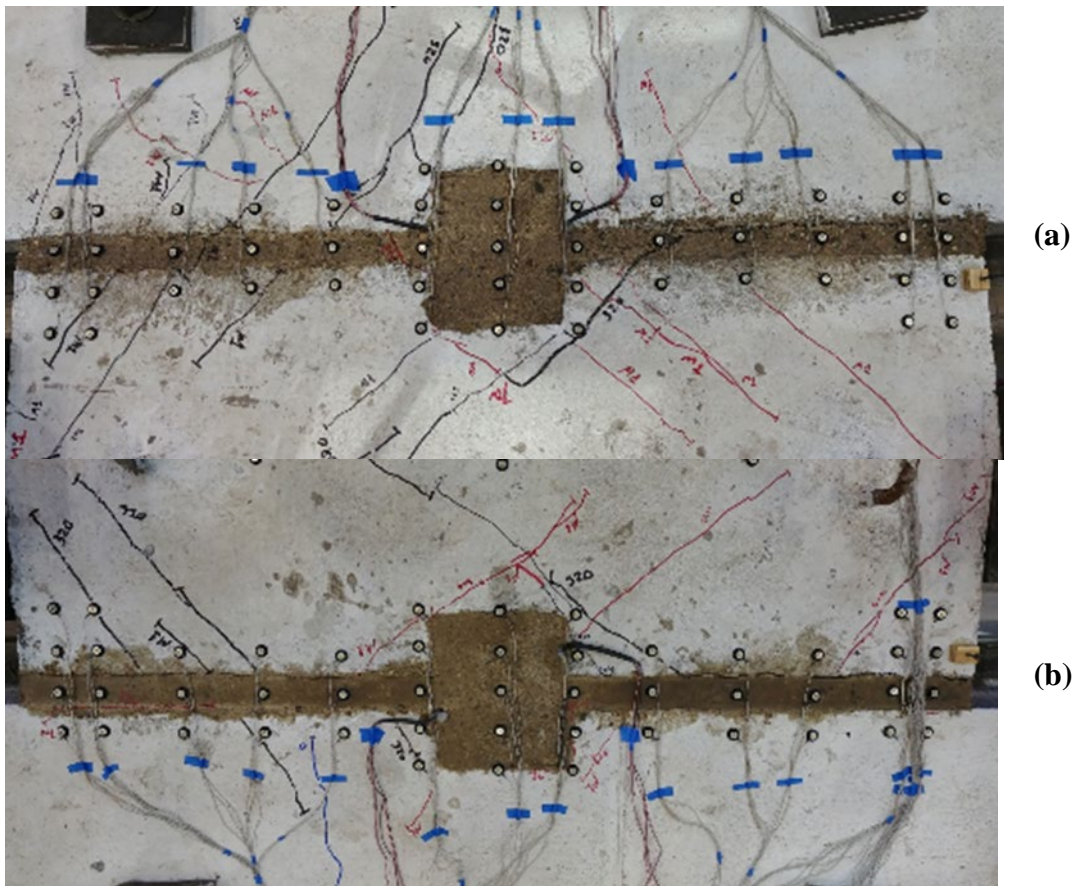


Figure 5.112: Test 6 Grouted Shear Key $-\Delta_{c1}$ -Third Cycle (a) Left Side (b) Right Side

During the first push cycle of Δ_{c2} (0.251 inches), little damage accumulation occurred with a load of 206 kips and rigid body rotation of -0.170° . On the first Δ_{c2} pull cycle, the load reached peak at -145 kips before ending at -50 kips with 0.001° of rotation. During this cycle, large diagonal cracks formed in both side blocks and the specimen. Additional cracks associated with spalling cover concrete formed on the left side block and a diagonal longitudinal crack formed through the right grouted pocket connecting existing longitudinal cracks in the right joint. Damage is visible in Figure 5.113. At the end of Δ_{c2} spalling cover concrete around the left joint was removed by hand as seen in Figure 5.114.

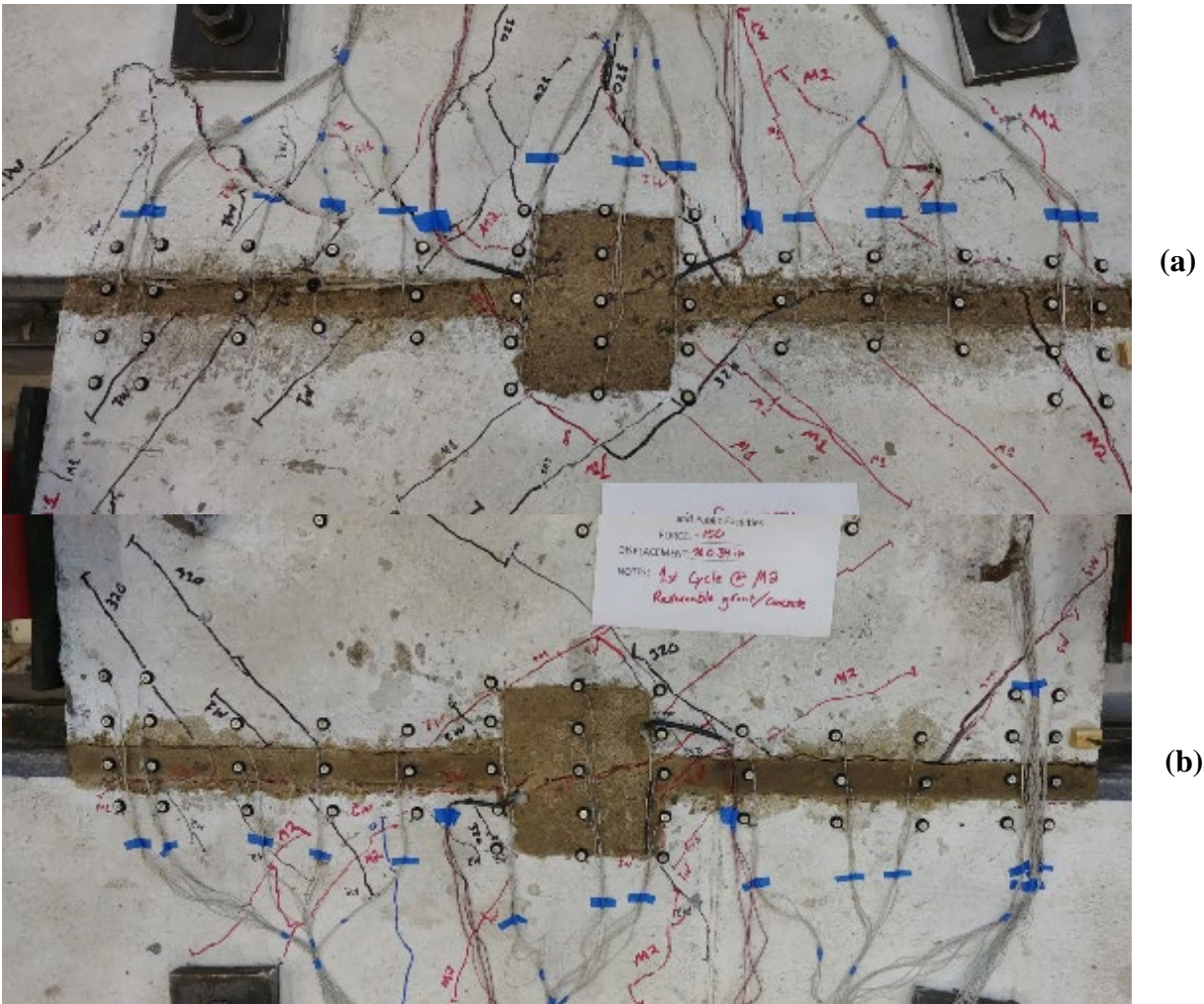


Figure 5.113: Grouted Shear Key - Δ_{c2} - First Cycle (a) Left Side (b) Right Side

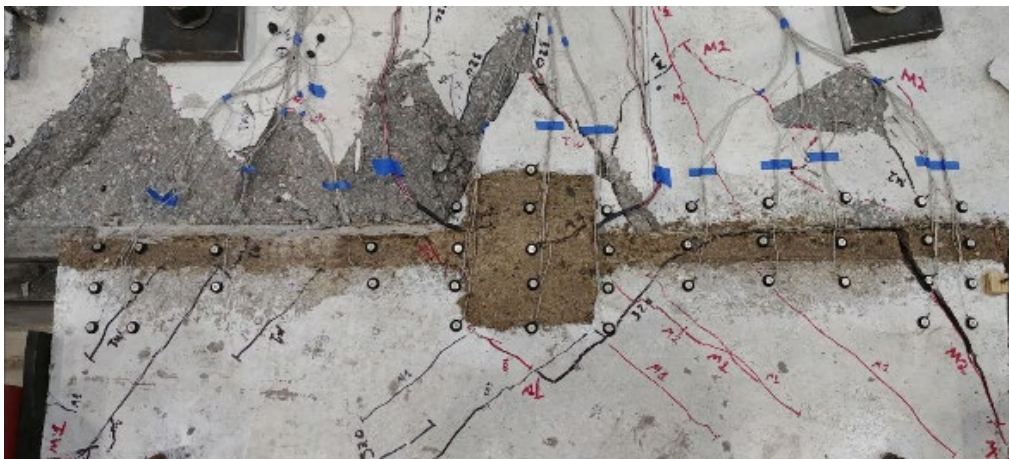


Figure 5.114: Left Side of Grouted Shear Key - Δ_{c2} - Third Cycle



Figure 5.115: Grouted Shear Key - Δ_{c3} –Third Cycle

Spalling of the left side block continued into the Δ_{c3} (Figure 5.115). The capacity of the joint began to reduce with more capacity in the push direction as opposed to the pull direction. At the end of the third cycle, the force was 48 kips and -27 kips with an associated rigid body rotation of -0.356° and 0.100° . Little damage was accumulated in the Δ_{c4} cycles, though the larger displacements exposed the left joint shear connector. No damage to the embedded rebar was observed. The first embedded rebar to fracture occurred during the first pull cycle of Δ_{c6} cycle. The second rebar fracture occurred during the second pull cycle. Both fractured rebar were embedded into the left side block leaving the specimen attached only through the grout. The damage can be seen in Figure 5.116. It should be noted that the longitudinal gap in the right joint was observed rotating as the longitudinal gap closed and opened in the push and pull cycles respectively (Figure 5.117).

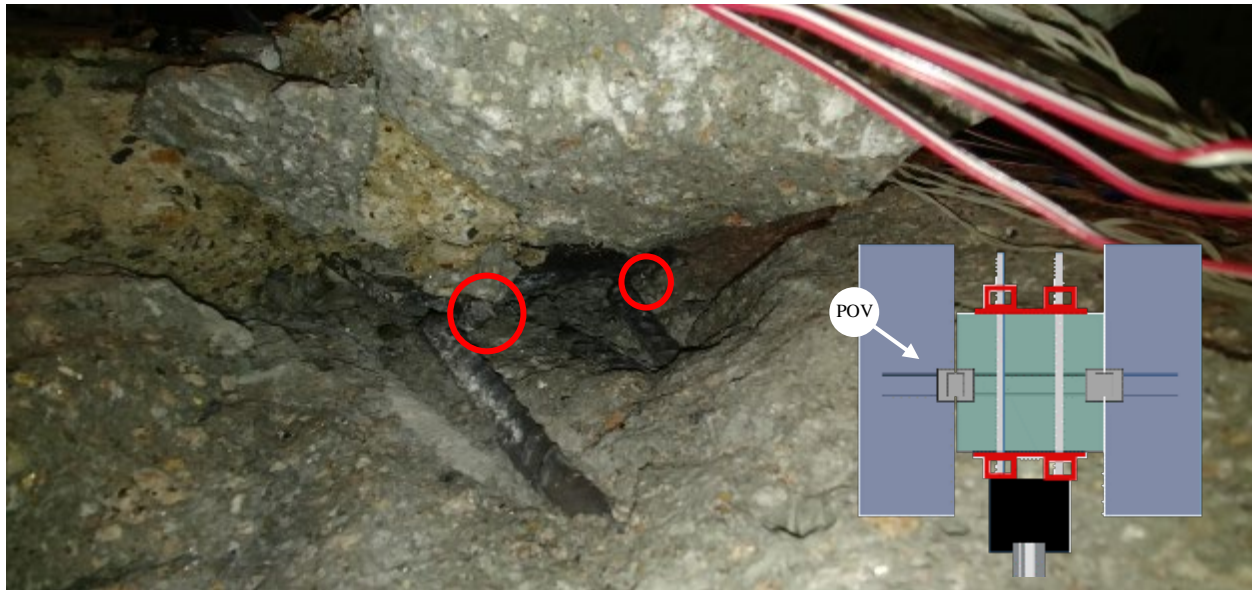


Figure 5.116: Damage to Left Side Shear Connector Insert at $-\Delta_{c6}$ – Second Cycle

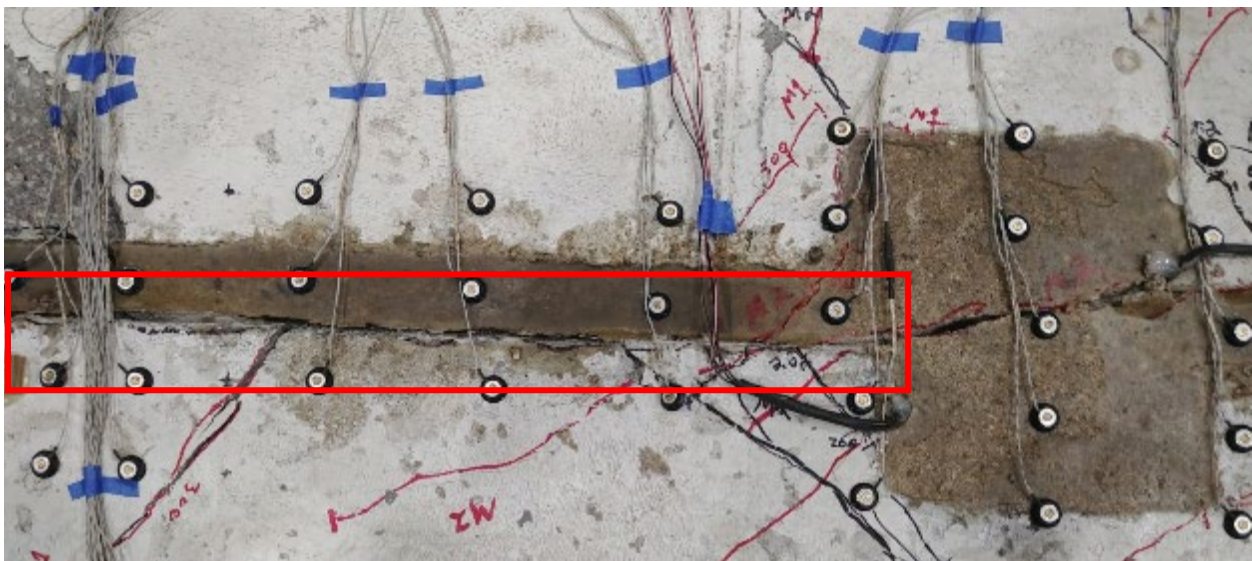


Figure 5.117: Right Side Longitudinal Joint Gap at $-\Delta_{c6}$ – Second Cycle

The test continued to Δ_{c8} with little associated additional damage. Rotation of the specimen became more prevalent and after completing the final cycle, the test was concluded and the specimen was returned to zero displacement. It should be noted that there was still 52 kips of residual strength at the first push cycle. The shear connector plates were removed from the specimen to examine the welds as seen in Figure 5.118. All of the welds remained undamaged.



(a)



(b)



(c)



(d)

Figure 5.118: Test 6 Removed Shear Connector Plate (a) Top View Left Connector (b) Bottom View Left Connector (c) Top View Right Connector (d) Bottom View Right Connector

5.7.2 Conclusion

Test 6 examined the shear slip response of a PPC substitute to conventional cementitious grout. The objective was to determine any benefits in performance a PPC would provide opposed to the commercially available high strength grouts. While the compressive strength of the PPC was 7 ksi compared to the required 9 ksi, the ultimate capacity of the joint exceeded expectations. The joint was able to resist 320 kips ($q_{\text{average}}= 3.3\text{k/in}$). When compared to Test 5, which had a similar compressive strength, the ultimate capacity was 280 kips ($q_{\text{average}}= 2.9\text{k/in}$). The main observable advantage to using a PPC is the residual strength provided after max capacity. At Δ_{c1} strength remained above 50% of max capacity in both the push and pull for all three cycles. Additionally, at large displacements the residual strength remained above 50 kips for at least the first cycle.

One main concern with the PPC may be creep. Figure 5.119 shows a comparison of the force-displacement response for both Test 6 and Test 5 during the force controlled loading portion of the tests. Both responses show signs of creep, with displacement drifting as the load is held constant. While the scale of drift is similar for both the conventional cementitious grout and the PPC, the main concern is the amount of time the force increment was held. Figure 5.120 and Figure 5.121 show the force histories of Test 6 and Test 5 respectively. It can be seen that the drift in Test 6 takes place in time intervals under a minute, where the Test 5 drift occurs over a 9 minute time interval. Despite creep as a concern, the grout will be responsible for transferring forces produced from live loads, such as vehicles or earthquakes, which are of course dynamic loads. Overall the PPC enhanced the shear slip capacity of the joint and the residual strength of the grout.

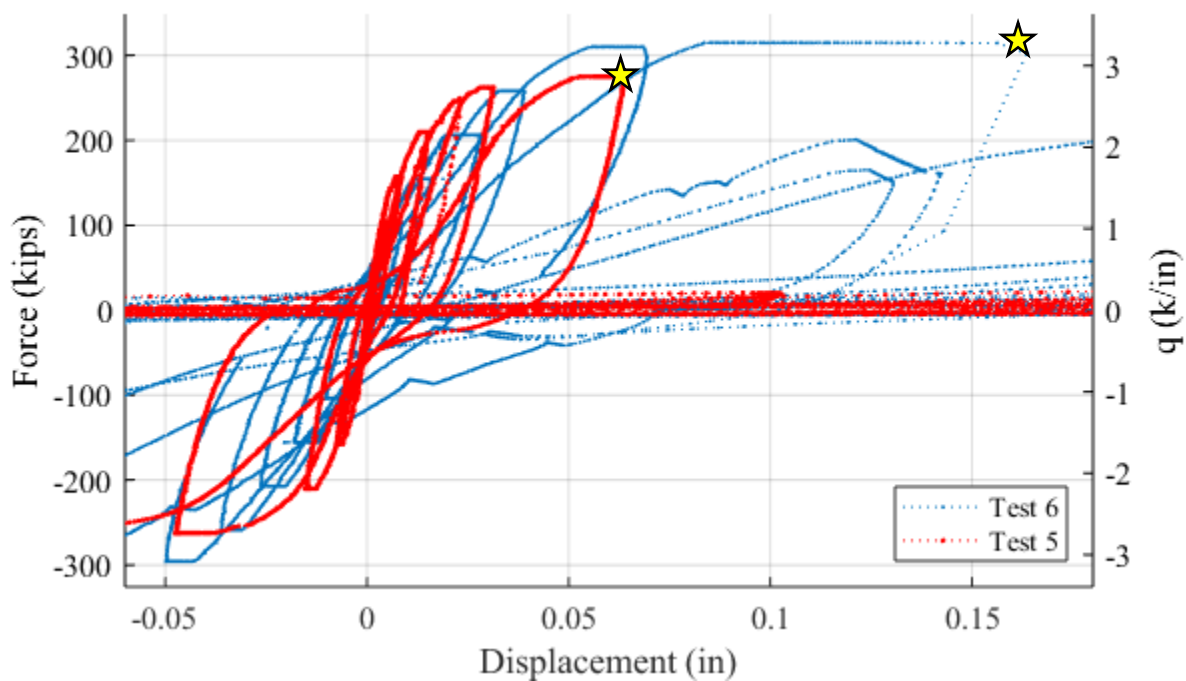


Figure 5.119: Force-Displacement Response Comparison of Test 5 and Test 6

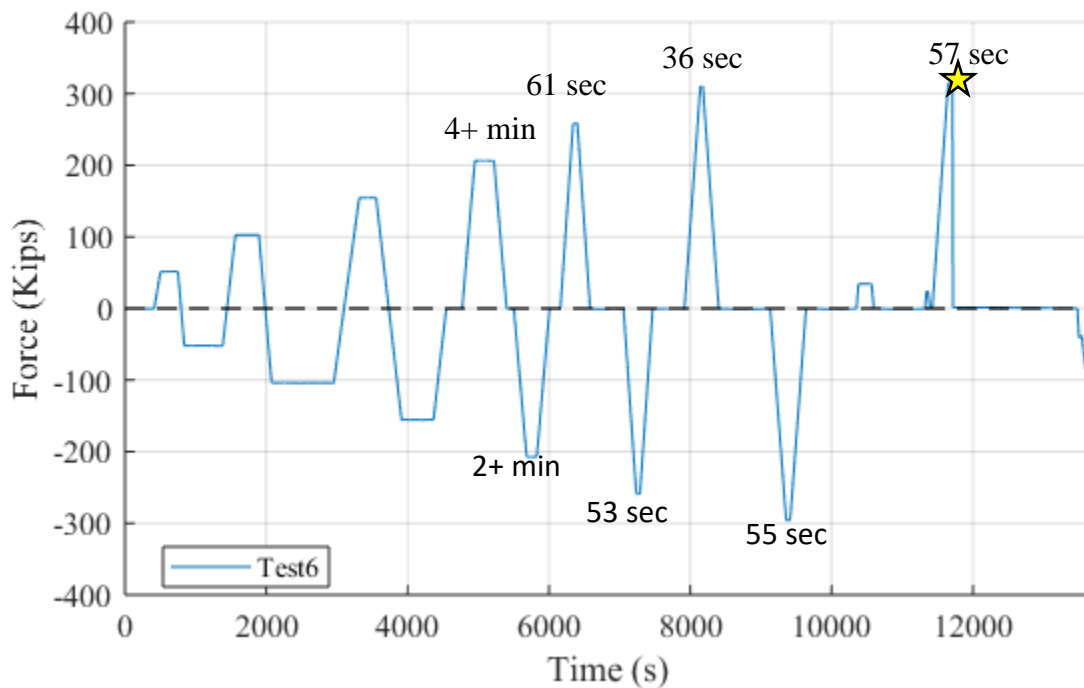


Figure 5.120: Test 6 Load History to Max Strength Capacity

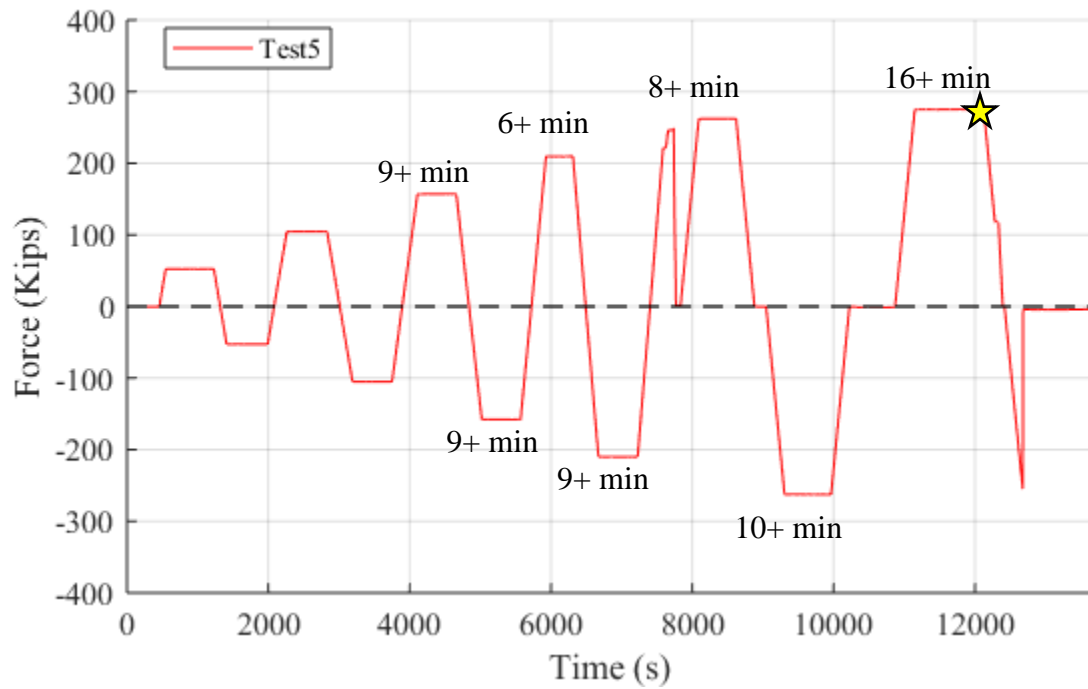


Figure 5.121: Test 5 Load History to Max Strength Capacity

5.8 Phase I Experimental Observations

After completion of the first phase of testing, initial observations of damage progression were made. Damage progression starts with cracking perpendicular to the joint. These cracks are minor and do not propagate into the surrounding concrete. As force and displacement increase, diagonal cracks begin to appear, propagating towards the source of loading. Generally, the first cracks initiate at the corners of the grouted pockets. As force increases, damage progresses in the form of existing cracks increasing in length and new diagonal cracks forming along the length of the joint. At the maximum force, diagonal cracks begin to form across the grouted connector pocket, always crossing the pocket from the side block to the specimen pointing towards the direction of loading. Before the crack crosses the grouted pocket, a longitudinal crack in the grout is present between the interface of grout and the side block. Once the crack crosses the pocket, the longitudinal crack is located along the interface of the specimen and the grout. As damage progresses, cracks associated with cover concrete spalling begin to form, predominantly around the shear connector pockets. As displacement increases, the cracks lead to cover concrete spalling which in turn reveals the inserted shear connectors below. The weak link in the connection was bar bending opposed to shear plate yielding. The bar bending was initiated from rebar bearing against the concrete and crushing of the surrounding concrete. Which is believed to initiate the cracking in cover concrete surrounding the shear pockets. Once the cover concrete around the shear pockets began to spall, the residual strength of the connections begins to drop dramatically. The cover concrete spalling leads to a significant serviceability issue. Spalling reveals the inserted shear connector plates beneath the grout. The welds between the shear tab connector were observed to remain elastic. Additionally, the welded shear tab remains undamaged. Damage is instead occurring in the embedded rebar that are used to anchor the connector inserts. The rebar bears against the concrete, crushing the concrete and changing the boundary condition of the rebar. The bar then undergoes double bending, which in turn led to large demands and deformation of the plate likely producing the cover concrete spalling around the pocket. Once the cyclic rebar demand reaches approximately ± 0.6 inches per connector along the joint, the rebar fractures. Therefore if only one inserted shear connector along the joint is active through damage of the surrounding cover concrete, the rebar will fracture at ± 0.6

inches. However, the rebar fracture at +/- 1.2 inches when both inserted shear connectors are activated. A schematic is visible in Figure 5.122.

The progression of damage for each grouted test can be seen in Figure 5.123 through Figure 5.127. While the loading protocol attempted to remain constant for all tests, due to the nature of the test setup and damage progression, some tests were pushed beyond certain damage states and photos were not available. For example, Test 3 underwent a large displacement once the capacity of the grout was exceeded. This led to grout failure of the grouted joint, spalling of cover concrete, and rebar fracture at the end of the loading step. Therefore, no photo is available for cover concrete spalling and only photos just prior to grout failure are available for failure of the grouted joint. The force and displacement at which each damage state occurred for the tests in Phase I can be found in Table 5.1. Damage states that did not occur in the test as well as values that are not known are left blank.

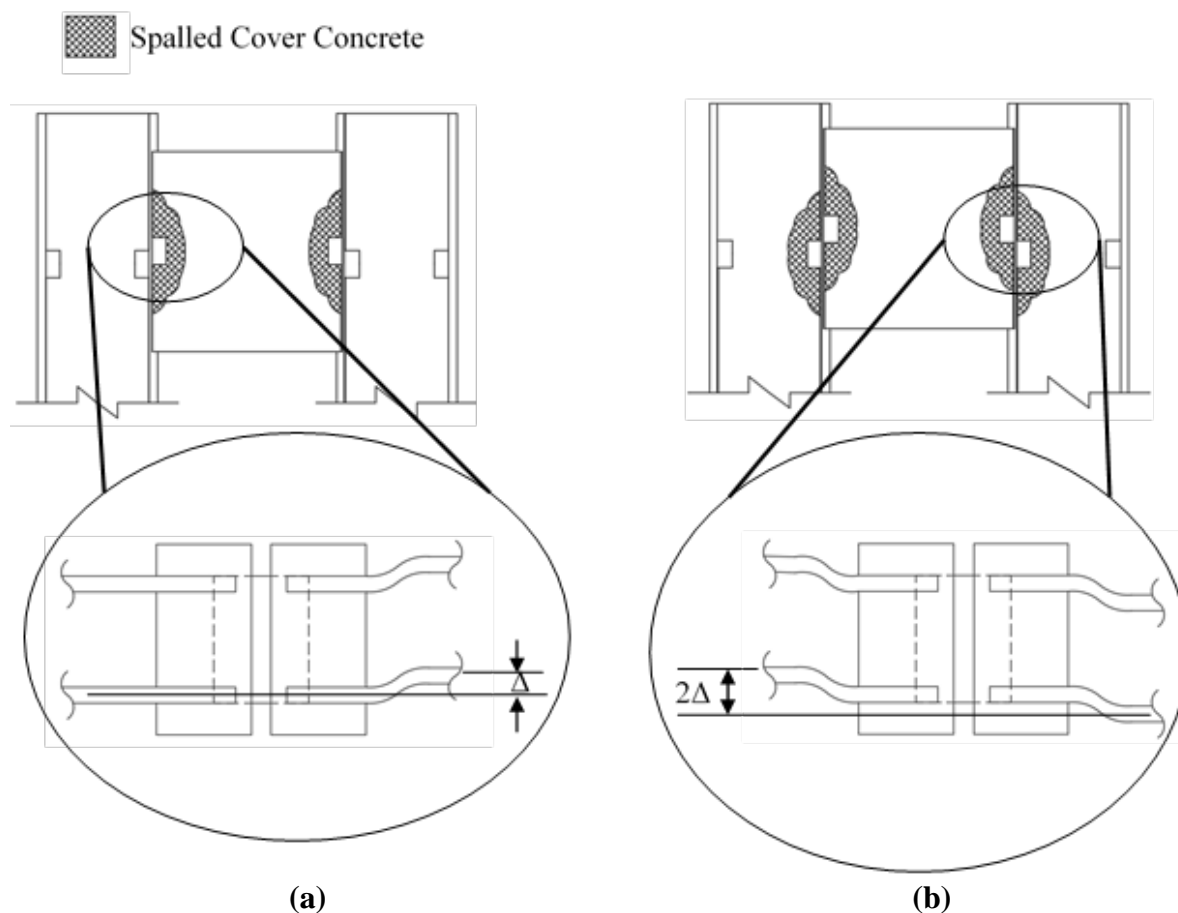
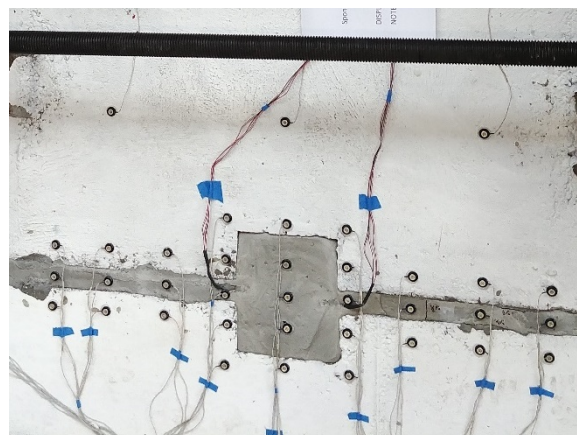


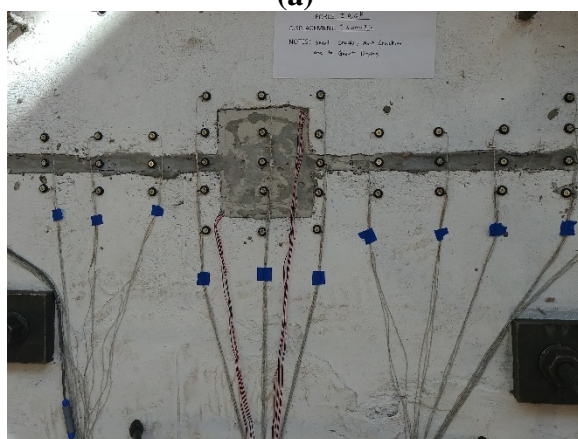
Figure 5.122: Activation of Bar Bending (a) One Side of Joint (b) Both Sides of Joint



(a)



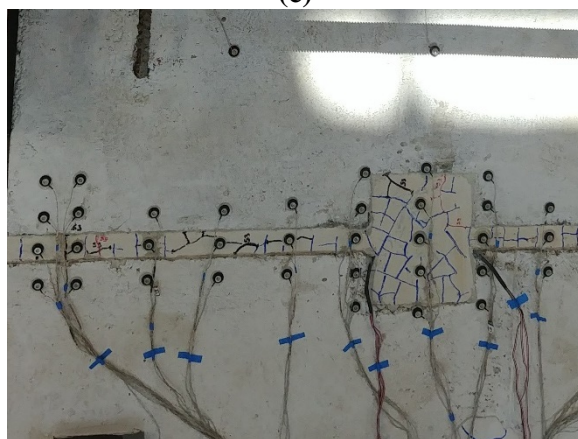
(b)



(c)



(d)



(e)

Image Not Available

(f)

Figure 5.123: Cracking Perpendicular to the Joint (a) Test 1b (b) Test 2 (c) Test 3 (d) Test 4 (e) Test 5 (f) Test 6

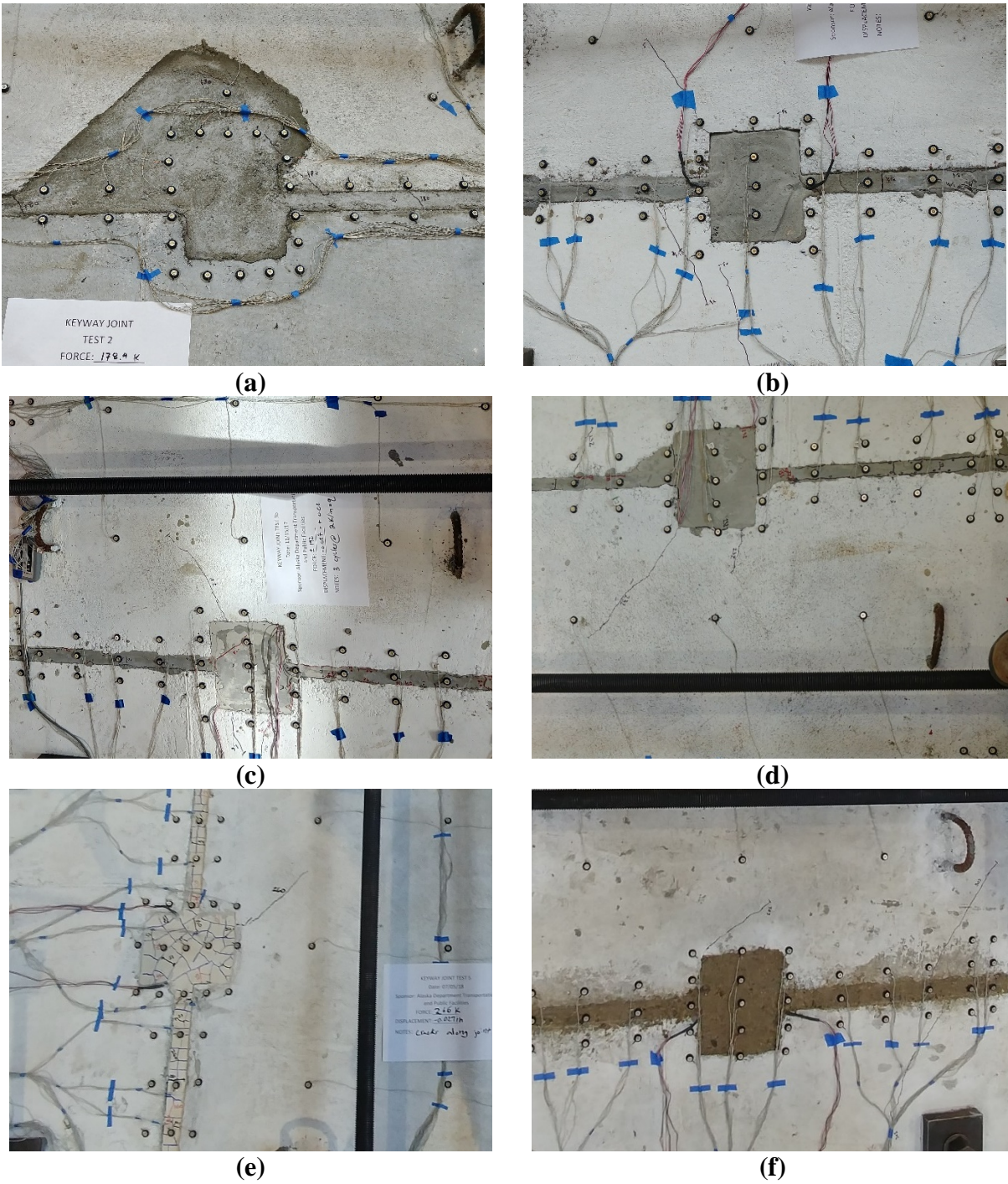
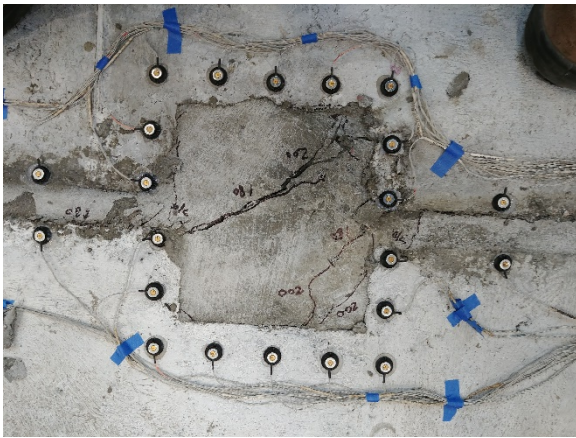
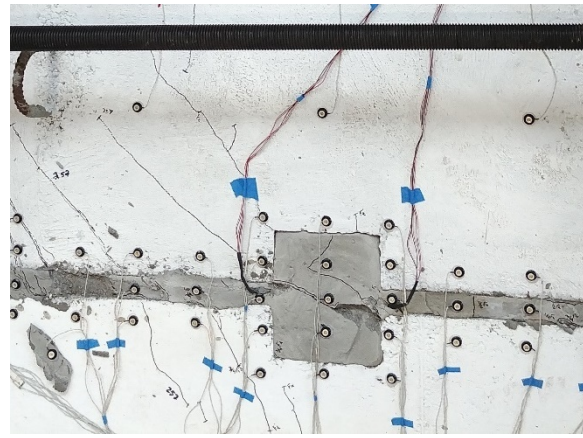


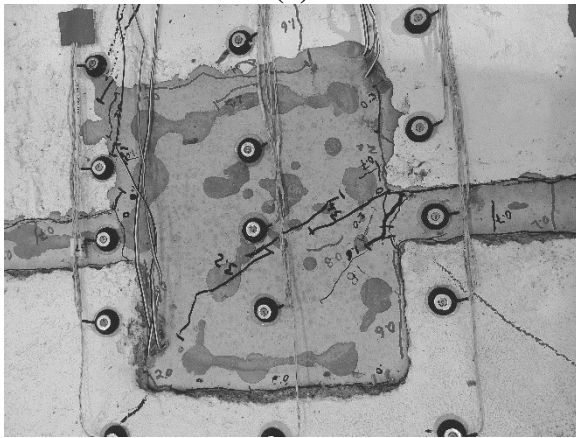
Figure 5.124 Diagonal Cracking (a) Test 1b (b) Test 2 (c) Test 3 (d) Test 4 (e) Test 5 (f) Test 6



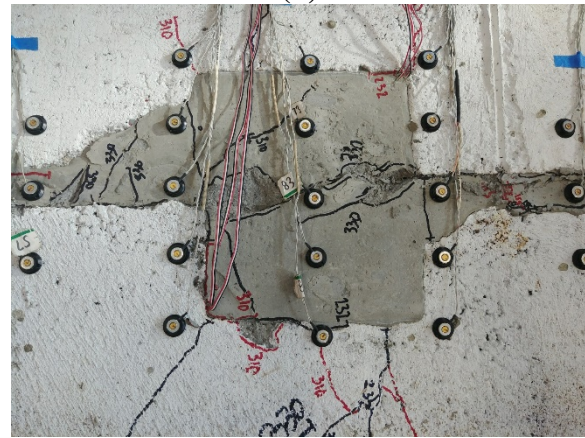
(a)



(b)



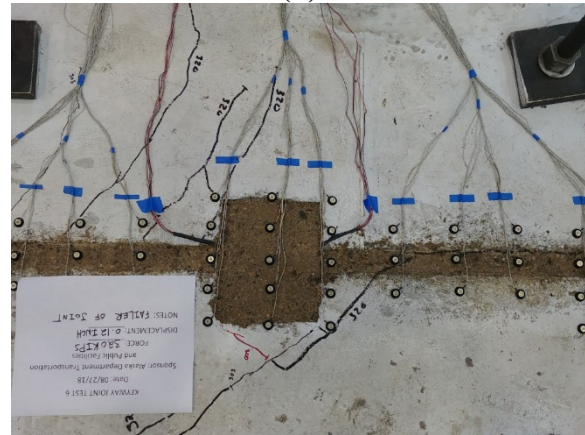
(c)



(d)

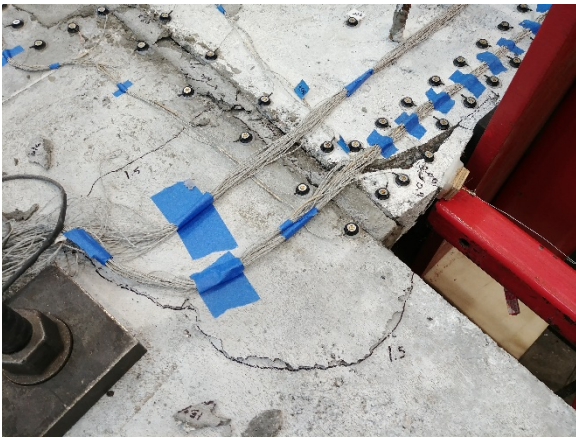
Image Not Available

(e)

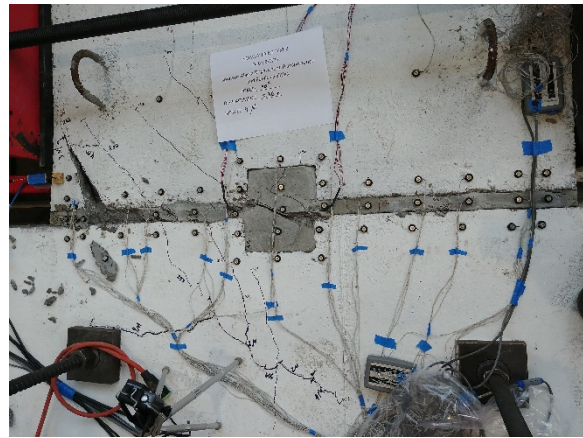


(f)

Figure 5.125 Failure of Grouted Joint (a) Test 1b (b) Test 2 (c) Test 3 (d) Test 4 (e) Test 5 (f) Test 6

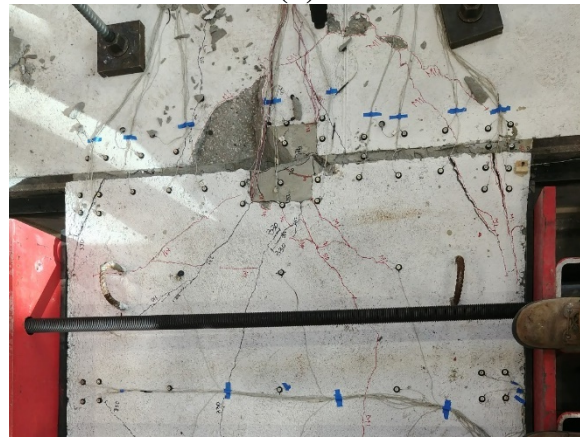


(a)

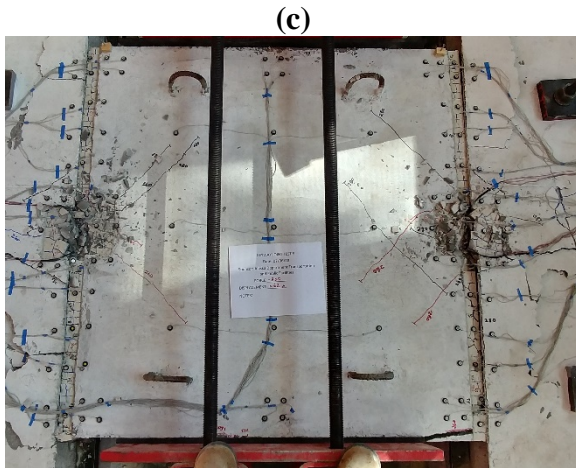


(b)

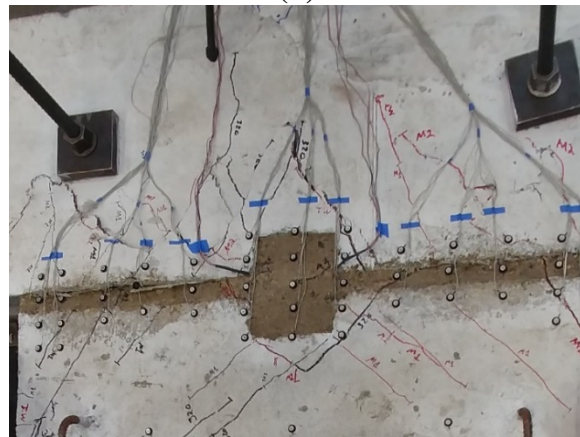
Image Not Available



(d)



(e)



(f)

Figure 5.126: Cover Concrete Spalling (a) Test 1b (b) Test 2 (c) Test 3 (d) Test 4 (e) Test 5 (f) Test 6



(c)



(d)



(e)



(f)

Figure 5.127 Rebar Fracture (c) Test 3 (d) Test 4 (e) Test 5 (f) Test 6

Table 5.1: Phase I Damage State Progression Force and Displacement

Test	Damage State					
	Perpendicular Cracking	Diagonal Shear	Failure of Joint	Cover Concrete	Bar Fracture	
1a	F [Kips]			46		
	Δ [in.]			0.683		
1b	F [Kips]	134	178	199	23	
	Δ [in.]	0.018	0.036	0.056	1.42	
2	F [Kips]	120	240	260	43	
	Δ [in.]	0.009	0.048	0.093	0.366	
3	F [Kips]	10	192	-286	26	
	Δ [in.]	-0.004	-0.032	-0.085	1.76	
4	F [Kips]	0	232	317	-64	21
	Δ [in.]	0.000	0.053	0.134	-0.586	1.30
5	F [Kips]	53	266	255		
	Δ [in.]	0.0018	0.031	0.075	-0.585	0.594
6	F [Kips]		305	315	-50	
	Δ [in.]		0.069	0.156	-0.377	-0.725

Other than visual damage, degradation in the system was observed in the load control portion and in the displacement controlled portion. Degradation in the load control portion of the test is only available from Test 3. While a reduction in the secant stiffness was noted among three cycle sets, the reduction was minor. Where the secant stiffness is defined as the force at maximum displacement of the cycle divided by the maximum displacement of the cycle as seen in Equation 5.3. The ratio of secant stiffness for the second and third cycle divided by the original secant stiffness of the cycle averaged at 0.96 in the push direction and 0.90 in the pull direction. Test 4 can also be compared with Test 3 due the fact that the grout for each test was poured from the same batch and similar grout strengths were achieved at the time of testing. Test 4 had 1.03 more strength than Test 3, while Test 4 was subjected 5 cycles of loading and Test 3 was subjected 61 cycles.

$$k_{secant} = F(f(\Delta_{max}) / \Delta_{max} \quad \text{Equation 5.3}$$

Degradation in the displacement controlled portion of loading was more perceptible and available in Test 4 and Test 6. Degradation in this portion of loading is best examined using the ratio of maximum force of second and third cycle divided by the maximum force of the first cycle. The average ratio of forces for Test 4 up until residual strength of the connection was reached was 0.58 and 0.63 for the push and pull directions respectively. The average ratio of forces for Test 6 up until residual strength of the connection was reached was 0.54 and 0.61 for the push and pull directions respectively.

5.9 Alternate Connections

The existing shear connector transfers forces from one girder to the next through the welded connector plate. The force is transferred into to shear connector inserts through the fillet welds of the welded connector plate. This applies a shear force into the plate of the shear connector inserts, which distributes the force to rebar through the welds on the bottom of the plate and the surrounding concrete. Initially both the plate and the rebar will bear against the surrounding concrete, until crushing of the concrete occurs. As the displacement increases, the concrete in contact with rebar continues to crush down the length of the rebar until the unbraced length of the rebar is sufficient to form a plastic hinge in the rebar. The force is only resisted by the hinges in the rebar and the bearing of the plate. The free body diagram of the current connection can be seen in Figure 5.121.

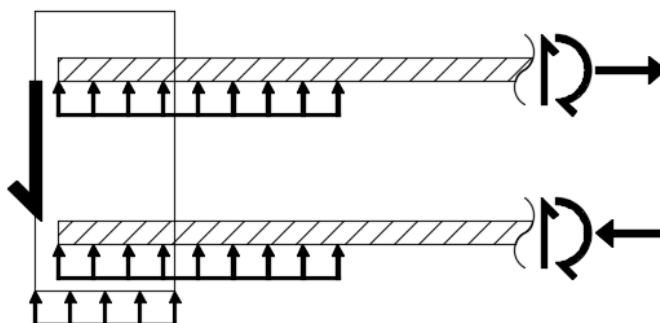


Figure 5.128: Existing Connection Free Body Diagram

It was desirable to reduce the deformation of the connection at peak strength of the shear key such that the overall damage level would reduce. With a reduction in damage, residual strength of the connection may increase. Another goal was to keep the alternate connection as similar to the existing connection as possible such that fabricators would not have to alter existing formwork. To achieve a more desirable behavior in an alternative connection, two methods were considered. The first is to change the mechanism from rebar bearing and bending on the surrounding concrete to a stiffer mechanism where force is transferred through axial forces in the rebar. Similar connections have been seen in the literature and (Cao & Naito, 2009; Hofheins et al., 2002; José A. Pincheira et al., 2005) and have used a 45° angle to the joint interface. The second method is to increase the bearing area of the concrete to mobilizes the

capacity of the welded 3 in. x 1/4 in. x 4 connector plate, which has been suggested by Hofheins et al.(2002).

Initially three connectors were proposed to the AKDOT. The three connections can be seen in Figure 5.129 through Figure 5.131. Alternate Connection Option 1 is the same as the existing connection but the rebar are now at 45° to change the force transfer mechanism into one of the axial tension and compression. One problem associated with the angled embedded rebar was cover concrete clearances. Since the angled bars must be rested under or on top of the top layer of reinforcing steel, the cover concrete of the deck would be reduced to less than 2 inches. Alternate Connection Option 2 uses an MC shape and shear studs to increase the bearing area of the connection in an attempt to mobilize the welded shear tab. While Alternate Connection Option 2 was liked, due to the concrete break out failure mechanism associated the geometry of the flange, the capacity to mobilize the weld could not be achieved (Precast/Prestressed Concrete Institute, 2010). Lastly Alternate Connection Option 3 was similar to Alternate Connection Option 1 but used an angle to increase bearing area and reduce rotation of the embedded shear connector, which was common among connections with embedded rebar at 45°(Cao & Naito, 2009). Not only did Alternate Connection Option 3 have the same cover concrete issue as Alternate Connection Option 1, the angle was not considered feasible by AGGPRO, the largest fabricator of decked bulb-T girders in Alaska.

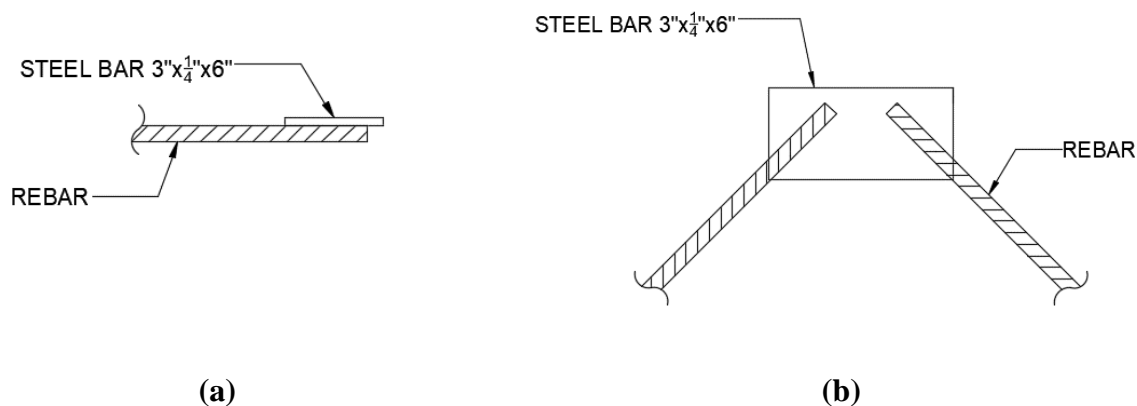


Figure 5.129: Alternate Connector Option 1 (a) Plan View (b) Elevation View

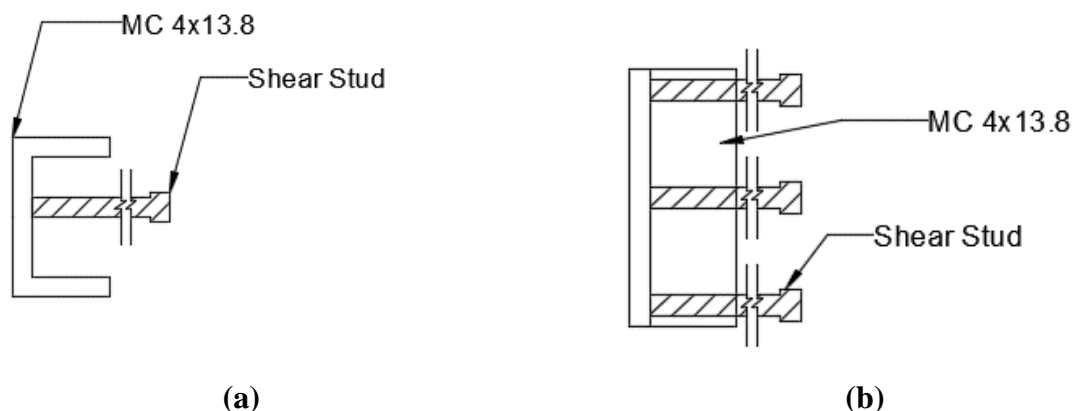


Figure 5.130: Alternate Connector Option 2 (a) Plan View (b) Elevation View

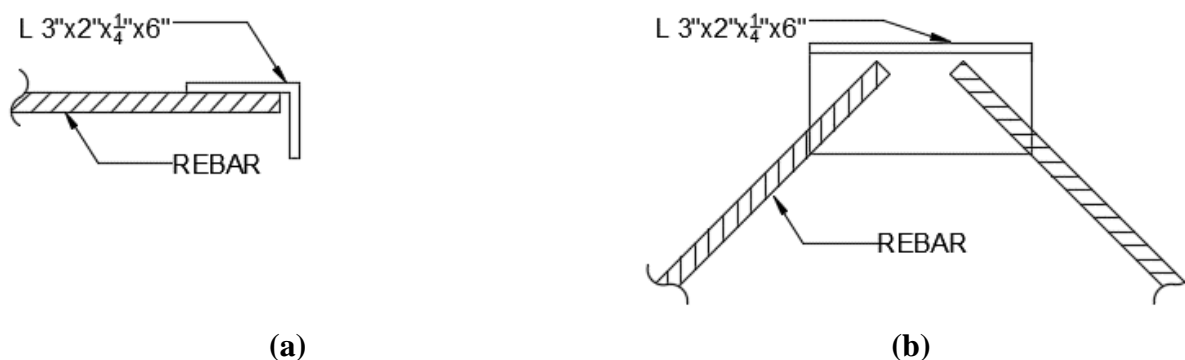


Figure 5.131: Alternate Connector Option 3 (a) Plan View (b) Elevation View

Based on feedback, four more alternate connection options were proposed and can be seen in Figure 5.132 through Figure 5.135. Alternate Connection Option 4 was suggested by AGGPRO and was a modified version of Alternate Connection Option 1 where the plate thickness was increased from $\frac{1}{4}$ in. to 1 in. to move the embedded rebar between the mats of rebar that reinforce the bulb-tee girder flanges. In addition, this modification increased the bearing area of the plate. Alternate Connection Option 5 was a modified version of Option 4, where a plate fin is welded on the plate perpendicular to the joint to increase bearing area and reduce potential rotation of the embedded shear connectors. Alternate Connector Option 6 is a modification of Option 5 but the rebar are perpendicular to the joint instead of 45 degrees. This is similar to the current connection but allows for more confinement around the embedded bars due to being layered between the mats of decking steel. Moreover, the additional welded plate will provide resistance to plate rotation. Lastly Alternate Connector Option 7 was proposed. This

connector is the same as the existing connector but with a steel plate fin welded perpendicular to the joint to increase bearing area and limit rotation.

Due to the nature of the experimental setup, details of the shear connectors must be decided upon prior to casting. Additionally, the amount of effort of casting side blocks for one test is about the same effort as casting side blocks for four tests. Thus it was decided to pursue Alternate Connector Option 4 as the most favorable connector and Alternate Connector Option 5 in advance to reduce damage from the potentially large rotational response of Alternate Connector Option 4.

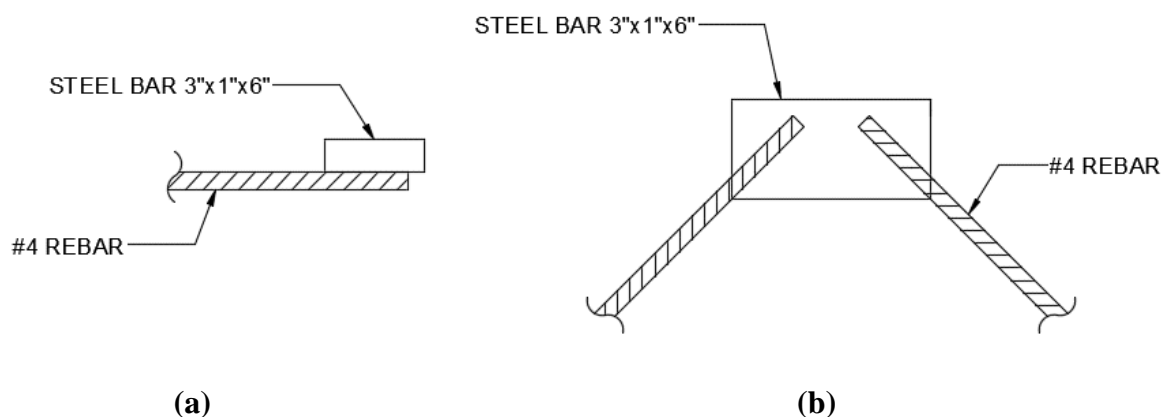


Figure 5.132: Alternate Connector Option 4 (a) Plan View (b) Elevation View

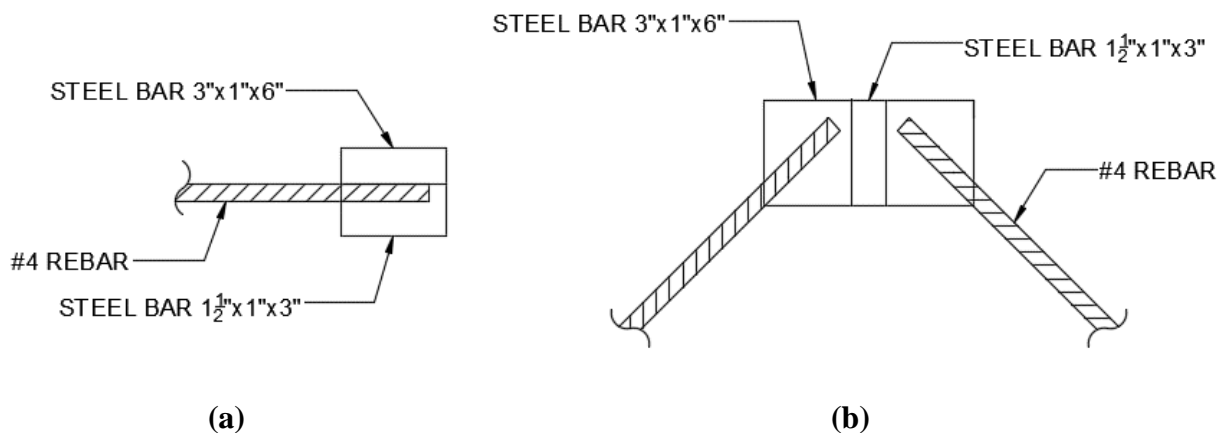


Figure 5.133: Alternate Connector Option 5 (a) Plan View (b) Elevation View

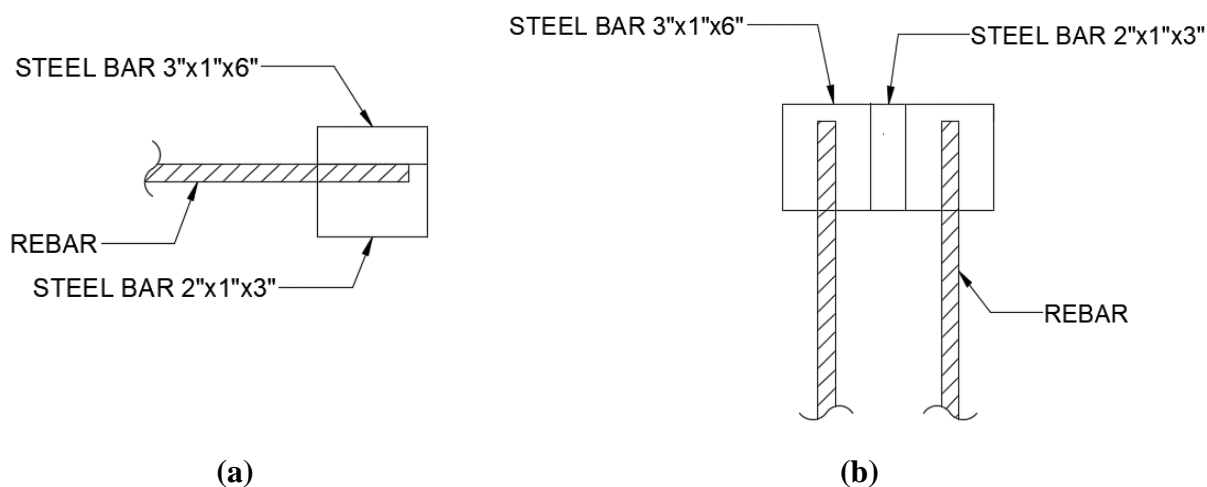


Figure 5.134: Alternate Connector Option 6 (a) Plan View (b) Elevation View

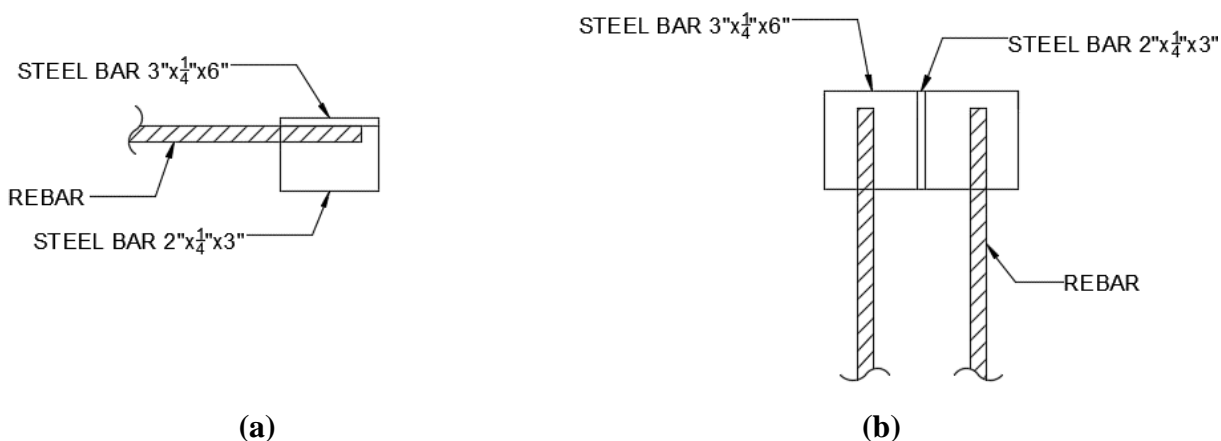


Figure 5.135: Alternate Connector Option 7 (a) Plan View (b) Elevation View

5.9.1 Design Strength

Using the PCI Handbook (2010) the connection can be designed to act as a truss mechanism as seen in Figure 5.136. Resistance factors, ϕ , are provided from the AISC Manual (2011). Note that this design has been found to be conservative in the literature and does not account for bearing. First the weld capacity to the plate must be calculated. Since only a #4 rebar can be used to ensure that cover concrete tolerances are met, the nominal tension capacity of the rebar, T_n , can be calculated using Equation 5.4. Were A_s is the area of steel and f_y is the yield stress of the steel. Then using a flare bevel weld on either side which has an effective throat for a single side of $t_w=0.2d_b$, the design strength of the weld, ϕ_r , can be calculated using Equation 5.5, and a length of weld, l_w , equal to 2½ inches. Lastly, the design strength of the base

metal, ϕV_n , was checked using Equation 5.6. Where t_{pl} is the thickness of the base metal, f_y is the yield strength of the plate and l_w is the length of the weld. It can be seen that yielding of the rebar will control.

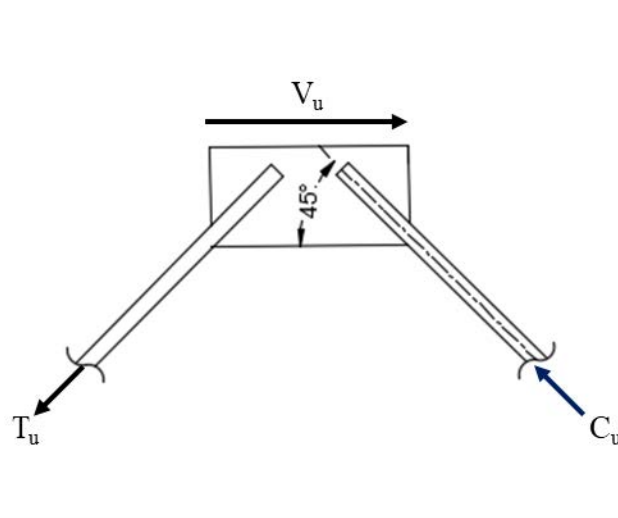


Figure 5.136: PCI Handbook Truss Mechanism

$$T_n = A_s f_y = (0.2 \text{ in}^2)(60 \text{ ksi}) = 12 \text{ kip} \quad \text{Equation 5.4}$$

$$\begin{aligned} \phi r_n &= \phi(0.6 F_{EXX}) t_w l_w \\ &= 0.75(0.6)(70 \text{ ksi})(0.2)(0.5)(2.5)(2) \\ &= 15.8 \text{ kip} \end{aligned} \quad \text{Equation 5.5}$$

$$\begin{aligned} \phi V_n &= \phi(0.6 f_y) t_{pl} l_w \\ &= 0.9(0.6)(36 \text{ ksi})(1)(2.5)(2) = 97.2 \text{ kip} \end{aligned} \quad \text{Equation 5.6}$$

The design strength shear strength of the shear connector insert, ϕV_n , can be calculated using Equation 5.7. Where ϕT_n , and ϕC_n , are the tension and compression design strength of the rebar and are given in Equation 5.8 and Equation 5.9 respectively.

$$\begin{aligned} \phi V_n &= \phi T_n \cos(45) + \phi C_n \cos(45) \\ &= (0.707)((10.8) + (7.8)) \\ &= 13.2 \text{ kips} \end{aligned} \quad \text{Equation 5.7}$$

$$\begin{aligned} \phi T_n &= \phi A_s f_y = (0.9)(0.2 \text{ in}^2)(60 \text{ ksi}) \\ &= 10.8 \text{ kip} \end{aligned} \quad \text{Equation 5.8}$$

$$\begin{aligned}\phi C_n &= \phi A_s f_y = (0.65)(0.2 \text{ in}^2)(60 \text{ ksi}) \\ &= 7.8 \text{ kip}\end{aligned}\quad \text{Equation 5.9}$$

Next the weld can be checked using the elastic method found in the AISC Manual (2011). For more precision, the instantaneous center of rotation method can be used. A sketch of the eccentrically loaded weld can be seen in Figure 5.137. The allowable stress in the weld, ϕr_n , can be calculated using Equation 5.10. Then the resultant force on the weld, r_u , can be calculated by combining force induced by eccentricity and the force induced by direct shear as given in Equation 5.11. The force induced by direct shear, r_{pux} , is calculated using Equation 5.12, where l_w is the length of weld. The forces induced by eccentricity, r_{mux} and r_{muy} are calculated using Equation 5.13 and Equation 5.14 respectively where e is the eccentricity of the nominal shear force V_u , C_x and C_y are the horizontal and vertical components respectively of the radial distance to the center of gravity of the weld group, and I_p is the polar moment of inertia given in Equation 5.15. Lastly using Equation 5.16, the design shear strength of the weld group can be calculated.

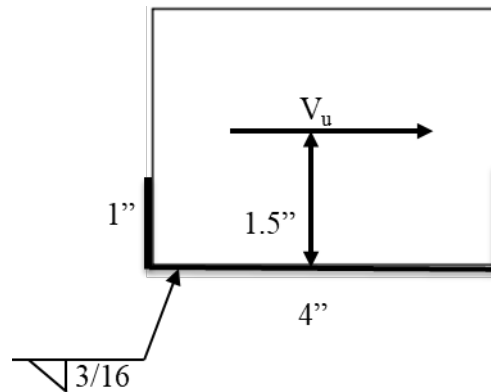


Figure 5.137: Sketch of eccentrically loaded weld

$$\begin{aligned}\phi r_n &= \phi(0.6 F_{EXX}) t_w \\ &= 0.75(0.6)(70 \text{ ksi})(0.707)(0.188) \\ &= 4.18 \text{ kip/in}\end{aligned}\quad \text{Equation 5.10}$$

$$r_u = \sqrt{(r_{pux} + r_{mux})^2 + (r_{muy})^2} = 0.313 \phi V_n \quad \text{Equation 5.11}$$

$$r_{pux} = \frac{\phi V_n}{l_w} = \frac{\phi V_n}{6} = 0.166 \phi V_n \quad \text{Equation 5.12}$$

$$r_{mux} = \frac{\phi V_n e(c_y)}{I_p} = \frac{\phi V_n 1.33(1 - 0.167)}{13.8} = 0.0803\phi V_n \quad \text{Equation 5.13}$$

$$r_{muy} = \frac{\phi V_n e(c_x)}{I_p} = \frac{\phi V_n 1.33(2)}{13.8} = 0.193\phi V_n \quad \text{Equation 5.14}$$

$$I_p = \frac{8(1)^3 + 6(1)(4)^2 + (4)^3}{12} - \frac{1^4}{2(1) + 4} = 13.8 \text{ in}^4 \quad \text{Equation 5.15}$$

$$\phi V_n = \frac{4.18}{0.313} = 13.3 \text{ kips} \quad \text{Equation 5.16}$$

Finally, the connector plate capacity can be calculated. The shear yielding of the connector plate is provided in Equation 5.17. Where f_y is the yield strength of the plate, A_p is the area of the plate in the plane of loading. The moment capacity of the connector plate is given in Equation 5.18. Where Z_p is the plastic section modulus of the plate given by Equation 5.19 and, e is the eccentricity of the plate given by the distance separating the center of gravity of the two weld groups on either side of the plate.

The rebar acting as a truss mechanism dictates the design of the connection in accordance with the PCI manual with a design strength of 13.2 kips. As stated above, this design is conservative and does not account for concrete bearing against embedded plates and rebar. Similar the same strength can be used for the connection with the fin, as fracture of the embedded rebar will also be the controlling mechanism.

$$\phi V_n = \phi(0.6f_y)(A_p) = 0.9(0.6)(36\text{ksi})(0.25)(4) = 19.4 \text{ kips} \quad \text{Equation 5.17}$$

$$\phi V_n = \frac{\phi(f_y)(Z_p)}{e} = \frac{0.9(36)(1)}{1.33} = 24.4 \text{ kips} \quad \text{Equation 5.18}$$

$$Z_p = \frac{bd^2}{4} = \frac{0.25(4)^2}{4} = 1 \quad \text{Equation 5.19}$$

CHAPTER 6 EXPERIMENTAL PHASE II

This chapter presents a summary of the experimental results of Phase II of the experimental program. The tests in this phase address effects of no surface preparation of the longitudinal keyway as well as the behavior of alternate connections proposed in section 5.9.

6.1 Test 7

Test 7 was performed at the CFL at NCSU on January 03, 2019. Test 7 was tested without any surface preparation to the shear key, limiting the bond strength of the grout and the shear key. This section presents the overall response of the specimen and then discusses experimental procedures, results and observations in chronological order. The displacement history measured at the center of the specimen is displayed in Figure 6.1. Complementary to the displacement history, the specimen load history is presented in Figure 6.2. Additionally the complete load-displacement response and rigid body rotation versus displacement of the specimen measured at the center of the specimen can be seen in Figure 6.3 and Figure 6.4 respectively.

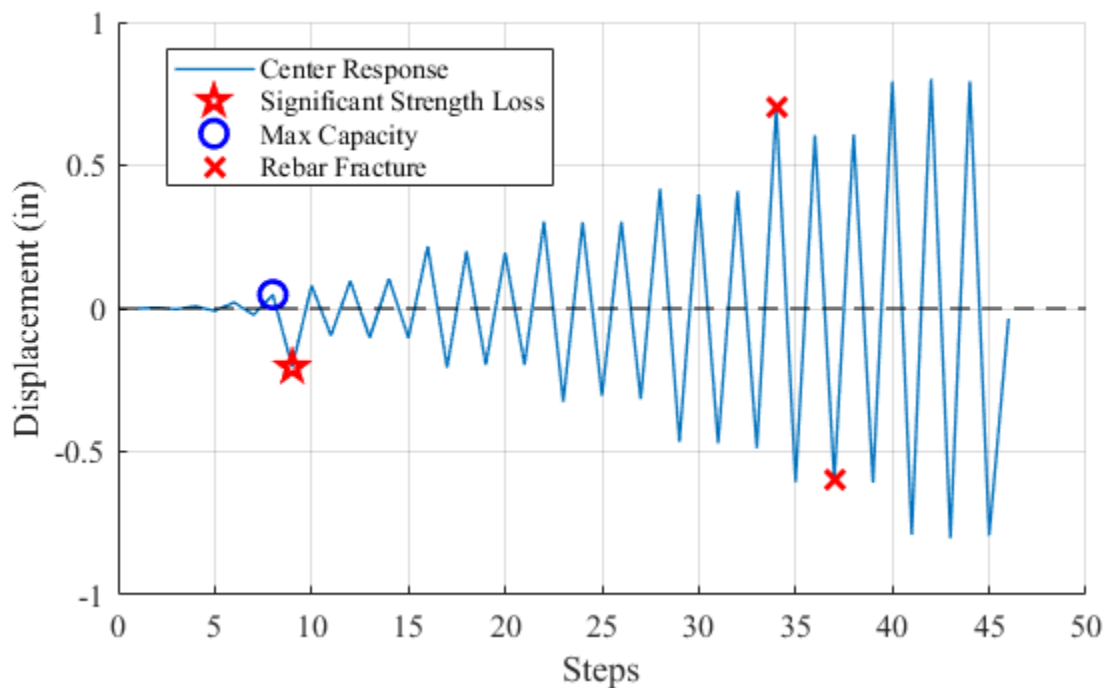


Figure 6.1: Test 7 Displacement History

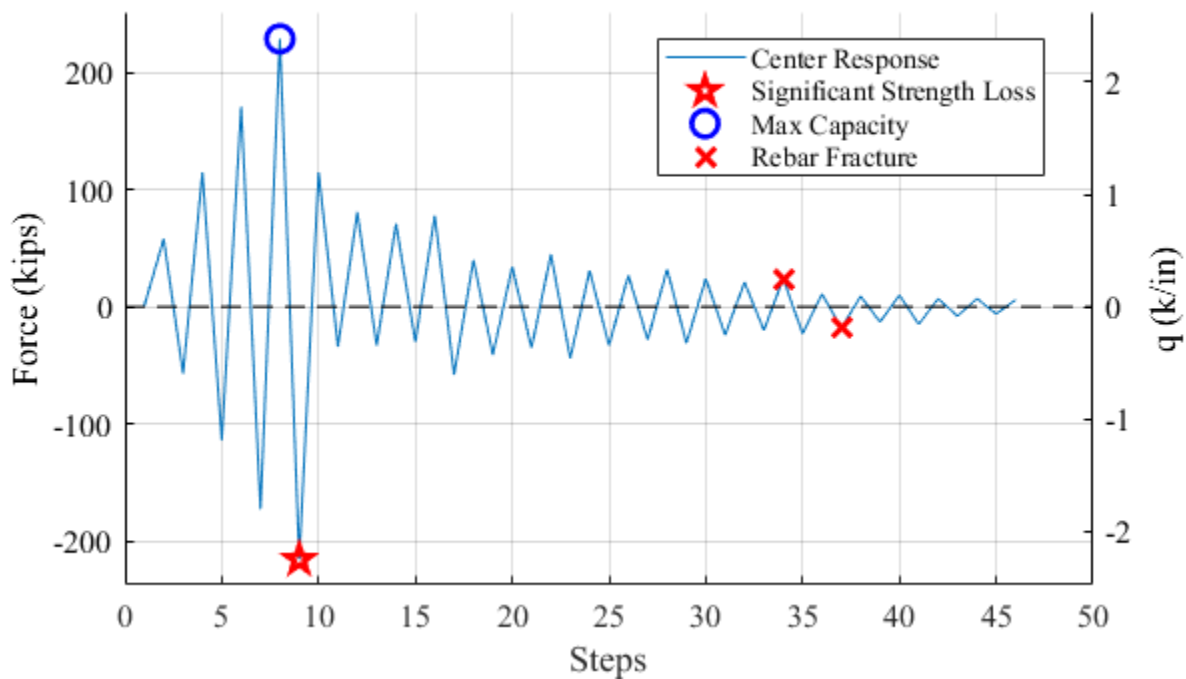


Figure 6.2: Test 7 Load History

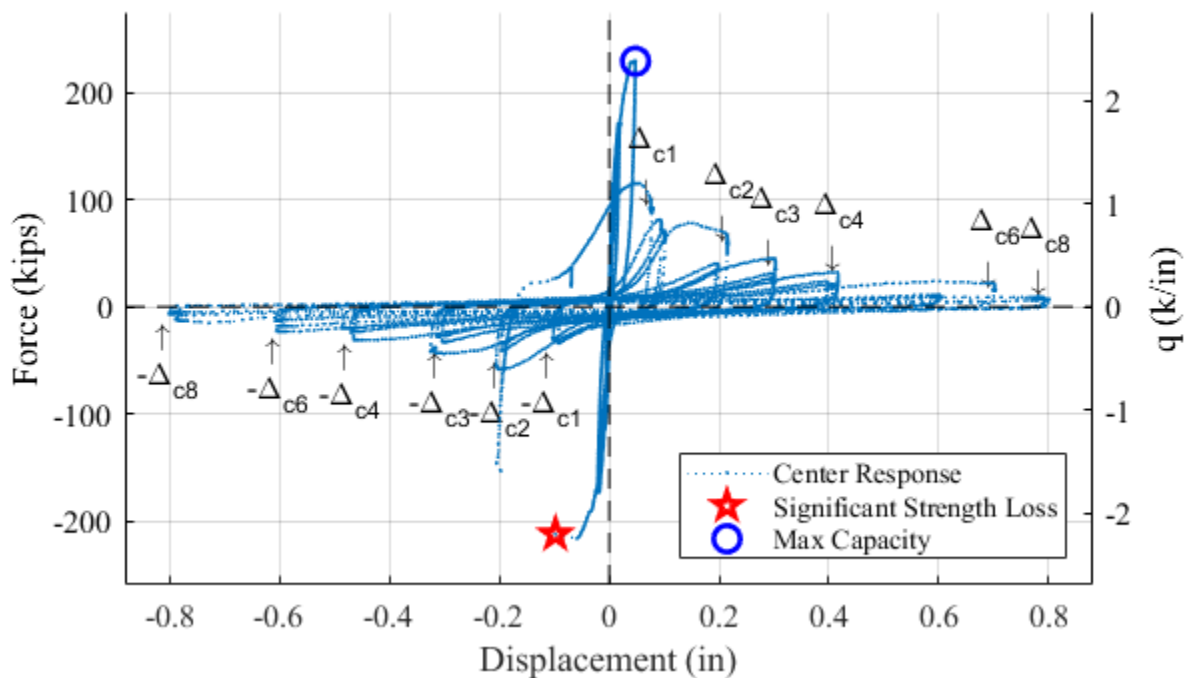


Figure 6.3: Test 7 Force-Displacement Response

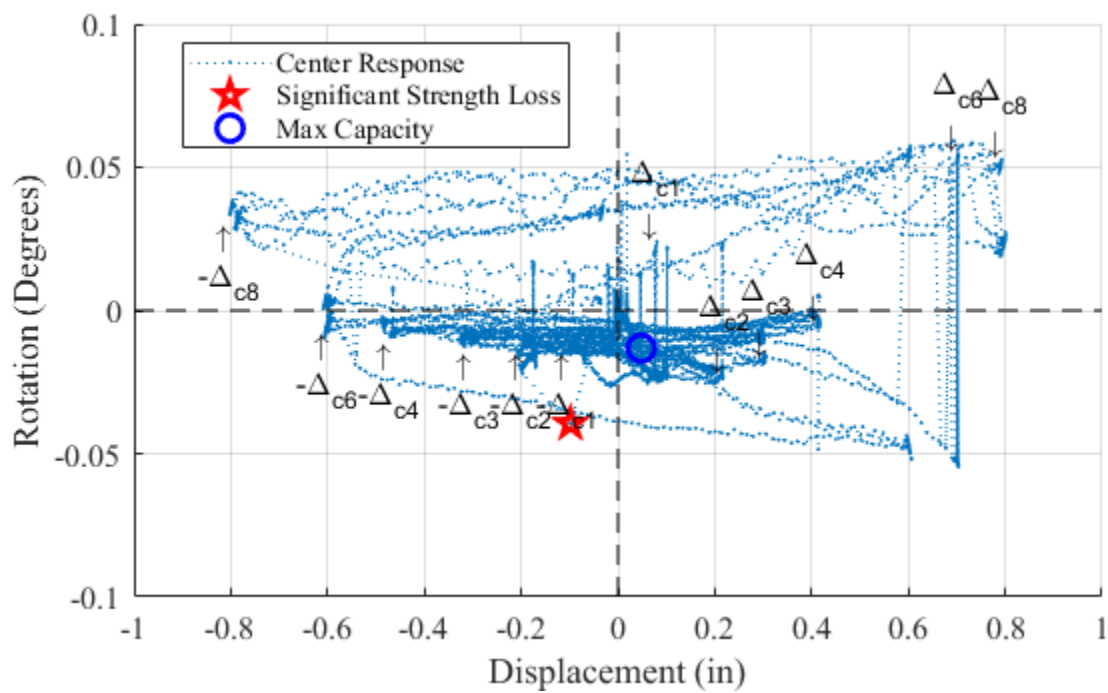


Figure 6.4: Test 7 Rigid Body Rotation

6.1.1 Test 7 Summary

Force was applied cyclically in single cycle sets, at increments of 58 kips ($q_{\text{average}} = 0.6\text{k/in}$). Prior to loading, minor shrinkage cracking was visible along the left joint and slab surface interface (Figure 6.5). During the first two increments of loading, additional cracking formed in the left joint, where cracks traced the interface of the grouted joint and slab, including the perimeter of the shear pocket. Upon the next load increment, 174 kips ($q_{\text{average}} = 1.8\text{k/in}$), the first visible cracks appeared in the specimen. The displacement at the center of the specimen was 0.021 inches with a rigid body rotation of 0.001° . The cracking started at both the left and right joint shear pockets and ran diagonally towards the direction of loading as seen in Figure 6.6. In addition to the damage in the specimen, a crack perpendicular to the right joint formed in the right side block. For the same cycle in the opposite direction, diagonal cracking appeared near the shear pocket and along the joint between the shear pocket and the applied load (Figure 6.7). At the anticipated capacity of the joint, 232 kips ($q_{\text{average}} = 2.4\text{k/in}$), the maximum positive displacement at the center of the specimen was 0.048 inches with an associated rigid body rotation of 0.013° . At this force, existing diagonal cracks continued to increase in length while a new diagonal crack formed through the left shear pocket as seen in Figure 6.8. Upon the reversal cycle, the specimen reached -216 kips with a displacement of -0.059 inches at the center of the specimen before the load began to decrease. The specimen reached -212 kips with an associated displacement and rotation of 0.098 inches and -0.039° before significant strength loss of the specimen occurred. The resulting damage can be seen in Figure 6.9. The damage included additional diagonal cracking through the specimen, cover concrete spalling of the specimen around the shear pocket, and cracking along the joint at the keyway interface that continued through the shear pockets.



Figure 6.5: Test 7 Left Side Grouted Shear Key with Applied Load = 0 kips



Figure 6.6: Grouted Shear Key with Applied Load = 174 kips (a) Left Side (b) Right Side

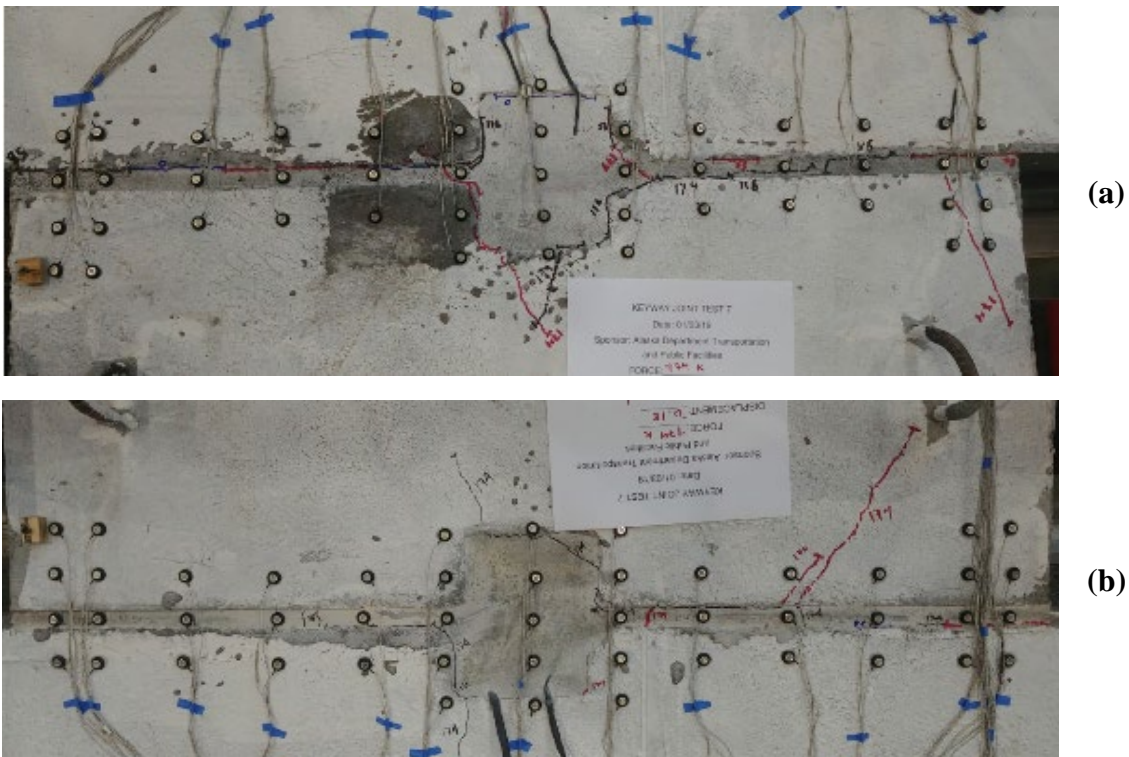


Figure 6.7: Test 7 Grouted Shear Key with Applied Load = -174 kips (a) Left Side (b) Right Side



Figure 6.8: Test 7 Left side of Grouted Shear Key with Applied Load = 232 kips

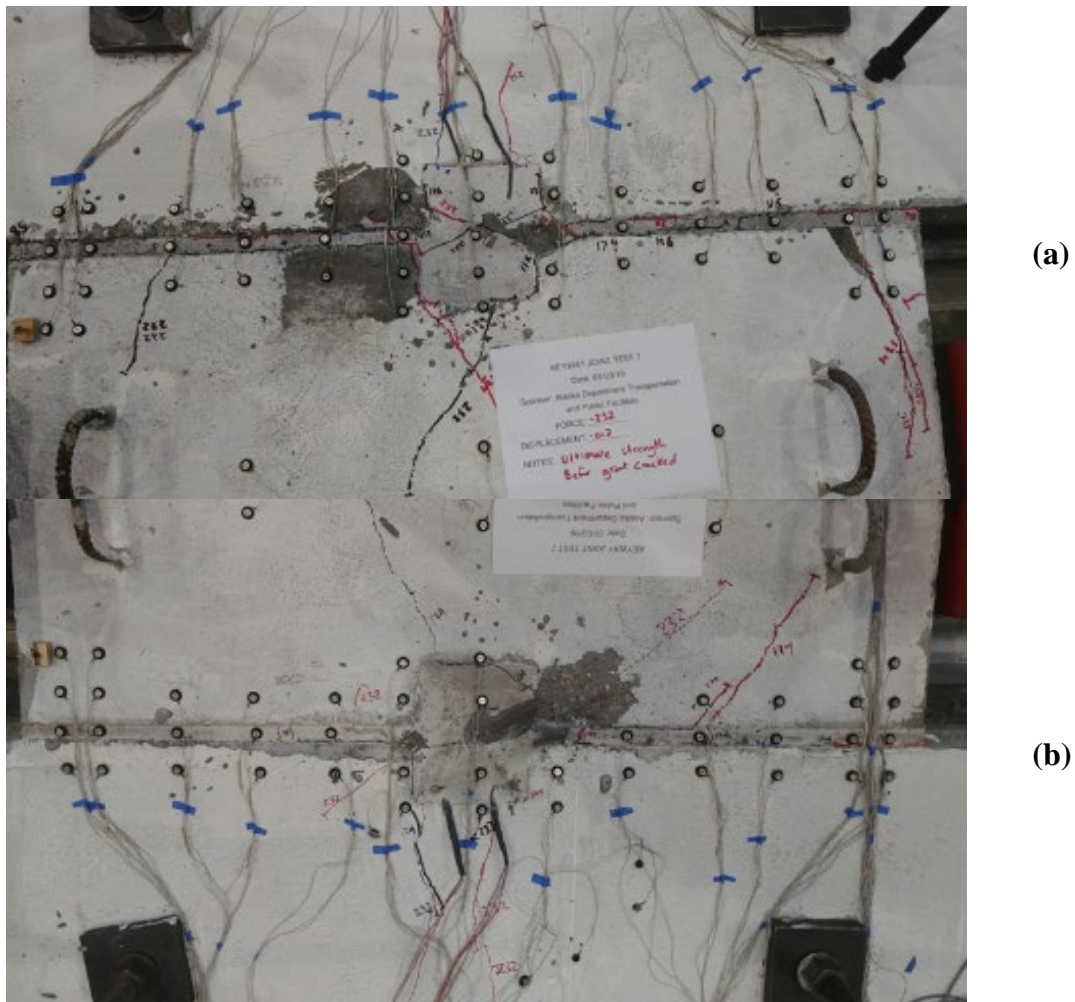


Figure 6.9: Test 7 Grouted Shear Key – Significant Strength Loss (a) Left Side (b) Right Side

The actuator was then switched to displacement control. The displacement at significant strength loss was estimated as 0.100 inches, which was used to define the displacement of significant strength loss of the joint, Δ_{c1} . Demand was applied in three cycle sets at increments proportional to Δ_{c1} . Due to the unpredictability of controlling the actuator displacement, the rate of loading was reduced and the displacement of the center of the specimen was monitored manually to conclude the loading for each cycle. During the first push cycle of Δ_{c1} , cracking in the right side block continued to propagate, forming large cracks around the shear pocket. These cracks have been associated with uplifting of the cover concrete. Throughout the remaining cycles of Δ_{c1} , the force dropped from 91 kips to 64 kips as new minor diagonal cracks formed increasing the damage around the right side block shear pocket as seen in Figure 6.10. During

Δ_{c2} , minor cracking continued to form in the left side block while cover concrete in the right side block began to lift up. Additionally a crack formed completely across the specimen to connect two existing diagonal cracks (Figure 6.11).

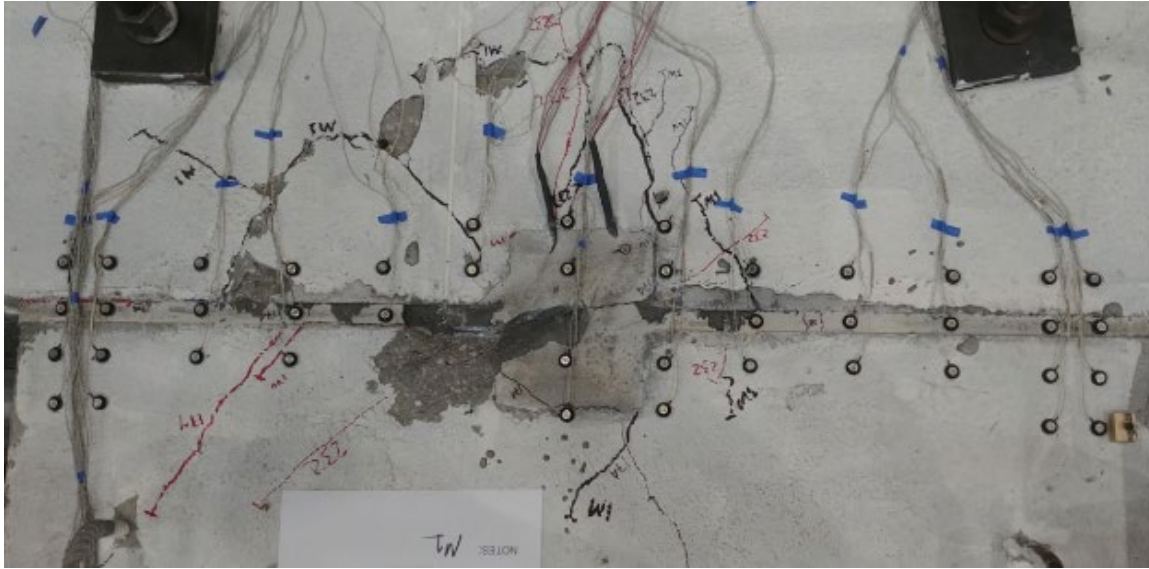


Figure 6.10: Test 7 Right Side of Grouted Shear Key $-\Delta_{c1}$ -Third Cycle



Figure 6.11: Test 7 Grouted Shear Key $-\Delta_{c2}$ -Third Cycle

As displacement increased to Δ_{c3} (+/- 0.3 inches), the width of cracks associated with prying cover concrete increased in size but few new cracks developed. During the first push cycle of Δ_{c4} , a large portion of cover concrete debonded on the right side block revealing the embedded shear connector (Figure 6.12). No ruptured bars were visible but initial damage around the weld was observed on one of the embedded rebar. The associated displacement was 0.417 inches with a force of 30 kips and rigid body rotation of -0.050° . During the subsequent pull cycle, the left side corner of the specimen closest to the applied load had cover concrete spall off from already existing diagonal cracks. The displacement at the center of the specimen was -0.466 inches with a force of -29 kips and a rigid body rotation of -0.007° . No significant damage occurred in the following cycles of Δ_{c4} . The first push cycle of Δ_{c6} fractured both exposed embedded rebar in the right joint connector plate as seen in Figure 6.13. The associated displacement was 0.704 inches with a force of 24 kips and rigid body rotation of 0.054° . Additionally, damage accumulated around the left shear pocket popping up the surrounding cover concrete. During the second cycle of Δ_{c6} , the cover concrete could be removed exposing the embedded rebar in the side block Figure 6.14.

Upon the third cycle of Δ_{c6} , the two newly exposed embedded rebar in the left side block fractured (Figure 6.16). The displacement at the center of the specimen was 0.607 inches with a force of 9 kips and rigid body rotation of -0.052° . The test continued to Δ_{c8} , where minimal strength was seen and no additional damage noted. The shear connector plates were removed from the specimen to examine the welds as seen in Figure 6.17. All of the welds remained undamaged.



Figure 6.12: Test 7 Right Side of Grouted Shear Key $-\Delta_{c3}$ -First Cycle

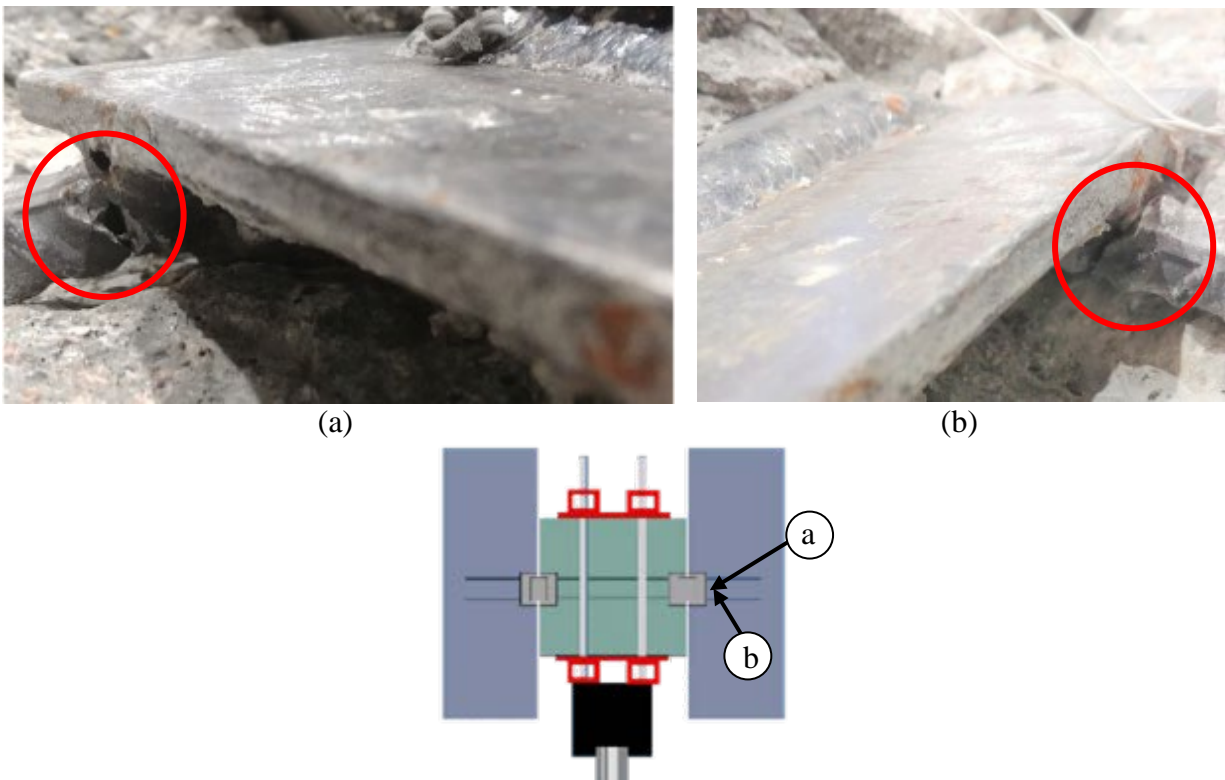


Figure 6.13: Test 7 Damage to Right Side Shear Connector Insert at Δ_{c6} – First Cycle

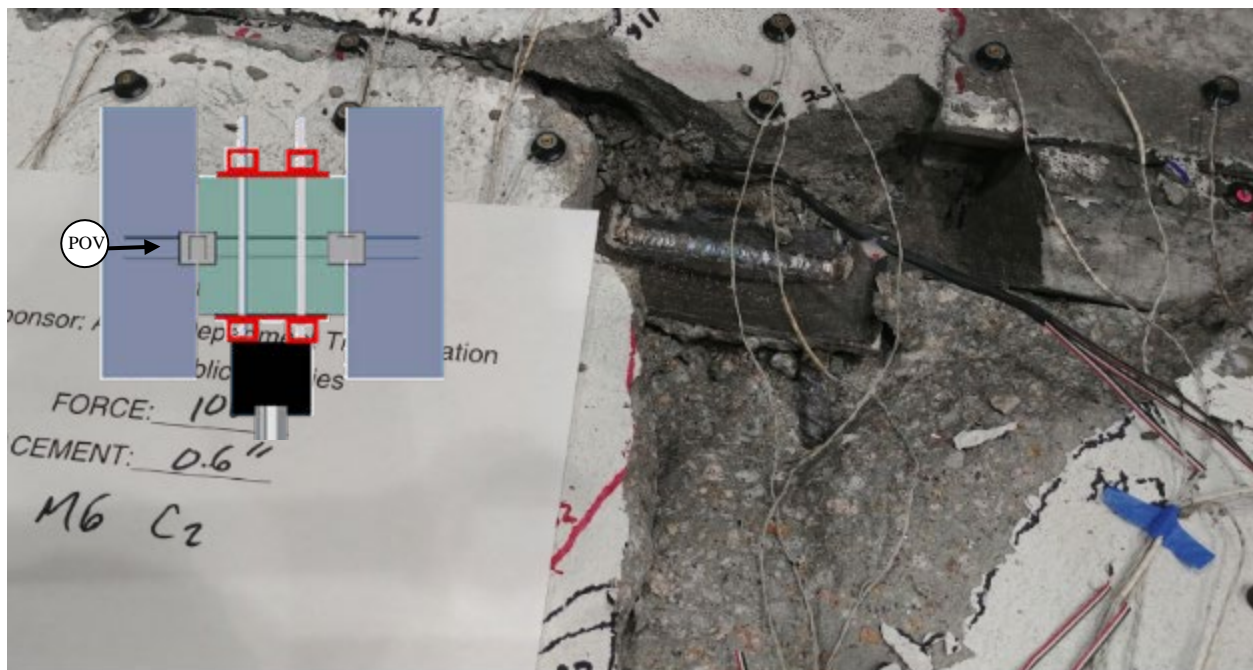


Figure 6.14: Test 7 Left Side Shear Connector Pocket at Δ_{c6} – Second Cycle

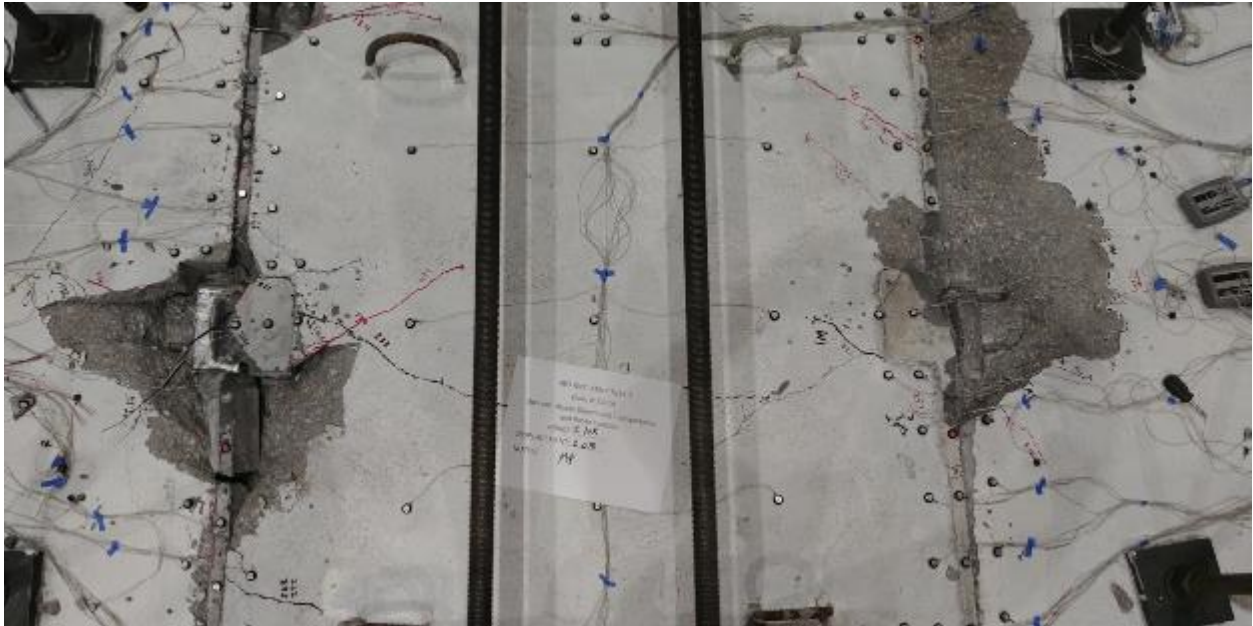


Figure 6.15: Test 7 Grouted Shear Key - Δ_{c8} -Third Cycle



Figure 6.16: Test 7 Damage to Left Side Shear Connector Insert at Δ_{c6} -Third Cycle



(a)



(b)



(c)



(d)

Figure 6.17: Test 7 Test 6 Removed Shear Connector Plate (a) Top View Left Connector (b) Bottom View Left Connector (c) Top View Right Connector (d) Bottom View Right Connector

6.1.2 Test 7 Conclusion

The focus of the test was to examine the effects of grout bond strength through surface preparation of the grouted shear key. AKDOT requires grout to be applied as directed by the manufacturer, which typically states that the grout is applied to sound and roughened concrete. In the case of this test, bond strength between the grout and the shear key was reduced by skipping preparation to the shear key as seen in Figure 6.18. Damage development throughout the test was similar to Test 5, where damage was concentrated in the side blocks. This led to an earlier onset of rebar fracture, which occurred at Δc_6 , approximately +/- 0.6 inches. The expected capacity was 232 Kips, which was achieved just prior to significant strength loss making the ratio of the maximum recorded load over the expected maximum load equal to 1.0. When the ratio of the maximum recorded load over the expected maximum load is compared to previous tests, the tests with a prepared surface had at least a 20% greater capacity. If that ratio was applied to the maximum load of Test 7, the capacity of the joint would be anticipated to be 46 kips larger which translates to the ability to reach an additional 0.5k/in $q_{average}$. Test 7 can also be compared with Test 1b and Test 2 to provide more insight. Due to these tests being welded into place prior to surface preparation, only the bottom faces of the shear key were accessible. So opposed to the full diamond shape being roughened, a V-shaped was roughened. Test 1b achieved a load ratio of 1.12 kips, while Test 2 achieved a ratio of 1.06. While one test may not be enough to determine the exact impact of a reduction in bond strength, there does appear to be an effect.



Figure 6.18: Variance in Surface Preparation of the Shear Key

6.2 Test 8

Test 8 was performed at the CFL at NCSU on January 14, 2019. Test 8 was constructed with the alternative connection shown in Figure 6.19. This section presents the overall response of the specimen and then discusses experimental procedures, results and observations in chronological order. The displacement history measured at the center of the specimen is displayed in Figure 6.20. Complementary to the displacement history, the specimen load history is presented in Figure 6.21. Additionally the complete load-displacement response and rigid body rotation versus displacement of the specimen measured at the center of the specimen can be seen in Figure 6.22 and Figure 6.23 respectively.

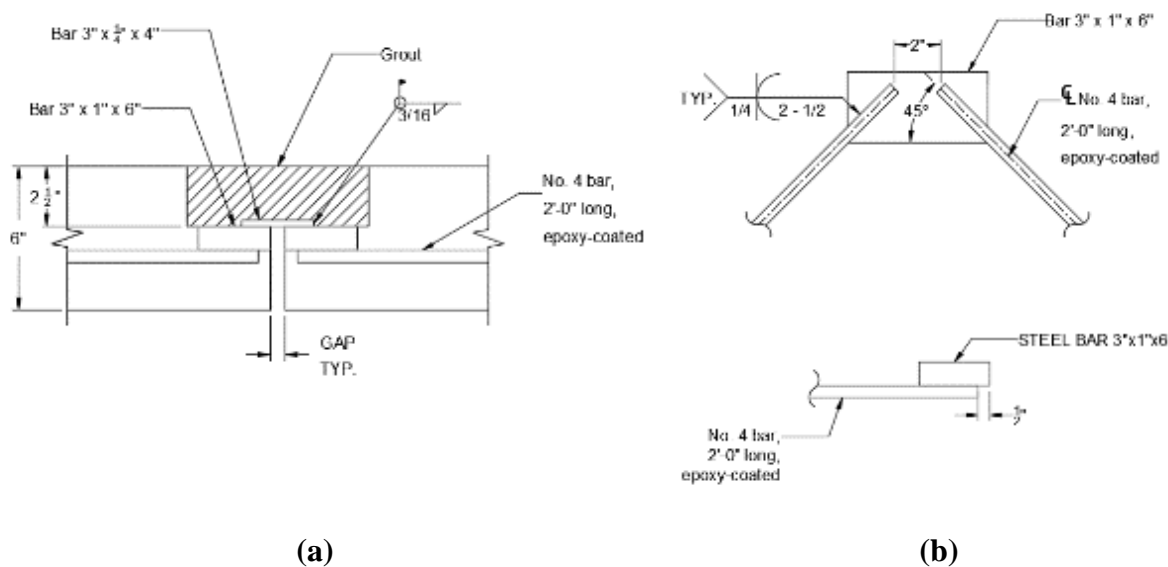


Figure 6.19: Alternate Shear Connector Detail 1 (a) Side View (b) Shear Connector Inserts

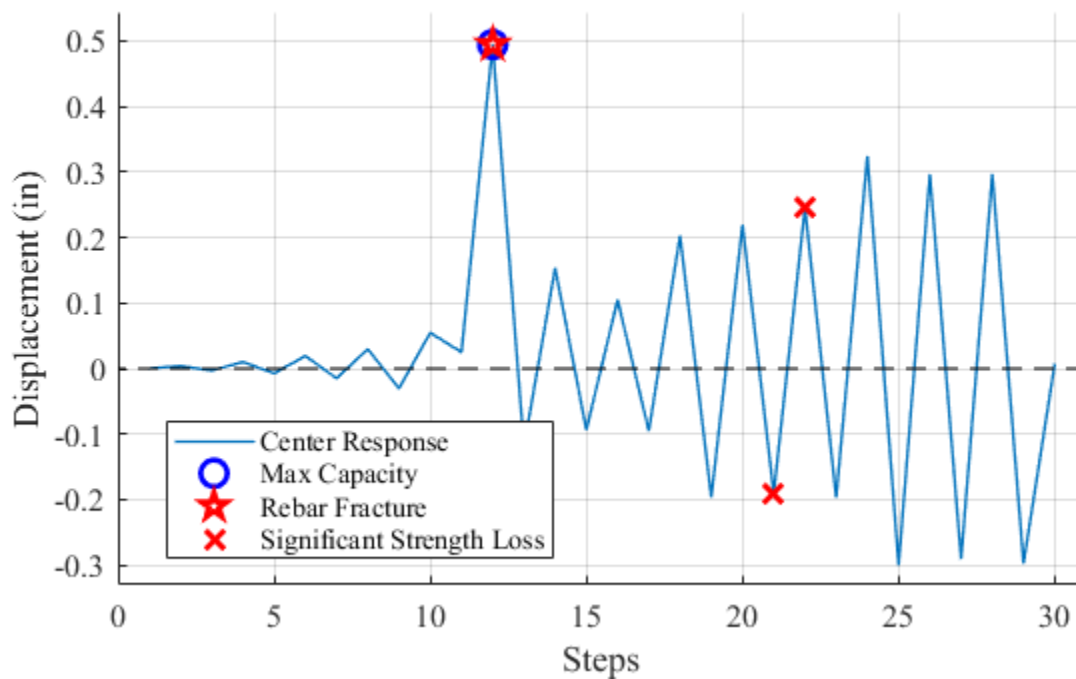


Figure 6.20: Test 8 Displacement History

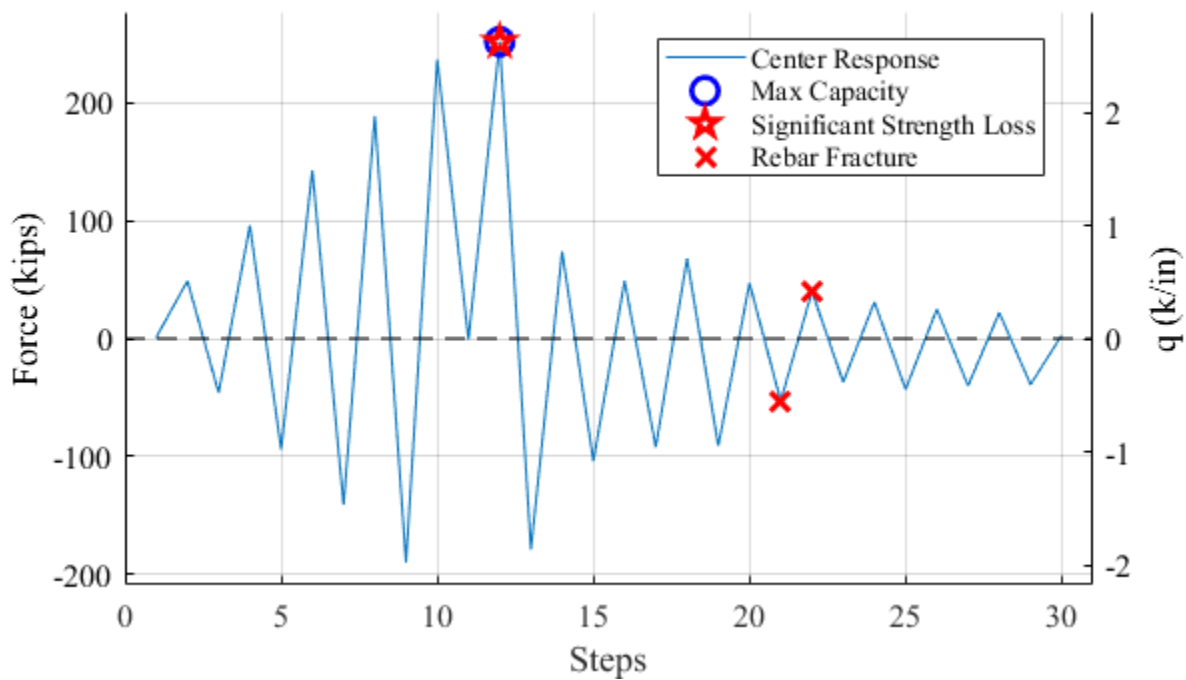


Figure 6.21 : Test 8 Load History

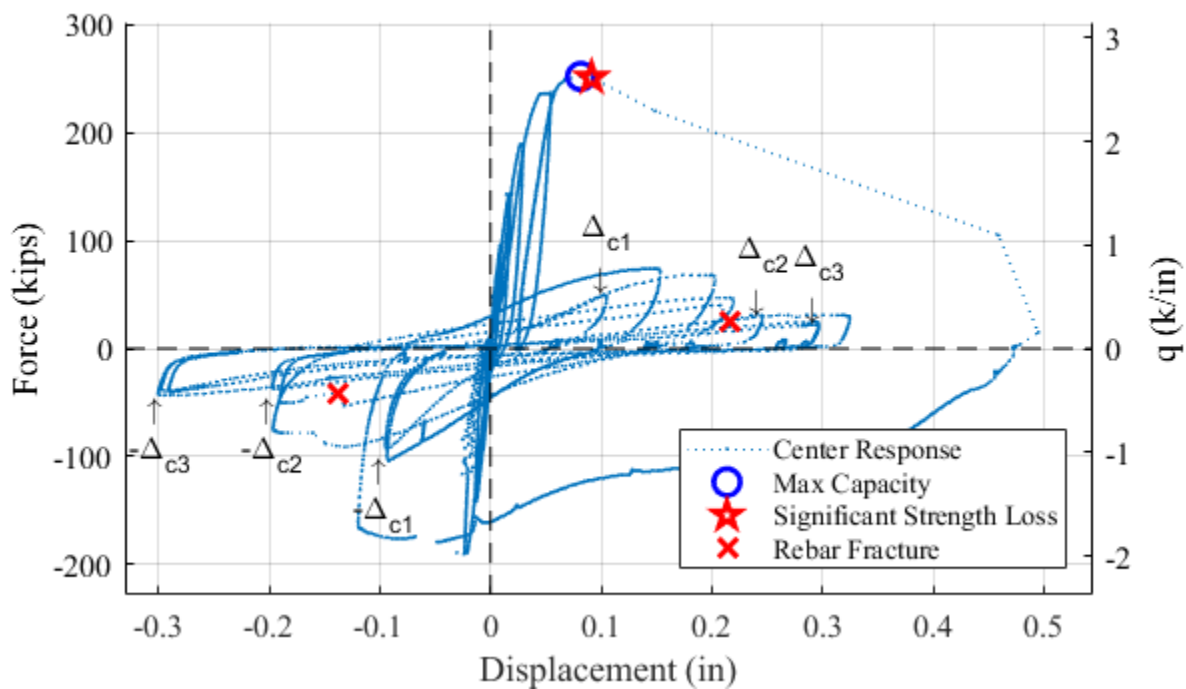


Figure 6.22: Test 8 Force-Displacement Response

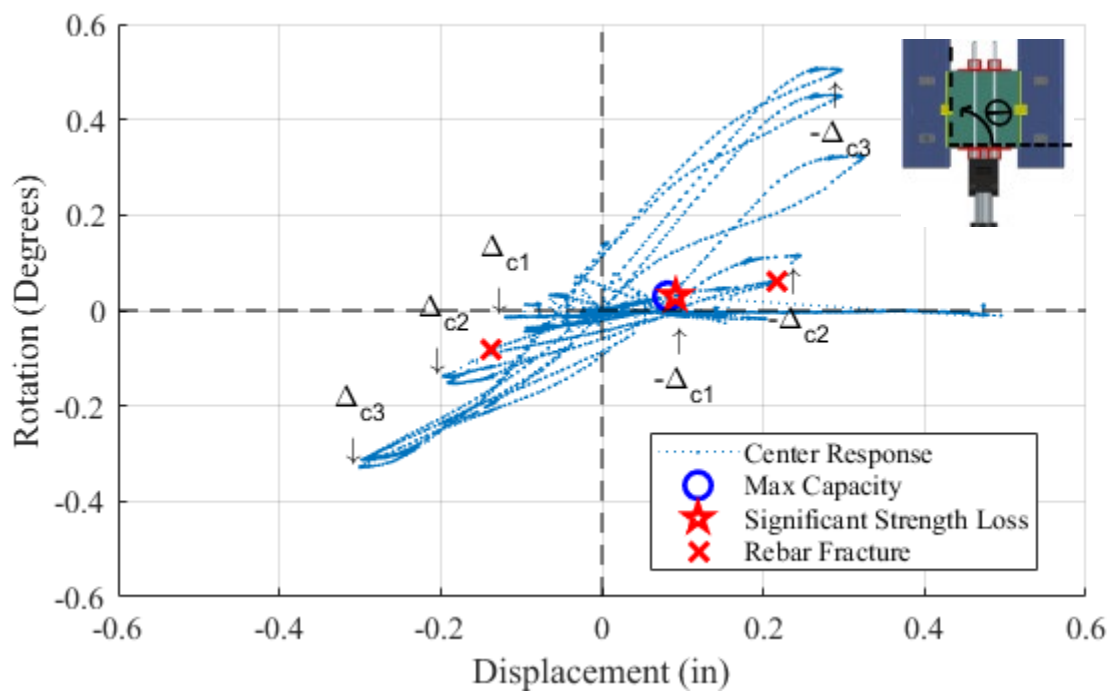


Figure 6.23: Test 8 Rigid Body Rotation

6.2.1 Test 8 Summary

Force was applied cyclically in single cycle sets, at increments of 48 kips ($q_{\text{average}} = 0.5 \text{ k/in}$). Prior to loading, longitudinal shrinkage cracking was prevalent in the grout of both joints as seen in Figure 6.24. Additionally, diagonal cracks were present in both side blocks, likely due to removal of the formwork. A crack propagated from each corner of the shear pocket in the left side block, while only one diagonal crack formed in the right pocket. During the first increment of loading, the right shear pocket also developed two diagonal cracks at the corners, mirroring the left pocket (Figure 6.25). The first crack in the specimen developed during the second increment of loading. This equated to a force of 96 kips ($q_{\text{average}} = 1.0 \text{ k/in}$). The displacement at the center of the specimen was 0.010 inches with a rigid body rotation of -0.004° . The crack propagated from the corner of the right shear pocket towards the direction of loading. In the pull portion of the cycle, a similar crack formed in the opposite corner of the right pocket. Additionally, the first signs of cracking inside the grouted pocket appeared. The damage can be seen in Figure 6.26. At a load of -144 kips ($q_{\text{average}} = 1.5 \text{ k/in}$), the displacement at the center of the specimen was -0.014 inches and the rigid body rotation was -0.004° . Similar to the right side of the specimen, the shear pocket on the left side developed diagonal cracking towards the direction of loading. Cracks were also prevalent at the interface between grout and the concrete along the perimeter of the shear pockets (Figure 6.27). As the load increased to 192 kips, the length of diagonal cracks grew but no new significant cracks formed.

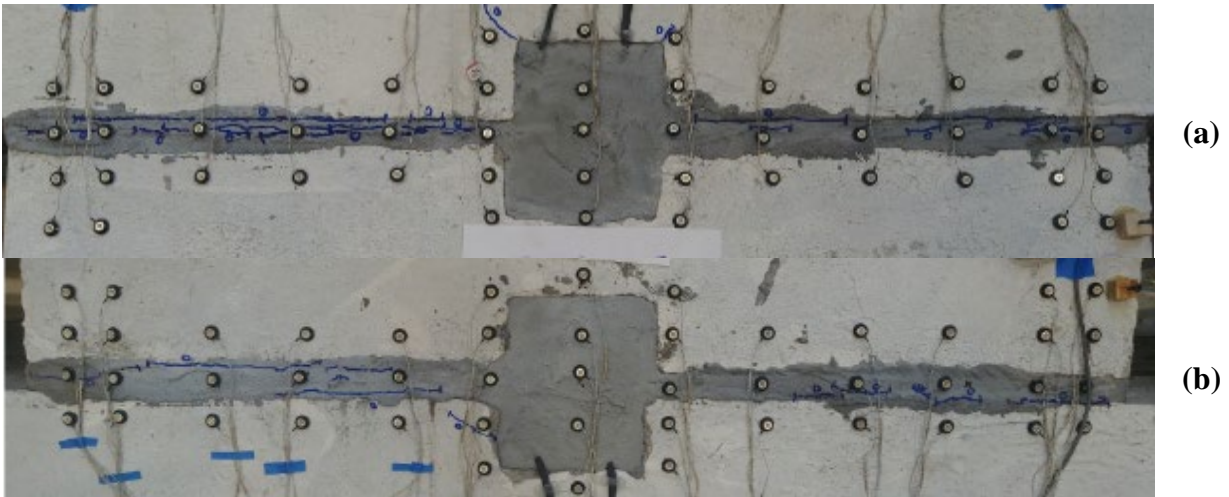


Figure 6.24: Test 8 Grouted Shear Key with Applied Load = 0 kips (a) Left Side (b) Right Side

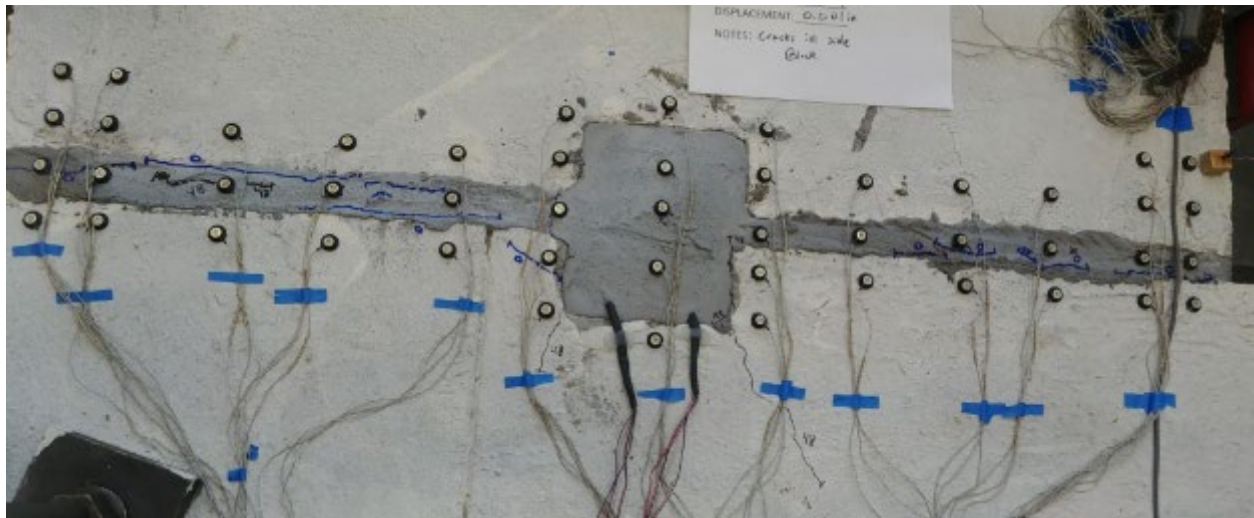


Figure 6.25: Test 8 Right Side of Grouted Shear Key with Applied Load = 48 kips

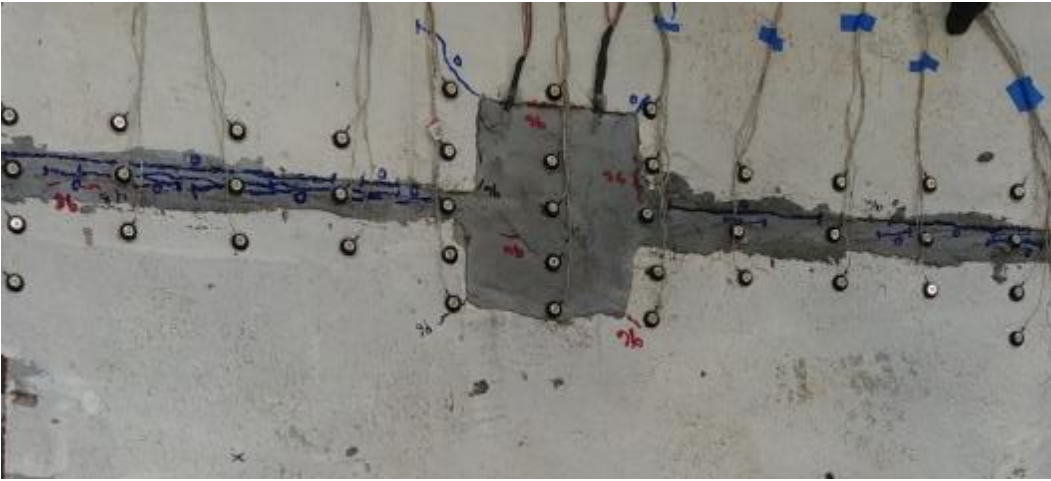


Figure 6.26: Test 8 Left Side of Grouted Shear Key with Applied Load = -96 kips

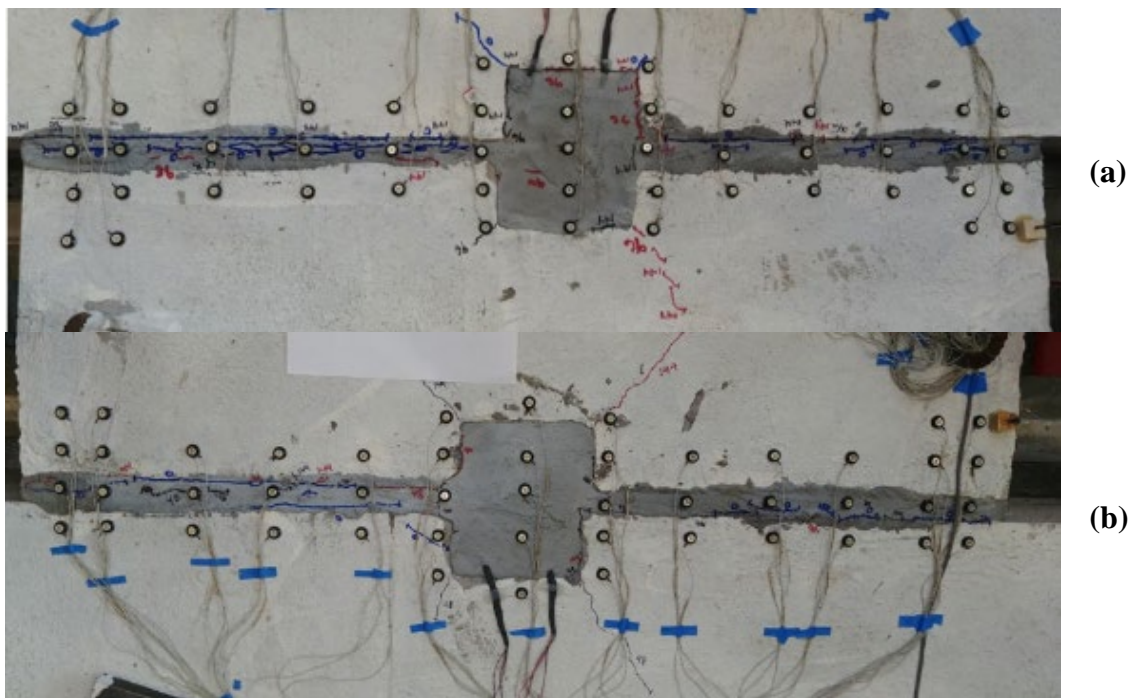


Figure 6.27: Test 8 Grouted Shear Key with Applied Load = 144 kips (a) Left Side (b) Right Side

During the push cycle of 240 kips ($q_{\text{average}} = 2.5\text{k/in}$), diagonal cracks formed inside the right shear pocket while existing diagonal cracks in the specimen grew. At this point the displacement at the center of the specimen was 0.055 inches and the rigid body rotation was -0.019° . While the load was being held, creep was prevalent so the load was taken off to mark cracks and take pictures. Damage can be seen in Figure 6.28. It was then decided to continue the test in the push direction to get a more desirable residual displacement after loss of strength occurs in the specimen. By doing so, there is less displacement stored in axial shortening of the test setup than there would be in axial elongation of the test setup and consequently a decrease in displacement of the specimen before the actuator limit is reached. Another load increment was applied corresponding to a total load 298 kips. However, the specimen only reached 252 kips with a displacement of 0.086 inches and a rigid body rotation of 0.030° at the center of the specimen right before strength loss occurred. At the end of the loading the center of the specimen reached a displacement of 0.495 inches with a rigid body rotation of -0.011° while maintaining a residual strength of 15 kips. Spalling of the grout occurred in both pockets with cracks running down the entire length of both joints. Cracks associated with uplifting of the cover concrete developed in two locations. One on the left side block on the opposite side of the actuator and the second on the right side of the specimen near the actuator. Damage accumulation can be seen in Figure 6.29.

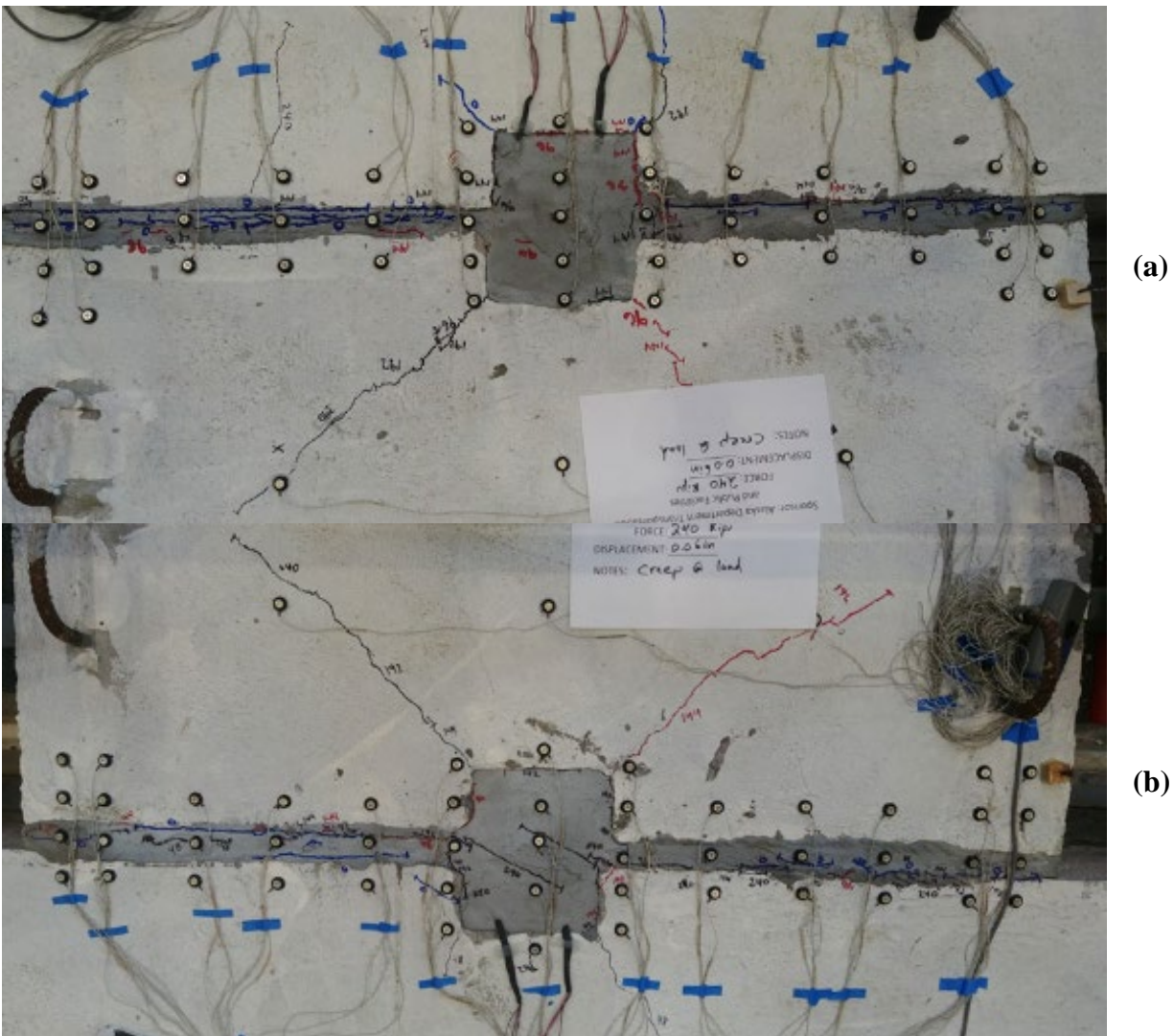


Figure 6.28: Test 8 Grouted Shear Key with Applied Load = 240 kips (a) Left Side (b) Right Side

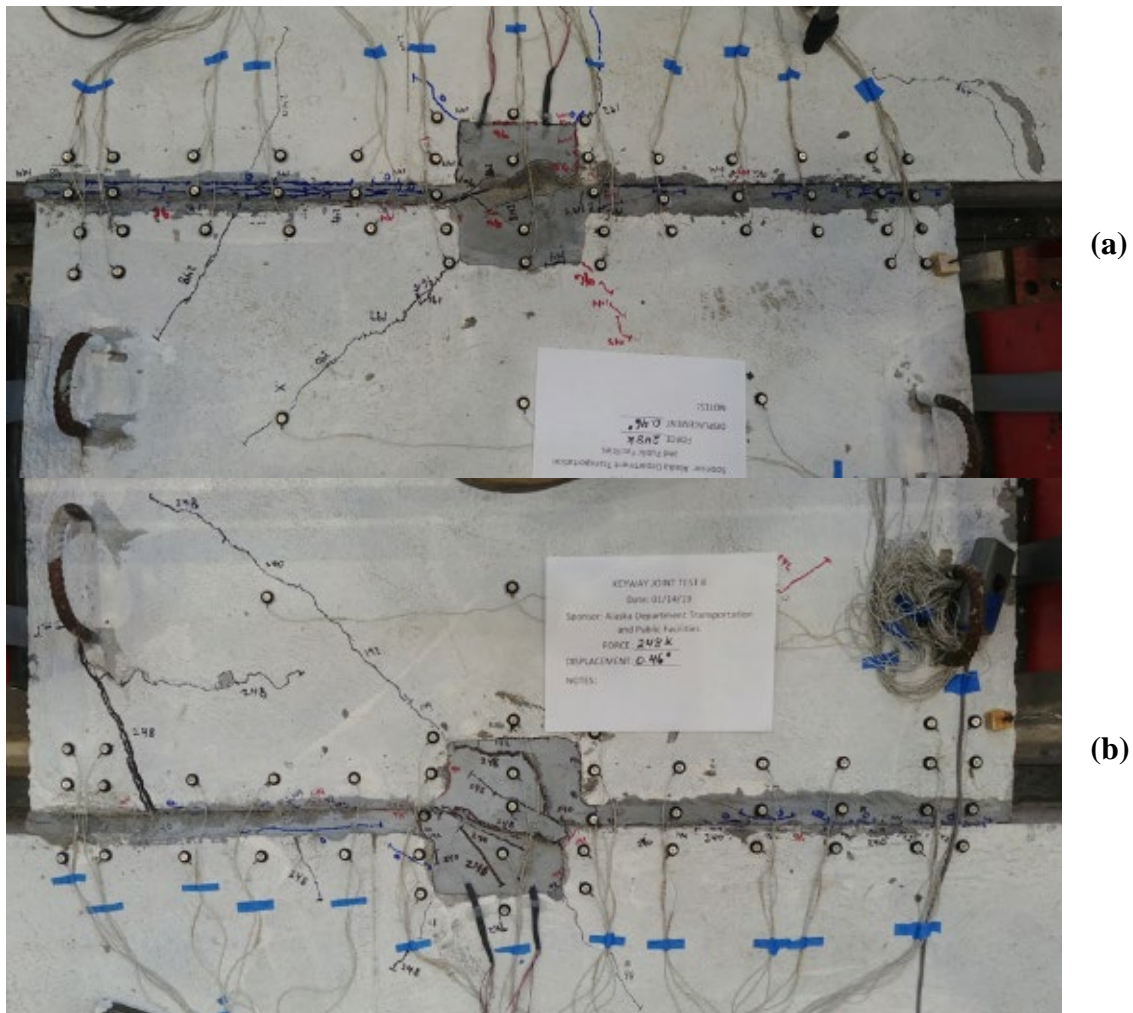


Figure 6.29: Test 8 Grouted Shear Key – Significant Strength Loss (a) Left Side (b) Right Side

The actuator was then switched to displacement control. The displacement at significant strength loss was estimated at 0.100 inches, which was used to define the displacement of significant strength loss of the joint, Δ_{c1} . Demand was applied in three cycle sets at increments proportional to Δ_{c1} . Due to the unpredictability of controlling the actuator displacement, the rate of loading was reduced and the displacement of the center of the specimen was monitored manually to conclude the loading for each cycle. During the first pull cycle of Δ_{c1} , additional cracking associated with cover concrete uplift formed on the right side block. Existing diagonal cracking continued to propagate towards the load and a new diagonal crack appeared stretching across the right keyway pocket into the specimen (Figure 6.30). The displacement at the center



Figure 6.31: Test 8 Grouted Shear Key - Δ_{c1} –Third Cycle

During the first push cycle of Δ_{c2} , the cover concrete surrounding the right joint spalled off from the previously mentioned cracks as seen in Figure 6.32. New cracks associated with cover concrete spalling formed around the right pocket in the side block. The displacement at the center of the specimen was 0.203 inches with a rigid body rotation of -0.018° and a force of -63 kips. The following pull cycle exposed the right pocket shear connector. The displacement at the center of the specimen was -0.197 inches with a rigid body rotation of -0.138° and a force of -73 kips. During the second push cycle, the embedded rebar became visible (Figure 6.33). No rebar bending was visible. The displacement at the center of the specimen was 0.220 inches with a rigid body rotation of -0.059° and a force of 43 kips. During the subsequent pull cycle, one of the embedded rebar welded to the right shear connector embedded in the side block fractured. The fracture is visible in Figure 6.34. Also visible is the damage to the $\frac{1}{4}$ in. x 3 in. x 4 in. welded shear tab, which shows a shear fracture in the plate. The displacement at the center of the specimen was -0.191 inches with a rigid body rotation of -0.151° and a force of -49 kips. Upon the next push cycle, the other exposed rebar in the right side block fractured (Figure 6.35). The displacement at the center of the specimen was 0.246 inches with a rigid body rotation of 0.115° and a force of 28 kips. On the last pull cycle of Δ_{c2} , cover concrete began to spall from the left joint as seen in Figure 6.36.



Figure 6.32: Test 8 Grouted Shear Key Δ_{c2} –First Cycle



Figure 6.33: Test 8 Right Shear Connector Δ_{c2} –Second Cycle



Figure 6.34: Test 8 Damage to the Right Shear Connector $-\Delta_{c2}$ –Second Cycle



Figure 6.35: Test 8 Damage to Right Shear Connector Δ_{c3} –Third Cycle

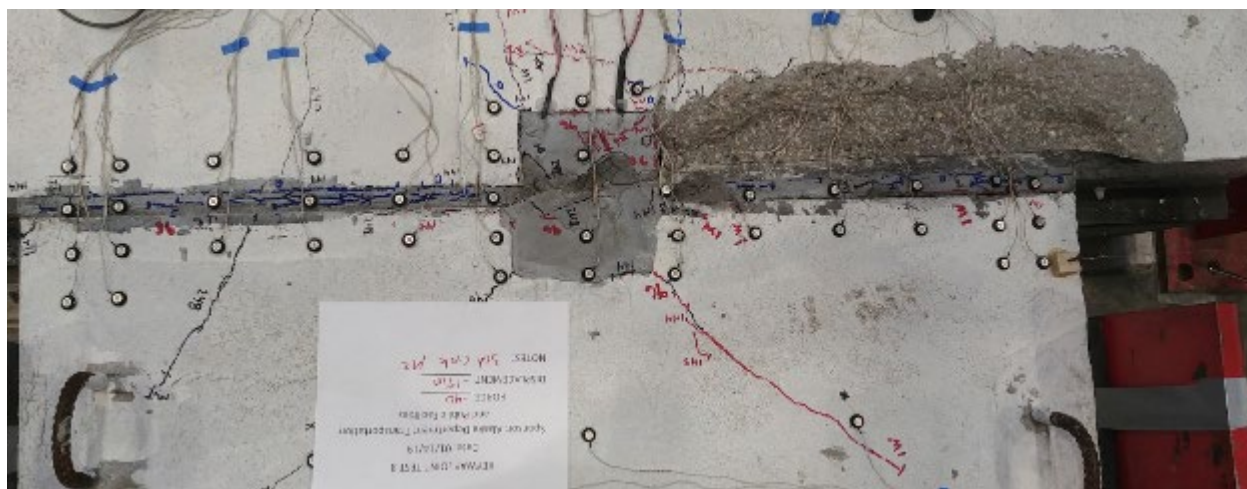


Figure 6.36: Test 8 Left Side of Grouted Shear Key - Δ_{c3} –Third Cycle

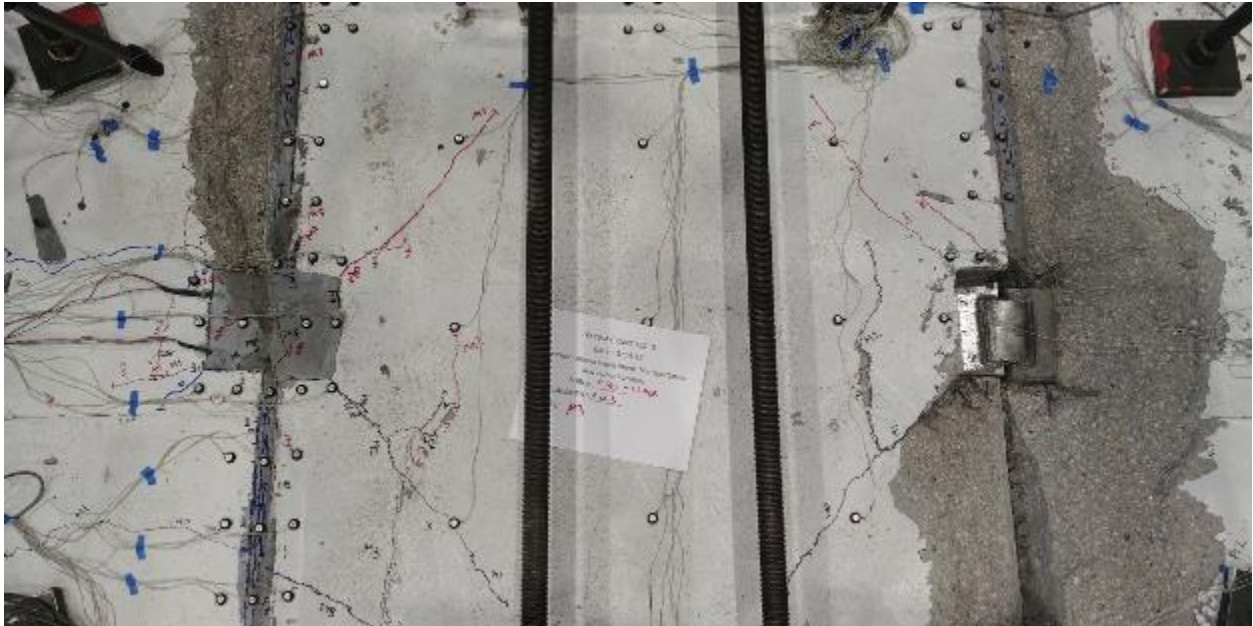


Figure 6.37: Test 8 Grouted Shear Key Δ_{c3} - Third Cycle

The displacement increased to Δ_{c3} . During these cycles, rotation about the left joint became prevalent. There was also little observable damage to the specimen, thus the test was terminated. The final state of the specimen can be seen in Figure 6.37. The shear connector plates were removed from the specimen to reveal the welds as seen in Figure 6.38. All of the welds involving the rebar were undamaged except for minor damage near the ruptured rebar. All of the welds for the plate to plate connection also remain undamaged except for a shear fracture propagating from the shear fracture of the shear tab itself.

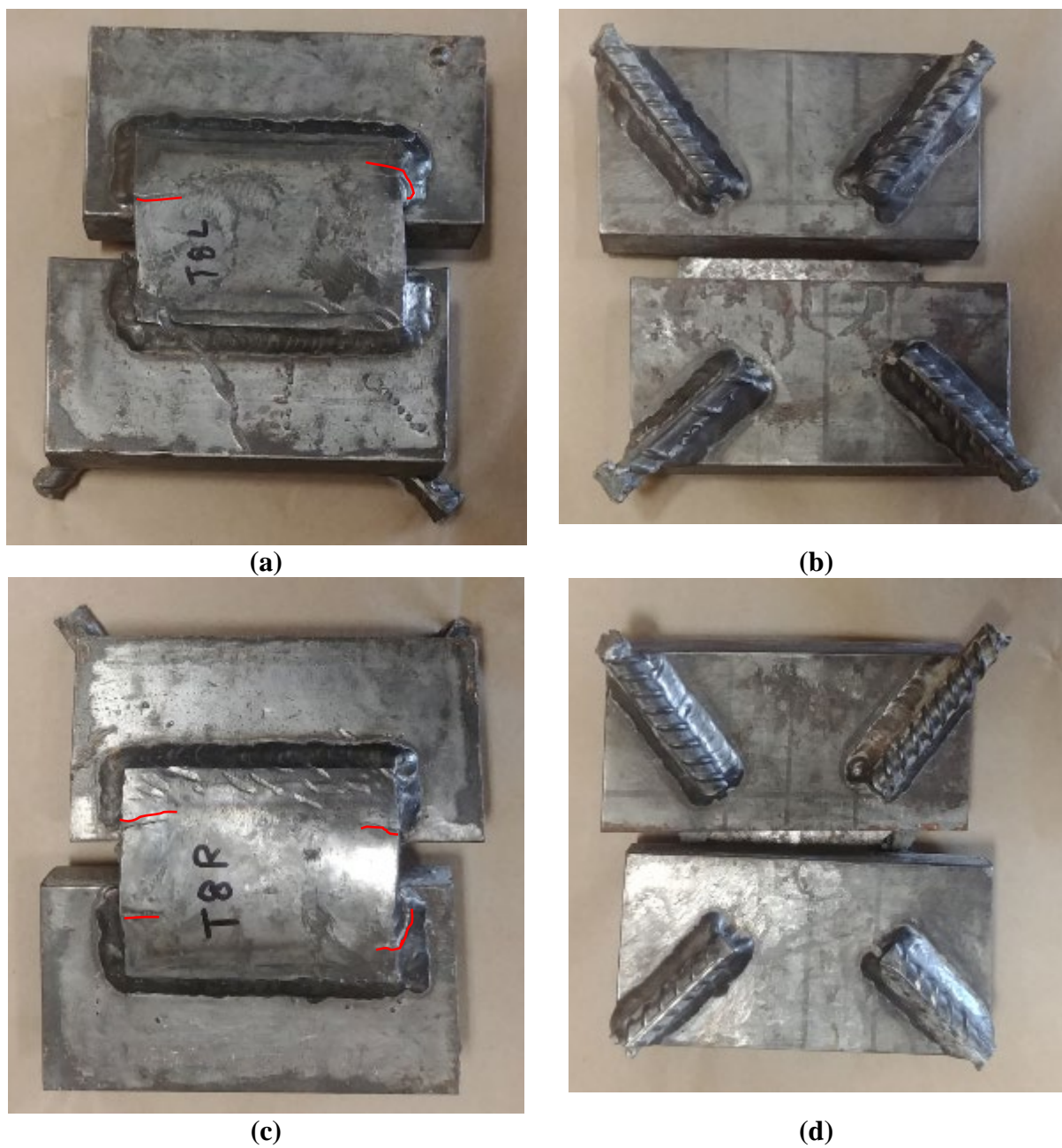


Figure 6.38: Test 8 Removed Shear Connector Plate (a) Top View Left Connector (b) Bottom View Left Connector (c) Top View Right Connector (d) Bottom View Right Connector

6.2.2 Test 8 Conclusion

The focus of the test was to examine an alternative shear connector insert to prolong damage accumulation of the joint and provide more residual strength after the maximum strength capacity is reached. The detail for the alternate joint is shown in Figure 6.19. Test 8 is best compared against Test 5 since both tests had large displacements occur right after the peak grout strength was reached and Test 8 has the closest grout strength to Test 5. While the ratio of maximum recorded loads over the expected maximum loads are similar, 1.31 and 1.29 for Test 8 and Test 5 respectively, the damage accumulated after the maximum load is reached is quite different. Test 8 reached a displacement of 0.495 inches with a rigid body rotation of -0.011° while maintaining a residual strength of 15 kips. Test 5 reached a displacement of 0.665 inches with a rigid body rotation of 0.047° and a residual load of -8 kips. Comparing the damage, Test 8 had spalling of the grout concentrated in the pockets and two places of cracking that are linked to cover concrete spalling, but which occurred away from the pocket. Test 5 on the other hand had cover concrete spalling down the entire joint in both in both side blocks, with grout spalling concentrated in the pockets. Additionally, examining Test 2, the monotonic test of the original connection, at a similar displacement to Test 8 saw similar damage. The difference between Test 8 and Test 2 was that cracks associated with spalling in Test 2 form around the shear pocket rather than on the ends of the joint. Test 2 had a displacement at the center of the specimen of 0.478 inches with a rigid body rotation of 0.089° and a load of 47.8 kips. A comparison of damage between Test 2, Test 5 and Test 8 can be seen in Figure 6.39.

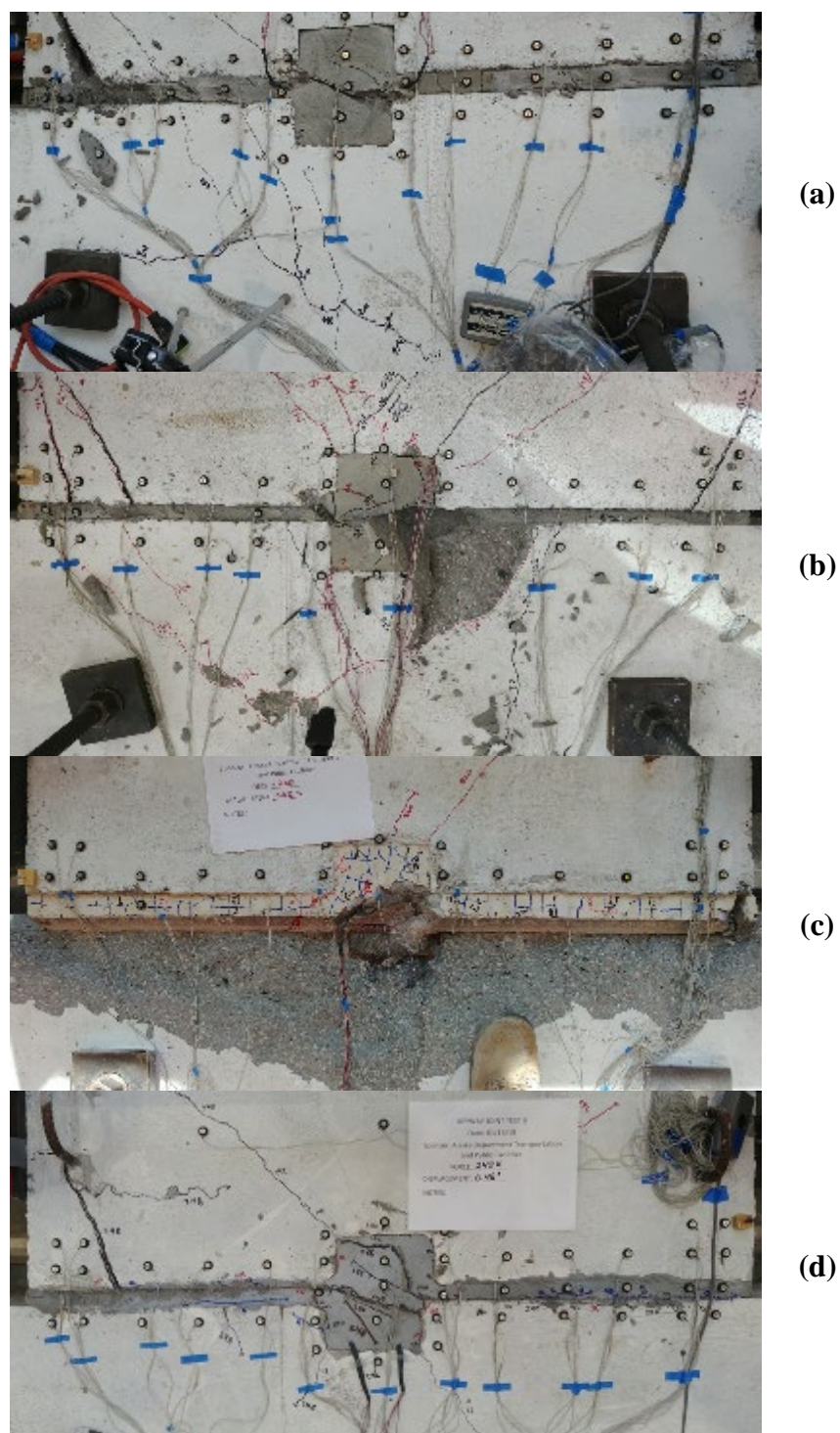


Figure 6.39: Comparison of Damage at $\Delta \approx 0.5$ in. (a) Test 2 (b) Test 4 (c) Test 5 (d) Test 8

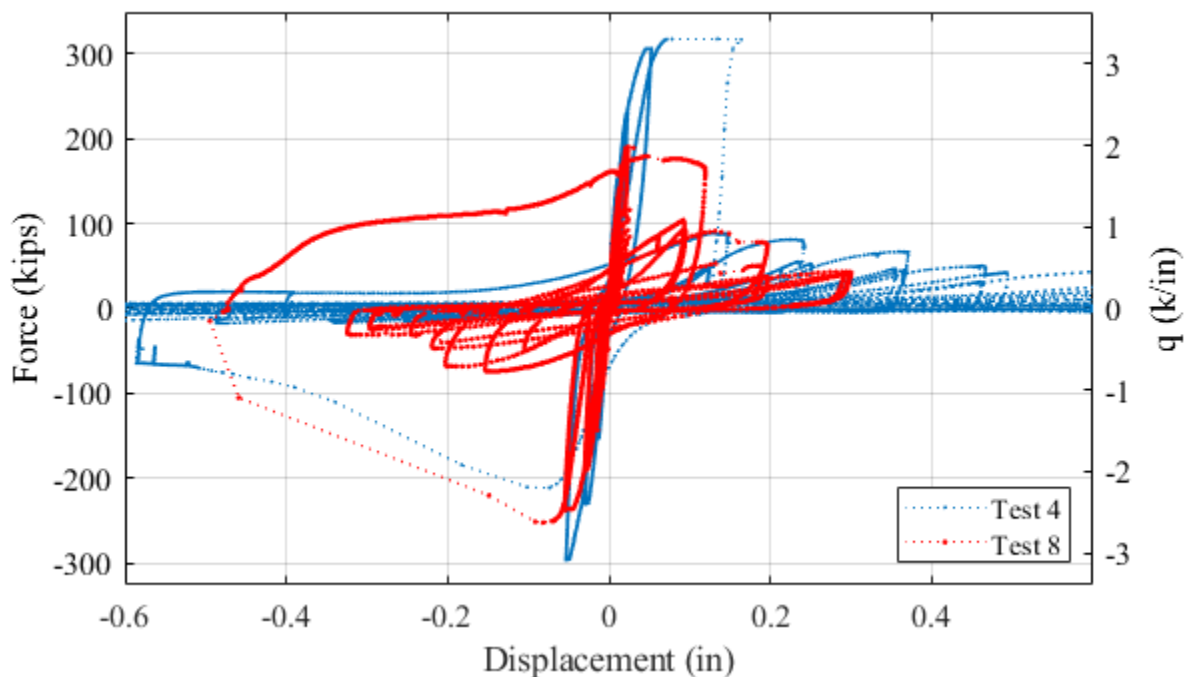


Figure 6.40: Force-Displacement Response Comparison of Test 4 and Test 8 (Rotated)

Test 4 also has a similar displacement history as Test 8. The main difference is that Test 4's joints failed separately. During a push cycle the left failed with relatively low displacement but during the following pull cycle the right joint failed and as it did the center of specimen displacement reached -0.586 inches with a rotation of -0.058° and a load of -64 kips. The damage accumulated in the pull cycle was significantly more than Test 8, with large cracks along the length of both joints associated with cover concrete spalling (Figure 6.39). Figure 6.40 shows a comparison of the force-displacement curves of both tests. It should be noted that Test 8 has been rotated 180° for ease of comparison. It can be seen that after the initial large displacement, there is similar residual strength in both the positive and negative displacement direction of Test 8, but Test 4 only provides residual strength in the positive displacement direction. Only when the displacement exceeds the previously reached displacement in the negative direction is there an increase in strength.

Additionally, Test 8 shows a significant force upon the first reversal that can likely be attributed to shear yielding/fracture of the shear tab, which has not been seen previously. It should be noted that the failure mechanism of the embedded rebar also transitioned from one of bending to axial loading and bar fracture. This has reduced the specimen displacement before bar

fracture is achieved. Where previous tests showed bar fracture to occur at a displacement of roughly +/-0.6 inches in single bending and +/-1.2 inches in double bending, Test 8 had bar fractures occur at roughly 0.2 inches.

6.3 Test 9

Test 9 was performed at the CFL at NCSU on February 08, 2019. Test 9 was constructed with the alternative connection seen in Figure 6.41. This section presents the overall response of the specimen and then discusses experimental procedures, results and observations in chronological order. The displacement history measured at the center of the specimen is displayed in Figure 6.42. Complementary to the displacement history, the specimen load history is presented in Figure 6.43. Additionally the complete load-displacement response and rigid body rotation versus displacement of the specimen measured at the center of the specimen can be seen in Figure 6.44 and Figure 6.45 respectively.

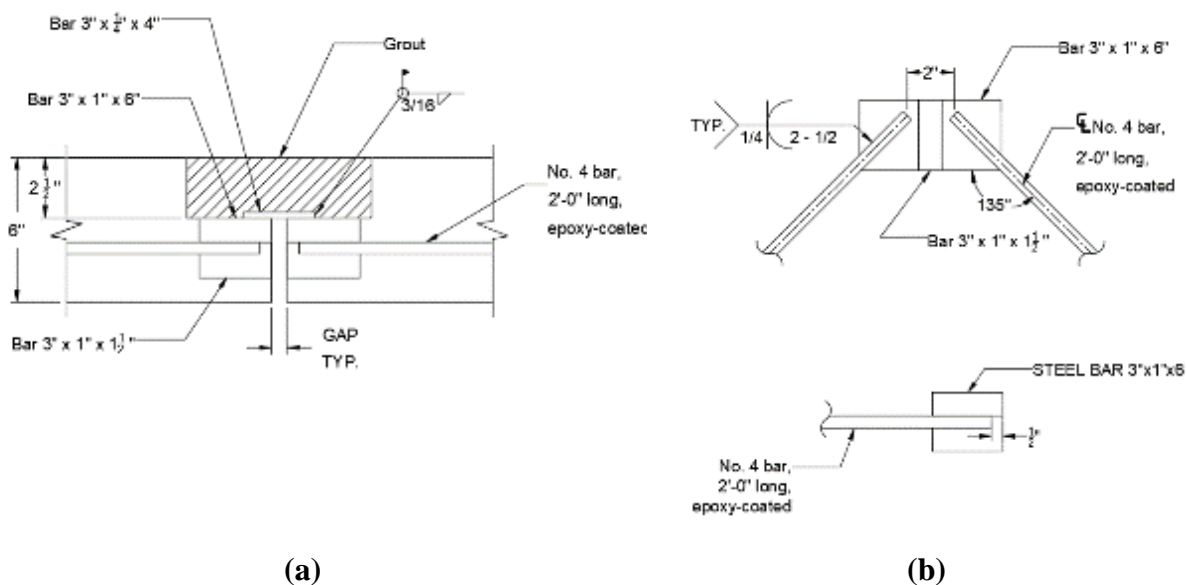


Figure 6.41: Alternate Shear Connector Detail 2 (a) Side View (b) Shear Connector Inserts

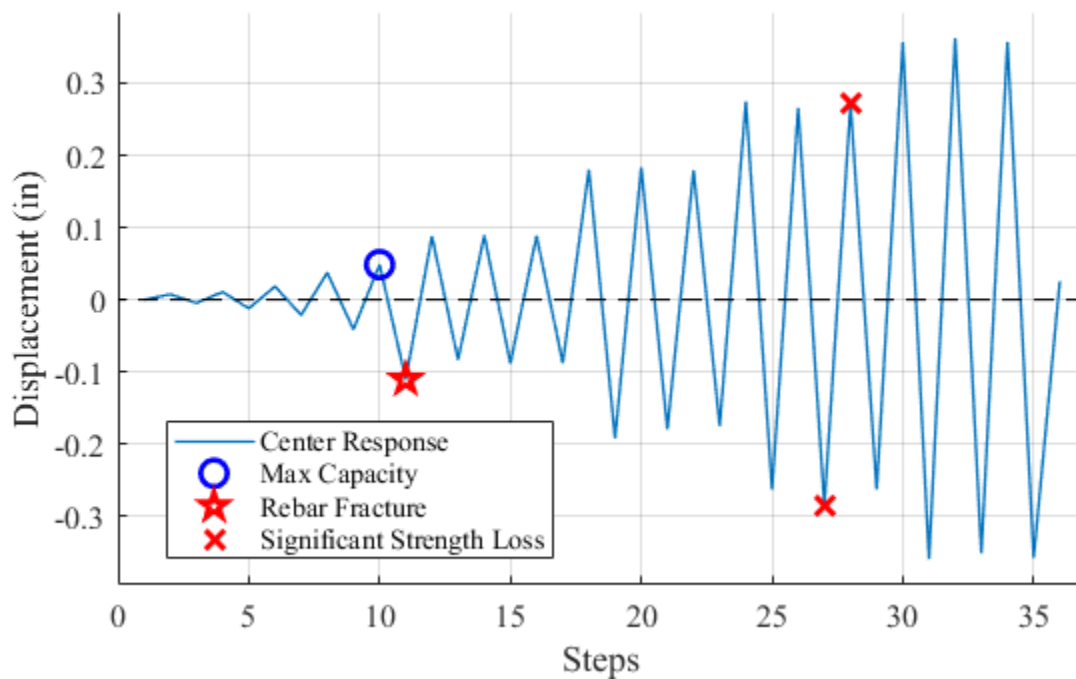


Figure 6.42: Test 9 Displacement History

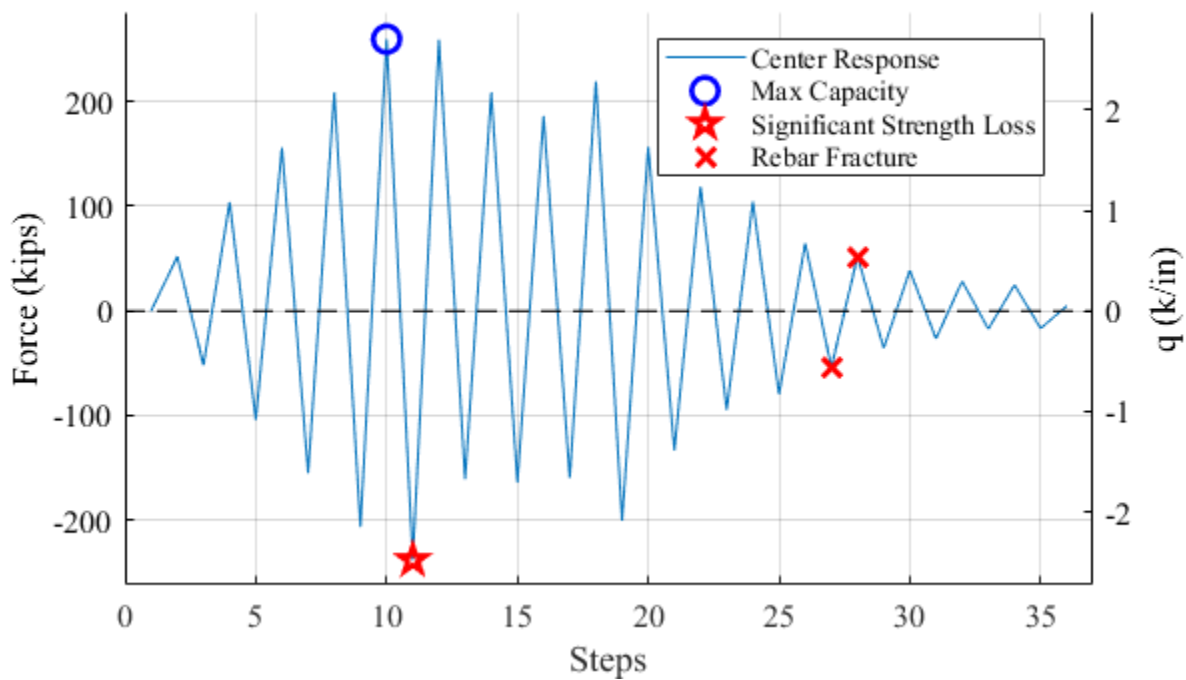


Figure 6.43: Test 9 Load History

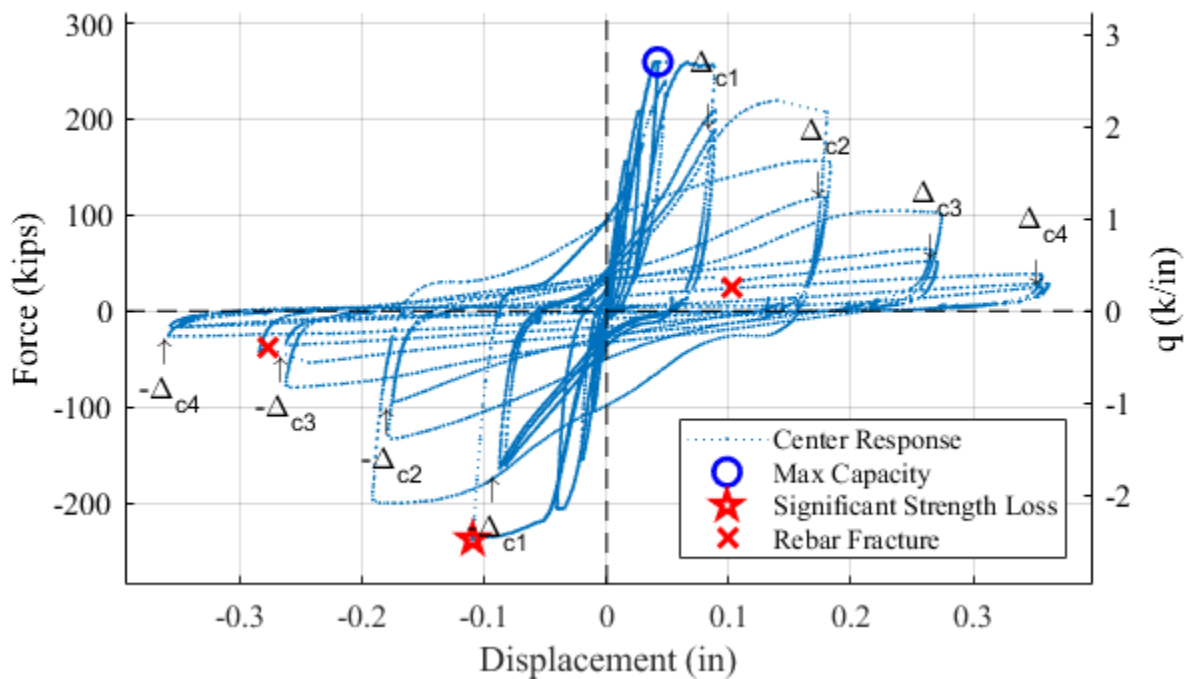


Figure 6.44: Test 9 Force-Displacement Response

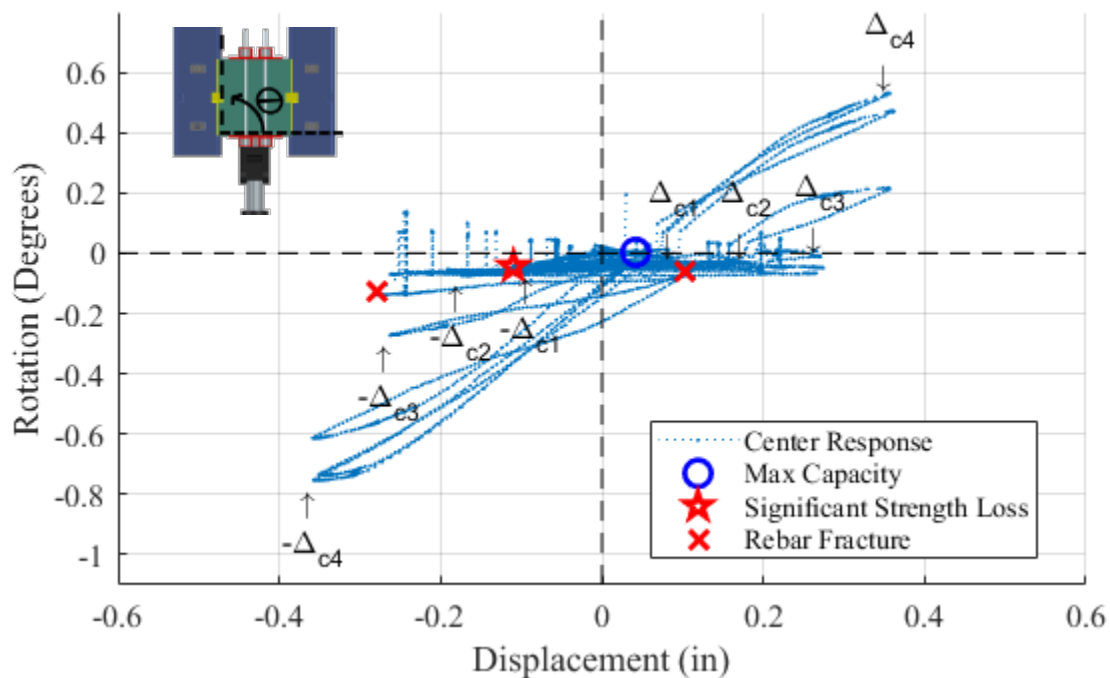


Figure 6.45: Test 9 Rigid Body Rotation

6.3.1 Test 9 Summary

Force was applied cyclically in single cycle sets, at increments of 53 kips ($q_{\text{average}} = 0.5 \text{ k/in}$). Prior to loading, cracking was present in the corner of both side blocks as seen in Figure 6.46. Minor damage occurred during the first two increments of loading, which comprised of minor cracks along the joint at the grout concrete interface. The first crack in the specimen occurred at a load of 156 kips ($q_{\text{average}} = 1.6 \text{ k/in}$), displacement at the center of the specimen was 0.018 inches with a rigid body rotation of 0.001° . The crack propagated from the right shear pocket corner towards the direction of loading (Figure 6.47). A crack also formed around the perimeter of the right pocket. No damage was observed in the subsequent pull cycle. Upon the next increment of loading, diagonal cracking became more prevalent. The right pocket's existing diagonal crack grew in length, while the left pocket acquired a similar diagonal crack. The right pocket also attained two new diagonal cracks inside the side block. The load was 208 kips ($q_{\text{average}} = 2.2 \text{ k/in}$) with a displacement at the center of the specimen of 0.028 inches and a rigid body rotation of 0.003° . The succeeding pull had a force of -206 kips ($q_{\text{average}} = 2.2 \text{ k/in}$) with a displacement of -0.040 inches at the center of the specimen and a rigid body rotation of 0.022° . This created the first diagonal cracks associated with the pull direction, which formed in the specimen at the corner of the right shear pocket and right joint near the loading plate. More significantly was the formation of diagonal crack through the right shear pocket. Additional cracking occurred in both shear pockets, cutting across the joint and going around the perimeter of the pocket interface. Damage is visible in Figure 6.48. Another diagonal crack appeared in grout of the right shear pocket under the load of 260 kips (Figure 6.49). The displacement was 0.049 inches at the center of the specimen and a rigid body rotation of 0.005° . During the following reversal, the specimen achieved -238 kips before the strength began to reduce. The maximum recorded load over the expected maximum load ratio was equal to 1.2. The center of the specimen reached a displacement of -0.110 inches with a rigid body rotation of -0.044° . Cracking ran down the entire length of both joints, starting on the specimen side closet to the load and crossing the joint through diagonal cracks in the pockets to reach the side block. Damage can be seen in Figure 6.50.

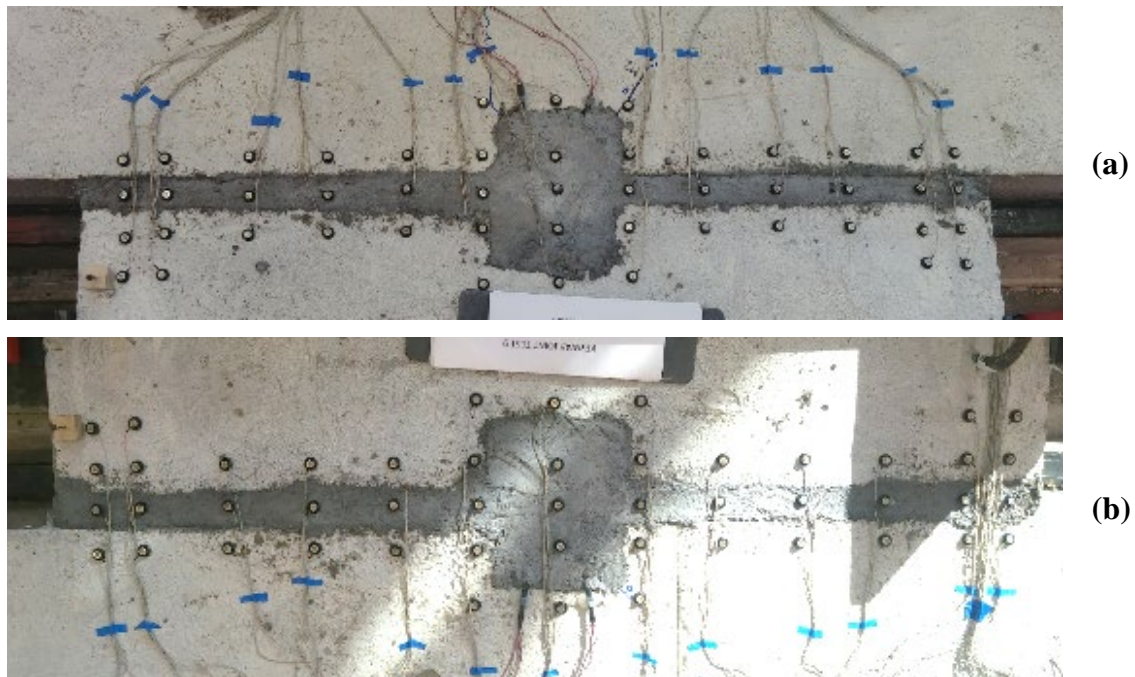


Figure 6.46: Test 9 Grouted Shear Key with Applied Load = 0 kips (a) Left Side (b) Right Side



Figure 6.47: Test 9 Right Side of Grouted Shear Key with Applied Load = 156 kips

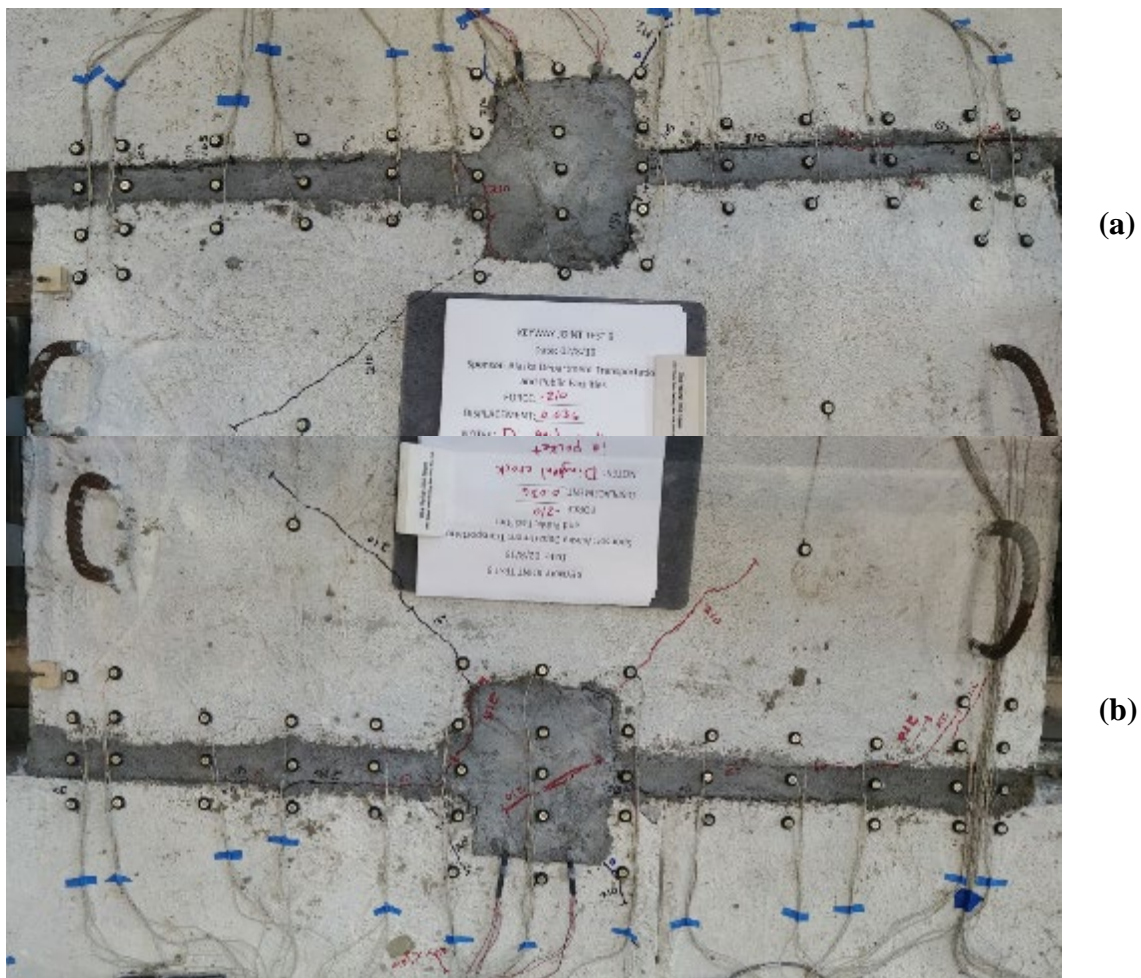


Figure 6.48: Grouted Shear Key with Applied Load = -206 kips (a) Left Side (b) Right Side

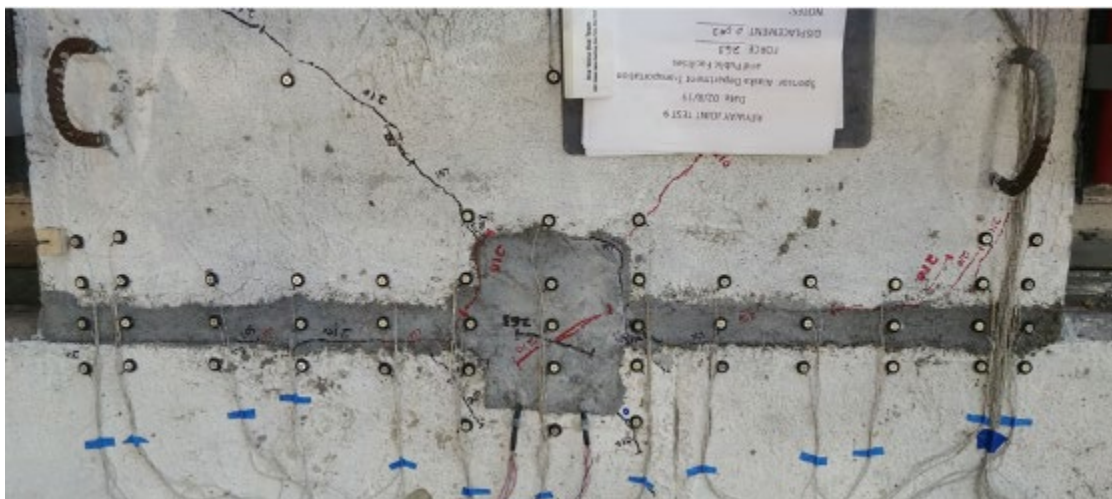


Figure 6.49: Grouted Shear Key with Applied Load = 260 kips (a) Left Side (b) Right Side



Figure 6.50: Grouted Shear Key – Significant Strength Loss (a) Left Side (b) Right Side

The actuator was then switched to displacement control. The displacement at significant strength loss was estimated at 0.090 inches, which was used to define the displacement at significant strength loss of the joint, Δ_{c1} . Demand was applied in three cycle sets at increments proportional to Δ_{c1} . Due to the unpredictability of controlling the actuator displacement, the rate of loading was reduced and the displacement of the center of the specimen was monitored manually to conclude the loading for each cycle. Little additional damage occurred during the first three cycles of Δ_{c1} (+/- 0.090 inches). At the end of the third cycle, the specimen displacement was -0.088 inches with a rigid body rotation of -0.047° and a force of -160 kips. The damage that did occur was concentrated in the pockets, with additional diagonal cracking and minor spalling (Figure 6.51). Similar damage occurred during the first cycle of Δ_{c2} , mainly consisting of spalling in the pocket and minor spalling of the cover concrete surrounding the pocket. Damage can be seen in Figure 6.52. The associated displacement was -0.179 inches with a rigid body rotation of -0.069° and a force of -130 kips. Upon the second push cycle of Δ_{c2} , cracking associated with cover concrete uplift occurred around the right pocket, in both the specimen and side block as shown in Figure 6.53. The center of the specimen reached a displacement of 0.179 inches with a rigid body rotation of 0.032° and a force of 115 kips. Minor additional cracking and associated cover concrete uplift occurred to the right side block during the remainder of Δ_{c2} . The last cycle of Δ_{c2} had a center of the specimen displacement of -0.175 inches with a rigid body rotation of 0.073° with a load of 89 kips.

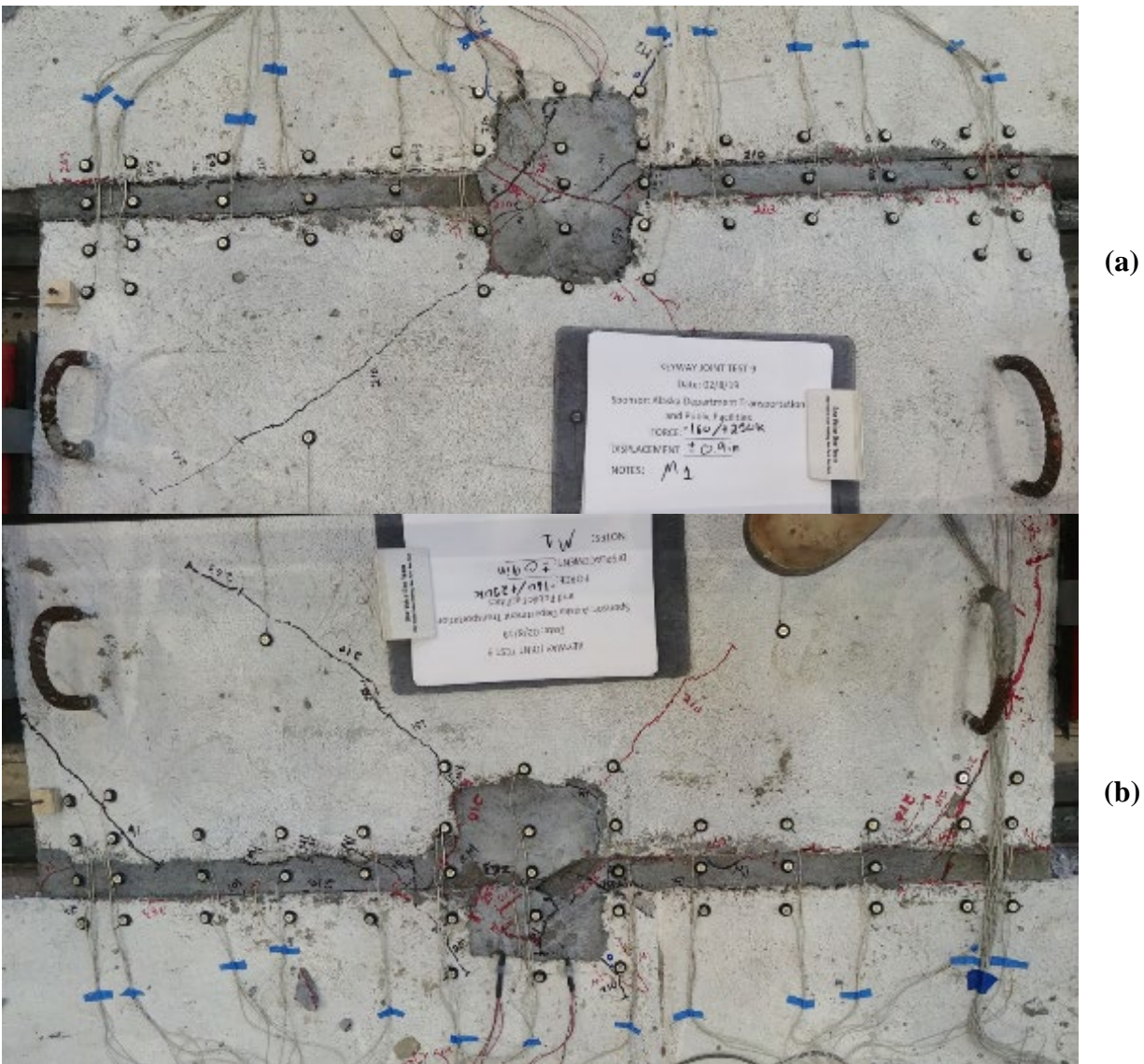


Figure 6.51: Grouted Shear Key at $-\Delta c_1$ -Third Cycle



Figure 6.52: Grouted Shear Key at $-\Delta c_2$ – First Cycle

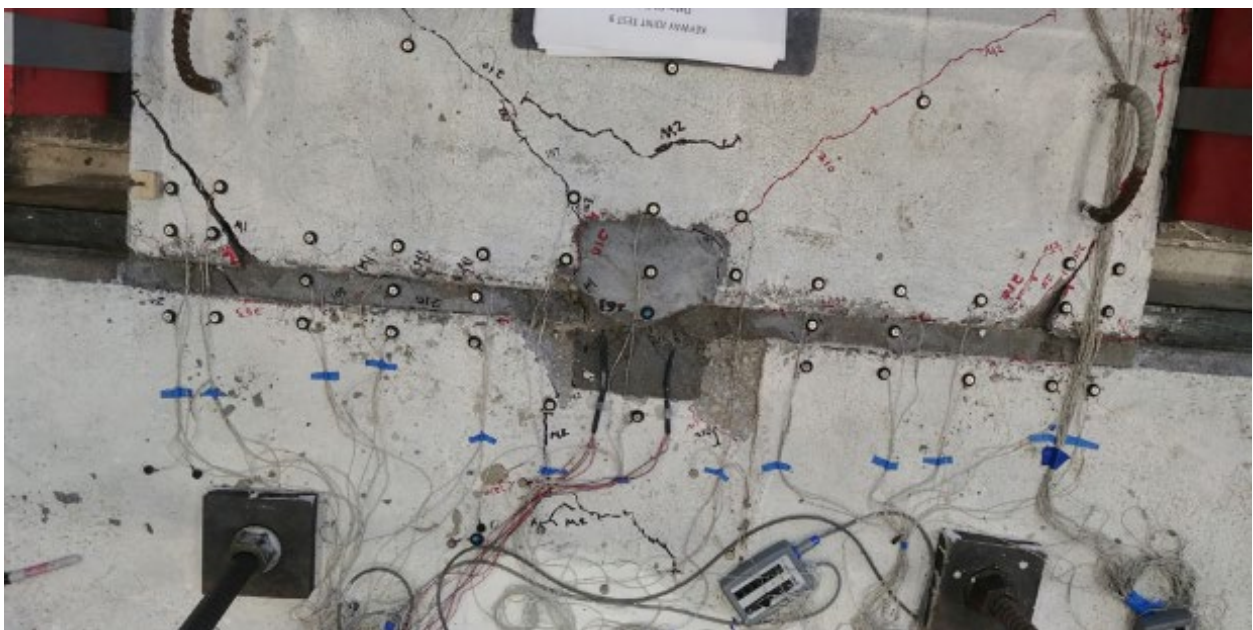


Figure 6.53: Right Side of Grouted Shear Key at Δc_2 – Second Cycle



Figure 6.54: Grouted Shear Key at Δ_{c3} –First Cycle



Figure 6.55: Grouted Shear Key at Δ_{c3} –Second Cycle

Upon the first push cycle of Δ_{c3} , significant cracking associated with cover concrete uplift began to occur in the left side block (Figure 6.54). The displacement was 0.274 inches at the center of the specimen with a rigid body rotation of -0.048° and a force of 99 kips. More cracking associated with cover concrete uplift occurred during the second push cycle of Δ_{c3} . Cracking ensued in the specimen along the left side as seen in Figure 6.55. Upon the following pull cycle, rebar fracture occurred causing the cover concrete on the right side block to debond and be removed (Figure 6.56). This exposed the right shear connector insert as seen in Figure 6.57. The embedded shear connector shows little sign of movement or damage. It was not clear which rebar fractured but was later confirmed as the embedded bar in the right side block farthest from the actuator ram. Additionally, minor shear fracture of the welded shear tab connecting the embedded shear connectors was noted. The displacement of the center of the specimen was -0.284 inches at the center of the specimen with a rigid body rotation of -0.137° and a force of -43 kips.



Figure 6.56: Grouted Shear Key at $-\Delta_{c3}$ –Second Cycle



Figure 6.57: Right Side Shear Connector Insert at $-\Delta_{c3}$ - Third Cycle

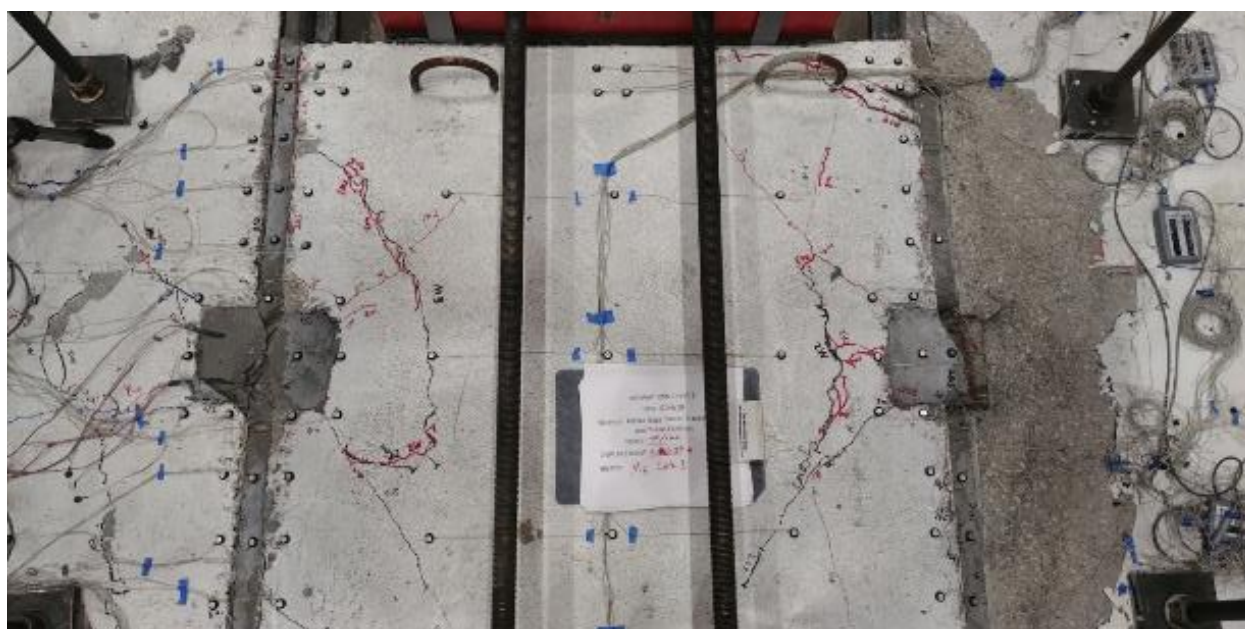


Figure 6.58: Grouted Shear Key at $-\Delta_{c3}$ - Third Cycle

During the subsequent push cycle, a second shear connector rebar fractured. It was not clear which bar fractured but was later confirmed as the shear connector rebar farthest from the actuator ram embedded in the right side of the specimen. The displacement of the center of the specimen was 0.271 inches with a rigid body rotation of -0.010° and a force of 50 kips. Little additional damage accumulated during the final cycle of Δ_{c3} as seen in Figure 6.58. During Δ_{c4} the right shear connector began to rotate and pry up the cover concrete on the right side of the specimen as seen in Figure 6.59. The displacement of the center of the specimen was -0.359 inches with a rigid body rotation of -0.613° and a force of -26 kips. Upon the third cycle, the specimen's right joint cover concrete could be removed, exposing the entire shear connector (Figure 6.60). The displacement of the center of the specimen was 0.362 inches with a rigid body rotation of 0.529° and a force of 24 kips. The test was terminated after the third cycle of Δ_{c4} due to large rotations. The final state of the specimen can be seen in Figure 6.61. The shear connector plates were removed from the specimen to reveal the welds as seen in Figure 6.62. All of the welds remained undamaged. A slight tear was visible in the left shear tab.



Figure 6.59: Right Side of Grouted Shear Key at $-\Delta_{c4}$ - First Cycle



Figure 6.60: Right Side of Grouted Shear Key at $-\Delta_{c4}$ - Third Cycle



Figure 6.61: Grouted Shear Key at $-\Delta_{c4}$ - Third Cycle

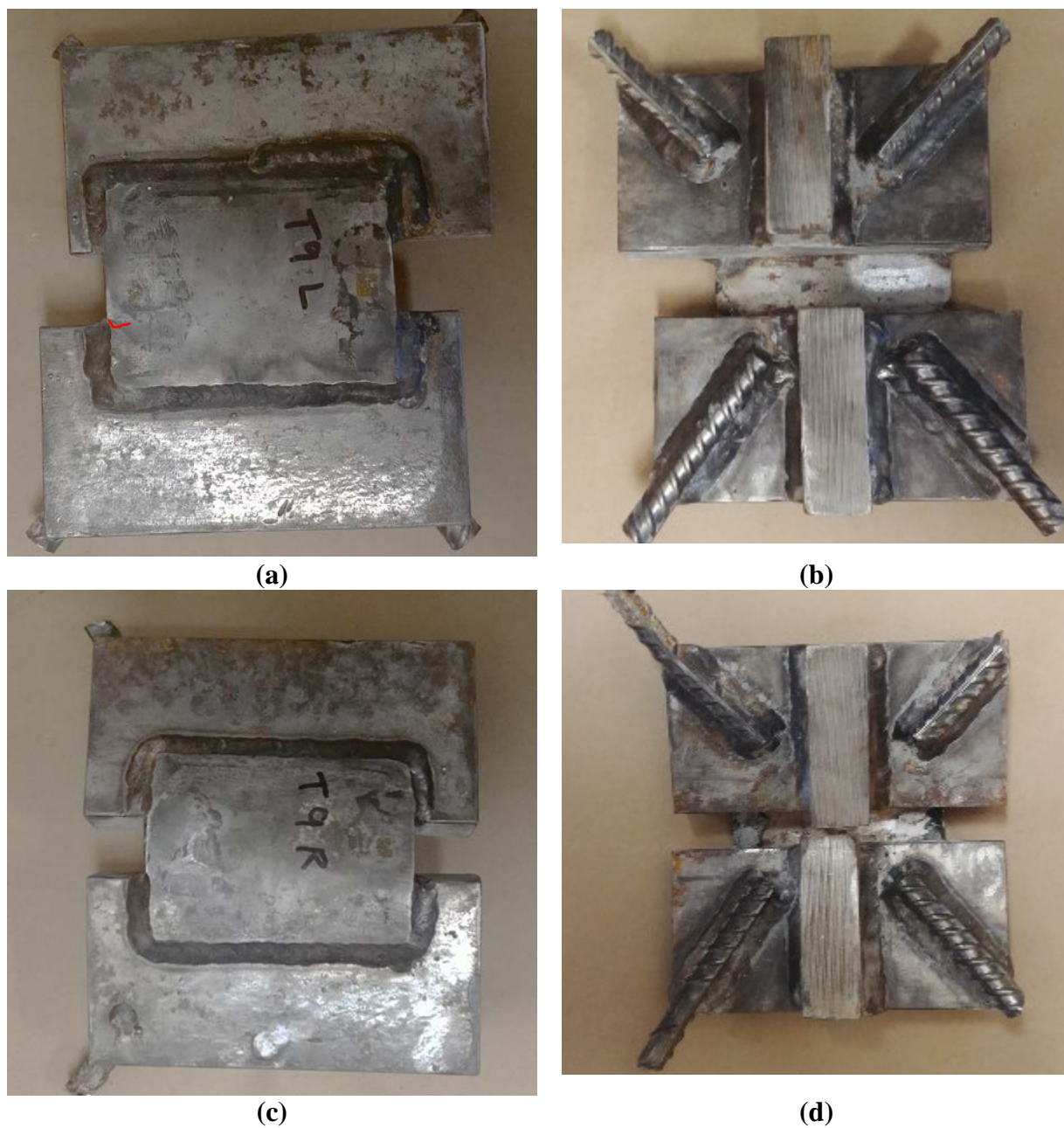


Figure 6.62: Test 9 Removed Shear Connector Plate (a) Top View Left Connector (b) Bottom View Left Connector (c) Top View Right Connector (d) Bottom View Right Connector

6.3.2 Test 9 Conclusion

The focus of the test was to examine the effects of using an alternative shear connector insert to prolong damage accumulation of the joint and provide more residual strength after the maximum strength capacity is reached. The detail for the alternate joint is shown in Figure 6.41. The shear connector insert performed well, with residual strength during all three cycles of Δ_{c1} above 70% of the max recorded force in both the negative and positive directions. As a comparison, the residual strength of Test 7 at Δ_{c1} was 50% and 16% of the second cycle and 35% and 15% for the third cycle in the positive and negative direction respectively. At the first cycle of Δ_{c2} , the residual strength only reduced to 80% of the peak recorded forces in both the negative and positive direction. Comparing the maximum force at Δ_{c2} , degradation remained relatively low. With 71% and 67% of residual strength in the second cycle and 55% and 47% in the third cycle for the positive and negative displacement respectively.

Similar to Test 8, the shear connector failed in bar fracture due to axial loading. This led to a similar displacement of +/- 0.27 inches when bar fracture was evident. Additionally, when fracture occurred, it was responsible for damaging the cover concrete above, leading to spalling of the surrounding concrete. Despite little damage to the welded shear tab, the residual strength of the shear connector in Test 9 was similar to the shear connector in Test 8 since both connectors are controlled by rebar fracture due to axial deformations.

6.4 Test 10

Test 10 was performed at the CFL at NCSU on February 15, 2019. Test 10 utilized the same connection found in Test 8 but with a polyester polymer concrete instead of conventional grout. This section presents the overall response of the specimen and then discusses experimental procedures, results and observations in chronological order. The displacement history measured at the center of the specimen is displayed in Figure 6.63. Complementary to the displacement history, the specimen load history is presented in Figure 6.64. Additionally the complete load-displacement response and rigid body rotation versus displacement of the specimen measured at the center of the specimen can be seen in Figure 6.65 and Figure 6.66 respectively.

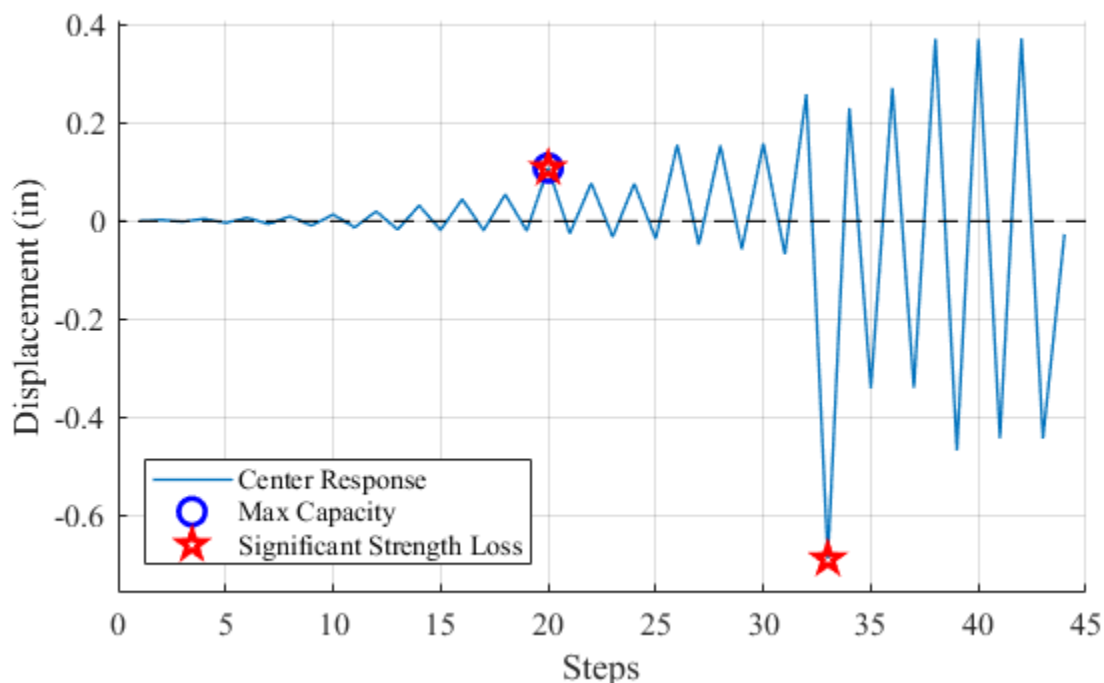


Figure 6.63: Test 10 Displacement History

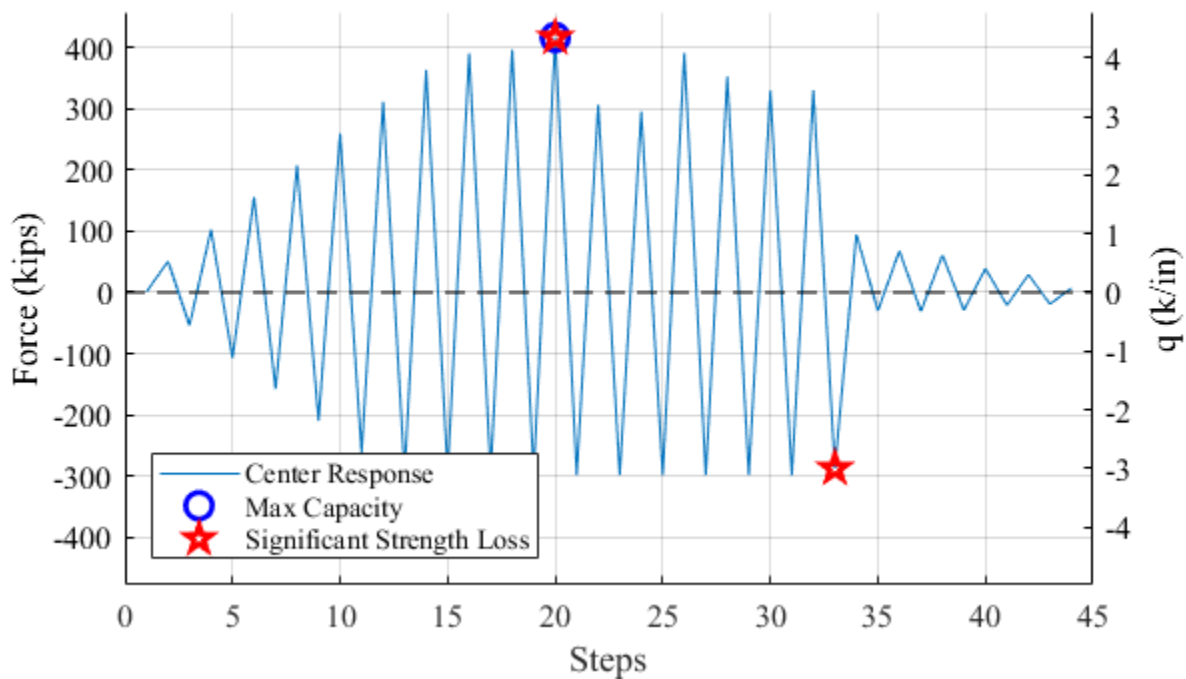


Figure 6.64: Test 10 Load History

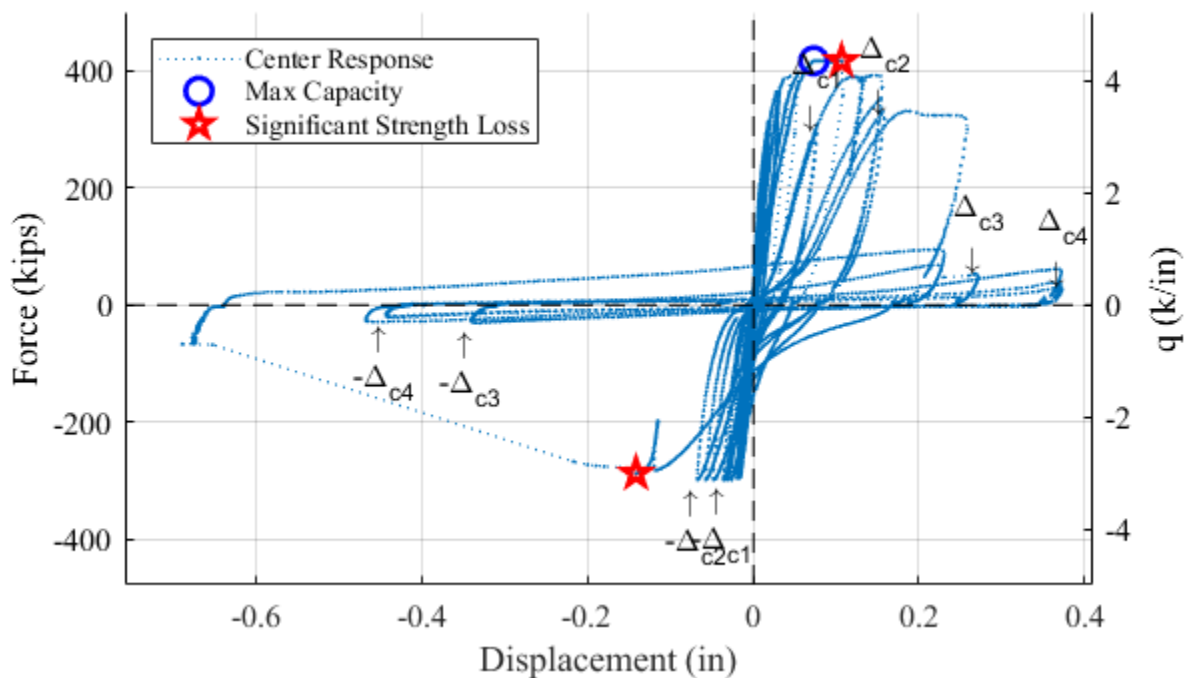


Figure 6.65: Test 10 Force-Displacement Response

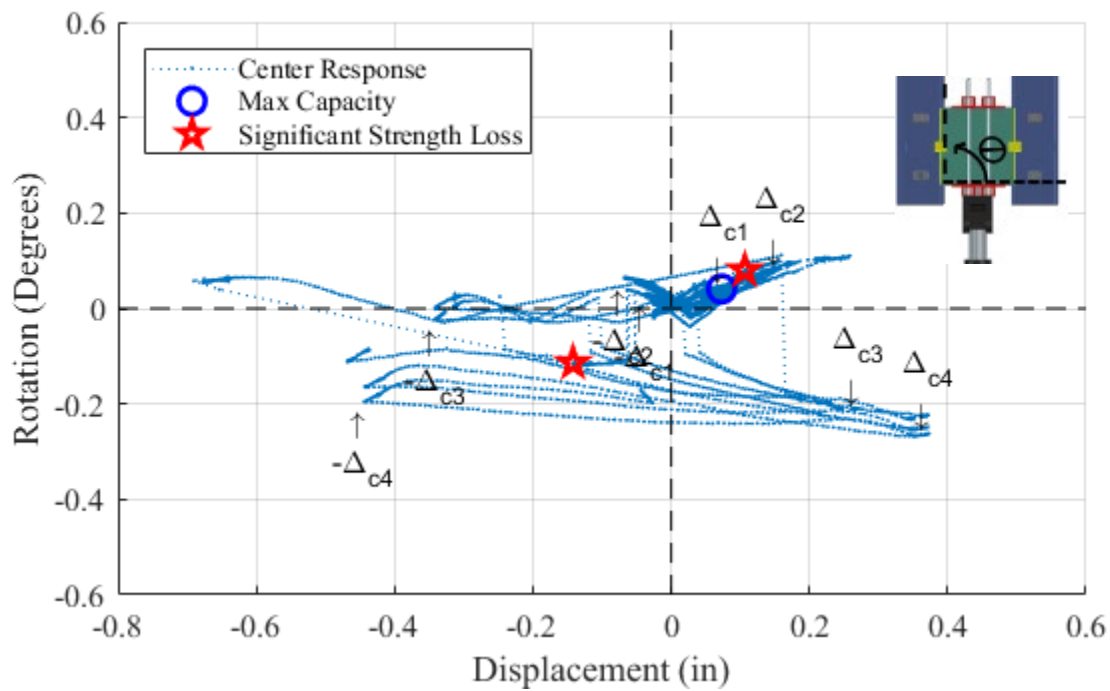


Figure 6.66: Test 10 Rigid Body Rotation

6.4.1 Test 10 Summary

Force was applied cyclically in single cycle sets, at increments of 53 kips ($q_{\text{average}} = 0.5 \text{ k/in}$). Prior to loading, two main cracks were present. One in each side block, starting from the shear pocket and running perpendicular away from the specimen as seen in Figure 6.67. The first crack associated with loading formed in the right side block, propagating diagonally away from the pocket closest to the actuator (Figure 6.68). The load was -107 kips ($q_{\text{average}} = -1.1 \text{ k/in}$) with a displacement at the center of the specimen of -0.004 inches and a rigid body rotation of -0.001° . Damage in the specimen occurred at an applied load of -265 kips ($q_{\text{average}} = -2.8 \text{ k/in}$), which equated to a displacement at the center of the specimen of 0.013 inches and a rigid body rotation of -0.006° . The crack propagated from the right shear pocket corner towards the direction of loading (Figure 6.69). Additional cracks associated with cover concrete uplift were observed around the left shear pocket.

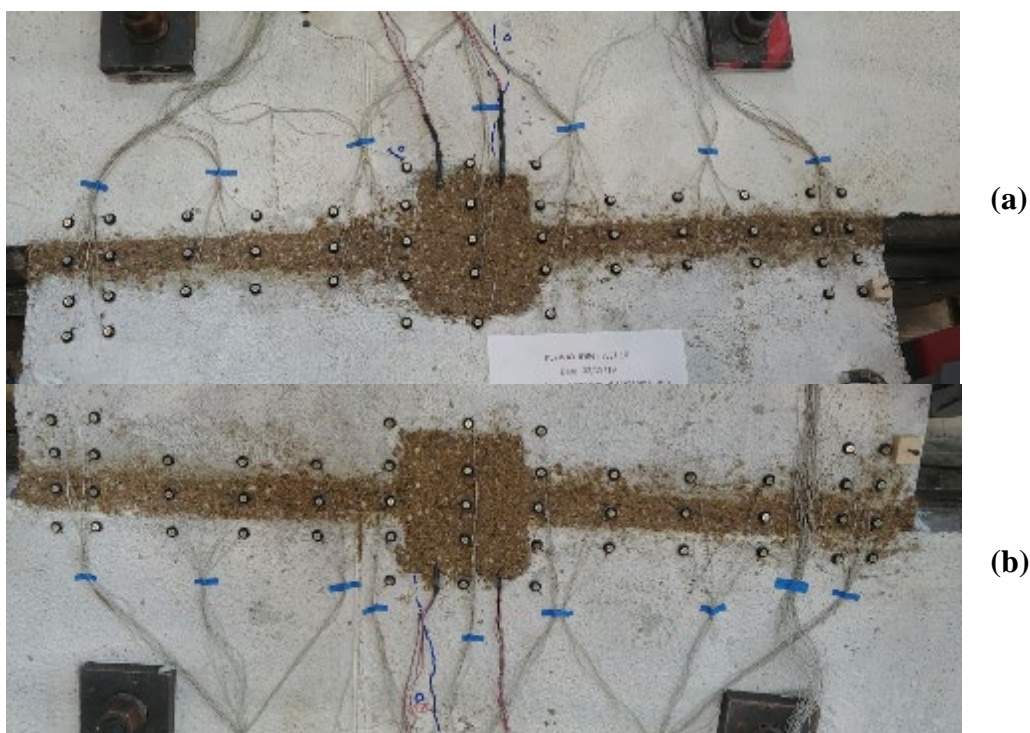


Figure 6.67: Test 10 Grouted Shear Key with Applied Load = 0 kips (a) Left Side (b) Right Side

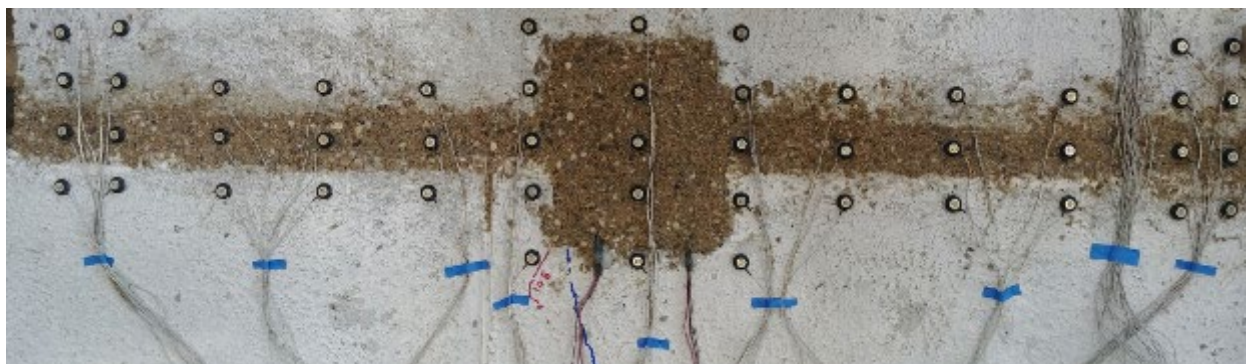


Figure 6.68: Test 10 Right Side of Grouted Shear Key with Applied Load = -107 kips

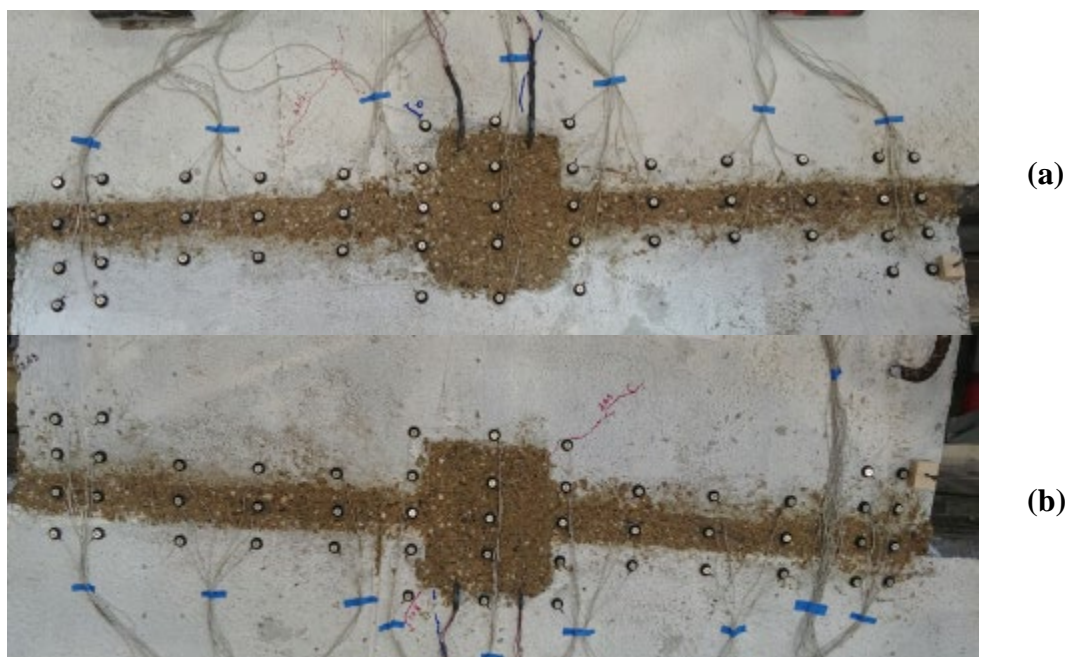


Figure 6.69: Test 10 Grouted Shear Key with Applied Load = -262 kips (a) Left Side
(b) Right Side

The first cracks accompanying the push direction formed at an applied load of 312 kips. The displacement at the center of the specimen was 0.020 inches with a rigid body rotation of 0.004° . One diagonal crack formed on the right side of the specimen at the corner of the shear pocket closest to the actuator. A second diagonal crack formed in left side block at the corner of the shear pocket farthest from the actuator. Additional damage accumulated in the left side block as an existing crack extending in length. Damage can be seen in Figure 6.70. The subsequent pull cycle was limited to 300 kips due to the capacity of the actuator. During which, the existing diagonal cracks on the right joint of the specimen grew in length and new cracks formed in the

left side block. Upon the following push cycle at a load of 364 kips diagonal cracks began to form in the left side of the specimen, near the corners of shear pocket. Diagonal cracks also formed away from the pockets on both the left and right side. The left side had a crack develop in the side block midway between the shear pocket and the unloaded end. The right side had two diagonal cracks form inside the specimen on either side of the pocket. Damage is visible in Figure 6.71. The associated displacement at the center of the specimen and rigid body rotation was 0.032 inches and 0.002° respectively. The next pull cycle led to a vertical crack developing parallel to the joint along the center of the specimen (Figure 6.72). The applied load was 296 kips with a displacement of -0.018 inches at the center of the specimen and a rigid body rotation of -0.008° . Two similar vertical cracks formed in the following push cycle along with two more diagonal cracks on the right side of the specimen (Figure 6.73). It should be noted that a crack developed through the entire depth of the specimen panel as seen in Figure 6.74. The load was 397 kips with a displacement of 0.053 inches at the center of the specimen and a rigid body rotation of 0.023° .

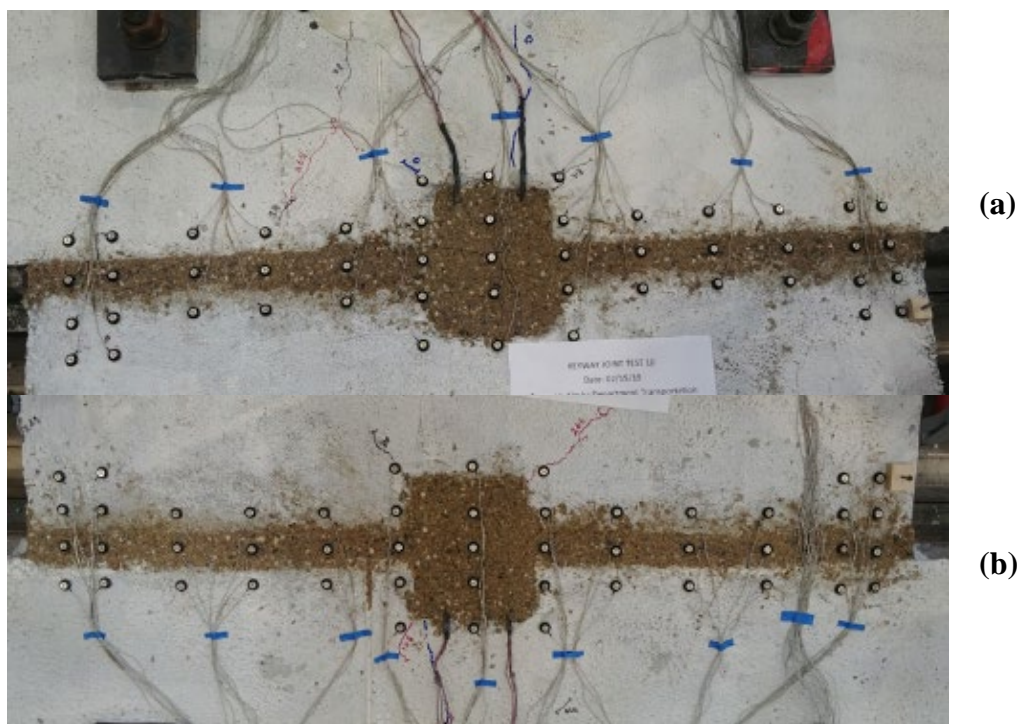


Figure 6.70: Test 10 Grouted Shear Key with Applied Load = 312 kips (a) Left Side (b) Right Side

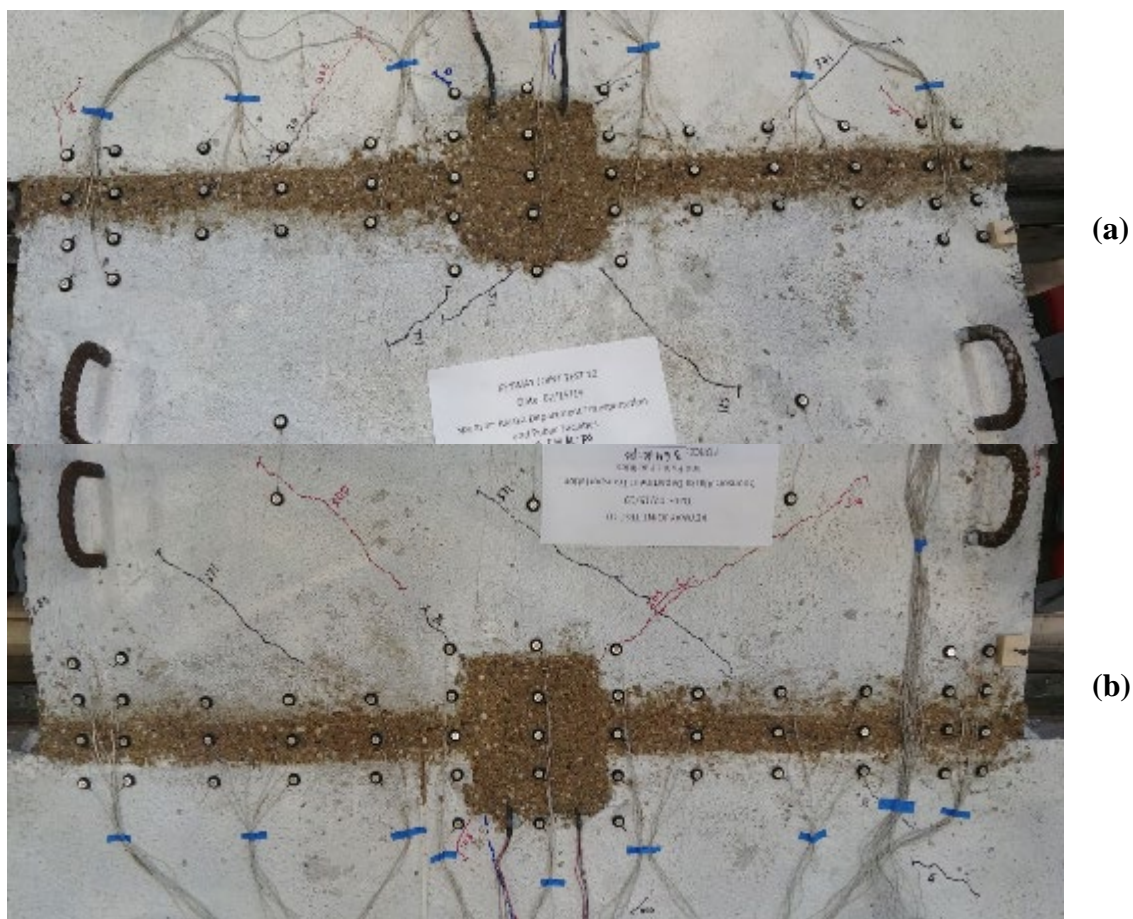


Figure 6.71: Test 10 Grouted Shear Key with Applied Load = 364 kips (a) Left Side (b) Right Side



Figure 6.74: Test 10 Damage to the Right Grouted Shear Key with Applied Load = 391 kips

Upon the next increment of loading, the maximum force capacity of 417 kips was reached. The specimen displacement was increasing, yet the force remained constant. A diagonal crack formed on the left side of the specimen but most of the damage was focused on the right joint between the shear pocket and the loading plate farthest from the actuator. A crack ran down that portion of the joint at the grout-concrete interface. The damage can be seen in Figure 6.75. When the specimen reached maximum strength, the center displacement was 0.073 inches with a rigid body rotation of 0.041° , but ended at 0.107 inches of displacement and 0.080° of rigid body rotation. It should be noted that during this cycle, the side blocks began to slip significantly with 0.033 inches in the right side block and 0.035 inches in the left side block. During the test, the slip was not noted and thus the displacement at maximum strength was estimated at 0.100 inches and was used to define the displacement of significant strength loss of the joint, Δ_{c1} . The actuator was then switched to displacement control. Demand was applied in three cycle sets at increments proportional to Δ_{c1} . Due to the unpredictability of controlling the actuator displacement, the rate of loading was reduced and the displacement of the center of the specimen was monitored manually to conclude the loading for each cycle, which did not account for slip of the side blocks.



Figure 6.75: Test 10 Grouted Shear Key – Significant Strength Loss (a) Left Side (b) Right Side

Since the strength of the pull cycles still exceeded the capacity of the actuator, the specimen was loaded to a force of 299 kips in the pull direction. During the first cycle, the remainder of the right joint cracked down the interface between the grout and the concrete with some slight diagonal cracking joining existing cracks (Figure 6.76). The specimen displacement was -0.026 inches with a rigid body rotation of -0.014° . The load dropped in the second push cycle of Δ_{c1} (+0.100 inches) to 307 kips at a displacement of 0.077 inches with little damage accumulation. During the second pull cycle of Δ_{c1} (-299 kips), cracking accumulated in the left side block typical of cover concrete pry up as seen in Figure 6.77. The specimen had a displacement of -0.032 inches and a rigid body rotation of 0.025° . The remaining Δ_{c1} cycle had similar loads and displacement as the previous cycle with no major damage. Minor damage accumulated Δ_{c2} (+0.200 inches/-299 kip), though it should be noted that slip in the side blocks became more predominate on the left side. During the first push cycle, slip in the left side block was 0.063 inches, while the slip in the right side block was 0.035 inches. At this point the displacement at the center of the specimen, after adjusting for slip, was 0.156 inches with a recorded load of 392 kips and a rigid body rotation of 0.094° . Damage from the three cycle set is shown in Figure 6.78 and Figure 6.79. Where Figure 6.79 shows another crack along the right joint develop through the entire depth of the specimen panel.

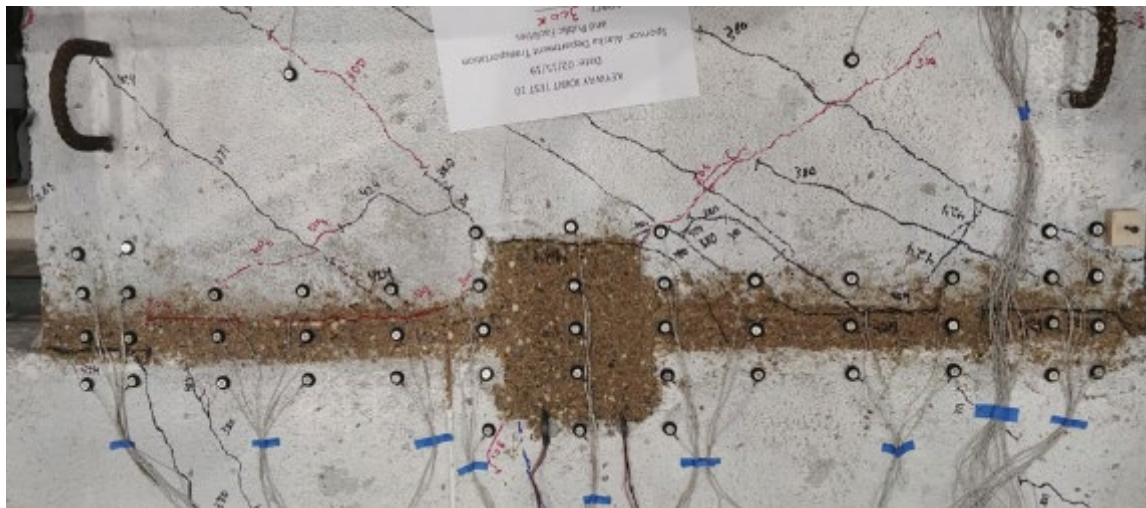


Figure 6.76: Test 10 Grouted Shear Key at $-\Delta_{c1}$ – First Cycle



Figure 6.77: Test 10 Right Side of Grouted Shear Key at $-\Delta_{c1}$ – Second Cycle



Figure 6.78: Test 10 Grouted Shear Key at Δ_{c2} – Third Cycle

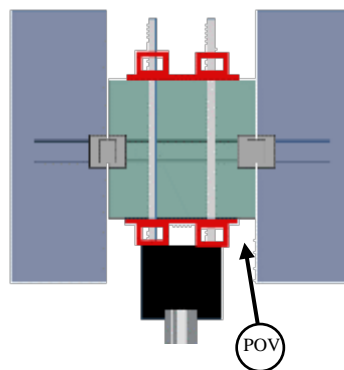


Figure 6.79: Test 10 Damage to the Right Grouted Shear Key at Δ_{c2} – Third Cycle



Figure 6.80: Test 10 Grouted Shear Key at Δ_{c3} – First Cycle

No new damage occurred during the first push cycle of Δ_{c3} (Figure 6.80). The displacement of the specimen was 0.258 inches with a rigid body rotation of 0.110° and a force of 300 kips. The next pull cycle led to significant damage and a significant decrease in strength. The specimen reached 288 kips before the force started to decrease. The center of specimen displacement was -0.142 inches with a rigid body rotation of -0.114° . At the end of the cycle, the force had decreased to -67 kips at a displacement of -0.690 inches with a rigid body rotation of 0.058° . Damage was focused predominantly around the left joint with cover concrete spalling off of the left side block around the shear pocket and exposing an embedded rebar. The right joint had a crack going through the shear pocket, connecting the cracks between the concrete grout interfaces on either side. Additionally there was minor cover concrete spalling in the specimen near the pocket. The damage is visible in Figure 6.81. With the pull cycle no longer exceeding the actuator capacity, the pull cycles were controlled in displacements at increments of Δ_c . The following pull cycle led to more cover concrete spalling in the left side block as seen in Figure 6.82. The center of the specimen reached a displacement of 0.341 inches with a rigid body rotation of 0.001° and a force of -27 kips. The final pull cycle of Δ_{c3} initiated spalling cover concrete along the right joint of the specimen (Figure 6.83). The center of the specimen reached a displacement of -0.341 inches with a rigid body rotation of -0.023° and a force of -27 kips.

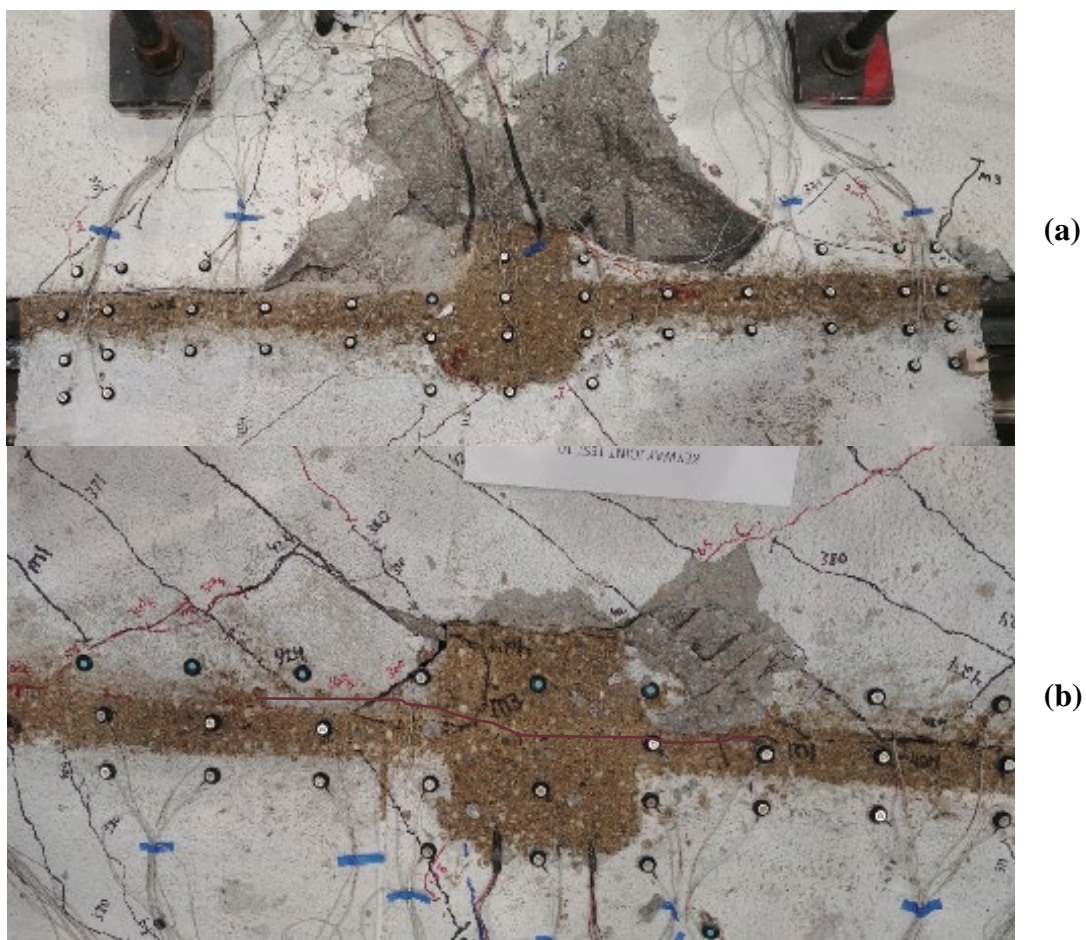


Figure 6.81: Test 10 Right Side Shear Connector Insert at $-\Delta_{c3}$ -First Cycle

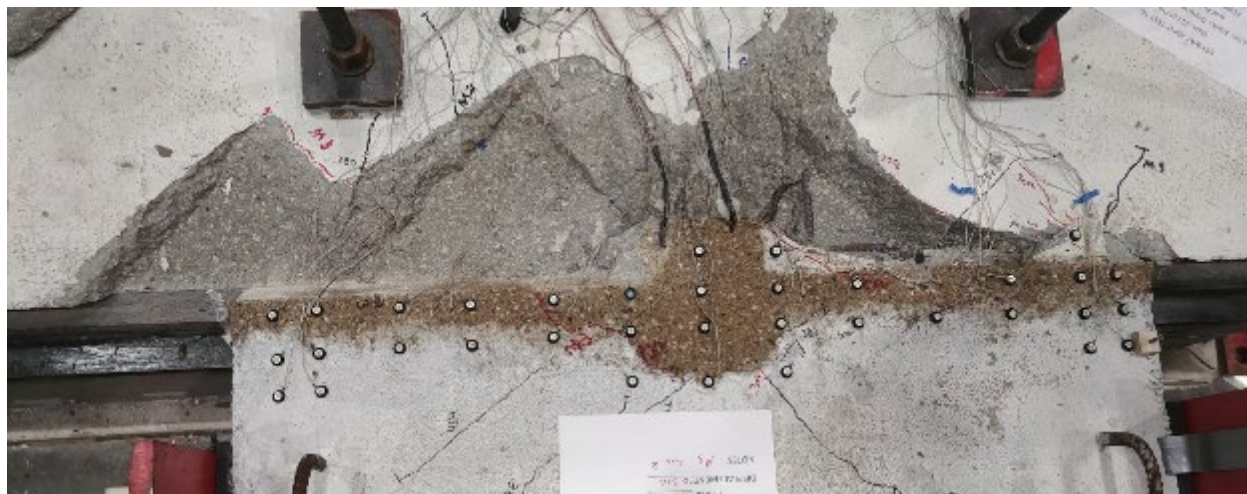


Figure 6.82: Test 10 Grouted Shear Key at $-\Delta_{c3}$ - Second Cycle

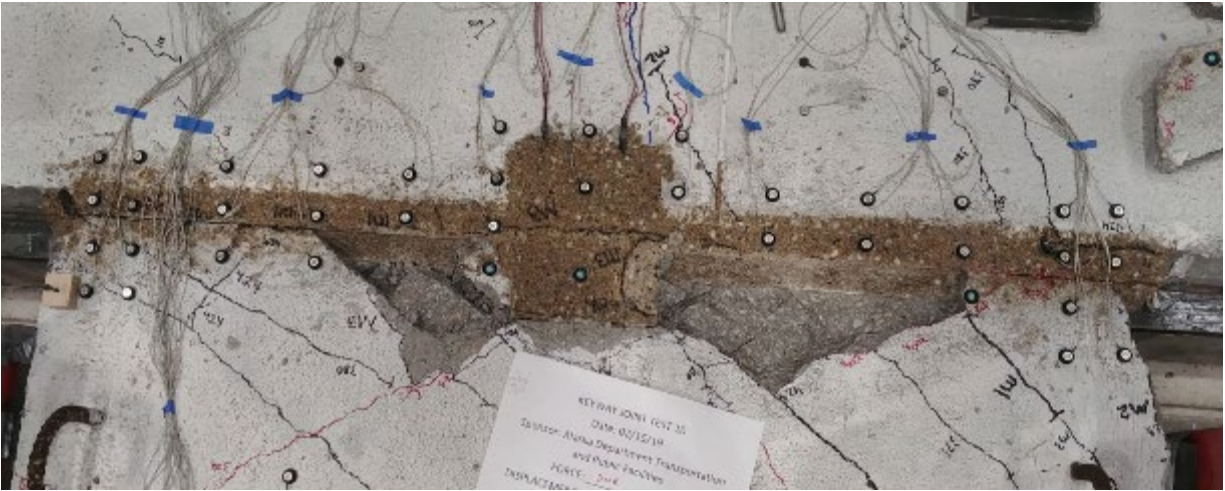


Figure 6.83: Test 10 Grouted Shear Key at $-\Delta c_3$ - Third Cycle

The increment was then increased to Δc_4 (± 0.400 inches), but no additional damage accumulated (Figure 6.84) during the three cycle set and little residual strength remained in the specimen, thus the test was terminated. The final push cycle had displacement at the center of the specimen of 0.373 inches with a rigid body rotation of -0.262° and a force of 26 kips. The final pull cycle had displacement at the center of the specimen of -0.444 inches with a rigid body rotation of -0.195° and a force of -17 kips. During the disassembling process, after the loading plates were removed, cracking and spalling of concrete was observed under the specimen (Figure 6.85). Therefore the specimen concrete failed rather than the grout concrete interface.

Additionally the two embedded rebar that compose of the shear connector insert on the right side of the specimen were found to be fractured. During the removal of the shear connectors, another fractured rebar was discovered in the left side block. The shear connector plates were removed from the specimen to reveal the welds as seen in Figure 6.86. All of the welds remained undamaged and no damage was observed in the shear tabs.

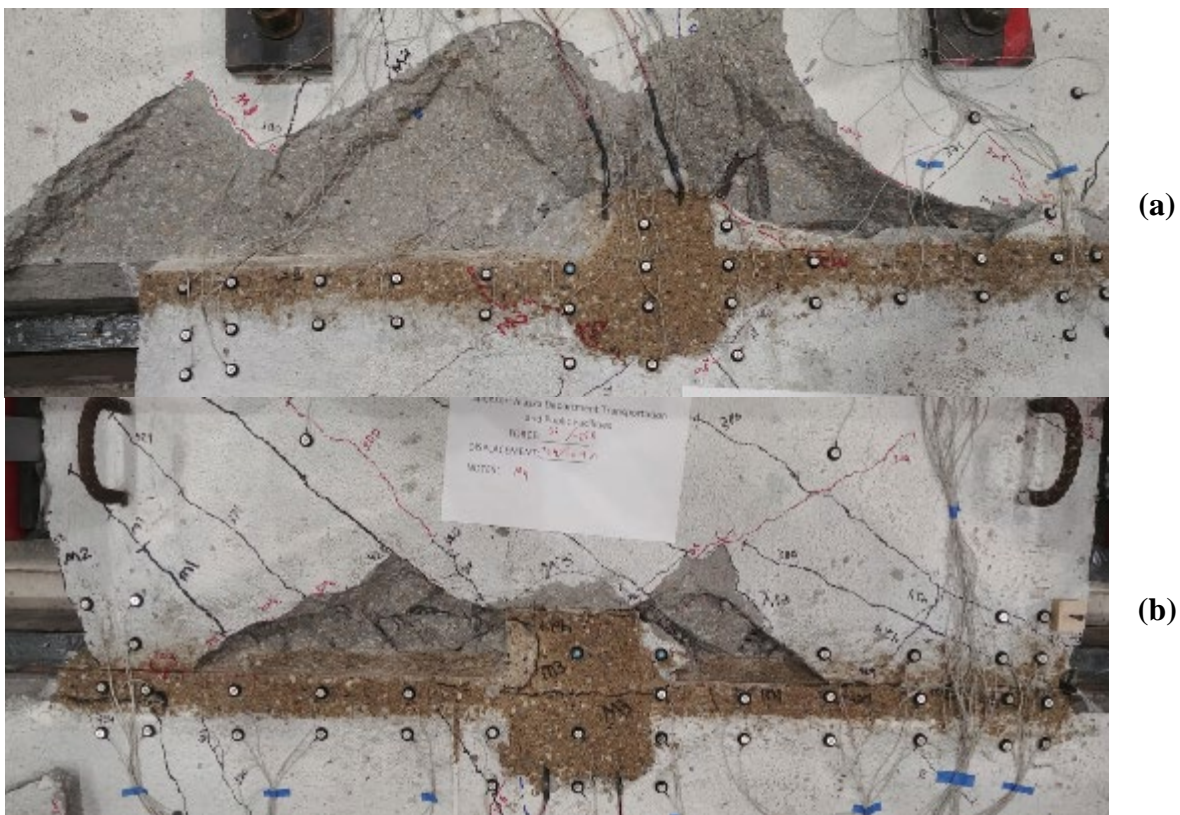


Figure 6.84: Test 10 Grouted Shear Key at $-\Delta_{c4}$ – Third



Figure 6.85: Test 10 Damage to Right Side of Grouted Keyway from Underneath

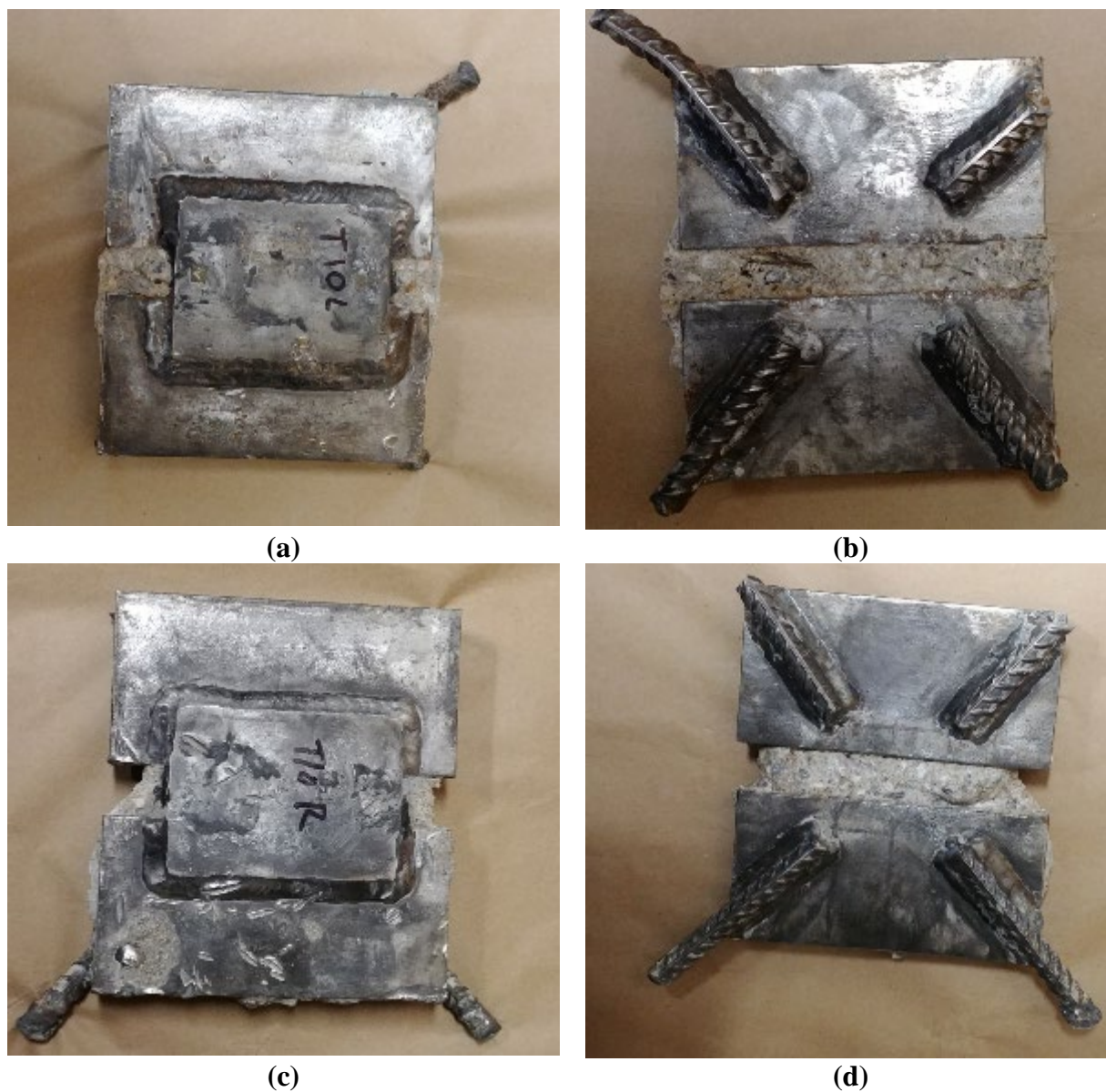


Figure 6.86: Test 10 Test 10 Removed Shear Connector Plate (a) Top View Left Connector (b) Bottom View Left Connector (c) Top View Right Connector (d) Bottom View Right Connector

6.4.2 Test 10 Conclusion

The focus of the test was to examine the effects of using an alternative shear connector insert along with a polyester polymer concrete. The detail for the alternate joint are shown in Figure 6.41. Test 10 is best compared against Test 6, which used the same polyester polymer concrete to fill the shear key. A comparison of the force-displacement hysteresis of both tests can be seen in Figure 6.87. The alternative shear connector insert performed well at displacements lower than those associated with bar fracture. The residual strength for the second and third cycle of Δ_{c1} were above 70% of the max recorded force in the positive direction. It should be noted that the actuator could not apply enough force to observe force degradation in the negative direction. In comparison, Test 6 had 64% and 52% for the second and third cycles respectively in the positive direction. Both tests exhibited similar visible damage. A more drastic trend in degradation held true during the displacement increment of Δ_{c2} where Test 10 reached 392 kips at a displacement of 0.195 inches during the first cycle which was only a 6% reduction in the maximum force recorded throughout the test. While test 6 only reached 207 kips at a displacement of 0.207 inches, which was a 33% reduction from the maximum recorded force. Throughout second and third cycle of Δ_{c2} , Test 10 maintained 90% and 84% of the maximum strength for that cycle in the positive direction. Test 6 only maintained 35% and 30% respectively. It should be noted that Test 6 underwent a displacement of -0.376 inches during the first pull cycle of Δ_{c2} . At this stage, Test 6 had much more damage to the cover concrete than test 10 as compared in Figure 6.88. It should be noted that due to creep, loading history may play a role in the PPC overall strength. Test 6 was held at maximum load for approximately one minute, while Test 10 was unloaded immediately.

The force-displacement hysteresis of Test 10 (the alternate connection with PPC) and Test 8 (the alternate connection with conventional grout), can be seen in Figure 6.89. In both Test 10 and Test 8, bar fracture occurred around a cyclic displacement of +/- 0.3 inches. In both cases this fracture resulted in a significant reduction in strength. It is difficult to compare maximum forces due to differences in compressive strength but PPC seems to increase the maximum shear flow that the joint can withstand.

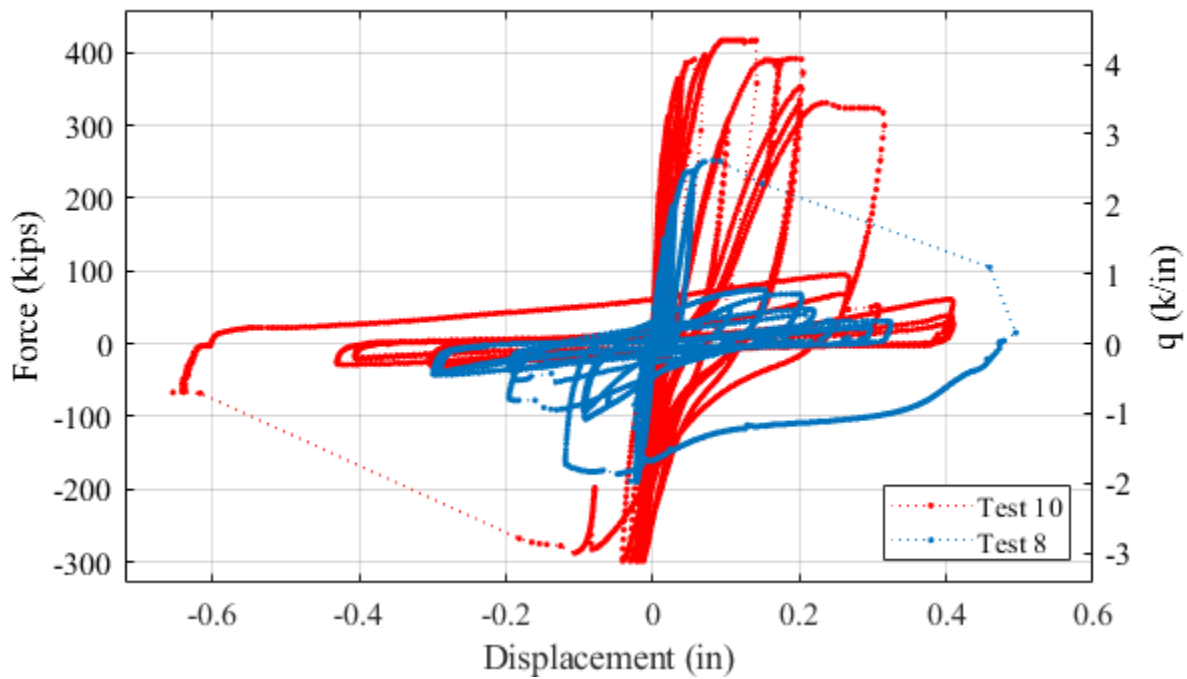


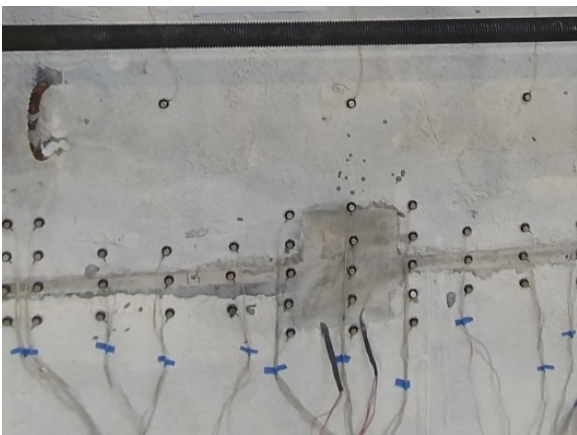
Figure 6.89: Force-Displacement Response Comparison of Test 6 and Test 10

6.5 Phase II Experimental Observations

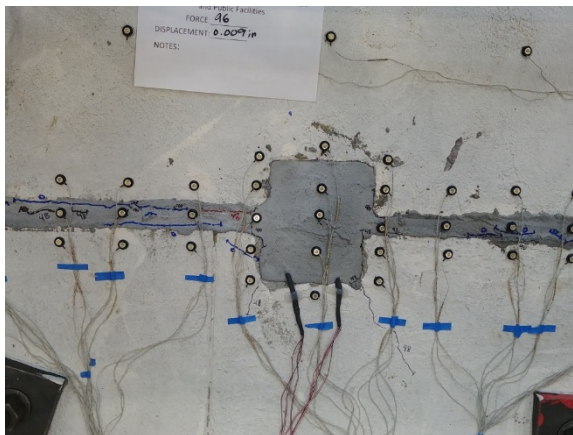
After completion of the second phase of testing, initial observations of damage progression were similar to that of Phase I mentioned in section 5.8. For the tests performed with the alternative connections, two differences in damage progression were observed. In Test 8 and 9, the connector plate was able to be activated, which must imply that bearing of the embedded plates was enough to activate the plate. This phenomenon could only be observed after spalling of the cover concrete but is believed to have occurred in Test 8 just after the maximum strength of the joint and failure of the grout. The second was a change in failure mechanism of the embedded shear connector. Instead of bending of the embedded rebar, axial elongation and bar fracture of the embedded rebar was observed for all tests with alternate connections. While cracks associated with cover concrete were present before bar fracture, only after fracture did significant cover concrete spalling occur and residual strength reached about +/-20 kips. For the test with alternate connections, rebar fracture occurred once the cyclic rebar demand reaches approximately +/- 0.3 inches

The progression of damage for each test in Phase II can be seen in Figure 6.90 through Figure 6.94. The force and displacement at which each damage state occurred for the tests in Phase II can be found in Table 6.1. Damage states that did not occur in the test as well as values that are not known are left blank.

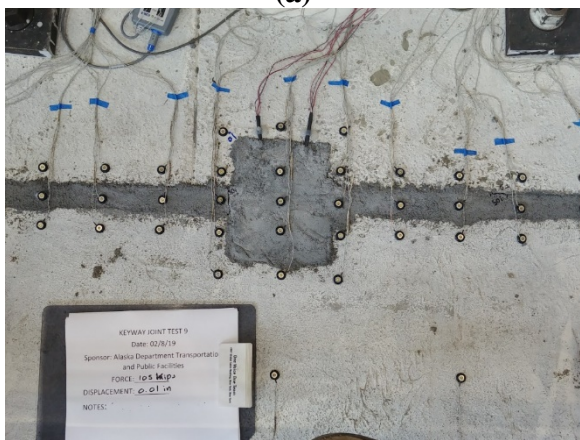
Since the force controlled portion of the loading protocol up to maximum strength was single cycle sets, no observation of degradation can be made. However the displacement controlled portion of the loading protocol could be evaluated. Degradation in this portion of loading is best examined using the ratio of maximum force of second and third cycle divided by the maximum force of the first cycle. Test 7 showed less degradation than the other existing shear connector counter parts, Test 4 and Test 6, with an average ratio of 0.62 and 0.75 for the push and pull directions respectively. The average ratio of forces for Test 8 up until bar fracture in the connection was reached was 0.70 and 0.65 for the push and pull directions respectively. The average ratio of forces for Test 9 up until bar fracture in the connection was reached was 0.66 and 0.69 for the push and pull directions respectively. The average ratio of forces for Test 10 up until bar fracture in the connection was reached was 0.70 and 0.81 for the push and pull directions respectively.



(a)



(b)



(c)

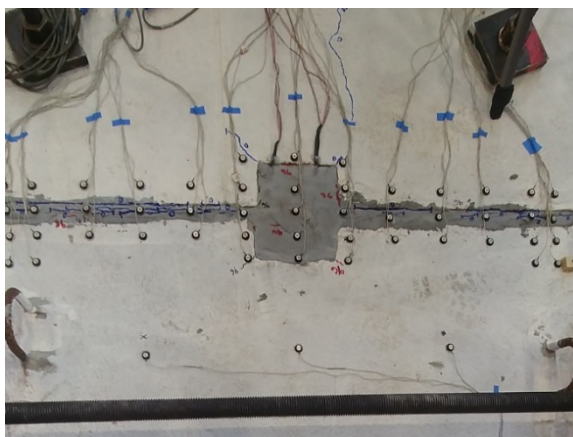
Image Not Available

(d)

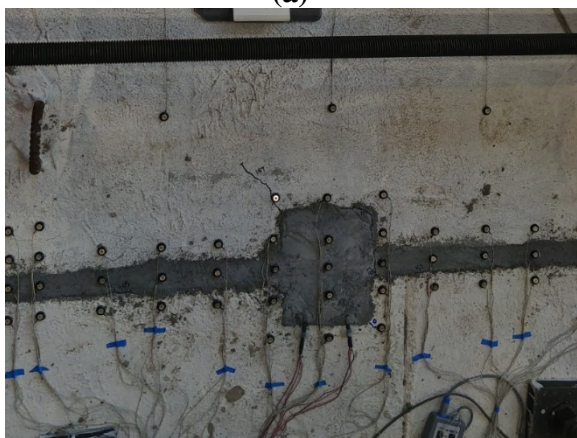
Figure 6.90: Cracking Perpendicular to the Joint (a) Test 7 (b) Test 8 (c) Test 9 (d) Test 10



(a)



(b)



(c)



(d)

Figure 6.91 Diagonal Cracking (a) Test 7 (b) Test 8 (c) Test 9 (d) Test 10

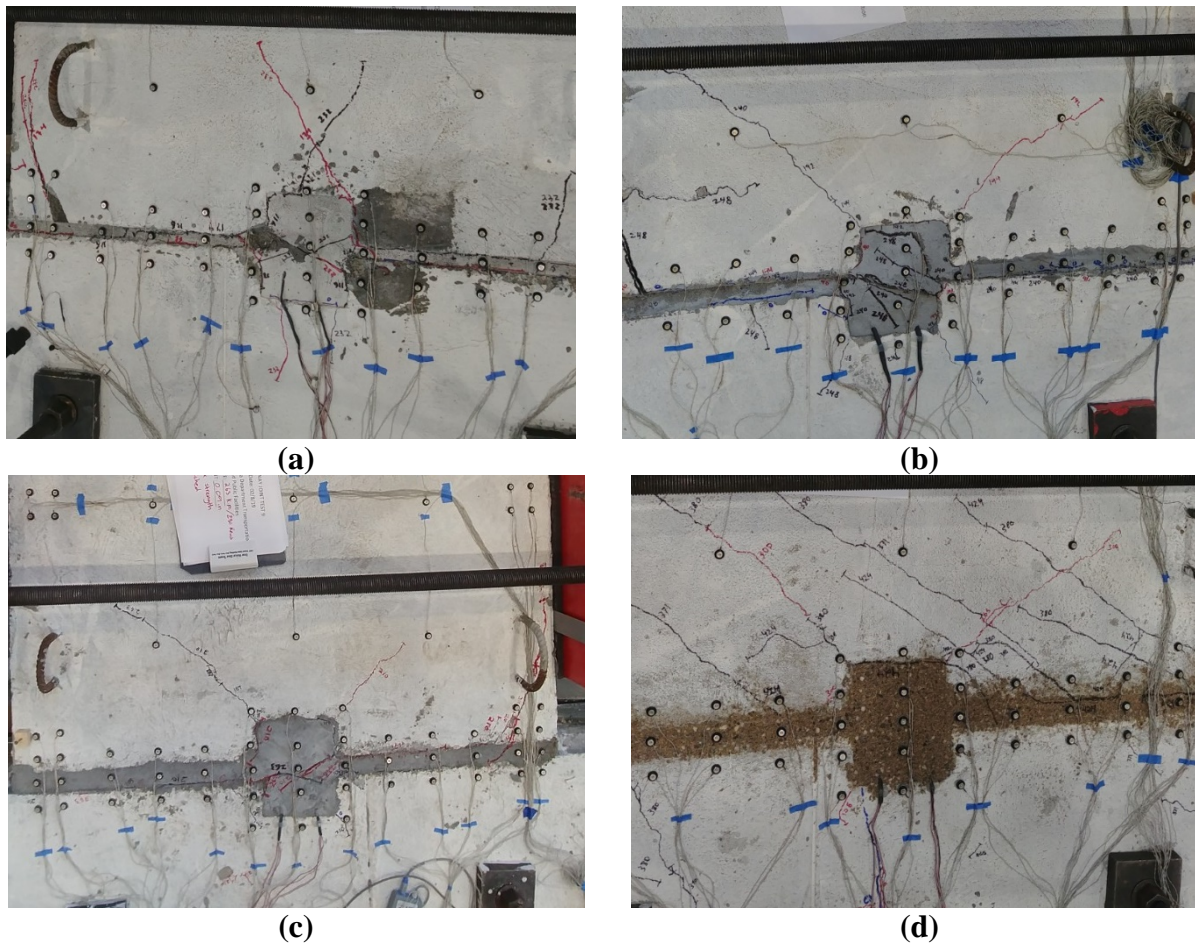
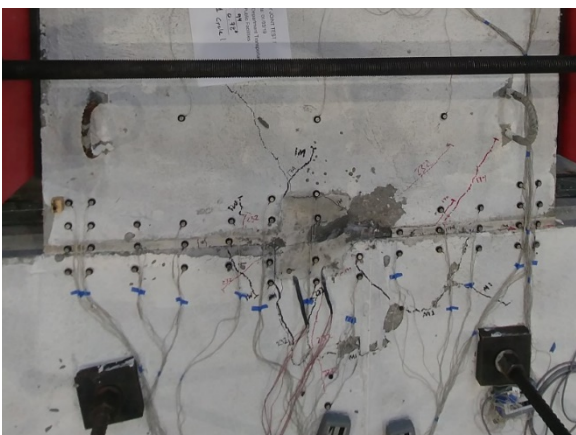
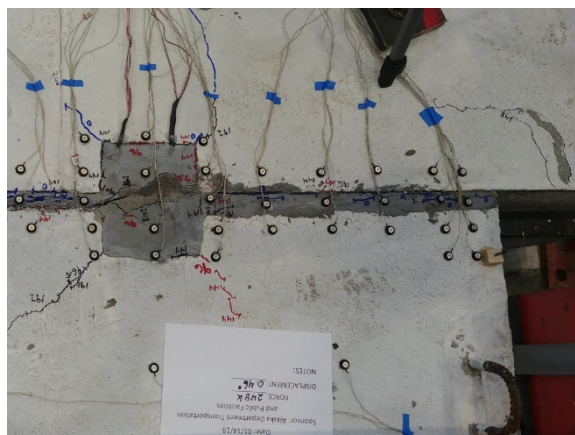


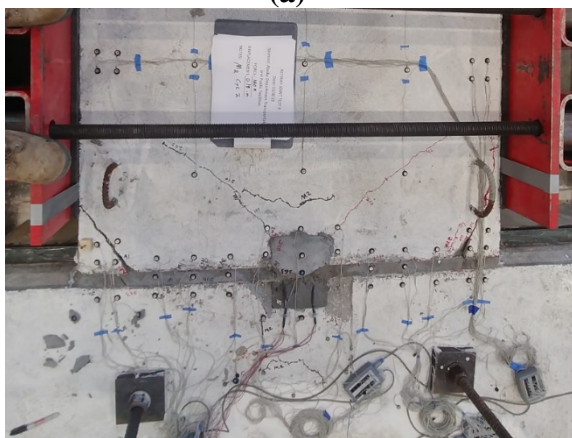
Figure 6.92 Failure of Grouted Joint (a) Test 7 (b) Test 8 (c) Test 9 (d) Test 10



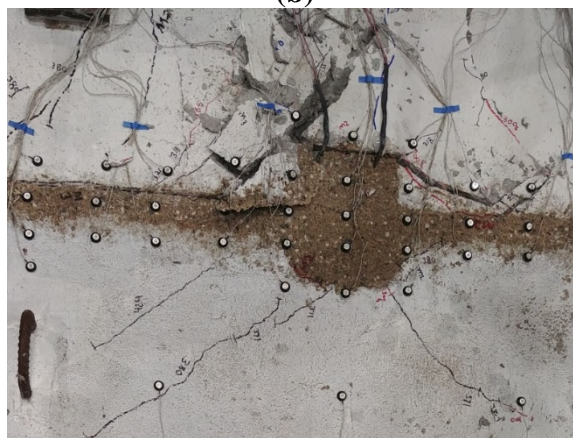
(a)



(b)



(c)



(d)

Figure 6.93: Cover Concrete Spalling (a) Test 7 (b) Test 8 (c) Test 9 (d) Test 10

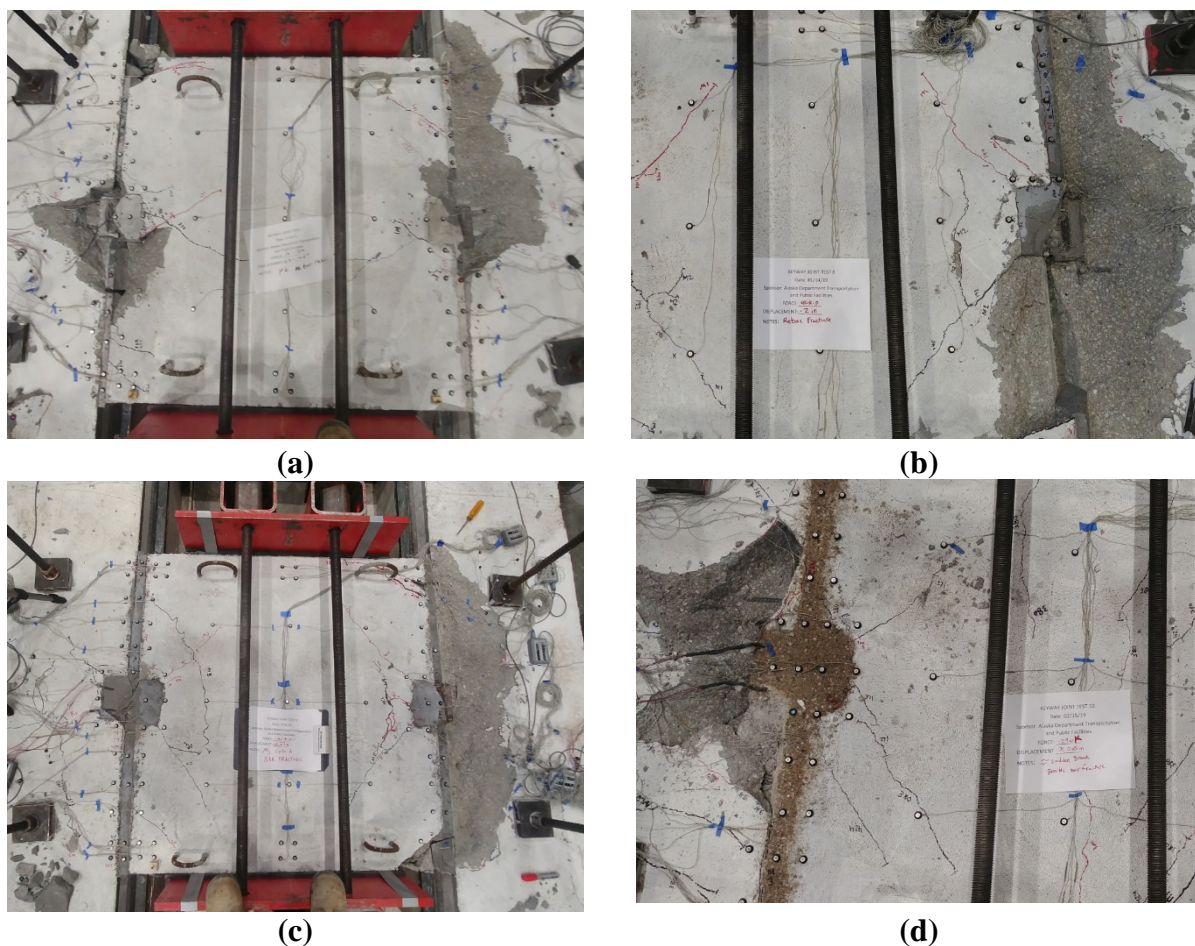


Figure 6.94 Rebar Fracture (a) Test 7 (b) Test 8 (c) Test 9 (d) Test 10

Table 6.1: Phase II Damage State Progression Force and Displacement

Test	Damage State					
	Perpendicular Cracking	Diagonal Shear	Failure of Joint	Cover Concrete	Bar Fracture	
7	F [Kips]	58	174	-216	64	24
	Δ [in.]	0.003	0.021	-0.059	0.075	0.704
8	F [Kips]	96	96	252	15	-49
	Δ [in.]	0.010	0.010	0.086	0.495	-0.191
9	F [Kips]	105	157	242	115	-43
	Δ [in.]	0.009	0.028	0.088	0.179	-0.284
10	F [Kips]		265	-296	-268	-268
	Δ [in.]		0.015	0.140	-0.217	-0.217

6.6 Limit States

Damage progression of the existing joint has been mentioned in the sections above but occurs as follows: formation of perpendicular cracking in the joint, development of diagonal shear cracking toward the direction of loading, extensive cracking to cause failure in the grouted joint, development of cracks associated with cover concrete spalling and subsequent spalling, and lastly embedded rebar fracture. While these steps occur, the one that controls the force behavior of the connection is failure of the grout in the joint. Once this occurs, there is a softening in the response, which is simultaneous with spalling of cover concrete and low residual strength left in the connection. In fact, rebar fracture is not a concern as a limit state, as the bar contributes very little to the response, especially when the cover concrete has already spalled. Thus, the two main limit states for the existing joint are failure of the grout and spalling of the cover concrete. While failure of the grout is more of a capacity limit state, it does not provide a hindrance in usability of the concrete deck because minor damage occurs at the surface. Spalling of the cover concrete, is a serviceability limit state as it does cause significant damage to the surface of the bridge.

The alternate connections behave similar to the existing connection up until failure of the grout. Then there is less damage in the cover concrete and the concerning limit state is the embedded rebar fracture. Once this occurs, cover concrete spalls off, leaving little residual strength behind as was seen in the existing connection. Similar to the existing connection, the failure of the joint is more of a serviceability issue.

As tests used different grout strengths, limit states are not easily categorized by strength. Rather limit states are better listed on a bases of slip displacement of the joint. It should be noted that more tests should be done to get a better approximation in values. The average limit state values are listed below based on connection type and grout type since PPC had an effect on when failure of the grout occurred.

Table 6.2: Longitudinal Shear Key Limit State Displacements

	Failure of grout [in]		Spalling [in]	Fracture [in]
	Grout	PPC		
Existing			0.398	
Alternate Connection	0.085	0.148		0.271

CHAPTER 7 GLOBAL COMPUTATIONAL BRIDGE MODEL

A global computational bridge model was developed to determine the effective stiffness of the super structure and determine when longitudinal keyway limit states may control the design of a bridge. In addition, a subassembly model was created to evaluate the use of nonlinear springs to represent the longitudinal shear key.

7.1 Sub-Assembly Computational Model

A 2D analytical model was developed in OpenSees (Mazzoni, McKenna, Scott, & Fenves, 2006) that represents the test set up used in the experimental portion of the research. The model takes advantage of inelastic zero length elements to represent the longitudinal joint. The shear key and shear connector were going to be modeled as separate entities but due to the complex nature of the connection and the interaction between the two, it was decided to combine both responses into a unit length element. The specimen is modeled using an elastic beam element and the side blocks are modeled as fixed end boundary conditions. A schematic is presented in Figure 7.1.

Load is applied in terms of displacement at 0.001 inch increments to a single node at the end of the specimen. Elastic beam element were used with a cross sectional area of 270 inches and modulus of elasticity according to Equation 7.1 (ACI 318, 2014). The zero length element uses the Pinching4 uniaxial material to represent force and displacement of the joint, which is discussed in section 7.2. While the model can successfully represent the existing and alternate connection as seen in Figure 7.2 and Figure 7.3 respectively, the subassembly model is load history dependent. The focus of the model was overall hysteretic behavior, rather than empirical adjustments of parameters to fit specific test results.

$$E_c = 57000\sqrt{f'_c} \text{ (psi) or } 1802\sqrt{f'_c} \text{ (ksi)}$$

Equation 7.1

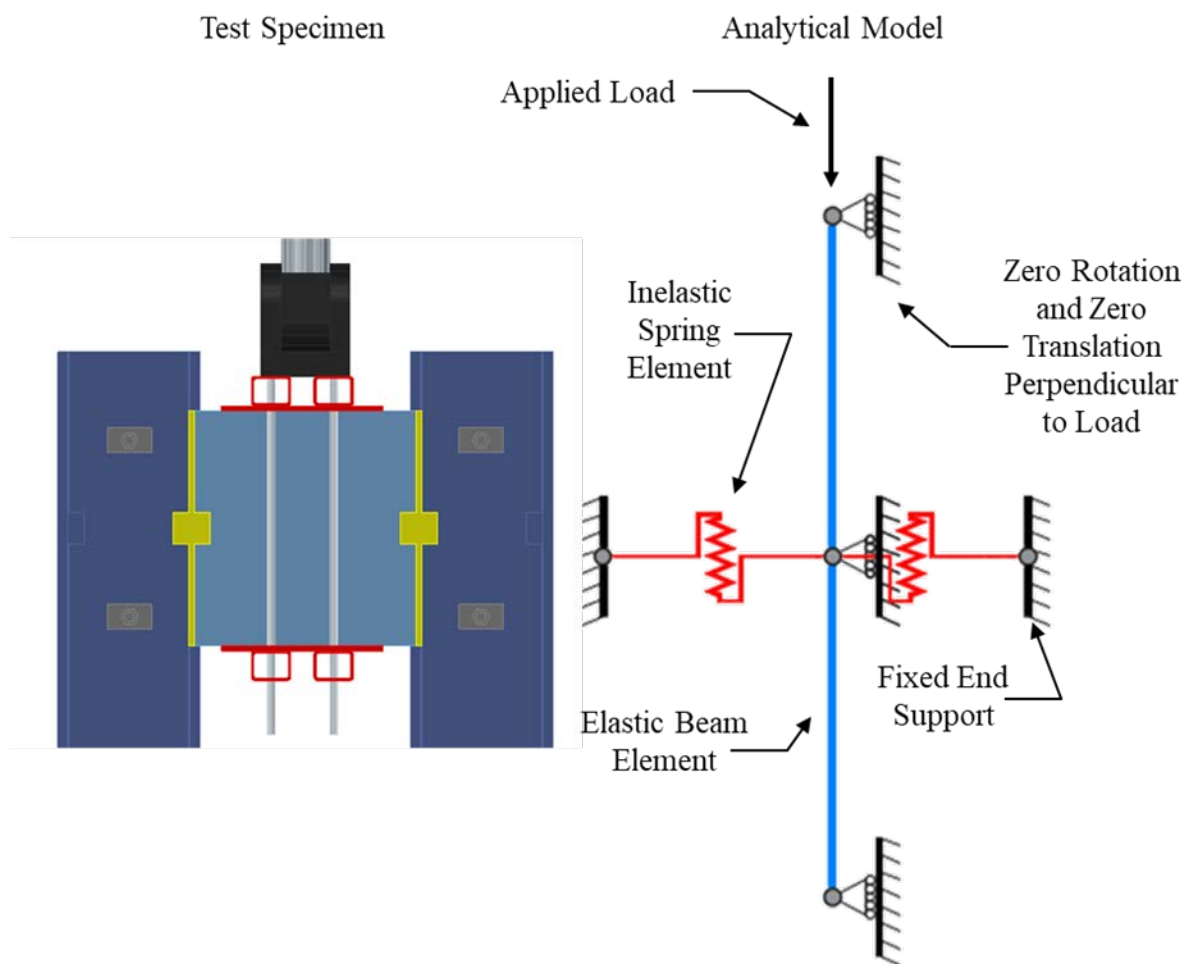


Figure 7.1: Sub-Assembly Computational Model Schematic

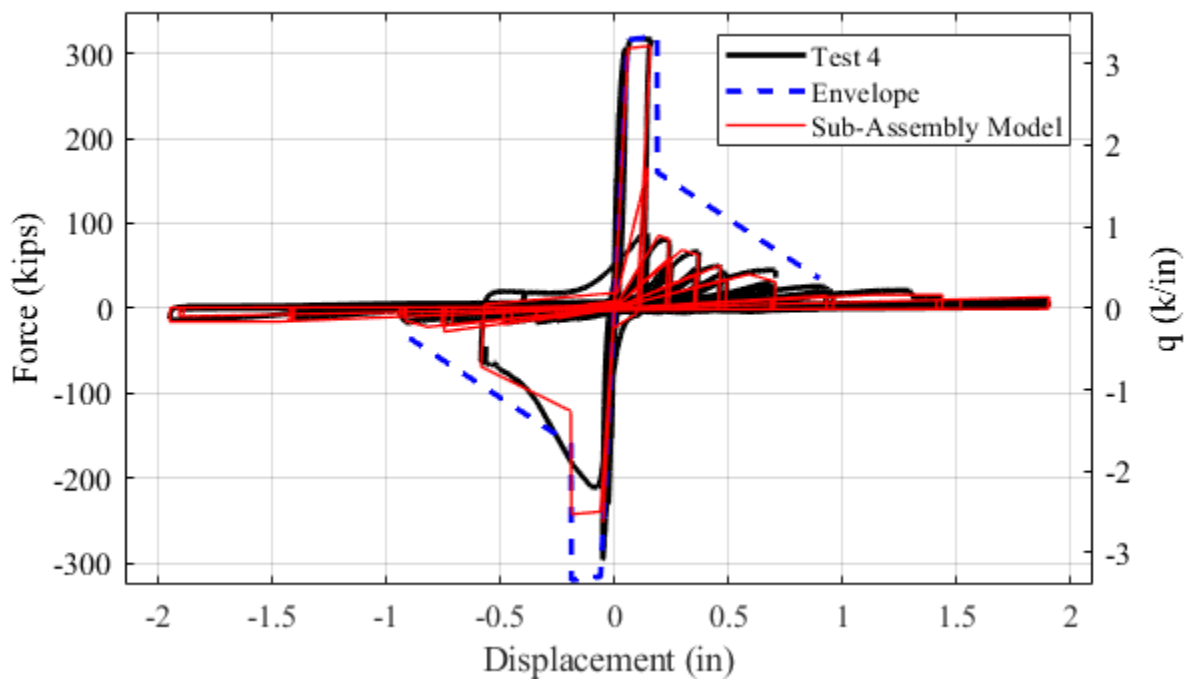


Figure 7.2: Test 4. Analytical Model Force-Displacement Response

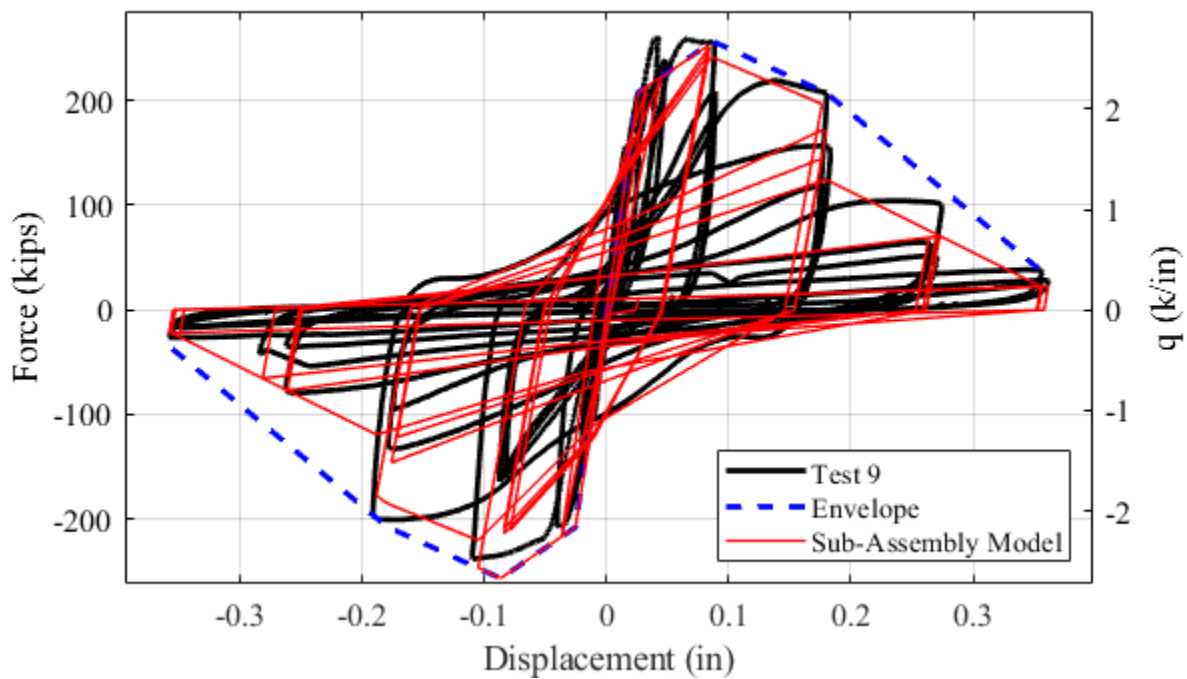


Figure 7.3: Test 9. Analytical Model Force-Displacement Response

7.2 Pinching 4 Material Model

The zero length element uses the Pinching4 uniaxial material to represent the force displacement response of the joint. The constitutive model was originally developed for beam-column joint response (Lowes, Mitra, & Altoontash, 2004) but the flexibility of the model allows its use for the longitudinal keyway. The model allows for modification of the envelope, loading and unloading characteristics and degradation. Degradation is based on a damage index (Young-Ji Park & H-S Ang, 1985), δ_i , as seen in Equation 7.2. The damage index is a function of displacement and energy dissipated and is presented in Equation 7.3, where α_1 through α_4 are constants used to modify the influence of displacement and energy dissipation. d_i is the ratio of the maximum displacement that has occurred in the loading history divided by the allowable maximum displacement before residual strength occurs as given in Equation 7.4. E_i is the energy that has been dissipated (Equation 7.5) and $E_{monotonic}$ is the energy under the defined monotonic envelope.

$$Degradation = 1 - \delta_i \quad \text{Equation 7.2}$$

$$\delta_i = \left(\alpha_1 (d_i)^{\alpha_3} + \alpha_2 \left(\frac{E_i}{E_{monotonic}} \right)^{\alpha_3} \right) \quad \text{Equation 7.3}$$

$$d_{max} = \max \left[\frac{d_{maxi}}{def_{max}}, \frac{d_{mini}}{def_{min}} \right] \quad \text{Equation 7.4}$$

$$E_i = \int_{load\ history} dE \quad \text{Equation 7.5}$$

7.3 Global Bridge Modeling Approach

The global computational bridge model is a 2-D model (Figure 7.4) that utilizes springs in the longitudinal direction to transfer shear flow between girders and provide composite action to the superstructure. The girders that make up the superstructure of the bridge are modeled as elastic beam elements with the geometric properties associated with predecked bulb-tee girders. The centerline of the elements are spaced at the width of the girder flange. The number of elastic beam elements that comprise the girder is dependent on the span of the girder. Since the longitudinal joint repeats itself every four feet, a node is placed every four feet. The nodes are spaced such that first and last node that make up the girder are two feet away from the next adjacent node for an effective tributary length of four feet for each spring. Boundary conditions are applied to the ends of the girder such that the system is simply supported and the girders can move freely in the longitudinal direction. To do this, all the end nodes are roller supported such that girders can move freely of one another. Only the first girder has a single end node acting as a pin support to ensure simply supported beam conditions. Restraint from one girder to the next is provided through the zero length longitudinal shear key element. These elements are what keep the girders supported by rollers stable. The zero length elements are connected to the girders through rigid links. The links have the appropriate geometry, a length equal to half the girder width, to ensure that the spring element is located along the joint. To ensure that only slip between joints occur while maintaining compatibility, a rigid spring is placed in the transverse direction, connecting the rigid links together. This enforces 'no separation' between joint interface while allowing slip and girder rotation to occur freely.

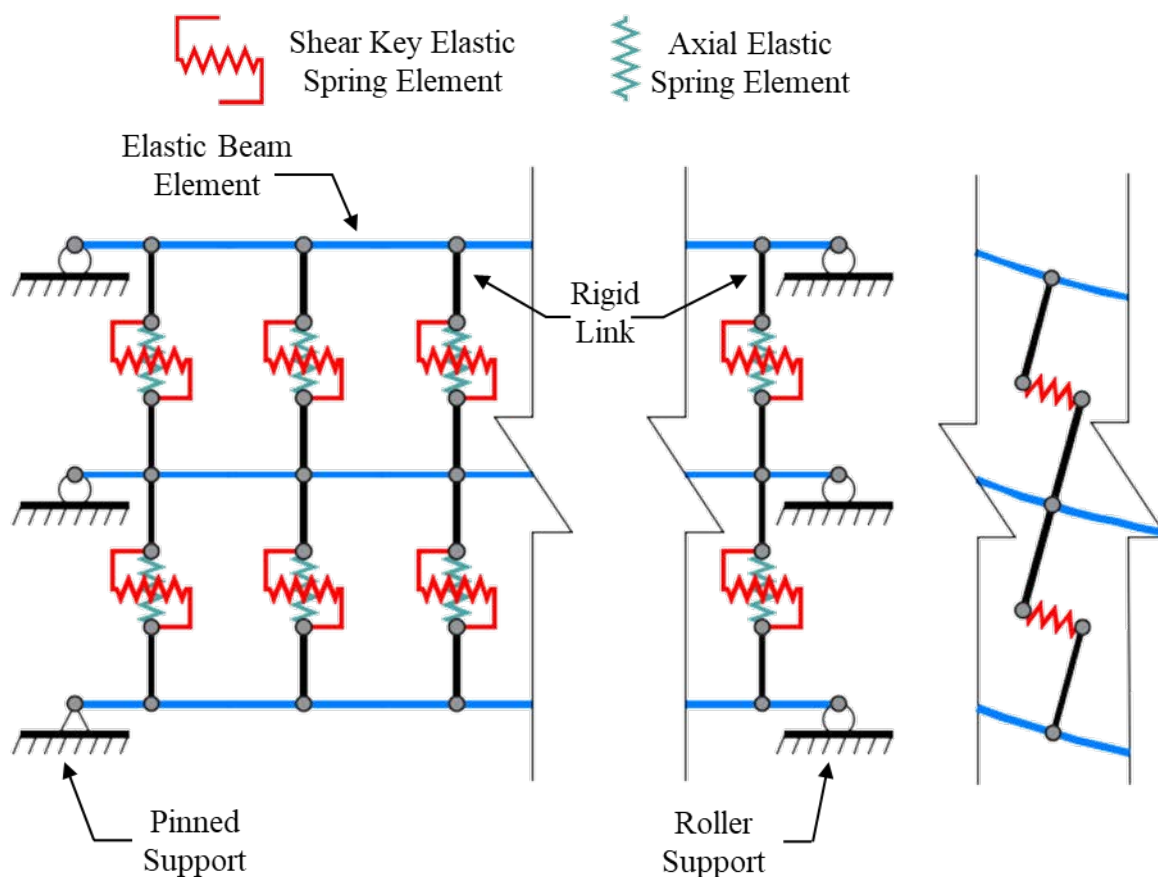


Figure 7.4: Global Computational Bridge Model

7.4 Validation

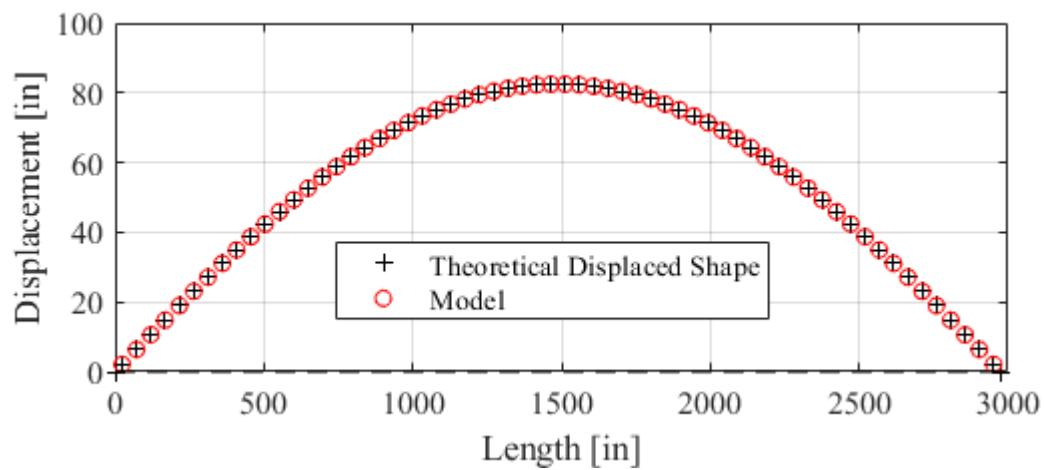
To validate the model, a single span, two girder bridge was modeled. The bridge model was statically loaded with a uniformly distributed load of 0.1 k/in applied to the girder elements. The length of span and geometry of the girders were based on Alaska Bridge 537. Bridge drawings can be seen in section 4.8.1 (Figure 4.24). A stiffness of $K_{\text{spring}} = 0.001$ k/in and $K_{\text{spring}} = 10000$ k/in was used to represent zero composite action and full composite action respectively. The closed form solution of displacement, Δ , and shear flow, q , were compared to model displacement and average shear flow. The average shear flow of the model is calculated with the force in the zero length spring divided by the tributary length, 4 feet. The closed form solutions are provided in Equation 7.6 and Equation 7.7. Where w is the uniformly distributed load, x is the length along the span, l is the span of the bridge, E is the modulus of elasticity, I is moment

of inertia, and Q is the first moment of area. While a single span is 125'-4 in., the span length was taken as 124' to be divisible by 4 in.. The distributed load was taken as 0.2k/in. I , E , and Q were calculated as 259517.5 in⁴, 4769 ksi, and 41850 in³ respectively. The comparison between the closed form solution and the computational models can be seen in Figure 7.5 through Figure 7.8 where error is given by Equation 7.8. It can be seen that the displaced shape is always bounded between the theoretical full composite displaced shape and the theoretical zero composite action displaced shape. Where the displaced shape error is less than -0.003% and 0.5% when assuming $K_{spring} = 0.001$ k/in and $K_{spring} = 10000$ k/in respectively. Error for the shear flow for $K_{spring} = 0.001$ k/in cannot be calculated because the theoretical value is zero, but the average shear flow of the computational model is negligible with a maximum value of 0.00014 k/in. The computational shear flow for the full interaction case ($K_{spring} = 10000$ k/in) had a maximum error of 0.235% to the theoretical solution.

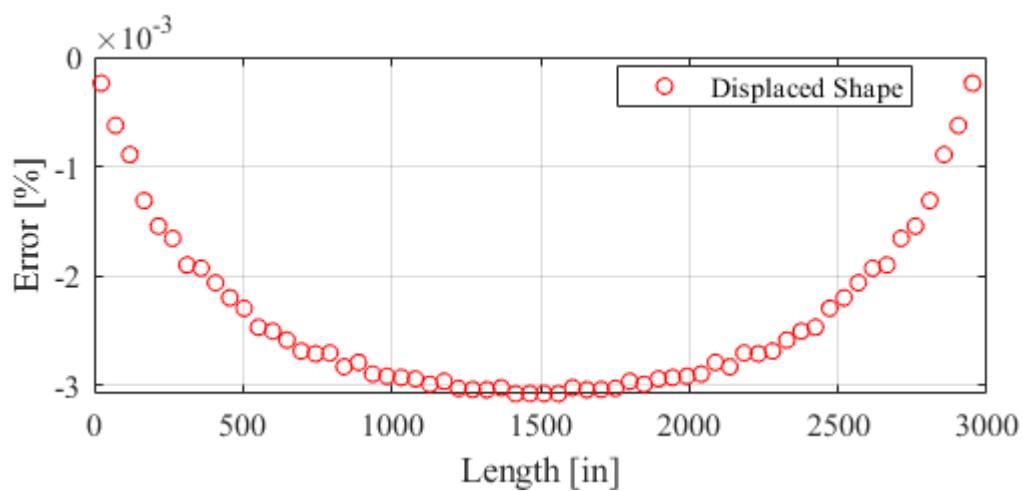
$$\Delta(x) = \frac{wx}{24EI} (l^3 - 2lx^2 + x^3) \quad \text{Equation 7.6}$$

$$q(x) = \frac{\left(\frac{wl}{2} - wx\right) Q}{I} \quad \text{Equation 7.7}$$

$$Error = \left(\left(\frac{model}{theroteical} \right) - 1 \right) \times 100\% \quad \text{Equation 7.8}$$



(a)



(b)

Figure 7.5: Displaced Shape Comparison with Theoretical Zero Composite Action when $K_{\text{spring}}=0.001\text{k/in}$ (a) Displaced Shape (b) Error

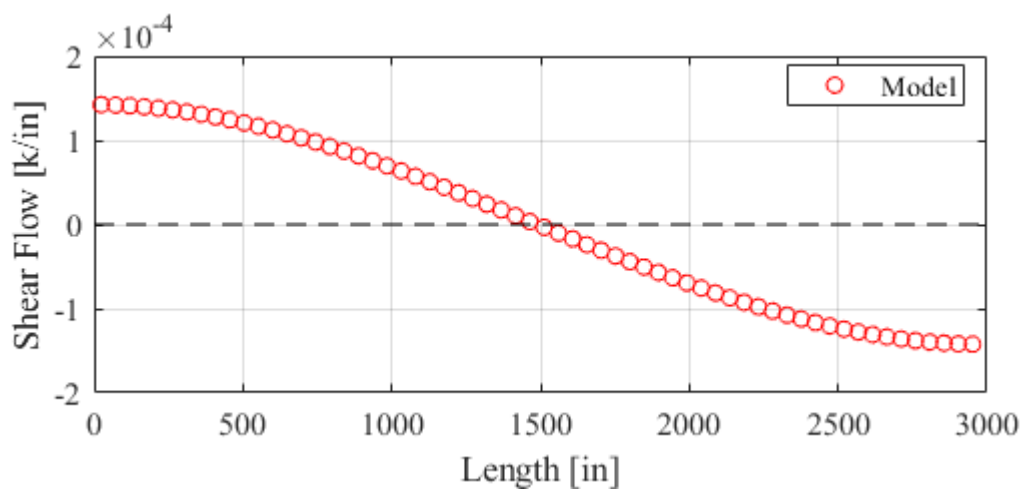
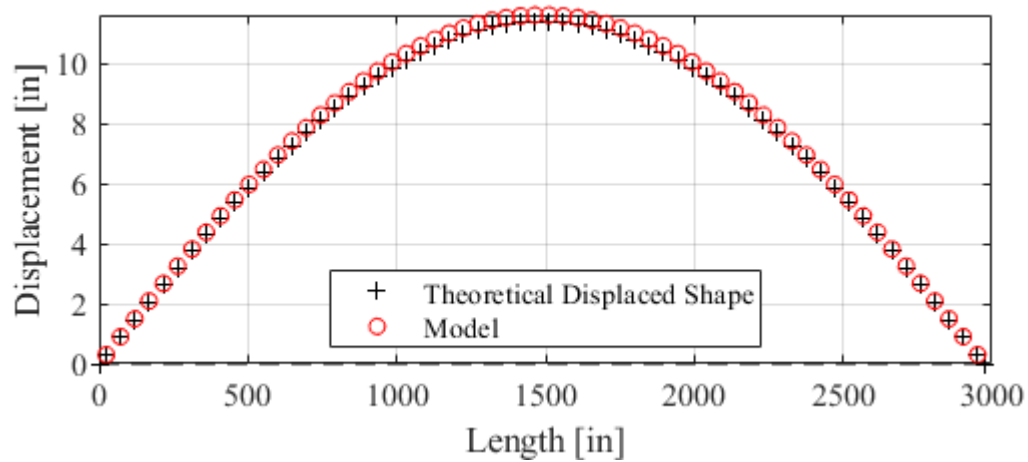
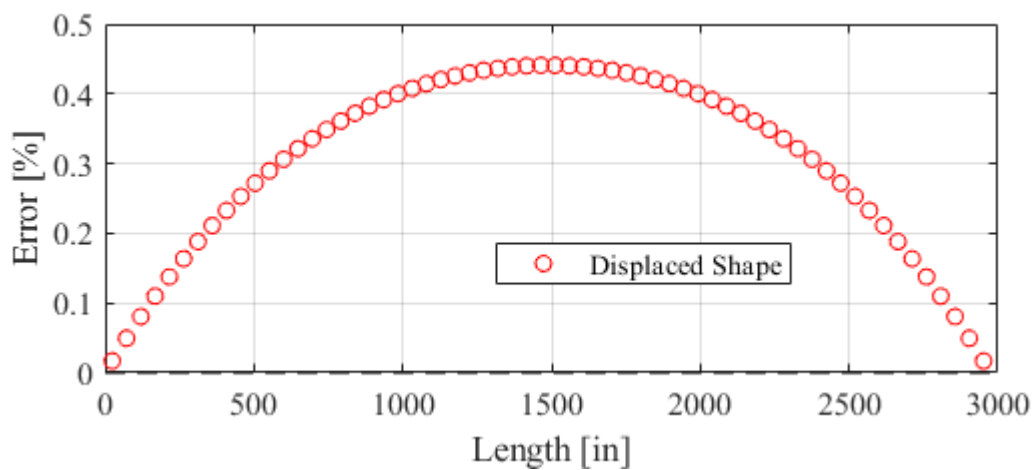


Figure 7.6: Shear Flow when $K_{\text{spring}}=0.001\text{k/in}$



(a)



(b)

Figure 7.7: Displaced Shape Comparison with Theoretical Full Composite Action when $K_{\text{spring}}=10000\text{k/in}$ (a) Displaced Shape (b) Error

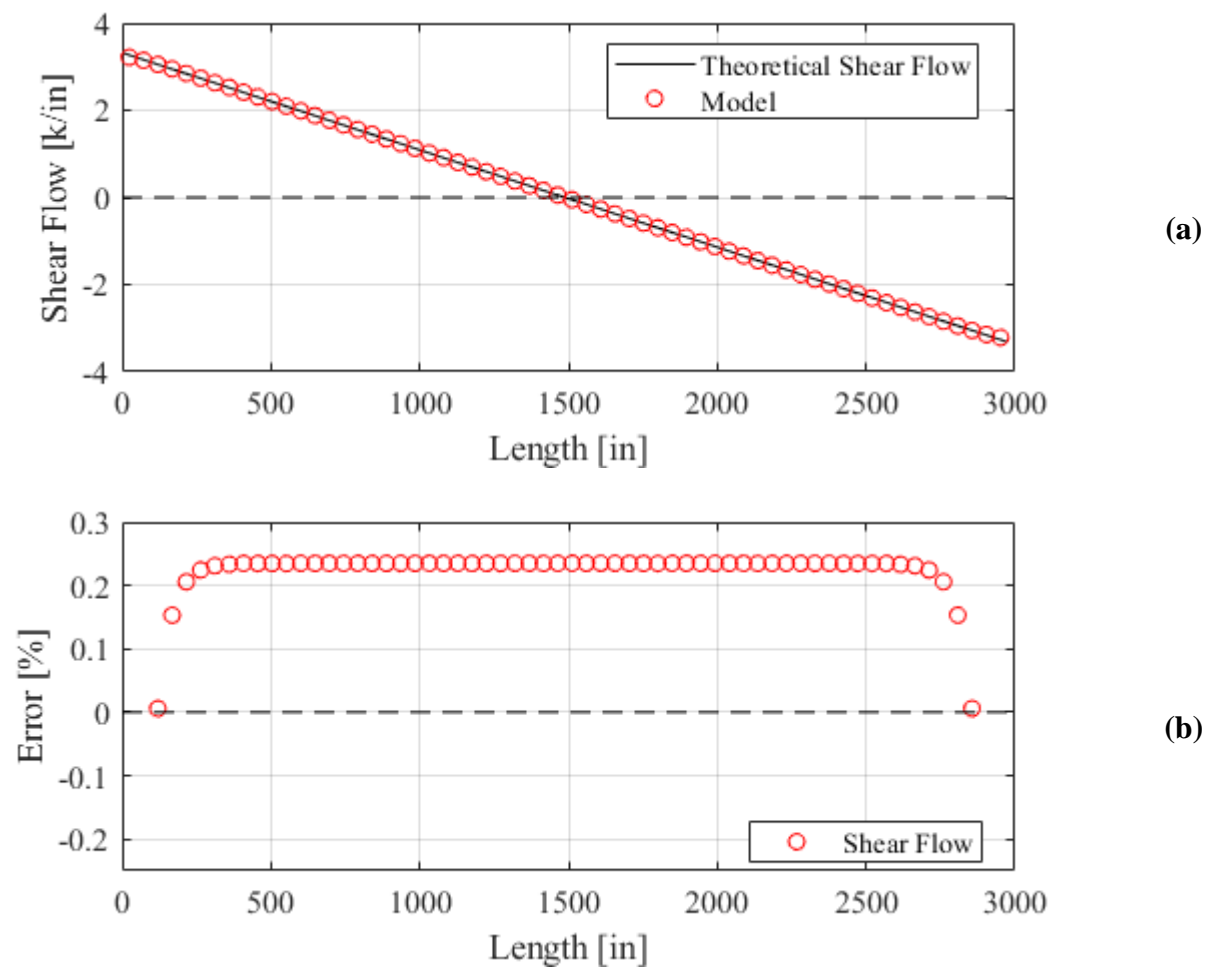
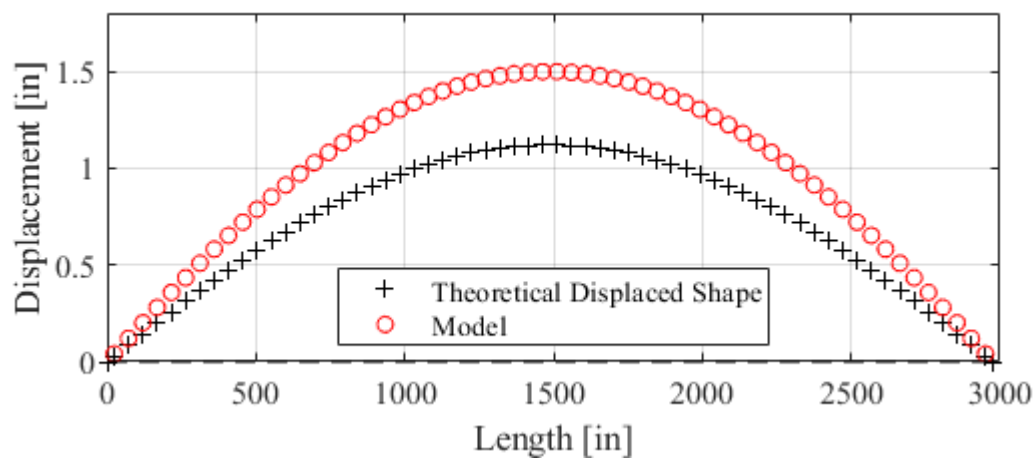


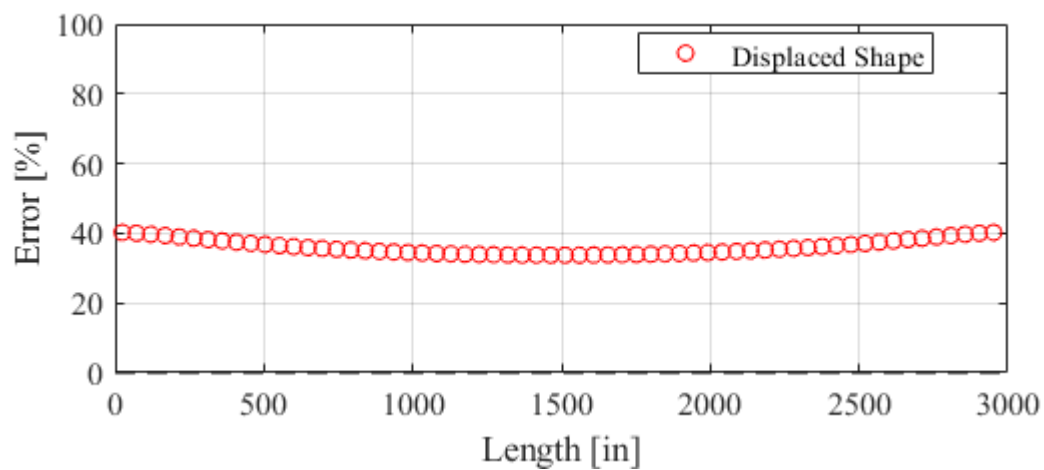
Figure 7.8: Shear Flow Comparison with Theoretical Full Composite Action when $K_{\text{spring}}=10000\text{k/in}$ (a) Shear Flow (b) Error

7.5 Bridge 537 Super Structure

The same was done for the six girder case to represent the actual geometry of Alaska Bridge 537. The secant stiffness associated with maximum capacity Test 7 ($K_{\text{spring}} = 2555 \text{ k/in}$) was used because Test 7 had the lowest capacity of all the tests and thus was more conservative. The results compared to the full composite action case and can be seen in Figure 7.9 and Figure 7.10. While error for the six girder case in the displaced shape at mid span is 34%, there is good agreement with the shear flow forces with error less than 6%. The maximum displacement at the center spring element was 1.50 inches. The displacements from assuming full composite action and zero composite action were 1.12 and 82.50 inches respectively. More analysis is needed to determine an appropriate equivalent stiffness, however it appears that before the maximum capacity of the joint is reached, the joint acts closer to full composite action.

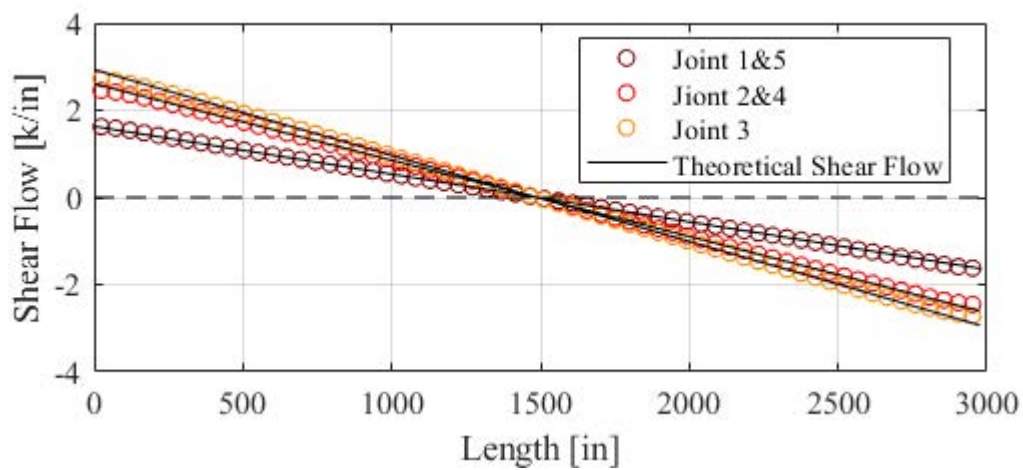


(a)

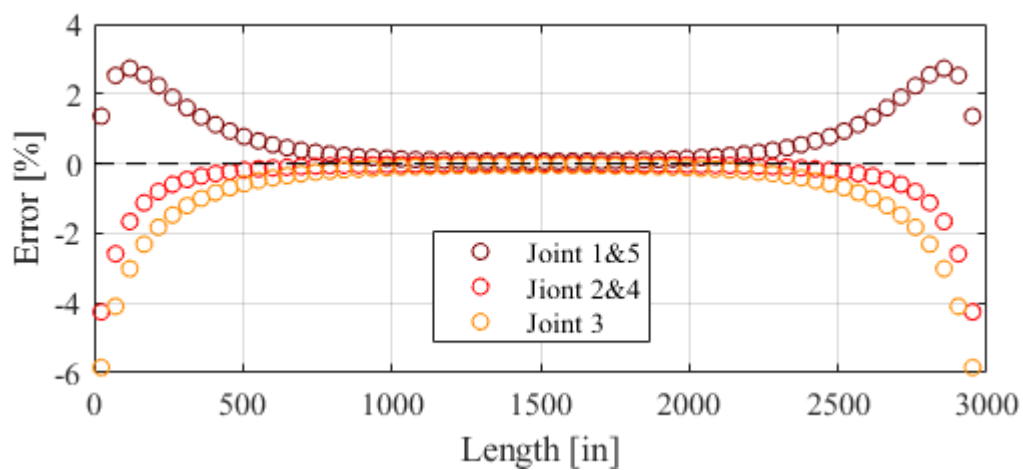


(b)

Figure 7.9: Six Girder Displaced Shape Comparison with Theoretical Full Composite Action when $K_{\text{spring}}=2555\text{k/in}$ (a) Displaced Shape (b) Error



(a)



(b)

Figure 7.10: Six Girder Shear Flow Comparison with Theoretical Full Composite Action when $K_{\text{spring}}=2555\text{k/in}$ (a) Shear Flow (b) Error

CHAPTER 8 EVALUATING YIELD LIMIT STATES FOR BRIDGE SUPERSTRUCTURES

It is necessary in DDBD and the AASHTO guide specification to use displaced shapes for design of bridge structures. In order to design the bridge to the limit state of choice, all possible vulnerabilities in a bridge system that can cause the design limit state must be addressed. One of these vulnerabilities will be yielding of the superstructure. This section addresses the nominal yield curvature for different bridge cross sections. The nominal yield curvature can be represented as shown in Equation 8.1, where c is a constant dependent on the cross section, ε_y is the yield strain of longitudinal rebar, and h is section width. Once the yield curvature is known, the yield displaced shape can be evaluated against the substructure.

In order to evaluate c , moment curvature analysis must be done on a range of possible sections. Two curvatures and corresponding moments need to be calculated to determine yield curvature, first yield curvature, ϕ'_y , first yield moment, M'_y , ultimate curvature, ϕ_u , and ultimate moment, M_u . The first yield curvature is the curvature profile at which the extreme longitudinal rebar yields. The ultimate curvature is defined as the extreme concrete fiber in compression reaching ultimate strain, extreme longitudinal rebar in tension reaching ultimate strain, or 20% strength loss of peak strength. The nominal yield curvature can then be represented by Equation 8.2.

$$\varphi_y = \frac{c\varepsilon_y}{h} \quad \text{Equation 8.1}$$

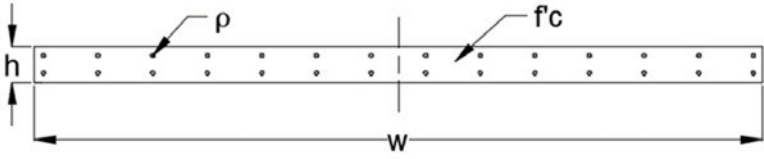
$$\varphi_y = \frac{M_u}{M'_y} \varphi'_y \quad \text{Equation 8.2}$$

8.1.1 Slab Bridges

In this section, conventionally reinforced slab bridge superstructures were examined via under a moment-curvature parametric study using the program CUMBIA (Montejo & Kowalsky, 2007). Four parameters were examined, and are provided in Table 8.1. The first parameter was width, which values were determined based on expected number of lanes a conventionally reinforced slab bridge is designed for. The second parameter was height of the slab, which

ranged from the minimum allowed depth of one foot to the value of two feet (AASHTO, 2010). Expected 28-day concrete strengths for typical bridges were used from 4 ksi to 8 ksi. The last parameter was longitudinal reinforcement ratio, which ranged from 1 to 3 percent. In total 54 moment-curvature analyses were performed. The constitutive models used for the materials were the Mander model (Mander, Priestley, & Park, 1988) for unconfined concrete and the King model (King, Priestley, & Park, 1986) for reinforcement steel. The ultimate strain values used for the concrete and steel were 0.12 and 0.0064 respectively. The curvature analysis provided ϕ'_y and ϕ_y values.

Table 8.1: Slab Bridge Yield Curvature Coefficient Study Matrix



The diagram shows a rectangular cross-section of a slab bridge. The width is labeled 'W' and the height is labeled 'h'. The concrete strength is labeled 'f'c' and the reinforcement ratio is labeled 'rho'. The diagram also shows a grid of reinforcement bars within the slab.

Width [in]	Height [in]	f'c [ksi]	ρ [%]
20	12	4	1
30	18	6	2
	24	8	3

To determine which variables were significant to ϕ'_y and ϕ_y , regression analysis was performed and the coefficient of determination, R^2 was established for each variable. Linear regression was used to compare yield curvatures with the four parameters, the results can be seen in Figure 8.1 to Figure 8.4. It was found that depth, 28-day concrete strength, and longitudinal steel reinforcement ratio have R^2 values lower than 0.05, thus are not significant. Width showed significance with, $R^2 = 0.936$ and 0.950 for ϕ'_y and ϕ_y respectively. Thus both definitions of yield curvature are a function of width. This has been seen in the past with other concrete cross sections and the dimension perpendicular to the axis of bending, such as circular columns, rectangular columns, and rectangular concrete walls (Priestley, Calvi, & Kowalsky, 2007).

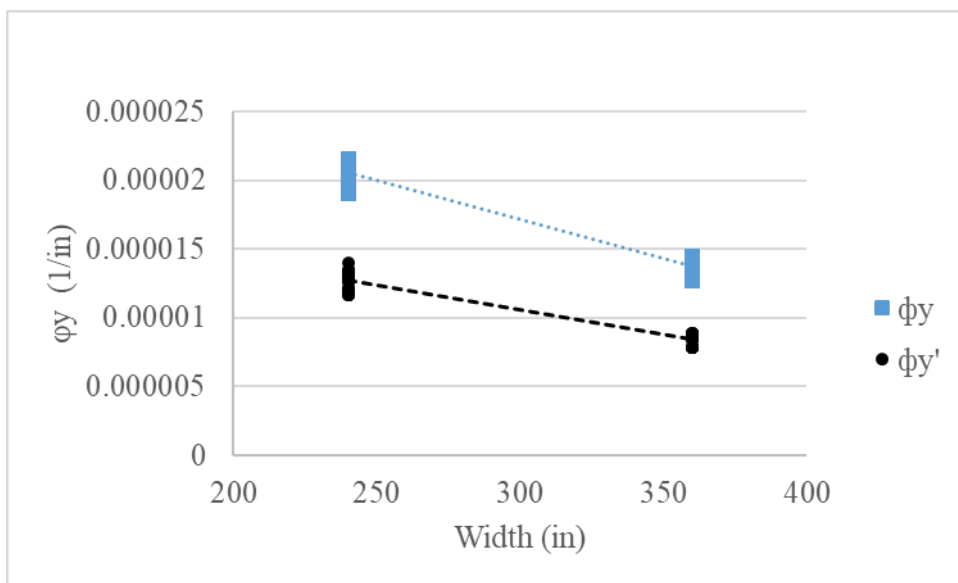


Figure 8.1: Slab Bridge Yield Curvature vs Width

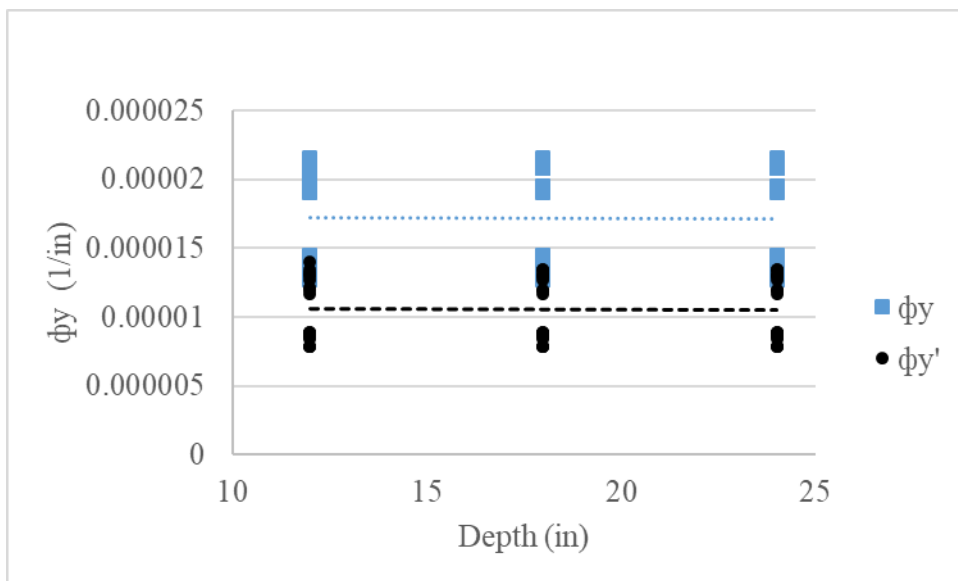


Figure 8.2: Slab Bridge Yield Curvature vs Depth

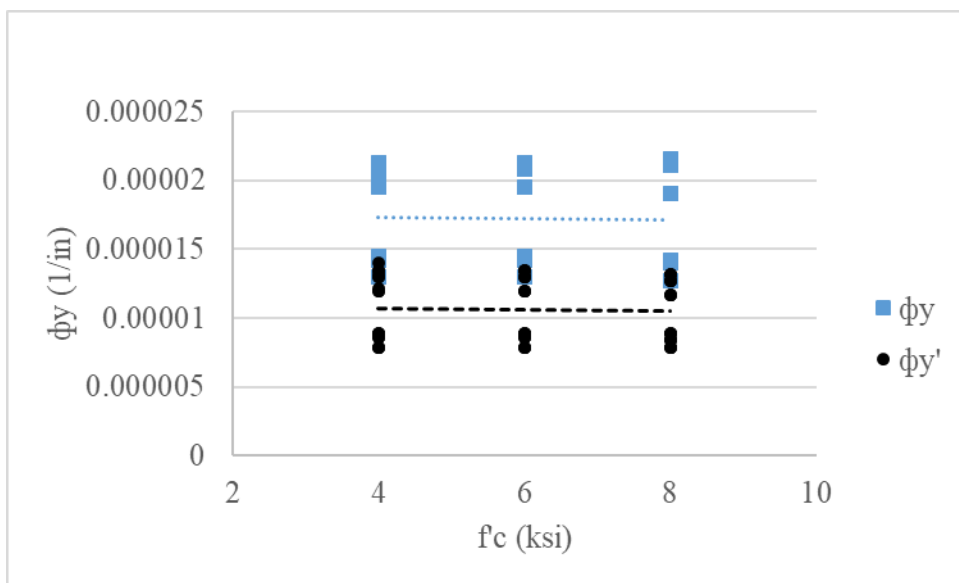


Figure 8.3: Slab Bridge Yield Curvature vs f'_c

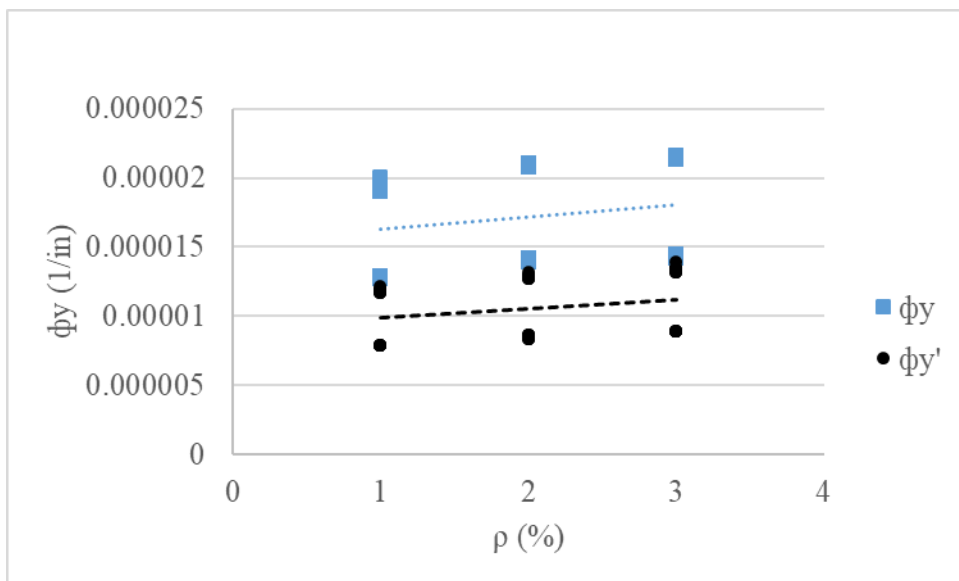


Figure 8.4: Slab Bridge Yield Curvature vs ρ

Yield curvature can then be taken as Equation 8.1 with no additional parameters and the non-dimensional coefficient C can be solved for both ϕ'_y and ϕ_y and denoted as C' and C respectively as seen in Figure 8.5. The mean values of C' and C were 1.34 and 2.18 respectively. All points fell within a +/- 10% band of the mean. Similar results for nominal yield curvature were found for rectangular concrete walls and rectangular masonry walls (Priestley et al., 2007).

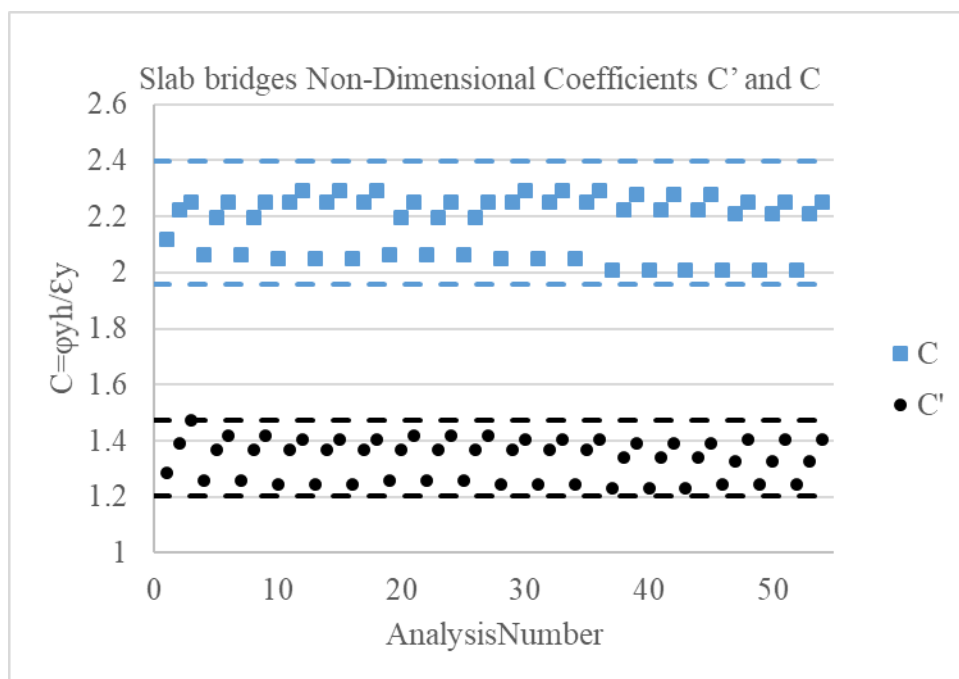


Figure 8.5 Slab bridges Non-Dimensional Coefficients C' and C

CHAPTER 9 SUMMARY, RECOMMENDATIONS AND FUTURE WORK

This report describes the research performed to establish the baseline characteristics of the bridges with longitudinal shear keys loaded in the transverse direction. An experimental program was conducted in which 10 large scale tests were performed on a unit length of a common used longitudinal joint found in bulb-tee girders. The program evaluated monotonic and cyclic loading, while looking at grout strength, bond strength, polyester polymers, and different shear connector inserts. A subassembly computational model was developed to represent the experimental test setup. A 2D global computational model was developed using OpenSEES that used springs to represent the longitudinal shear keys. Lastly moment curvature analysis was utilized to develop yield curvature equations for bridge superstructures. This section provides a summary and recommendations based on these observations.

9.1 Experimental Program

The experimental program was conducted to determine the shear-slip behavior a commonly used longitudinal shear key detail found in bulb-tee girder bridges. The program was separated into Phase I and Phase II. Phase I focused on monotonic and cyclic loading, grout strength and polyester polymers. While Phase II examined bond strength, alternate connectors and the use of polyester polymer with an alternate connector. The key observations are listed below.

1. The first observation made was that the existing shear connector insert does not behave as originally anticipated. Instead of shear yielding of the shear plate, the embedded rebar that compose the connector inserts bear against the concrete until concrete crushing occurs. The crushing alters the boundary conditions of the rebar and the rebar develops a plastic hinge and begins to act in double bending. This bending is believed to cause cracks in the cover concrete, which leads to spalling and a significant reduction in strength.

2. Additionally, the strength and stiffness of the joint are dominated by the grout component of the connection. This makes the strength of the connection proportional to the strength of the grout. Additionally, Equation 9.1 was found to be a suitable estimator of grout strength. It should be noted that equation is intended to be used in areas moderate corrosion conditions according AASHTO (2010)

$$f_t = 0.19 \sqrt{f'_c} \text{ (ksi) or } f_t = 6\sqrt{f'_c} \text{ (psi)} \quad \text{Equation 9.1}$$

3. It was observed that cyclic loading had minor effect on the joint up until maximum strength capacity was achieved. Where slight degradation was observed in the loading stiffness of the response. But once maximum strength is exceeded, cyclic loading was observed to reduce the force capacity and therefore stiffness of the connection between increments of three cycle sets.
4. Experiential testing found that surface preparation to the concrete interface of the shear key improves performance of the joint under shear loading. Surface preparation should be done according to manufacturer recommendations which typically means grout being applied to sound and roughened concrete. Tests that followed manufacturer recommendations had a peak strength of at least 120% greater than those tests where recommendations were neglected.
5. Once the grout cracks down the length of the joint, the strength of the joint begins to drop. It is not until cracks run down the vertex of the shear key face and the cover concrete spalls that the strength reduced. This was examined for conventional grout and PPC. It was observed that the existing connection encourages this behavior as the inserted connectors displace in bending, prying up the cover concrete.
6. While polyester polymer concrete has a low compressive strength compared to conventional grouts, the experiments show that the PPC provided the highest connection strength capacity. Additionally, the displacement at which strength loss begin was

noticeably higher. The PPC was also observed to better redistribute force in the inelastic range. Shear cracks forming in the concrete took longer to occur and were more evenly distributed along the length of the joint. Additionally, compared to conventional high strength grout, combined strains provided from early age shrinkage and the thermal coefficient of expansion are comparable.

7. Two new shear connector inserts were developed as seen in Figure 9.1. Alternate connector 1 utilized #4 embedded rebar welded at 45° to a 1 in. thick steel plate to locate the rebar between the mats of steel that compose the reinforcement in the deck of the bulb-tee girders. Alternate connector 2 was a modified version of alternate connector 1, where a plate fin is welded on the plate perpendicular to the joint to increase bearing area and reduce potential rotation of the embedded shear connectors

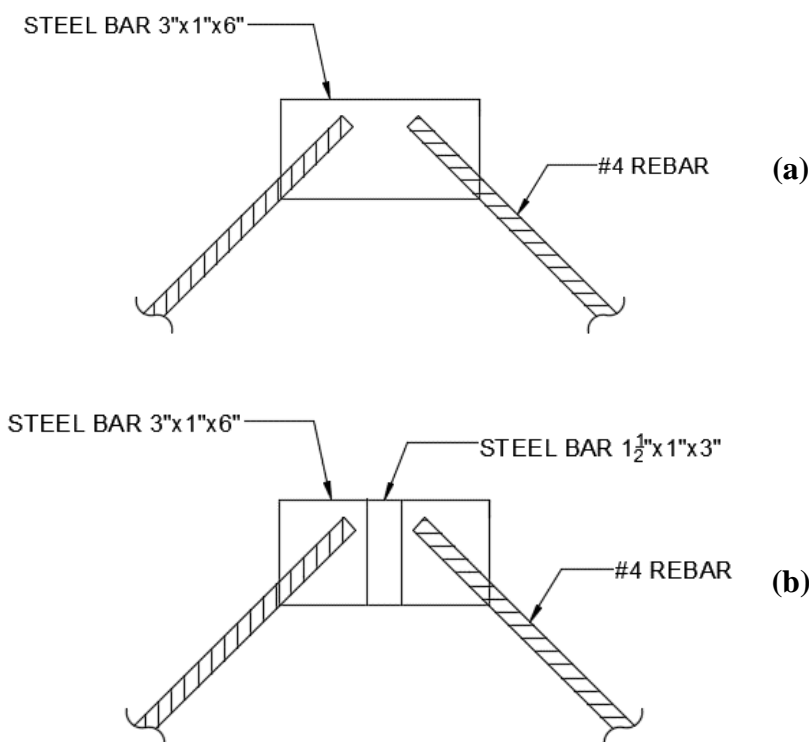


Figure 9.1: Elevation View (a) Alternate Connector 1 (b) Alternate Connector 2

8. While a truss analogy has been used to estimate capacity, the method underestimates the strength as it doesn't account for bearing. The alternate connections were observed to maintain more residual strength up until rebar fracture, which occurs at approximately a cyclic displacement of +/- 0.3 inches. Additionally, the rebar no longer exhibit bending but rather axial deformation up until fracture. Since both connections exhibited the same failure mechanism and the additional welded plate did not add to the alternate connection performance, alternate connector 1 is proposed. While it is unclear if the alternate connection is desirable under earthquake loading, the alternate connection provides less damage up until bar fracture and is recommended pending additional computational studies.

9.2 Global Computational Model

A 2D analytical model was developed in OpenSees to represent the continuous bridge superstructure. The model was subjected to uniformly distributed static loading applied to the girders. Elastic beam elements were used to represent the girders, while zero length springs in the longitudinal direction represented the longitudinal shear key. Rigid links and springs in the transverse direction were utilized to enforce geometry and compatibility.

1. While currently the model uses elastic elements, the model has been validated to provide the displaced shape and shear flow of the closed form solution for full composite action and zero composite action. These two conditions represent the lower and upper bound behavior of the bridge.
2. A 2D analytical model was developed using OpenSees to represent the experimental portion of the research. The model utilized zero length springs with the Pinching4 material model to capture the shear slip behavior observed in the tests. Due to the results being load history dependent, the model only validates the use of nonlinear springs to represent the joint.
3. Using a spring stiffness consistent with the joint before maximum strength loss ($K_{\text{spring}} = 2555 \text{ k/in}$) and bridge geometry representative of Alaska Bridge 537, the response of the

global computational model was most similar to full composite action. The maximum displacement at the center spring element was 1.50 inches. The displacements from assuming full composite action and zero composite action were 1.12 and 82.50 inches respectively. Based on the case study, it is recommended that if the expected shear flow is below the capacity of the joint, the joint should be treated as acting in full composite action until more computational studies are done.

4. More computational studies will be done with an increased complexity of the model. Items to be added to model are listed below:
 - Incorporating the inelastic springs mentioned in the sub-assembly model.
 - Alternative boundary conditions to represent fixed and flexible abutments and flexible abutments.
 - Including nonlinear springs to represent bridge bents along the length of the bridge.
 - Including rigid links or high axial stiffness elements to represent intermediate diaphragms.
 - Conduct nonlinear time history analysis using earthquake ground motions.

The goal of the future work will be to determine important variables for lateral displacement predictions such as superstructure stiffness, substructure stiffness, and end support conditions. Another goal is to define the effective stiffness of the superstructure based on the longitudinal keyway.

9.3 Evaluating Yield Limit States for Bridge Super Structures

Moment curvature analysis has been used to develop equations for first yield and nominal yield curvature of superstructures. The yield curvature can be used to in design to ensure the superstructure does not exceed the yielding limit state before substructure limit states are meet. Two yield limit state can be defined, first yield and equivalent yield. While equivalent yield has been used in the past for displacement based design, first yield may be more appropriate for superstructures which should remain elastic. The findings and future work for this portion of the work are listed below.

1. The yield curvature for slab bridges can be defined by Equation 9.2 and Equation 9.3 for first yield and nominal yield respectively, where C' and C were found to be 1.34 and 2.18 respectively.

$$\varphi'_y = \frac{c'\varepsilon_y}{h} \quad \text{Equation 9.2}$$

$$\varphi_y = \frac{c\varepsilon_y}{h} \quad \text{Equation 9.3}$$

2. Future work will be done to determine C' and C for other bridge cross sections as listed below:
 - Bulb-tee girder
 - Box girder

REFERENCES

- AASHTO. (2010). AASHTO LRFD Bridge Design Specifications. *Chemistry &*, 280(7), 1635 pp. <https://doi.org/10.1111/febs.12237>
- ACI 318. (2014). *Building code requirements for structural concrete and commentary*. ACI *Standard and Report*. <https://doi.org/10.2748/tmj/1232376167>
- Afey, H. M., Sennah, K., Tu, S., Ismail, M., & Kianoush, R. (2015). Development and study of deck joints in prefabricated concrete bulb-tee bridge girders: Experimental evaluation. *Bridge Structures*, 11(1,2), 55–71. <https://doi.org/10.3233/BRS-150086>
- AKDOT. (2017). Alaska Bridges and Structures Manual. Alaska Of, Department Transportation And Facilities, Public.
- ASTM. (2010). Standard Test Method for Compressive Strength of Hydraulic Cement Mortars (Using 2-in . or [50-mm] Cube Specimens) 1. *Chemical Analysis*, (C109/C109M – 11b), 1–9. <https://doi.org/10.1520/C0109>
- ASTM. (2014). ASTM A370: Standard Test Methods and Definitions for Mechanical Testing of Steel Products. *ASTM International*, 1–50. <https://doi.org/10.1520/A0370-14.2>
- ASTM. (2017). ASTM C490: Standard Practice for Use of Apparatus for the Determination of Length Change of Hardened Cement Paste, Mortar, and Concrete¹ This, 1–5. <https://doi.org/10.1520/C0490>
- ASTM C39. (2016). Standard Test Method for Compressive Strength of Cylindrical Concrete Specimens. *American Society for Testing and Materials*, 1–7. <https://doi.org/10.1520/C0039>
- ASTM C579-01. (2001). Standard Test Methods for Compressive Strength of Chemical-Resistant Mortars , Grouts , Monolithic Surfacing , and Polymer Concretes 1, *01*(Reapproved 2012), 1–4. <https://doi.org/10.1520/C0579-01R12.2>

- ASTM C666/C666M - 03. (2008). *Astm C666/C666M - 03. Standard Test Method for Resistance of Concrete to Rapid Freezing and Thawing, 03*, 1–6.
<https://doi.org/10.1520/C0666>
- ASTM E1356-08. (2018). *Standard Test Method for Assignment of the Glass Transition Temperatures by Differential Scanning, 08(Reapproved 2014)*, 8–11.
<https://doi.org/10.1520/E1356-08R14.2>
- C496-17, A. (2018). *Standard Test Method for*, 1–5. <https://doi.org/10.1520/C0496>
- Cao, L., & Naito, C. (2009). *Precast Concrete Double-Tee Connectors, Part 2: Shear Behavior. PCI Journal, 54(2)*, 97–115.
- Djazmati, B., & Pincheira, J. A. (2004). *Shear stiffness and strength of horizontal construction joints. ACI Structural Journal*.
- Fattah Shaikh, A., & Feile, E. P. (2004). *Load Testing of a Precast Concrete Double-Tee Flange Connector. PCI Journal*. Retrieved from <http://www.pci.orgwww.pci.org/pdf/publications/journal/2004/May-June/JL-04-MAY-JUNE-6.pdf>
- Fleischman, R. B., Naito, C. J., Restrepo, J., Sause, R., Ghosh, S. K., Wan, G., ... Cao, L. (2005). *Seismic design methodology for precast concrete diaphragms part 2: Research program. PCI Journal, 50(6)*, 14–31. Retrieved from https://www.engineeringvillage.com/share/document.url?mid=cpx_18a992f10891494e16M5b8e2061377553&database=cpx
- Fleischman, R. B., Restrepo, J., Ghosh, S. K., Naito, C. J., & Sause, R. (2005). *Seismic design methodology for precast concrete diaphragms part 1: Design framework. PCI Journal, 50(5)*, 68–83. Retrieved from

https://www.engineeringvillage.com/share/document.url?mid=cpx_18a992f1078f416527M6c6a2061377553&database=cpx

- Fleischman, R. B., Sause, R., Pessiki, S., & Rhodes, A. B. (1998). Seismic Behavior of Precast Parking Structure Diaphragms. *PCI Journal*, 38–53.
- He, Z. Q., Ma, Z. G. J., Chapman, C. E., & Liu, Z. (2013). Longitudinal Joints with Accelerated Construction Features in Decked Bulb-Tee Girder Bridges: Strut-and-Tie Model and Design Guidelines. *Journal of Bridge Engineering*, 18(5), 372–379.
[https://doi.org/10.1061/\(asce\)be.1943-5592.0000378](https://doi.org/10.1061/(asce)be.1943-5592.0000378)
- Hofheins, C. L., Reaveley, L. D., & Pantelides, C. P. (2002). Behavior of welded plate connections in precast concrete panels under simulated seismic loads. *PCI Journal*, 47(4), 122–133. Retrieved from
https://www.engineeringvillage.com/share/document.url?mid=cpx_ed465f22d6033a6M59d51981717318&database=cpx
- Issa, M. A., Anderson, R., Domagalski, T., Asfour, S., & Islam, M. S. (2007). Full-scale testing of prefabricated full-depth precast concrete bridge deck panel system. *ACI Structural Journal*, 104(3), 324–332.
- Jayaprakash, A., Nau, J. M., Kowalsky, M., & Pour-Ghaz, M. (2019). *Durability of the Grouted Shear Stud Connection in Cold Climates*. Raleigh, NC.
- Kim, H.-Y., Lee, S.-Y., & Song, J.-J. (2013). A STUDY ON A GROUT JOINT FOR PRECAST PRESTRESSED. <https://doi.org/10.3850/978-981-07-5354-2.St-38-95>
- Kim, Y. H., & Trejo, D. (2014). Shear-transfer mechanism and design of shear connectors for full-depth precast deck panel system. *ACI Structural Journal*, 111(4), 935–944.
<https://doi.org/10.14359/51686740>

- King, D. J., Priestley, M., & Park, R. (1986). *Computer Programs for Concrete Column Design. Research Report 86/12*. NewZealand.
- Li, L., & Ma, Z. J. (2010). Effect of Intermediate Diaphragms on Decked Bulb-Tee Bridge System for Accelerated Construction. *Journal Of Bridge Engineering*, 15(December), 715–722. [https://doi.org/10.1061/\(ASCE\)BE.1943-5592.0000108](https://doi.org/10.1061/(ASCE)BE.1943-5592.0000108)
- Li, L., Ma, Z. J., Griffey, M. E., & Oesterle, R. G. (2010). Improved Longitudinal Joint Details in Decked Bulb Tees for Accelerated Bridge Construction: Concept Development. *Journal of Bridge Engineering*, 15(3), 327–336. [https://doi.org/10.1061/\(ASCE\)BE.1943-5592.0000067](https://doi.org/10.1061/(ASCE)BE.1943-5592.0000067)
- Li, L., Ma, Z. J., & Oesterle, R. G. (2010). Improved Longitudinal Joint Details in Decked Bulb Tees for Accelerated Bridge Construction: Fatigue Evaluation. *Journal of Bridge Engineering*, 15(5), 511–522. [https://doi.org/10.1061/\(ASCE\)BE.1943-5592.0000097](https://doi.org/10.1061/(ASCE)BE.1943-5592.0000097)
- Lowes, L. N., Mitra, N., & Altoontash, A. (2004). A Beam-Column Joint Model for Simulating the Earthquake Response of Reinforced Concrete Frames A Beam-Column Joint Model for Simulating the Earthquake Response of Reinforced Concrete Frames, PEER Report 2003/10. *PEER Report 2003/10*.
- Ma, Z., Chaudhury, S., Millam, J. L., & Hulsey, J. L. (2007). Field test and 3D FE modeling of decked bulb-tee bridges. *Journal of Bridge Engineering*, 12(3), 306–314. [https://doi.org/10.1061/\(ASCE\)1084-0702\(2007\)12:3\(306\)](https://doi.org/10.1061/(ASCE)1084-0702(2007)12:3(306))
- Ma, Z. J., Cao, Q., Chapman, C. E., Burdette, E. G., & French, C. E. W. (2012). Longitudinal joint details with tight bend diameter U-bars. *ACI Structural Journal*, 109(6), 815–824. [https://doi.org/10.1061/\(ASCE\)ST.1943-541X.0000518](https://doi.org/10.1061/(ASCE)ST.1943-541X.0000518).
- Mander, J. B., Priestley, M. J. N., & Park, R. (1988). Theoretical Stress-Strain Model for

- Confined Concrete. *Journal of Structural Engineering, ASCE*.
[https://doi.org/10.1061/\(ASCE\)0733-9445\(1988\)114:8\(1804\)](https://doi.org/10.1061/(ASCE)0733-9445(1988)114:8(1804))
- Mazzoni, S., McKenna, F., Scott, M. H., & Fenves, G. L. (2006). Open System for Earthquake Engineering Simulation (OpenSEES) User Command-Language Manual. Pacific Earthquake Engineering Research Center. *University of California, Berkeley*, 465.
- Montejo, L. A., & Kowalsky, M. J. (2007). CUMBIA – Set of Codes for the Analysis of Reinforced Concrete Members. Title. *Technical Report No. IS-07-01*.
- Muir, L., & Duncan, C. J. (2011). The AISC 2010 Specification and the 14th Edition Steel Construction Manual. [https://doi.org/10.1061/41171\(401\)58](https://doi.org/10.1061/41171(401)58)
- Naito, C., Pao, L. L., & Peter, W. (2009). Precast concrete double-tee connections, part 1: Tension Behavior. *Pci Journal*, 54(1), 49–66.
- Northern Digital Inc. (2019). Certus HD. Retrieved from
<https://www.ndigital.com/msci/products/certus-hd/>
- Pincheira, J. A., Oliva, M. G., & Kusumo-Rahardjo, F. I. (1998). Tests on double tee flange connectors subjected to monotonic and cyclic loading. *PCI Journal*, 43(3), 82–96.
Retrieved from
https://www.engineeringvillage.com/share/document.url?mid=cpx_b753f811bffc2df601b262061377553&database=cpx
- Pincheira, J. A., Oliva, M. G., & Zheng, W. (2005). Behavior of Double-Tee Flange Connectors Subjected to In-Plane Monotonic and Reverse Cyclic Loads. *PCI Journal*, c, 2–24.
- Precast/Prestressed Concrete Institute. (2010). *PCI design handbook: precast and prestressed concrete*. Precast/Prestressed Concrete Institute.
- Priestley, M., Calvi, G. M., & Kowalsky, M. J. (2007). Displacement-based seismic design of

- structures. *Building*, 23(33), 1453–1460. [https://doi.org/10.1016/S0141-0296\(01\)00048-7](https://doi.org/10.1016/S0141-0296(01)00048-7)
- Sennah, K., & Afefy, H. M. (2015). Development and study of deck joints in prefabricated concrete bulb-tee bridge girders: Conceptual design. *Bridge Structures*, 11(1–2), 33–53. <https://doi.org/10.3233/BRS-150087>
- Smith, M. Z., Yue Li, & Bulleit, W. M. (2011). A method for evaluation of longitudinal joint connections of decked precast concrete girder bridges. *Structural Engineering and Mechanics*, 40(3). Retrieved from https://www.engineeringvillage.com/share/document.url?mid=inspec_ef5502138de283f20M69582061377553&database=ins
- Stanton, J. F., & Mattock, A. H. (1987). LOAD DISTRIBUTION AND CONNECTION DESIGN FOR PRECAST STEMMED MULTIBEAM BRIDGE SUPERSTRUCTURES. *National Cooperative Highway Research Program Report*. Retrieved from https://www.engineeringvillage.com/share/document.url?mid=cpx_2082566&database=cpx
- Venuti, W. J. (1970). Diaphragm Shear Connectors Between Flanges of Prestressed Concrete T-Beams. *PCI Journal*, 67–78.
- Wood, S. L., Stanton, J. F., & Hawkins, N. M. (2000). New Seismic Design Provisions for Diaphragms in Precast Concrete Parking Structures. *PCI Journal*, 50–65.
- Young-Ji Park, B., & H-S Ang, A. (1985). MECHANISTIC SEISMIC DAMAGE MODEL FOR REINFORCED CONCRETE. *Journal of Structural Engineering*. <https://doi.org/10.1061>
- Zhu, P., Ma, Z. J., & French, C. E. (2012). Fatigue Evaluation of Longitudinal U-Bar Joint Details for Accelerated Bridge Construction, 17(April), 201–210. [https://doi.org/10.1061/\(ASCE\)BE.1943-5592.0000255](https://doi.org/10.1061/(ASCE)BE.1943-5592.0000255).

APPENDIX